

NORTHWESTERN UNIVERSITY

Accelerating the Materials-by-Design Approach for Hairy Nanoparticle Assemblies  
using Coarse-grained Molecular Dynamics Simulations

A DISSERTATION

SUBMITTED TO THE GRADUATE SCHOOL

IN PARTIAL FULFILLMENT OF THE REQUIREMENTS

for the degree

DOCTOR OF PHILOSOPHY

Field of Mechanical Engineering

By

Nitin Krishnamurthy Hansoge

EVANSTON, ILLINOIS

March 2021

© Copyright by Nitin Krishnamurthy Hansoge 2021

All Rights Reserved

## ABSTRACT

Recent advancements in processing and manufacturing techniques have spurred an exponential increase in use of polymer nanocomposites in a variety of applications. A key challenge in using these nanocomposites effectively is the dispersion of nanoparticles in the polymer matrix. Matrix-free assemblies of polymer grafted nanoparticles, called hairy nanoparticles assemblies (aHNPs) have come into spotlight as they overcome the dispersion issues of traditional polymer nanocomposites. These aHNPs provide better structural order that allows functional and mechanical properties to be tailored more accurately.

Traditional material development involves iterative experimentations to characterize and optimize the mechanical properties, which is a costly and time-consuming process. The timeframe, from material discovery to market deployment, can be significantly reduced with the help of high performance computational tools. In this work, we describe computational approaches that significantly accelerate the materials-by-design process. The first step towards achieving this goal is to develop an effective coarse-graining (CG) strategy, namely the energy renormalization approach, that enhances the spatiotemporal scales of molecular dynamics (MD) simulations while quantitatively capturing the thermomechanical behavior of materials.

Next, we apply these CG techniques to model the aHNPs and explore the mechanics of these materials. While experimental studies have characterized the mechanical properties of aHNPs, effective strategies to improve both the mechanical stiffness and toughness of aHNPs are lacking given the general conflicting nature of these two properties and the large number of molecular parameters involved in the design of aHNPs. Thus, we develop a computational framework combining machine learning with CG-MD simulations, called metamodel based design

optimization, to establish design strategies for achieving optimal mechanical properties. We develop theoretical scaling laws that govern the polymer chain conformations in these aHNPs and show the universality of these laws by examining the conformations of grafted polymers with varying chemistry, persistence length and side-group size.

Finally, we develop an effective interaction between nanoparticles in aHNPs with different design parameters, i.e., polymer chain length, grafting density and polymer chemistry using the potential of mean force approach. With the development of this interatomic potential between the nanoparticles, we propose a mesoscopic model for nanoparticle assemblies that circumvents the need to explicitly simulate polymer chains, significantly improving the computational efficiency by extending the spatiotemporal scales by 6-7 orders of magnitude.

All-together, these studies provide guidance and strategies to accelerate the materials-by-design approach for hairy nanoparticle assemblies. The insights obtained from this work will lay the foundation in advancing mechanical performance of composites and other relevant structural materials.

**Thesis Advisor:**

Dr. Sinan Ketten

Department of Civil and Environmental Engineering and Department of Mechanical Engineering

**Final Examination Committee:**

Dr. Sinan Ketten (Chair)

Dr. Wei Chen

Dr. Kenneth Shull

## ACKNOWLEDGEMENTS

The first person whom I am eternally grateful for providing me this opportunity is Dr. Sinan Ketten, my PhD advisor. He introduced me to the exciting world of computational modeling and mechanics of polymer nanocomposites. He gave me the freedom to pursue the project of my choice and allowed me explore the nanoscale mechanics of polymer grafted nanoparticles. His guidance and support has helped me immensely throughout my graduate school.

My parents (Mr. H.S. Krishnamurthy and Mrs. Geeta Krishnamurthy) mean the world to me and their love and support has been a key motivation for me to complete this dissertation. My mom, who is also doing her PhD at the age of 60, has been a true inspiration for me. My deepest gratitude to Sruthi Venkataramanababu, my fiancé, for her constant source of support and encouragement. I would also like to mention Nishu, my dog, for (not) helping me with my thesis writing.

I am immensely thankful to my committee members, Dr. Wei Chen and Dr. Kenneth Shull. I took the design course offered by Dr. Chen which kick started my PhD thesis. Through her able guidance, I was able to convert the final project of the course to my first publication. I also would like to thank Dr. Shull who has guided me throughout my PhD via the Center for Hierarchical Materials Design (CHiMaD) collaboration.

Next I would like to thank my group members who made the PhD journey an enjoyable experience. I would like to specifically acknowledge two members of our group, Kerim Dansuk and Andrea Giuntoli. Kerim, who joined the group with me, has been a fantastic desk partner in the lab. The board game nights he hosted combined with his jovial nature always kept me entertained. In 2019, Andrea joined as a postdoc and I found a new collaborative friend in the

group. We worked together on many projects, including star polymers, ballistic simulations and epoxy modeling. From playing chess to cycling to lagoons, we have shared wonderful memories that made my grad life a fun life. I have been incredibly lucky to work with outstanding individuals in our group and would like to give a shout out to Martha Dunbar, Robert Sinko, Wenjie Xia, Heather White, Ao Wang, Zhaoxu Meng, Elizabeth DeBenedictis, Suwei Liu and Jenny Liu. From random conversations about current affairs to in depth analysis of research problems, these people have always been very helpful.

Lastly I would like to acknowledge my friends, without whom I would not have been able to enjoy this PhD journey. A special thanks to Arman Khan, my roommate, fellow batch mate and best friend, for being beside me through the ups and downs during my time here at Northwestern. I would also like to thank Anant Jain, Krithika Ramachandran, Rajita Vatapalli, Shweta Jagadish, Namratha Sastry and Nikhil Madhusudhan for all the fun we had together over the five years.

Finally, I would like to acknowledge the support from ONR Director of Research Early Career Award (PECASE, award #N00014163175) which funded my PhD. I was also supported by the Center for Hierarchical Materials Design (CHiMaD), which is funded by the National Institute of Standards and Technology (NIST) (award #70NANB14H012). Additionally, I acknowledge funding through a supercomputing grant from the Northwestern University High Performance Computing Center (Quest) as well as computing resources provided through the Department of Defense High Performance Computing Modernization Program (HPCMP).

## ABBREVIATIONS

AA	All-Atomistic
aHNPs	Hairy Nanoparticle Assemblies
CG	Coarse-Grained
CNC	Cellulose Nano Crystal
CPB	Concentrated Polymer Brush
DWF	Debye Waller Factor
ER	Energy Renormalization
IBM	Inverse Boltzmann Method
LAMMPS	Large-scale Atomic/Molecular Massively Parallel Simulator
LJ	Lennard-Jones
MBDO	Metamodel Based Design Optimization
MSD	Mean Square Displacement
MD	Molecular Dynamics
$N_{cr}$	Critical Chain Length
PMF	Potential of Mean Force
RDF	Radial Distribution Function
SDPB	Semi Dilute Polymer Brush
SMD	Steered Molecular Dynamics
$T_g$	Glass transition temperature
vdW	van der Waals

## **DEDICATION**

This dissertation is dedicated to my loving parents, Mr. H.S. Krishnamurthy and Mrs. Geeta Krishnamurthy, who have provided endless support and love that helped me complete my PhD.

## TABLE OF CONTENTS

<b>Chapter 1:</b>	<b>Introduction.....</b>	<b>14</b>
1.1	Assembled Hairy Nanoparticles .....	15
1.2	Recent developments and shortcomings in the field of aHNPs.....	17
1.3	Thesis outline.....	20
<b>Chapter 2:</b>	<b>Computational Methods.....</b>	<b>22</b>
2.1	Overview of molecular dynamics simulations.....	22
2.2	Steered molecular dynamics (SMD) simulations .....	26
2.3	Background on CG simulations.....	27
2.4	Energy renormalization approach towards coarse-graining.....	30
<b>Chapter 3:</b>	<b>Energy Renormalization approach for coarse-graining .....</b>	<b>34</b>
3.1	CG Model for OTP .....	34
3.1.1	CG model description .....	35
3.1.2	Simulation parameters .....	39
3.1.3	Performance of CG model.....	40
3.1.4	Conclusion .....	45
3.2	CG model for Polycarbonate .....	46
3.2.1	CG Model description.....	47
3.2.2	Simulation parameters .....	52
3.2.3	Performance of CG model.....	53
3.2.4	Conclusion .....	59
3.3	CG Modeling of Epoxy .....	59
3.3.1	CG Model description.....	61
3.3.2	Simulation parameters .....	65
3.3.3	Non-bonded parametrization using machine learning.....	67
3.3.4	Performance of the CG model .....	71
3.3.5	Conclusion .....	72
3.4	Conclusion .....	73
<b>Chapter 4:</b>	<b>Materials by design for hairy nanoparticle assemblies .....</b>	<b>75</b>
4.1	Introduction.....	75

		10
4.2	<b>Metamodel based design optimization framework.....</b>	<b>78</b>
4.2.1	<b>Design of experiments.....</b>	<b>79</b>
4.2.2	<b>CG-MD system setup and simulation protocols.....</b>	<b>80</b>
4.2.3	<b>Gaussian Process Modeling.....</b>	<b>83</b>
4.2.4	<b>Constructing the Pareto Frontier .....</b>	<b>86</b>
4.2.5	<b>Metamodel Validation and Verification .....</b>	<b>88</b>
4.2.6	<b>Variance-based Statistical Sensitivity Analysis.....</b>	<b>93</b>
4.3	<b>Mechanical property optimization .....</b>	<b>97</b>
4.4	<b>Conclusion .....</b>	<b>105</b>
<b>Chapter 5:</b>	<b>Scaling laws to predict polymer conformation.....</b>	<b>107</b>
5.1	<b>Introduction.....</b>	<b>107</b>
5.2	<b>Simulation setup.....</b>	<b>108</b>
5.3	<b>Critical chain length, <math>N_{cr}</math> .....</b>	<b>109</b>
5.4	<b><math>N_{cr}</math> for other polymers .....</b>	<b>116</b>
5.5	<b>Conclusion .....</b>	<b>124</b>
<b>Chapter 6:</b>	<b>Mesoscale modeling based on potential of mean force.....</b>	<b>126</b>
6.1	<b>Introduction.....</b>	<b>126</b>
6.2	<b>Simulation methods .....</b>	<b>129</b>
6.3	<b>Cohesive energy and entanglement analysis.....</b>	<b>132</b>
6.4	<b>Functional form of the potential.....</b>	<b>139</b>
6.5	<b>Relations between constants and design parameters.....</b>	<b>143</b>
6.6	<b>Rate dependence.....</b>	<b>152</b>
6.7	<b>Conclusion .....</b>	<b>158</b>
<b>Chapter 7:</b>	<b>Conclusion .....</b>	<b>160</b>
7.1	<b>Future outlook.....</b>	<b>161</b>

## LIST OF FIGURES

Figure 1.1-1: Schematic of hairy nanoparticle assemblies .....	17
Figure 3.1-1: CG mapping scheme for OTP.....	35
Figure 3.1.1-1: Bond and angle distributions and resulting potential energy.....	36
Figure 3.1.1-2: Matching density of AA to obtain $\sigma(T)$ .....	36
Figure 3.1.1-3: Matching DWF of AA to obtain $\varepsilon(T)$ .....	38
Figure 3.1.3-1: Comparison of MSD and $F_s(q, t)$ between AA and CG models .....	41
Figure 3.1.3-2: Relation between $\tau$ , $D$ and $u_2$ .....	43
Figure 3.1.3-3: Radial distribution function of CG bead sites.....	44
Figure 3.1.3-4: Comparison of diffusion coefficient between experiments, AA and CG models.....	45
Figure 3.2.1-1: CG mapping scheme of PC .....	47
Figure 3.2.1-2: Bonds, angles and dihedral distribution and potential energies .....	48
Figure 3.2.1-3: Matching DWF to obtain $\alpha(T)$ .....	50
Figure 3.2.1-4: Comparison of density between AA and CG models.....	51
Figure 3.2.3-1: Comparison of MSD between AA and CG models .....	53
Figure 3.2.3-2: Comparison of segmental relaxation time between AA and CG models.....	55
Figure 3.2.3-3: Comparison of diffusion coefficient between AA and CG models .....	57
Figure 3.2.3-4: Comparison of isothermal compressibility between AA and CG models....	58
Figure 3.3.1-1: CG mapping scheme for DGEBA, PACM and D400. ....	61
Figure 3.3.1-2: Bond, angle and radial distribution for PACM beads and corresponding potential energies .....	63
Figure 3.3.3-1: Target macroscopic properties of the atomistic simulations .....	68
Figure 3.3.4-1: CG validation based on predictions by the ML algorithm .....	71
Figure 4.2.2-1: CG mapping scheme for CNC and PMMA and representative volume element for CG simulations.....	83
Figure 4.2.4-1: Young's modulus vs toughness Ashby plot.....	88
Figure 4.2.5-1: Comparison of metamaterial and CG-MD simulations .....	90
Figure 4.2.5-2: CG-MD Validation of Parteo frontier.....	92
Figure 4.2.5-3: Response surface between output and most influential inputs.....	93
Figure 4.2.6-1: Variation of Young's modulus of the nanocomposite with respect input parameters .....	96
Figure 4.2.6-2: Variation of toughness of the nanocomposite with respect to inputs parameters .....	97
Figure 4.3-1: Young's modulus vs toughness Ashby plot with respect to the input parameters.....	99
Figure 4.3-2: Young's modulus vs. stiffness of the nanocomposite for different weight percentages of NP.....	103
Figure 5.2-1: CG mapping scheme for PMMA, PS, PC and PB .....	109
Figure 5.3-1: Scaling relationships between monomer position and distance from nanoparticle.....	111
Figure 5.3-2: Plots to obtain $a$ and $b$ parameters.....	112
Figure 5.3-3: Relation between $\gamma_{pp}$ and toughness.....	115

Figure 5.3-4: Schematic of intermingling of polymer chains at various grafting densities	116
Figure 5.3-5: Size effect on chain conformations .....	116
Figure 5.4-1: Scaling of monomer position index with respect to distance from nanoparticle for various polymers .....	117
Figure 5.4-2: Obtaining parameters $a$ and $b$ for various polymers.....	119
Figure 5.4-3: Relation between length scale parameters.....	121
Figure 5.4-4: Scaling of monomer position index with respect to distance from nanoparticle as a function of persistence length and side-group size .....	122
Figure 5.4-5: Universal scaling law governing chain conformations .....	124
Figure 6.2-1: Schematic of system setup and representative PMF curves .....	131
Figure 6.3-1: Relation of peak PMF and equilibrium distance with respect to chain length and grafting density. ....	133
Figure 6.3-2: Peak PMF in per unit area .....	135
Figure 6.3-3: Relation between $\gamma_{pp}$ and $\psi_{max}$ .....	136
Figure 6.3-4: Relation between $\langle Z \rangle$ and $\psi_{max}$ .....	137
Figure 6.3-5: Relation between $\langle Z \rangle$ and $\psi_{max}$ for various grafting densities.....	138
Figure 6.4-1: Comparison of fitting of the data with different potential forms.....	140
Figure 6.4-2: Functional form of the potential with residual values.....	142
Figure 6.5-1: Dependencies of the empirical parameters on (a) chain length and (b) grafting density .....	146
Figure 6.5-2: Estimated potential from empirical constants along with predicted $x_0$ and $\psi_{max}$ .....	147
Figure 6.5-3: Representative PMF curves for each polymer chemistry at different chain lengths .....	148
Figure 6.5-4: Representative PMF curves for each polymer chemistry at different grafting densities .....	149
Figure 6.5-5: Ashby plot of Young's modulus vs toughness for different polymers. ....	151
Figure 6.6-1: Rate dependence of PMF.....	152
Figure 6.6-2: Harmonic approximation of PMF around equilibrium position.....	154
Figure 6.6-3: Rate dependence of $\psi_{max}$ .....	155
Figure 6.6-4: Validation of extrapolation to zero rate.....	157

## LIST OF TABLES

<b>Table 3.1.1-1: Potential forms and parameters of the force field for the CG model of OTP.</b>	<b>39</b>
<b>Table 3.1.1-2: Functional forms and parameters of the temperature dependent nonbonded potentials of the CG model from the energy-renormalization method.</b>	<b>39</b>
<b>Table 3.1.3-1: Summary of the characteristic temperatures predicted from the AA and CG models from the energy-renormalization method and their comparison with literature values.</b>	<b>42</b>
<b>Table 3.2.1-1: Force field forms and parameters for the CG model of PC.</b>	<b>48</b>
<b>Table 3.2.1-2: Functional forms and parameters of the temperature dependent nonbonded potentials of the CG model from the energy-renormalization method.</b>	<b>51</b>
<b>Table 3.3.1-1: Force field forms and parameters for the CG model of DGEBA-PACM-D400.</b>	<b>64</b>
<b>Table 4.2-1: Design bounds of the material parameters studied using CG-MD simulations.</b>	<b>79</b>
<b>Table 4.2.2-1: Force field forms and parameters for the CG model of PMMA and CNC.</b>	<b>80</b>
<b>Table 4.2.3-1: Summary of MAPE for different metamodels for the two outputs, modulus and toughness.</b>	<b>85</b>
<b>Table 4.2.5-1: Seven random input points chosen from the Pareto curve for validation of the metamodel prediction.</b>	<b>91</b>
<b>Table 4.2.6-1: Summary of the main, interaction and total sensitivity indices obtained from the statistical sensitivity analysis of the metamodel.</b>	<b>95</b>
<b>Table 5.4-1: Material parameters and polymer characteristics for different aHNPs.</b>	<b>119</b>
<b>Table 6.5-1: Constants of relation between repulsive parameters and <math>N</math> and <math>\sigma^*</math>.</b>	<b>144</b>
<b>Table 6.5-2: Constants of relation between attractive parameters and <math>N</math> and <math>\sigma^*</math>.</b>	<b>146</b>

## Chapter 1: Introduction

Rapid discovery and deployment of new advanced materials is crucial to sustain the development of mankind. At current state, the entire process of discovery to deployment of a new material takes about 10-20 years. The reason it takes so long is due to the time-consuming and repetitive experiment and characterization loops. Reducing this timeframe down to a few years is essential to drive economic growth in the society. In order to enable this acceleration, in 2011, the United States government started the Materials Genome Initiative (MGI), which aims to “discover, develop, manufacture, and deploy advanced materials at least twice as fast as possible today, at a fraction of the cost”<sup>1</sup>. MGI aims to accomplish this goal through a materials-by design approach which emphasizes establishing new databases, computational tools, and high-throughput experiments that speed up each step of the materials continuum. Using predictive simulations to accelerate the materials development process while also increasing the number of new advanced materials brought to market is a central element of the MGI framework. The idea is to create a new research paradigm which will reduce the reliance on physical experimentation by increasing the strength of computational analysis. These powerful computational tools will minimize or optimize traditional experimental testing (most time-consuming aspect of materials discovery). These tools will also help predict materials performance under various conditions, thus enabling faster and better design. While significant knowledge base as well innovative methods to accelerate design, such as machine learning assisted high throughput experiments, have already been developed for metal alloys<sup>2</sup>, such methods for nanostructured polymeric materials and nanocomposites are still in its infancy. This is due to the complexity of these materials, where the basic polymer physics and principles needs to be fully understood, as well as a lack of detailed knowledge of molecular

structure, which requires sufficient description of self-assembly phenomena, polymer-nanoparticle interactions and nanocomposite preparation processes.

With this idea in mind, my PhD dissertation focuses on developing computational methods based on molecular dynamics framework that will help the acceleration of materials-by-design process for polymer nanocomposites. In conjunction with analytical theories, I will demonstrate the capabilities of these computational techniques using assembled hairy nanoparticles (aHNPs) as a model material. While the focus here is on one specific material system, it is important to emphasize the generality of these methods and that it can be extended to any number of material systems in the future to speed up the mechanical characterization process. In fact, I will showcase this by extending one of the computational method developed for polymers to a much more complicated system of crosslinked epoxy resins.

In this chapter, I will first introduce the concept of assembled hairy nanoparticles, focusing on the advantages of aHNPs over traditional polymer nanocomposites. Next, I will summarize key knowledge gaps in the field of aHNPs. Finally, I will conclude the chapter with an outline of the thesis and how these new developed techniques accelerate the materials-by design process.

## **1.1 Assembled Hairy Nanoparticles**

Research into polymer nanocomposites<sup>3-7</sup> over the past few decades have resulted in numerous studies showing that introducing a small fraction of nanoparticles into polymers can significantly enhance the stiffness, toughness, and strength of the composite among other properties<sup>8-10</sup>. These nanocomposites have been extensively used in many applications since 20<sup>th</sup> century including aerospace<sup>11</sup>, electronics<sup>12</sup>, solar cells<sup>13</sup>, drug delivery<sup>14</sup> and tissue engineering<sup>15</sup>.

However, there is a major problem hampering the efforts to develop these high-performance polymer nanocomposites. While addition of nanoparticles enhances the properties, adding too many nanoparticles leads to aggregation which degrades the mechanical properties<sup>16, 17</sup>. Various methods have been pursued to tackle the issue of nanoparticle aggregation including surface modification<sup>18</sup> and polymer grafting<sup>19</sup>. Grafting polymers onto nanoparticles to generate so-called “hairy” nanoparticles (HNPs) has been a particularly promising direction of research, since stiff central core is surrounded by a soft polymeric corona that facilitates steric repulsion to prevent aggregation while also providing cohesion in the case of sufficiently long grafts. In this context, grafted nanoparticle dispersion in a polymer matrix and the emergent mechanical properties depend strongly on factors such as graft density, and the nature and degree of polymerization of the corona and matrix<sup>20</sup>.

Superior mechanical properties can be attained by HNPs when they are very well dispersed in these nanocomposites. Achieving good dispersion requires tuning relative interfacial energies while not adversely affecting interphase properties, which is challenging<sup>17, 21, 22</sup>. Thus, instead of dispersing the HNPs in a polymeric matrix, one can create a nanocomposite with only HNPs, where the grafted chains themselves form the “matrix” phase and the nanoparticles serve as both a reinforcing phase as well as tethering points for the polymer chains as shown in **Figure 1.1-1**<sup>23-26</sup>. These matrix-free self-assembly of polymer grafted nanoparticles could overcome the dispersion issue, leading to composites with relatively regular spacing between particles. The emergent properties of so-called hairy nanoparticle assemblies (aHNPs)<sup>27</sup> are promising because better structural order allows functional and mechanical properties to be tailored more accurately<sup>28</sup>, and higher volume fraction of the nanoparticles can be achieved<sup>29, 30</sup>.

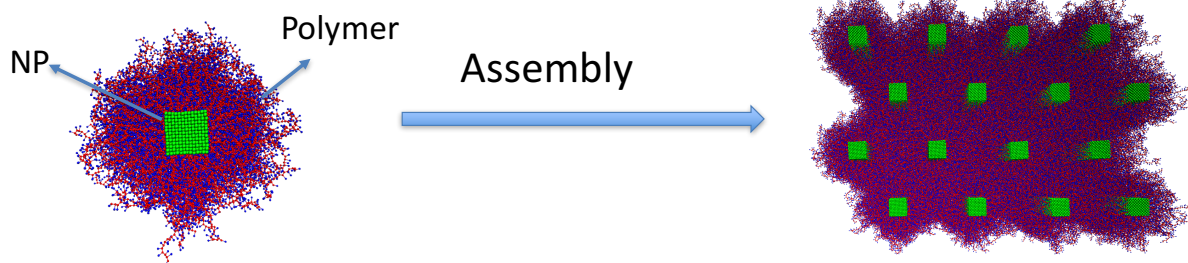


**Figure 1.1-1: Schematic of hairy nanoparticle assemblies:** Matrix-free self assembly of polymer grafted nanoparticles leads to orderly structured aHNPs.

The wide design parameter space available for architectural choices for these aHNP systems provides a large application space. By using ionic groups on the periphery of the polymer chains, it is possible to synthesize layer-by-layer films that are used in switchable conducting membranes<sup>31</sup>, antifouling coatings<sup>32</sup>, multicolored quantum dot films<sup>33</sup> and photovoltaics<sup>34</sup>. The choice of functional group of the polymer graft provides versatility to tailor aHNPs to have some reactivity towards external gases such as carbon dioxide. The entropic effects in the structural ordering of the polymer improves the uptake capacity as compared to ungrafted polymer, thus making it ideal to use in CO<sub>2</sub> capture<sup>35</sup>. The concept can be extended to other gases such SO<sub>2</sub>, NO<sub>2</sub> and CO as well.

## 1.2 Recent developments and shortcomings in the field of aHNPs

Owing to its wide range of versatile applications, aHNPs have become a central focus for several experimental, computational and theoretical studies. In most of these studies, aHNPs are made out of spherical nanoparticles which are grafted to a homopolymer, which is usually polystyrene. A summary of these studies will be provided in this section while discussing the shortcomings.

Mechanical properties have been characterized using nanoindentation techniques where it was found that the fracture toughness of aHNPs increases substantially beyond a certain degree of polymerization, specifically when the polymer conformations transition from a concentrated brush regime (CPB) to a semidilute brush regime (SDPB)<sup>29, 30</sup>. It has also been observed that the toughening effect due to the degree of polymerization decreases with larger particle sizes, which has been attributed to the increased dimensions of interstitial regions that reduce the entanglement density. Brillouin light spectroscopy has been used to evaluate the linear elastic properties of aHNPs and to understand the contribution of the core and polymer towards the elastic properties<sup>36</sup>. Thin film buckling method has been employed to obtain tensile stress-strain curve to understand properties such as strength and fracture toughness<sup>28</sup>. Viscoelastic measurements using mechanical rheometry have been carried out which revealed jamming mechanisms in the suspensions of aHNPs<sup>37</sup>. The relaxation dynamics of polymer chains have also been characterized<sup>38</sup>. While these experimental measurements provide a good understanding of macroscopic properties such as modulus and strength, the molecular mechanisms underpinning these properties are still not understood.

Computational studies, specifically MD simulations, on aHNPs have focused on evaluating the polymer chain conformations and analyzing the self-assembly behavior. Most of these simulations have employed a generic bead-spring CG model which can capture the conformational behavior of a polymer chain, but lacks in chemical specificity. The self-assembly process in aHNPs leading to different morphologies have been extensively analyzed<sup>39, 40</sup>. The complex geometry and topology formed due to polymer grafted to nanoparticles of different shapes leads to morphologies that are potentially far richer than those known for conventional block copolymer, surfactant, and

liquid-crystal systems<sup>41,42</sup>. Structural changes and adsorption in hairy nanoparticles have also been studied using generic bead-spring CG-MD simulations<sup>43,44</sup>. There is a clear need for computational studies of aHNPs which includes a chemistry specific molecular modeling approach. Moreover, these studies have focused on aHNPs with a spherical nanoparticle and a modeling framework with high aspect ratio nanoparticle is needed to further advance the knowledge base.

Scaling laws for star polymers developed by Daoud-Cotton help in making qualitative deductions on chain structure by extending the core of the star to a nanoparticle<sup>45,46</sup>. This theory was further extended to study the polymer chain structure in aHNPs<sup>40,47</sup>. However, a comparative analysis geared towards understanding the effect of different polymer chemistries on the confined conformations of anisotropic aHNPs, specifically on the CPB to SDPB transition, has not yet been carried out. Furthermore, there is a need to convert these theoretical scaling laws to models that can predict the macroscopic properties of aHNPs.

Thus, in this thesis, we provide solutions to fill in these knowledge gaps in the field of aHNPs. Firstly, we develop a CG modeling approach that can be applied to any polymeric system. These models can later be used to model chemistry-specific aHNPs. Next, we combine CG-MD simulations with machine learning to develop a material-by-design framework for optimizing mechanical properties of aHNPs with high aspect ratio nanoparticles. Furthermore, we develop a universal scaling law that govern the chain conformations in aHNPs and has the ability to predict macroscopic properties such as nanoparticle spacing. Finally, we develop an effective interaction between nanoparticles in aHNPs that will eliminate the need to explicitly simulate the polymer chains which significantly enlarges the spatiotemporal scales of CG-MD simulations. All the

computational methods developed in this thesis aim towards accelerating the materials-by design process for aHNPs.

### 1.3 Thesis outline

Despite advancements in supercomputing methods, all-atomistic MD simulations are still prohibitively expensive to characterize material properties due limitations in time and length scales. A brief overview of MD simulations is provided in Chapter 2:. In order to overcome the spatiotemporal limitations, there is a need to develop meso-scale techniques such as coarse-graining. Chapter 2: also gives a background of different kinds of CG approaches and their limitations.

In Chapter 3:, we propose a new approach towards coarse-graining, called the Energy Renormalization (ER) approach. In this approach, loss of entropy due to coarse-graining is compensated by increasing the enthalpy/cohesive energy of the system (known as entropy-enthalpy compensation effect). We develop this approach for three different kinds of materials; a small molecule, a polymer and an epoxy resin; showing the versatility of the approach. This approach is temperature transferable and is two to three orders of magnitude faster than AA-MD simulations.

In the design of a polymer nanocomposite, there are several parameters that can affect mechanical properties such as length of polymer chains, dimensions of the nanoparticle etc. While CG simulations are definitely faster than AA, exploring the vast design space becomes exponentially expensive even for CG simulations. Thus, in Chapter 4:, we explore the use of machine learning to accelerate this process. Specifically, we develop a metamodel based on inputs and outputs of 100 CG simulations, which later allows us to carry out one million “pseudo-CG”

simulations. This technique offers a speed up of six to seven orders of magnitude as compared to AA simulations.

In Chapter 5:, we develop theoretical scaling laws that will predict the conformations of polymer chains in a polymer grafted nanocomposite. Specifically, we derive an equation for critical chain length, which governs the conformational transition, and show that for a nanocomposite to have optimum mechanical properties, chain length of the polymer needs to be higher than the critical chain length. We also develop a universal equation governing the conformations and show the conformational data of more than 100 different designs fall under the same curve.

Next, in Chapter 6:, we develop a technique to parametrize a meso-scale model that will determine interactions between nanoparticles in the nanocomposite. Developing this inter-nanoparticle potential will allow us to simulate implicit polymer chains that will tremendously increase time and length scales accessible with these MD simulations. We find a universal functional form of the potential that fits different kinds of polymers and we correlate the empirical constants of the equation with physical design parameters.

Finally, the dissertation is wrapped up in Chapter 7: with conclusion and outlook. Key contributions in the development of CG model, combination of machine learning with MD simulations and the development of PMF based meso-scale model are summarized. Future work that can build up from the frameworks developed in this dissertation is also discussed.

## Chapter 2: Computational Methods

This chapter will give the reader a high level overview of the computational framework used for all the work in this thesis; molecular dynamics (MD) simulations. Next, we discuss a subset of MD simulations that will be used in Chapter 6: called steered MD. Furthermore, a brief background on coarse graining (CG) strategies and different types of CG techniques will be provided. Finally, we provide an overview of a new approach towards CG called the energy renormalizing approach.

### 2.1 Overview of molecular dynamics simulations

Molecular Dynamics (MD) simulation is a computational technique that simulates the movement of atoms by solving the Newton's equation of motion:  $\vec{F} = m\vec{a}$ , where  $\vec{F}$  is the force acting on the atom,  $m$  is the mass and  $\vec{a} = d^2\vec{r}/dt^2$  is the acceleration of the atom,  $\vec{r}$  being the position of the atom and  $t$  is time. One of the earliest MD simulation was carried out in 1959<sup>48</sup>, where it was used to study a system of hard spheres and obtain the phase diagram of solid and liquid regions. Aneesur Rahman from Argonne National Laboratory published a famous paper in 1964, studying a number of properties of liquid Argon which pioneered the use of this computational technique<sup>49</sup>. MD simulations became increasingly popular to study the physics of polymer chains in the 1970s<sup>50-52</sup>. Since then, MD simulations have been at the core of computational research. With the advent of high performance supercomputing technology, this computational technique is being increasingly used to investigate the properties and behavior of materials at the molecular level. Highly parallelizable MD packages and complex force fields for soft matter such as Chemistry at Harvard Macromolecular Mechanics (CHARMM)<sup>53</sup> were developed. In fact, the Nobel Prize in Chemistry in 2013 was awarded to the developers of CHARMM.

The time evolution of the movement of atoms is done by integrating this equation of motion for all particles. While there are various methods to obtain the time evolution, an important breakthrough in the time integration of the equation of motion was achieved by Loup Verlet in 1967<sup>54</sup>. He used MD simulations to study phase diagrams of liquid Argon, but more importantly he developed the Verlet time integration algorithm which is used even today in commercial MD packages. In this algorithm, velocity and position of the atoms are updated at each time step based on the following equations:

$$r(t + \delta t) = r(t) + v(t)\delta t + \frac{1}{2}a(t)(\delta t)^2 + O(\delta t)^3; a(t) = \frac{f(t)}{m} \quad (2.1-1)$$

$$v(t + \delta t) = v(t) + \frac{1}{2}[a(t) + a(t + \delta t)](\delta t)^2 + O(\delta t)^3 \quad (2.1-2)$$

To put in words, we initialize the system by giving each atom a position and velocity. Next, positions of the atoms ( $r(t + \delta t)$ ) are updated using Eq. 2.1-1. Note that the higher orders terms in these equations ( $O(\delta t)^3$ ) are omitted. Based on the new position, new forces acting on the atoms are calculated. This in turn provides the new acceleration ( $a(t + \delta t)$ ) which updates the velocity ( $v(t + \delta t)$ ). Now that the new position and velocity of the atoms are obtained, the process is repeated to obtain time evolution. The choice of the timestep,  $\delta t$ , is very important and is decided based on the atom with the highest vibrational frequency. This is usually hydrogen in all-atom simulations and the timestep for AA simulations is usually around 0.5 to 1 fs. Coarse-grained simulations can have a slightly larger timestep, which will be discussed in the next section.

The force acting on the atom is calculated from gradient of the force field ( $U(r)$ ) where  $\vec{F} = -\nabla U(r)$ . The force field can encompass various kinds of interactions between atoms such as bonded potentials (bonds, angles, dihedrals, impropers), non-bonded potentials (van der Waals

(vdW)), charges etc. For example, covalent bonds between two atoms can be thought of as two masses attached with a harmonic spring. Thus, potential between two atoms is:

$$U_{bond} = \frac{1}{2}k(r_1 - r_2)^2 \quad (2.1-3)$$

$k$  being the spring constant and  $r_1$  and  $r_2$  being the positions of the atoms. In general, covalent bonds between atoms are represented using harmonic potential, however, in complex systems, bonds are also represented by Morse, FENE or a tabulated potential. Other bonded interactions such as angles, dihedrals and impropers capture the realistic angle bending, bond torsion, and out-of-plane bending angles, respectively.

Non-bonded interactions such as the van der Waals (vdW) is often represented using pairwise interatomic potentials, most common being the Lennard-Jones potential;

$$U(r)_{LJ} = 4\varepsilon \left[ \left( \frac{\sigma}{r} \right)^{12} - \left( \frac{\sigma}{r} \right)^6 \right] \quad (2.1-4)$$

where  $\varepsilon$  represents the cohesive strength of the interaction,  $\sigma$  represents the effective size of the atom and  $r$  is the distance between atoms. These pair potentials include both attractive and repulsive part of the interaction.

Thus, in order to carry out a MD simulation, three key things need to be provided: initial position of the atoms, initial velocity and the force field. The forces calculated based on the force field is used to update the positions and velocities of the atoms using the Verlet algorithm and thus, the time evolution of system will be obtained. There are various force fields that have been developed and verified for certain systems. For example, Optimized Potentials for Liquid Simulations (OPLS)<sup>55</sup>, as the name suggests, are mainly used for liquid simulations. Assisted Model Building with Energy Refinement (AMBER)<sup>56</sup> is widely used to simulate DNA, CHARMM<sup>53</sup> is used to simulate proteins and Groningen Molecular Simulation (GROMOS)<sup>57</sup> is

used to simulate biomolecules. While these are some of the common uses of these force fields, it should be noted that it is not restricted to only these systems and that they can be applied to study a wide range of systems. There are various coarse-grained force fields as well which will be discussed in the next section.

MD simulations are typically run in a statistical ensemble, which describes all possible microstates of the system. Each ensemble has a specific constraint that dictates the simulation environment. Micro canonical ensemble constrains number of particles (N), volume (V) and energy (E) of the system. Hence, it's also commonly known as NVE ensemble. Similarly, other ensembles include canonical (NVT, T being temperature), isothermal-isobaric (NPT, P being pressure) and grand canonical ( $\mu$ VT,  $\mu$  being chemical potential). Choice of the ensemble entirely depends on the type of simulation that one wants to carry out, for example, to evaluate equilibrium properties such as density, one might use an NPT ensemble with zero external pressure, or during ballistic simulations, where energy has to be conserved, NVE ensemble is used.

There are various commercial MD packages available such as Large-scale Atomic/Molecular Massively Parallel Simulator (LAMMPS)<sup>58</sup>, Nanoscale Molecular Dynamics (NAMD)<sup>59</sup> and Groningen Machine for Chemical Simulation (GROMACS)<sup>60</sup>. One can also write their own MD code to carry out simulations. Each commercial package has its own advantage and disadvantage. NAMD is extensively used to simulate proteins whereas LAMMPS is widely used to carry out coarse-graining simulations (explained in the next section). We have used LAMMPS for all the work that is discussed in this thesis.

This is MD simulation in a nutshell. From these MD simulations, one can obtain a lot of information regarding the system such as temperature, pressure, energy etc. The algorithms used

are also parallelizable, which means, one can simulate millions of atoms by using multiple processors in a supercomputer. The largest MD simulation done so far is a billion-atom AA simulation of the entire DNA gene sequence carried out by researchers at Los-Alamos National Laboratory<sup>61</sup>. Thus, MD simulation is a powerful computational tool that help with exploring molecular scale mechanisms in materials.

## 2.2 Steered molecular dynamics (SMD) simulations

Steered molecular dynamics (SMD)<sup>62</sup> is simulation technique where time-dependent external forces are applied to the system to induce conformational changes in the time-scales accessible to MD simulations. This technique can be used to replicate experimental processes such as atomic force microscope and surface force apparatus tests that can measure the adhesion force between polymer and substrate<sup>63, 64</sup>. These experimental techniques focus on extracting the interfacial properties of nanoscale materials, however, it is difficult to control parameters such as applied force and pulling velocity and to make accurate measurements<sup>65</sup>. In SMD simulations, parameters can be controlled precisely, allowing us to make accurate measurements while also observing molecular details<sup>66</sup>.

SMD simulations are a non-equilibrium technique where force is applied to a part of the system while keeping the other part fixed to a constraint. This allows for the sampling of the free energy landscape (potential of mean force (PMF)) as a function of reaction coordinate. The group of atoms is steered (pulled) through a spring tethered to a virtual atom. This virtual atom is moved with a constant force or velocity, which in turn steers the group of atoms attached to it. The force acting on each atom of the steered group is given by:

$$F_{smd} = K \frac{(R-R_0)M_i}{M} \quad (2.2-1)$$

where  $K$  is the spring constant,  $M$  is the total mass of all atoms in the group,  $M_i$  is the mass of the atom and  $R_0$  is the distance between the virtual atom and the center of mass of the steered group of atoms. From this force, the non-equilibrium work done ( $W$ ) to move from state A to state B is calculated by integrating the force along the reaction coordinate (displacement):

$$W = \int_A^B F dx \quad (2.2-2)$$

This work is obtained from an irreversible process and one might argue that the free-energy landscape (PMF) has to be obtained from reversible work. However, Jarzynski<sup>67</sup> in 1997 formulated an equality that connects the ensemble average of the exponential of irreversible work done ( $W$ ) to the free energy difference ( $\Delta F$ ) between the two states.

$$\langle e^{\frac{-W}{k_b T}} \rangle = e^{\frac{\Delta F}{k_b T}} \quad (2.2-3)$$

We make use of this equality to obtain the potential of the mean force between restrained and steered group of atoms. It should be noted that in MD simulations, this is an estimation as the whole sample would need to be sampled for the equality. This technique has been widely used to study polymer substrate interface properties<sup>68, 69</sup> In this dissertation, we use this approach to develop an interparticle potential between nanoparticles in aHNPs. Specifically, we obtain the PMF between nanoparticles by steering one nanoparticle while keeping the other restrained, which can then be converted to an interatomic potential. The details of this approach is discussed in Chapter 6:.

### 2.3 Background on CG simulations

Assessing the complex dynamic and mechanical properties of polymers and polymer nanocomposites using all-atomistic (AA) MD simulations is computationally challenging due to

their spatiotemporal limitations<sup>70</sup>. With a reasonable supercomputer, the time scale for AA simulations can reach a few nanoseconds and the length scales of a few tenths of nanometers. This generates a time-scale and length-scale gap between computational and experimental methods which can reach up to a few microns and microseconds. This necessitates a multi-scale modeling technique that can bridge this gap and coarse-graining (CG) is one such approach. In CG simulations, a few atoms are grouped together to form a “superatom”. CG parameters that are derived from atomistic data can be used to carry out CG simulations to overcome the limitations imposed by AA-MD simulations. In order to improve computational efficiency, the “unessential” atomistic features can be removed from the AA system thereby reducing the number of degrees of freedom<sup>71</sup>.

One of the earliest attempts at coarse-graining of polymers was done by Flory<sup>72</sup> which led to models including the freely joined chain and freely rotating chain. DeGennes<sup>73</sup>, Rubenstein<sup>74</sup> and Doi<sup>75</sup> are pioneers in polymer physics and use the bead-spring representation of polymers to develop scaling laws. Coarse-graining techniques are also applied to biomolecules. One of the early concepts of coarse graining for proteins was introduced by Levitt and Warshel<sup>76</sup> where they provided a simpler representation of proteins to study the conformational behavior and their folding. Anisotropic network model<sup>77</sup>, introduced in early 2000s is also a popular CG approach to model proteins. MARTINI<sup>78</sup>, a CG force field used to simulate lipids and peptides, uses a four to one representation.

The CG models for polymers can be split into two categories: generic bead-spring model and chemistry-specific systematic CG model. The generic models are very useful in understanding the physics of polymer chains under various conditions such as confinement. The most common

generic CG model is the finite-extensible non-linear elastic (FENE) model<sup>79</sup>. Kumar and Grest are pioneers in using this model to explore the dynamics of polymer chains under various kinds of confinements<sup>80-84</sup>. Various scaling laws characterizing the effect of molecular weight on dynamics or rheology have been obtained using this model<sup>46, 82, 85, 86</sup>. While large spatiotemporal scales are easily accessible with these generic models, the key drawback of this approach is a lack of chemical specificity which makes comparison of properties with specific polymers difficult.

Chemistry-specific CG models can capture the physical and chemical features of a polymer such as glass transition, radius of gyration and diffusion coefficient. There are two kinds of systematic CG methods: parametrized and derived<sup>87</sup>. In parametrized CG method, target properties such as radial distribution function are obtained from AA simulations and CG potentials are constructed to reproduce those target properties. Some of the parametrized CG approaches include inverse Boltzmann method (IBM)<sup>88</sup>, force matching (also called the multiscale coarse-graining)<sup>89, 90</sup>, relative entropy<sup>91</sup> and inverse Monte Carlo (IMC) methods<sup>92</sup>. IBM, relative entropy and IMC are structure-based whereas multiscale coarse graining is a force-based CG approach. Of these, IBM is the most commonly used method and details will be explained in next section.

Although the above mentioned methods preserve the static structure of the AA system (e.g. radial distribution function (RDF)), the diffusion of atoms measured using these models turn out to be higher than experimental values<sup>93, 94</sup>. Mechanistically, this is mainly attributed to the reduced configurational entropy  $s_c$  of the system as the degrees of freedom are integrated out upon coarse-graining<sup>95-97</sup>, which has a huge influence on the dynamics. The other kind of systematic CG methods, the derived CG methods, overcome this issue as these methods employ direct AA simulations between the defined superatoms to derive the corresponding coarse-grained

interactions. These derived potentials represent the PMF between the superatoms. We extend this concept from CG to meso-scale model in Chapter 6:

There are few other approaches to CG such as introducing time-scaling factors<sup>98</sup> or non-conservative forces such as frictional and dissipative forces<sup>99, 100</sup>. These approaches have been shown to capture the AA dynamics as well as thermodynamics. However, “temperature transferability” of CG modeling remains challenging because of a lack of understanding of effect of temperature on molecular friction parameters and relaxation properties of polymeric materials. For example, Muller-Plathe and co-workers obtained CG potential for polystyrene through IBM and studied the systematic transferability of the potentials with respect to temperature and found that the coarse-grained PS model was only transferable over a very narrow temperature range<sup>101</sup>. Jan Andzelm and co-workers also developed CG potential for polystyrene, where the bonded interactions were obtained through IBM, non-bonded interactions were obtained through force matching and constant temperature friction parameter was used to slow down the dynamics<sup>102</sup>. While earlier studies<sup>103-105</sup> have introduced several strategies such as pressure-matching method to address the temperature transferability issue by focusing on preserving the structural and thermodynamic properties of CG models, our focus here is to develop a practical and efficient method for temperature-transferable coarse-graining that preserves correct AA dynamics to the greatest extent possible.

## 2.4 Energy renormalization approach towards coarse-graining

As discussed in the previous section, there is a need to develop a temperature-transferable CG method that captures the dynamics of polymer chains. To address this fundamental problem, we propose a CG strategy, called the *energy-renormalization* (ER) approach. This approach

borrowed from essential ideas of the Adam-Gibbs (AG) theory<sup>106</sup> and the more recent generalized entropy theory (GET) of glass formation<sup>107</sup>, which have emphasized the critical role of configurational entropy  $s_c$  in glass formation. As the system's  $s_c$  decreases under coarse-graining, the effective enthalpy must correspondingly increase to preserve the overall properties of the fluid as evidenced in many experimental observations, namely the “entropy-enthalpy compensation effect”<sup>108-110</sup>. The GET further predicts that the strength of the monomeric cohesive interaction in glass forming systems, which is often described by the Lennard-Jones (LJ) parameter  $\epsilon$  in nonbonded interactions, has a strong influence on dynamics and mechanical response of glass forming molecules through its influence on  $s_c$ <sup>111, 112</sup>. By renormalizing  $\epsilon$  as a function of temperature, we aim to “correct” for the decrease activation free-energy and thus preserve dynamics of the CG polymers during glass formation.

To develop a CG model, the first step is to identify “superatoms”, i.e., the atoms that can be clustered to form a bead in the CG simulation. This is called CG mapping scheme. There are no strict guidelines as to how many atoms can be combined to make a super atom. Each CG model will be slightly different based the choice of the mapping scheme. One of the most commonly used methods for CG is the united atom method which allows savings in computational time by removing some high frequency vibrational modes which can limit the integration time step in MD simulations<sup>113, 114</sup>. A common example is the CH<sub>2</sub> group in a polymeric chain that is represented by a single bead. The CG scheme employed in this dissertation is discussed in Chapter 3:.

Once the bead centers have been identified, the next step is to obtain the distributions of the bonds, angles and dihedrals corresponding to these force centers. These distributions are then inverted through Boltzmann inversion (IBM), as depicted by Eq. 2.4-1-2.4-3,

$$U_{bond}(l) = \frac{1}{N} \left[ \sum_{i=1}^N -k_B T \ln \left( \frac{P(l)}{l^2} \right) \right] \quad (2.4-1)$$

$$U_{angle}(\theta) = \frac{1}{N} \left[ \sum_{i=1}^N -k_B T \ln \left( \frac{P(\theta)}{\sin(\theta)} \right) \right] \quad (2.4-2)$$

$$U_{dihedral}(\phi) = \frac{1}{N} \left[ \sum_{i=1}^N -k_B T \ln(P(\phi)) \right] \quad (2.4-3)$$

where  $k_B$  is the Boltzmann constant,  $T$  is the temperature,  $P$  is the probability distribution functions for bond length  $l$ , angle  $\theta$  and dihedral angle  $\phi$ . Direct implementation of the atomistically derived Boltzmann potential estimate is typically not perfect, and thus CG potentials are optimized iteratively to create a good match with atomistic target distributions. The iterative process is described by Eq 2.4-4.

$$U_{i+1}(r) = U_i(r) + k_B T \ln \left( \frac{P_i(r)}{P_{target}(r)} \right) \quad (2.4-4)$$

Once bonded potentials are obtained through IBM, the next step is to parametrize the vdW interactions. The non-bonded interactions between the CG beads are represented by the standard 12-6 LJ potential:

$$U(r) = 4\varepsilon \left[ \left( \frac{\sigma}{r} \right)^{12} - \left( \frac{\sigma}{r} \right)^6 \right] \quad (2.4-5)$$

where  $\sigma$  governs effective vdW radius and marks the distance where  $U(r)$  is 0 and  $\varepsilon$  is the depth of the potential, a parameter associated with cohesive interaction strength of the material. In other words,  $\sigma$  governs the length scale of the system and  $\varepsilon$  governs the energy scale. In order to achieve temperature transferability, we introduce temperature-dependent renormalization factors,  $\alpha(T)$  and  $\beta(T)$  to rescale  $\varepsilon$  and  $\sigma$  respectively. Thus the interatomic LJ potential is transformed to:

$$U(r) = 4\varepsilon(T) \left[ \left( \frac{\sigma(T)}{r} \right)^{12} - \left( \frac{\sigma(T)}{r} \right)^6 \right] \quad (2.4-6)$$

where  $\varepsilon(T) = \varepsilon_0 \times \alpha(T)$  and  $\sigma(T) = \sigma_0 \times \beta(T)$ .  $\varepsilon_0$  and  $\sigma_0$  are constants that are to be taken as initial estimates of  $\varepsilon$  and  $\sigma$  from the RDF of the bead.

The next chapter focuses on applying the ER approach to three different kinds of materials: a small molecule, a polymer and an epoxy resin, thus showcasing the universality and versatility of this approach.

## Chapter 3: Energy Renormalization approach for coarse-graining

This chapter focuses on developing a new approach towards coarse-graining, called the energy renormalization approach, for different types of materials, viz., ortho-terphenyl (OTP), a small molecule; polycarbonate (PC), a polymer and an epoxy resin. We start out with CG model for OTP as it's a simpler problem to solve prior to tackling polymers and much more complicated epoxy resins. These CG models extend the spatiotemporal scales of MD simulations and thus speeds up property evaluations. The CG model for epoxy was developed in collaboration with Prof. Wei Chen's group at Northwestern University who helped us develop the machine learning algorithm. Portions of the text and figures within chapter are reprinted or adapted with permission from Xia et al. JPCB 2018<sup>115</sup> and Xia et al. Science Advances 2019<sup>116</sup>.

### 3.1 CG Model for OTP

Terphenyls are a group of aromatic hydrocarbons that consists of three benzene rings. Ortho-terphenyl (OTP) is an isomer in which the two benzene rings are bonded to adjacent carbon atoms (in 1,2 positions **Figure 3.1-1**). OTP is a common glass forming molecule that has been widely studied in the literature for its glass forming properties<sup>117-120</sup>. Previous CG efforts have focused on capturing the structure where the potentials were derived through IBM<sup>121</sup>. Despite its glass formation ability and widespread usages in industrial and scientific applications, there hasn't been any effective coarse-graining method focused on predicting the dynamic behaviors of OTP. Thus, we consider whether the energy renormalization (ER) approach (discussed in Chapter 2:) can be applied to coarse-graining small molecule glass forming liquid by taking OTP as a model system.

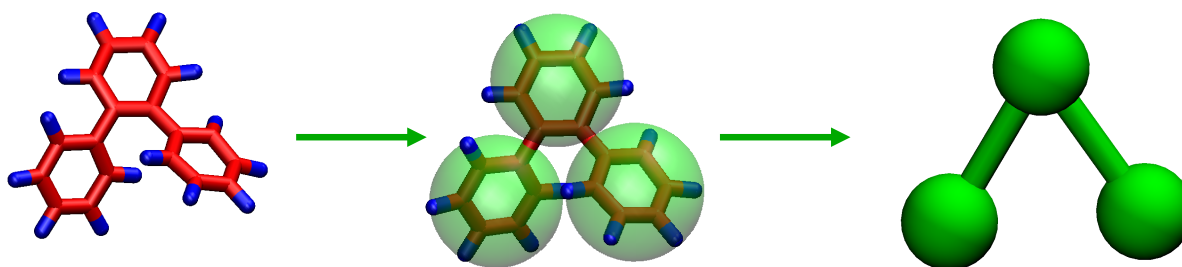


**Figure 3.1-1: CG mapping scheme for OTP.** The atomistic structure of OTP is shown in the leftmost figure. The bead centers are identified (middle figure) and the final coarse-grained model is shown in the rightmost figure.

### 3.1.1 CG model description

To coarse-grain OTP, each phenyl ring is grouped into one CG bead with the force center located at the center of mass of each ring, resulting in three consecutive CG beads per molecule (**Figure 3.1-1**). This mapping is consistent with other CG work<sup>121</sup> and allows for preserving the essential degrees of freedom under coarse-graining but omits atomic details that are less relevant to large-scale dynamic behaviors. The bond and angle interactions of the CG model are derived from the probability distributions of the AA system using IBM, which can be captured by harmonic potential forms as shown in **Figure 3.1.1-1**.

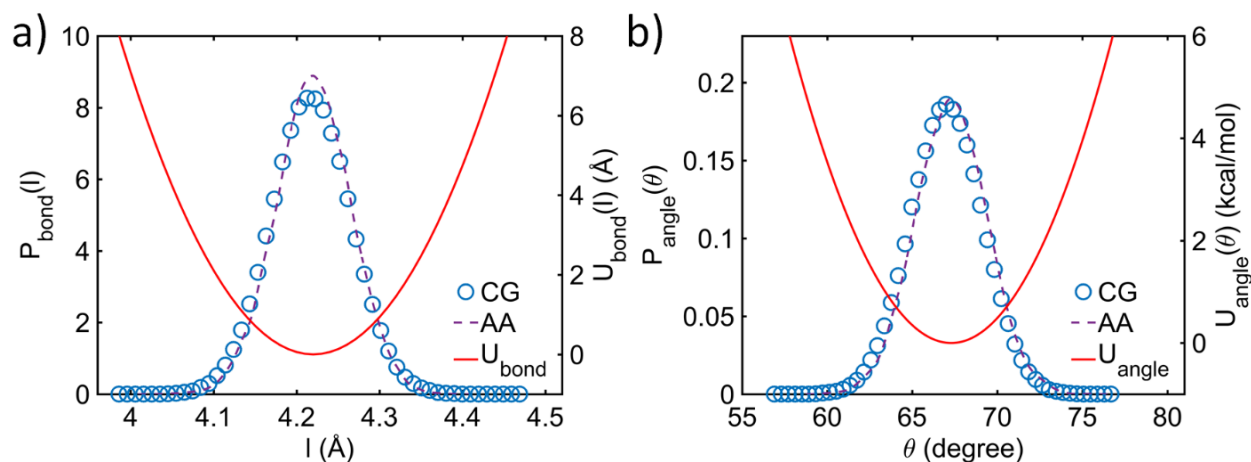


**Figure 3.1.1-1: Bond and angle distributions and resulting potential energy.** Probability distribution functions  $P$  of CG and AA models and resulted CG bonded potentials (i.e.,  $U_{bond}$  and  $U_{angle}$ ) derived from the inverse Boltzmann method (IBM) for the CG a) bonds and b) angles. The functional forms and parameters of  $U_{bond}$  and  $U_{angle}$  are summarized in **Table 3.1.1-1**.

For the nonbonded interaction, we employ a commonly applied 12-6 LJ potential for our CG modeling:  $U(r) = 4\epsilon \left[ \left( \frac{\sigma}{r} \right)^{12} - \left( \frac{\sigma}{r} \right)^6 \right]$ , where  $\sigma$  is the distance (often known as the “size of the bead”) at which  $U$  is zero and  $\epsilon$  is the depth of the potential well associated with the cohesive interaction strength of the materials. To achieve temperature transferability, we generalize the parameters  $\sigma$  and  $\epsilon$  to be temperature dependent (i.e.,  $\sigma(T)$  and  $\epsilon(T)$ ).  $\sigma(T)$  can be derived by matching the AA density, yielding a linear dependence of temperature as shown in **Figure 3.1.1-2**. This matching of density to obtain  $\sigma(T)$  has been done in several studies<sup>115, 116, 122, 123</sup>. The functional forms and bonded parameters of the CG potentials are summarized in **Table 3.1.1-1**.

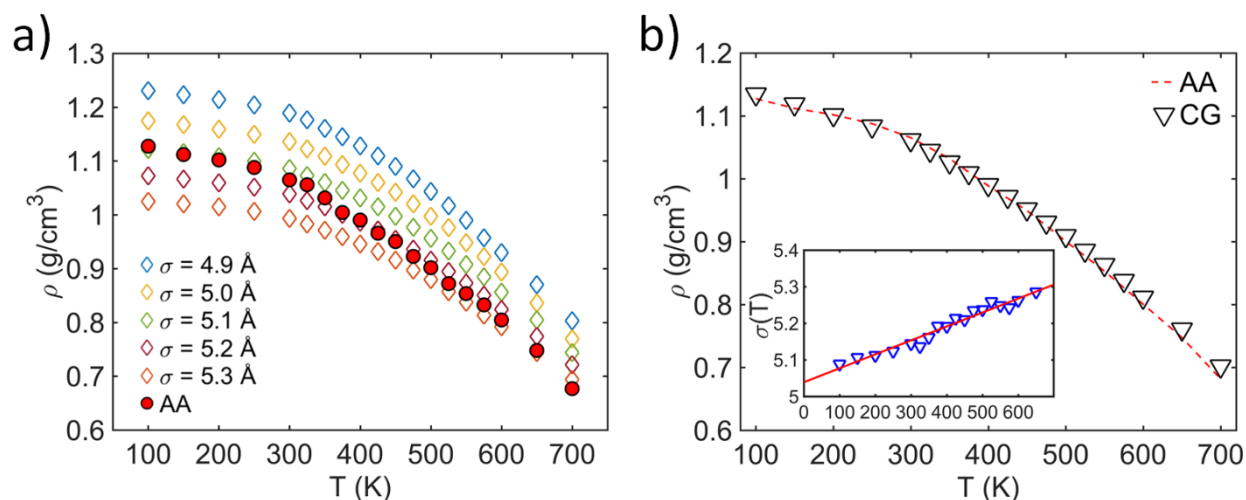


**Figure 3.1.1-2: Matching density of AA to obtain  $\sigma(T)$ .** a) The density  $\rho$  vs.  $T$  for the AA and CG models with varying CG bead size through the LJ potential parameters  $\sigma$ . b) Comparison of

the density  $\rho$  as a function of temperature for the AA and CG models by introducing  $\sigma(T)$ . (Inset) The result of  $\sigma(T)$  against  $T$  for the CG model by matching the  $T$ -dependent AA  $\rho$ . The line shows the linear fit to the  $\sigma(T)$ .

Next, we derive the temperature dependent  $\varepsilon(T)$  through consideration of a short-time scale dynamic property, the Debye-Waller Factor  $\langle u^2 \rangle$ , that has demonstrated the importance of cohesive interactions on the dynamics and strength of the materials<sup>112, 124, 125</sup>.  $\langle u^2 \rangle$  can be readily obtained from experimental measurements and short-time (on the order of picoseconds) simulations of the materials. We hypothesize that by preserving  $\langle u^2 \rangle$  of the AA system via renormalizing  $\varepsilon$ , we might be able to recover the temperature dependent dynamics for the CG modeling. To test this idea, we begin our analysis by evaluating the influence of cohesive interaction  $\varepsilon$  on  $\langle u^2 \rangle$ . The  $\langle u^2 \rangle$  is calculated from the segmental mean-squared displacements (MSD)  $\langle r^2(t) \rangle$  at around  $t_c \approx 3$  ps, which is estimated from the localized caging effect from our simulations. As shown in **Figure 3.1.1-3**, the  $\langle u^2 \rangle$  increases nonlinearly with  $T$  for the AA and CG systems with varying  $\varepsilon$ . The lower  $\langle u^2 \rangle$  of the CG model with higher  $\varepsilon$  over  $T$  indicates a suppressed segmental mobility which arises due to stronger cohesive interactions. For each  $\varepsilon$ , it is clear that the  $\langle u^2 \rangle$  of the CG model intersect with the AA  $\langle u^2 \rangle$  at different temperature, demonstrating the necessity of rescaling  $\varepsilon$  at different temperature to preserve the AA  $\langle u^2 \rangle$ . Accordingly, the  $\varepsilon(T)$  can be determined by preserving the AA  $\langle u^2 \rangle$  at each temperature state (inset in **Figure 3.1.1-3**), leading to a sigmoidal functional form

$$\varepsilon(T) = (\varepsilon_A - \varepsilon_g)\Phi + \varepsilon_g \quad (3.1.1-1)$$

where  $\varepsilon_g$  and  $\varepsilon_A$  refer to  $\varepsilon$  values at in the low  $T$  glassy and high  $T$  Arrhenius regimes, respectively;  $\Phi$  is the two-state crossover function taking the form:  $\Phi = 1/[1 + \exp(-k(T - T_T))]$ , where  $k$  is

a parameter related to the temperature breadth of the transition, and  $T_T$  ( $\approx 475$  K) describes the crossover point of this sigmoidal function from the Arrhenius to glassy regimes. These parameters of  $\varepsilon(T)$  are summarized in **Table 3.1.1-2**. (Note that a slight change of  $t_c$  at picosecond timescale yields nearly the same result for  $\varepsilon(T)$ .)

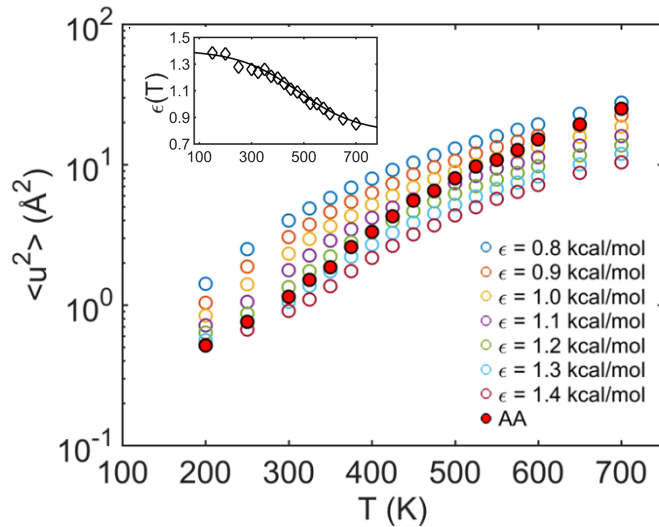


**Figure 3.1.1-3: Matching DWF of AA to obtain  $\varepsilon(T)$ .** The Debye-Waller Factor  $\langle u^2 \rangle$  vs. temperature  $T$  for the AA and CG models with varying cohesive interaction strength  $\varepsilon$ . The renormalized  $\varepsilon(T)$  for the CG model is determined by matching  $T$ -dependent AA  $\langle u^2 \rangle$ . The cohesive interaction strength  $\varepsilon(T)$  (with a unit of kcal/mol) for the CG model determined from matching temperature dependent Debye-Waller Factor  $\langle u^2 \rangle$  of AA model.

In the high- $T$  Arrhenius and low- $T$  glassy regimes, the  $\varepsilon(T)$  tends to be plateau with a larger magnitude at lower  $T$ . However, in the non-Arrhenius regime associated with glass formation,  $\varepsilon(T)$  is strongly varied with  $T$ , which is qualitatively similar to the picture of how the activation energy of relaxation  $\Delta G(T)$  changes with  $T$ . The sigmoidal dependence of  $\varepsilon$  on  $T$  can be understood from the GET and AG theory, which predict that the  $\Delta G(T)$  of glass forming liquids increases with decreasing  $T$  as  $s_c$  decreases upon cooling but saturate at both high  $T$  and low  $T$

limits<sup>106, 107</sup>. Many of these features have been confirmed by the recent molecular simulations<sup>126, 127</sup>. Therefore, the  $\Delta G(T)$  of CG model (without  $\varepsilon$  renormalization) should follow a similar  $T$  dependence of the AA model but with different magnitudes due to their reduced number of degrees of freedom.

**Table 3.1.1-1:** Potential forms and parameters of the force field for the CG model of OTP.

Interaction	Potential form	Parameters
Bond	$U_{bond}(l) = k_b(l - l_0)^2$	$k_b = 146.37 \text{ kcal/mol}\cdot\text{\AA}^2$ $l_0 = 4.22 \text{ \AA}$
Angle	$U_{angle}(\theta) = k_a(\theta - \theta_0)^2$	$k_a = 218.40 \text{ kcal/rad}^2$ $\theta_0 = 67.29^\circ$
Nonbonded	$U(r) = 4\varepsilon(T) \left[ \left( \frac{\sigma(T)}{r} \right)^{12} - \left( \frac{\sigma(T)}{r} \right)^6 \right]$	$\varepsilon(T)$ and $\sigma(T)$ , see <b>Table 3.1.1-2</b>

**Table 3.1.1-2:** Functional forms and parameters of the temperature dependent nonbonded potentials of the CG model from the energy-renormalization method.

	Functional form	Parameters
$\varepsilon(T)$	$\varepsilon(T) = \frac{\varepsilon_A - \varepsilon_g}{1 + \exp[-k(T - T_T)]} + \varepsilon_g$	$\varepsilon_A = 0.74 \text{ kcal/mol}$ , $\varepsilon_g = 1.41 \text{ kcal/mol}$ $k = 0.0086 \text{ K}^{-1}$ , $T_T = 475 \text{ K}$
$\sigma(T)$	$\sigma(T) = \sigma_a T + \sigma_0$	$\sigma_a = 3.8 \times 10^{-4} \text{ \AA/K}$ , $\sigma_0 = 5.04 \text{ \AA}$

### 3.1.2 Simulation parameters

All the molecular dynamics (MD) simulations including the all-atomistic (AA) and coarse-grained (CG) simulations are carried out using the Large-scale Atomic Massive Parallel Simulator (LAMMPS) package<sup>58</sup>. The AMBER force field<sup>128</sup> is applied to the AA simulations. The AA and

CG simulations consist of 600 and 2876 ortho-terphenyl (OTP) molecules, respectively, corresponding to 19200 atoms and 8628 CG beads. Periodic boundary conditions in all three dimensions are applied to the simulation box to model the bulk materials. An energy minimization using the conjugate gradient algorithm is performed for all the simulations<sup>129</sup>, followed by two annealing cycles from 100 K to 700 K. Then, the systems are further equilibrated at 500 K for 4 ns. These simulations are performed using the NPT (i.e., constant number of particles, pressure and temperature) ensemble with fixed 1 bar pressure (i.e.,  $1 \times 10^5$  Pa). An integration time step  $\Delta t$  of 1 fs and 4 fs is applied to the AA and CG simulations, respectively. The dynamic properties (i.e., diffusivity, the Debye-Waller factor, mean-squared displacement and structural relaxation time) are calculated after equilibration run for 2 ns at each temperature.

### 3.1.3 Performance of CG model

In order to evaluate the performance of the CG model, we examine the segmental dynamics by evaluating time-dependent segmental  $\langle r^2(t) \rangle$  and the self-part of the intermediate scattering function  $F_s(q, t)$  of the AA and CG models at various temperatures. **Figure 3.1.3-1a** shows the comparison of  $\langle r^2(t) \rangle$  for the AA and CG models at varying  $T$ . Remarkably, by preserving AA  $\langle u^2 \rangle$ , the CG model can reproduce nearly the entire MSD curves of the AA system in different temperature regimes spanning from glassy to melt regimes. To calculate  $F_s(q, t)$ , the wave number  $q$  ( $=14 \text{ nm}^{-1}$ ) is chosen from the first peak of the static structure factor  $S(q)$ , which is consistent with previous experimental measurement<sup>130</sup>. **Figure 3.1.3-1b** also shows an excellent agreement of  $F_s(q, t)$  between the AA and CG models over a wide temperature range.

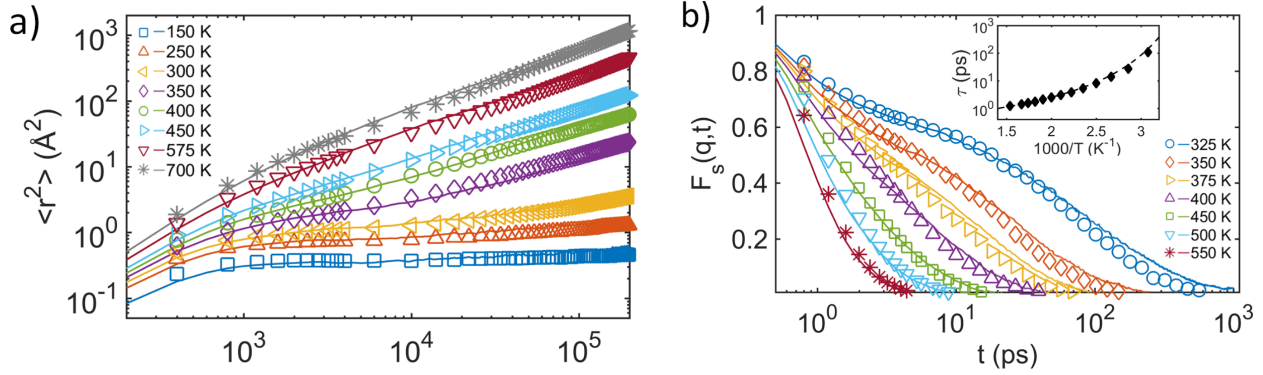


**Figure 3.1.3-1: Comparison of MSD and  $F_s(q, t)$  between AA and CG models.** a) Segmental MSD  $\langle r^2 \rangle$  vs. time for the AA (lines) and CG (symbols) models. b) Comparison of  $F_s(q, t)$  for the AA (lines) and (symbols) CG models. (Inset) Temperature dependent structural relaxation time  $\tau$  for the AA (dashed line) and CG (symbol) models.

From the  $F_s(q, t)$  calculation, we further evaluate the  $\tau$  and characteristic temperatures associated with the glass formation for the OTP. The inset in **Figure 3.1.3-1b** shows the temperature dependent  $\tau$  for both AA (dashed line) and CG (symbol) models, which can be well described by the Vogel-Fulcher-Tammann (VFT) relation<sup>131-133</sup>:  $\tau(T) = \tau_0 \exp\left(\frac{B}{T-T_0}\right)$ , where  $\tau_0$ ,  $B$  and  $T_0$  are parameters associated with relaxation process.  $T_0$ , also called Vogel temperature, is determined to be about 234 K for the AA and CG systems, which dictates the end of glass-formation where the structural relaxation time becomes astronomically large. The glass-transition temperature ( $T_g$ ) is estimated by extrapolating the relaxation data to the empirical observation time scale,  $\tau(T_g) \approx 100$  s, in which we find  $T_g$  to be about 250 K for the AA and CG models. The onset temperature  $T_A$ , defined as temperature below which glassy dynamics becomes dominant, is estimated to be around 500 K from the  $\tau$  data. We also calculate the crossover temperature  $T_c$ , defined as the temperature at which the behavior changes from liquid like to solid like, by fitting

the  $\tau$  data with  $\tau \sim (T - T_c)^{-\gamma}$  from the mode-coupling theory<sup>134</sup>, where  $\gamma$  is an adjustable parameter. The resulted  $T_c$  is estimated to be around 291 K for our models. These characteristic temperatures from our model predictions agree well with literature values (within  $\sim 7\%$  of the measured values)<sup>135-137</sup>, which are summarized in **Table 3.1.3-1**. We also note that the  $T_T$ , which is the empirical transition point in our derived  $\varepsilon(T)$ , lies between  $T_A$  and  $T_g$ , which confirms that the degree of the temperature-dependent rescaling needed for the cohesive interaction is related to the glass forming processes of the CG model.

**Table 3.1.3-1:** Summary of the characteristic temperatures predicted from the AA and CG models from the energy-renormalization method and their comparison with literature values.

Predictions	$T_g$ (K)	$T_0$ (K)	$T_A$ (K)	$T_c$ (K)
AA	251	234	490	289
CG	249	231	490	291
Exp.	243 <sup>136</sup>	231 <sup>136</sup>	455 <sup>135</sup>	290 <sup>137</sup>

We proceed to test quantitative scaling relationship for the AA and CG models. **Figure 3.1.3-2a** confirms that the quantitative relationship between  $\tau$  and  $\langle u^2 \rangle$  determined from our simulations can be well captured by the localization model. Remarkably, our CG model through the ER approach is able to closely reproduce the scaling relationship of the  $\langle u^2 \rangle$  and  $\tau$  for the AA model. The exponent  $\alpha$ , which is related to the geometry of free volume, is determined to be about 1.9 from the best fit of the data for both AA and CG models, which might be associated with the ring-like structure of the OTP. This result implies that the developed CG model cannot only predict the dynamics but also the anisotropic geometry of the segmental free volume.

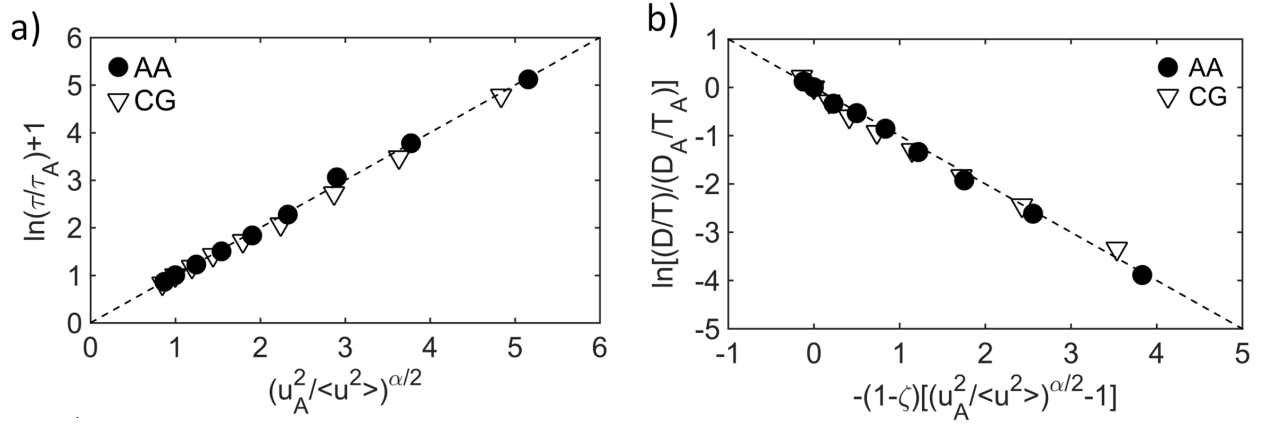


**Figure 3.1.3-2: Relation between  $\tau$ ,  $D$  and  $\langle u^2 \rangle$ .** a) Test of the localization model predictions of  $\tau$  for the AA and CG models. b) Quantitative relationship between  $D$  and  $\langle u^2 \rangle$  predicted from the modified localization model in conjunction with the decoupling relation:  $D/T \sim (1/\tau)^{1-\zeta}$  for the AA and CG models. The dashed lines in b) and c) show the predictions of data from the localization model. The fitting constants  $\alpha$  and  $\zeta$  for the OTP models are determined to be 1.9 and 0.1, respectively.

Recent studies have shown that the temperature dependent diffusion coefficient  $D$  of metallic alloys can be linked to  $\tau$  via a fractional Stokes-Einstein (FSE) relation (i.e., an extension of the Stokes-Einstein relation)<sup>138, 139</sup>:  $D/T \sim (1/\tau)^{1-\zeta}$ , where  $\zeta$  is a decoupling exponent that is usually nonzero for most glass forming liquids and  $T$  is the temperature.  $\zeta$  is zero for the original Stokes-Einstein relation. Employing the LM in conjunction with the FSE relation, the  $D$  can be quantitatively predicted by the  $\langle u^2 \rangle$  via the form:

$$\ln \frac{D}{T} = \ln \frac{D_A}{T_A} - (1-\zeta) \left[ \left( \frac{u_A^2}{\langle u^2(T) \rangle} \right)^{\alpha/2} - 1 \right] \quad (3.1.3-1)$$

where  $D_A$  is the  $D$  at  $T_A$ . **Figure 3.1.3-2b** shows the scaling relation of  $D$  and  $\langle u^2 \rangle$  for the AA and CG models by normalizing its value at  $T_A$ , which is well predicted from the LM. We estimated  $\zeta$  to be equal to 0.1 for our models, suggesting a relatively weak decoupling for the OTP comparing to metallic glasses<sup>138</sup>. This result directly demonstrates the success of using  $\langle u^2 \rangle$ , a short-time (i.e., picosecond) physical quantity, to resolve the large-scale long-time dynamics under coarse-graining spanning over a wide range of glass formation. Therefore, our ER approach in conjunction with the LM model appears to correct all the usual shortcomings of single state-point derived CG models of their dynamics (i.e., faster dynamics and a lack of temperature transferability). To showcase the accuracy of prediction by the ER approach, we also calculate the non-bonded interactions from the radial distribution function through IBM as shown in **Figure 3.1.3-3**. From this non-bonded potential, we also calculate the diffusion coefficient  $D$ .

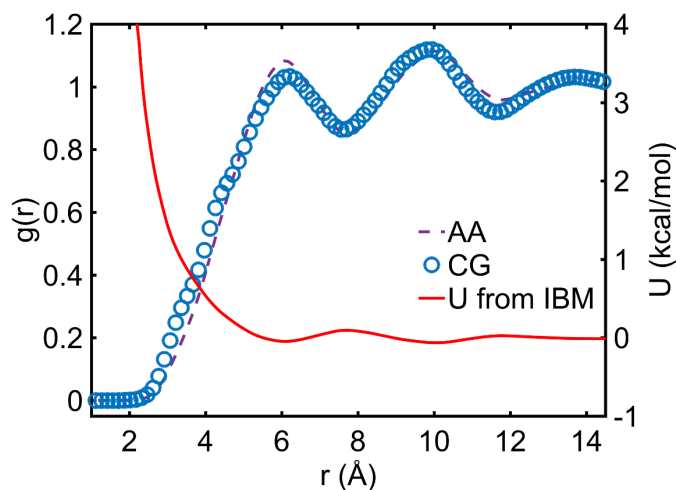


**Figure 3.1.3-3: Radial distribution function of CG bead sites.** Comparison of  $g(r)$  of CG bead sites in AA and CG models using the IBM. The red line shows the CG nonbonded potential  $U$  derived from the IBM.

By implementing the  $\varepsilon(T)$ , the temperature-dependent self-diffusivity  $D$  of AA model calculated using the Einstein relation is well captured by the CG model via the ER approach (**Figure 3.1.3-4**), which also agrees with the experimental measurement<sup>117</sup>. As a comparison, the  $D$  of the CG model derived from the IBM is greatly larger than the AA model (by 1 to 4 orders of magnitude depending on  $T$ ), which necessitates ER to preserve AA dynamics over temperatures.

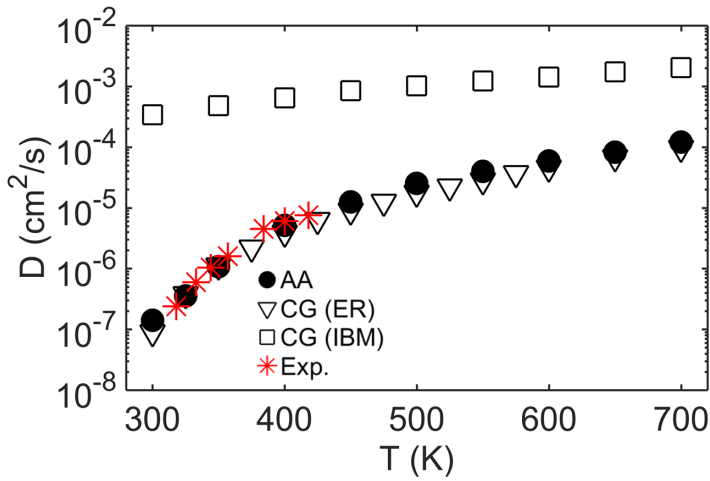


**Figure 3.1.3-4: Comparison of diffusion coefficient between experiments, AA and CG models.** The self-diffusion coefficient  $D$  between the AA and CG models using both ER and IBM at varying temperatures, and their comparison with experimental data from Ref<sup>117</sup>.

### 3.1.4 Conclusion

In summary, we have established a unified framework that builds upon the energy-renormalization approach and glass formation theories to achieve temperature transferrable coarse-graining of OTP. By exploiting the localization model (LM), the cohesive interaction parameter  $\varepsilon(T)$  of the CG OTP model from the  $\langle u^2 \rangle$  analysis exhibits a sigmoidal temperature dependence with a higher magnitude upon cooling. The developed CG model using the ER approach and LM

can quantitatively predict the glass forming dynamics of the AA system over a wide temperature range from high  $T$  Arrhenius melt to the low  $T$  non-Arrhenius and glassy regimes. Our findings demonstrate the effectiveness of ER approach towards building temperature-transferable CG modeling for glass forming materials, and highlight the critical role of caging dynamics in predicting the glass forming properties.

### 3.2 CG model for Polycarbonate

Polycarbonate (PC) is one of most ubiquitously used polymers in today's world owing to its excellent mechanical properties (e.g., high impact strength and ductility and light weight), electrical resistance, and optical transparency<sup>140</sup>. PC is widely used in automotive parts, airplane windows, and high-quality optical lenses. Several previous studies on the development of the CG models of PC (developed via the IBM) have focused more on the static and structural properties, and those models typically exhibit a marked speedup in dynamics compared to its AA counterpart<sup>101, 141, 142</sup>.

In this study, we aim to develop a CG model using the ER method that can capture its temperature-dependent dynamic properties over a wide temperature range. Here, we show that preserving  $\langle u^2 \rangle$  of the AA model under coarse-graining through ER allows for predictions of dynamics over a wide temperature range. Our study reveals that the derived ER functions for the cohesive interaction of the CG polymer models exhibit a universal sigmoidal temperature dependence, which is strongly associated with their glass formation.

### 3.2.1 CG Model description

We choose a 4:1 CG mapping scheme to coarse grain PC as shown in **Figure 3.2.1-1**. Each repeat unit is represented by four CG beads denoted as “A”, “B” and “C” type in the CG model, corresponding to two phenylene, one isopropylidene and one carbonate subunits, respectively.

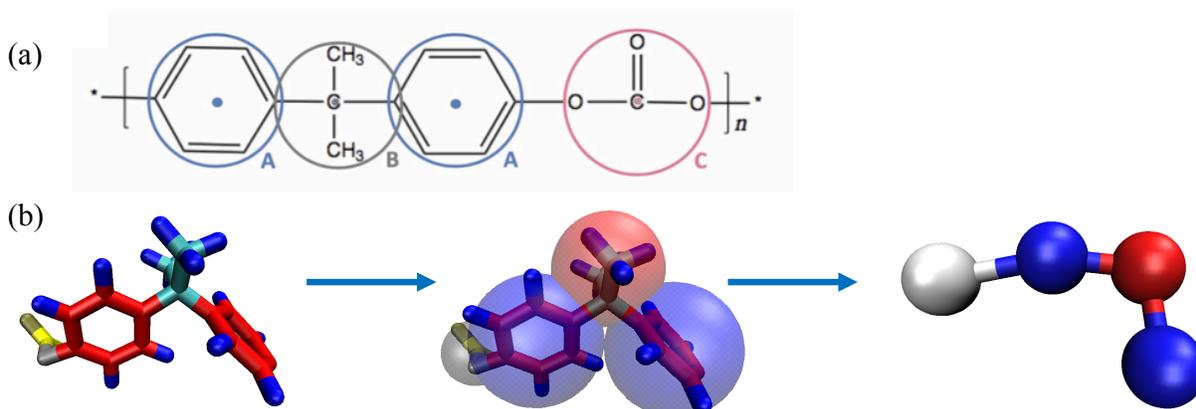


**Figure 3.2.1-1: CG mapping scheme of PC.** (a) PC chemical structure and the corresponding CG bead types and their force center locations. (b) CG-mapping scheme for PC. Each monomer consists of four CG beads with three bead types. The CG bead type “A,” “B,” and “C” represent the phenylene, isopropylidene, and carbonate groups, respectively.

The probability distributions of bonds, angles and dihedrals are obtained from AA simulations, which is then used to derive the CG bonded potentials. The AA bonded probability distributions of PC are obtained in the melt state ( $T = 450\text{ K}$ ), which are used to derive the CG potentials via the iterative Boltzmann Inversion (discussed in Chapter 2:). Direct implementation of the atomistically derived Boltzmann potential estimate is typically not perfect, and thus the CG potentials are optimized iteratively to create a good match with atomistic target distributions. **Figure 3.2.1-2** show the probability distributions and corresponding CG potentials for the bonds, angles and dihedrals. The CG bond potentials are fitted analytically to a shifted harmonic function.

The CG potentials for the angles and dihedrals are derived by matching their atomistic probability distributions, which are implemented using tabulated potential forms within LAMMPS.

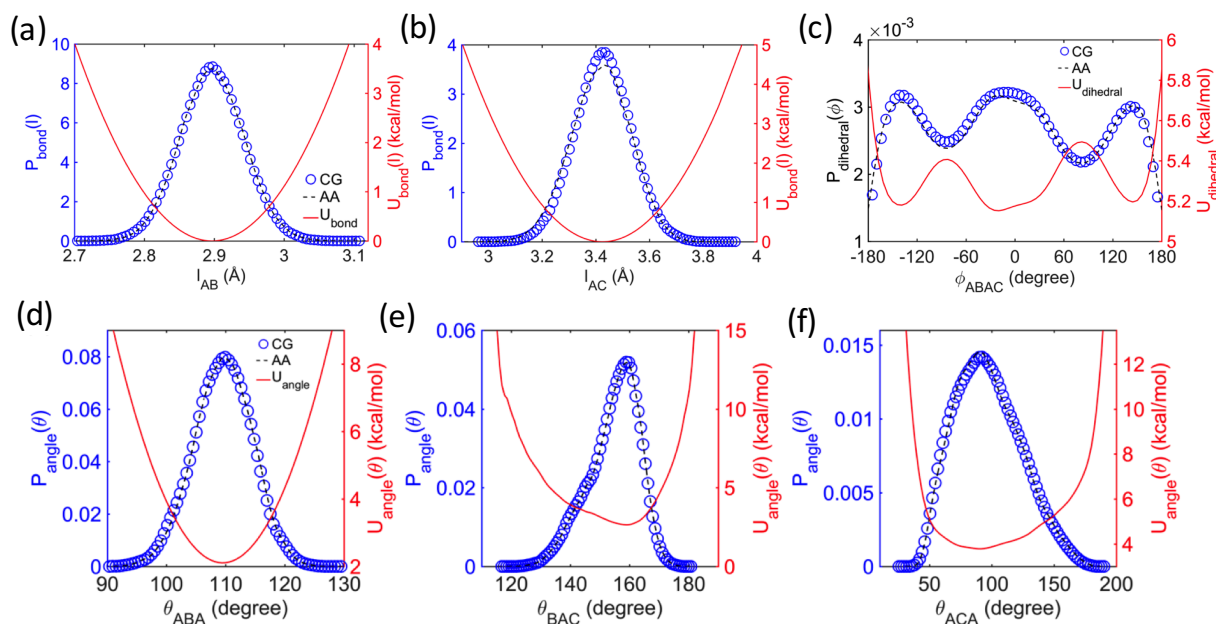


**Figure 3.2.1-2: Bonds, angles and dihedral distribution and potential energies.** Probability distribution functions of CG (blue dots), AA (dashed lines) and the resulting inverted potential (red line) derived from the inverse Boltzmann method for (a) & (b) bonds, c) dihedrals and (d) to (f) angles.

**Table 3.2.1-1: Force field forms and parameters for the CG model of PC.**

Interaction	Potential form	Parameters
AB-bond	$U(l) = k_b(l - l_0)^2$	$k_b = 40.4 \text{ kcal/mol} \cdot \text{Å}^2$ , $l_0 = 2.897 \text{ Å}$
AC-bond	$U(l) = k_b(l - l_0)^2$	$k_b = 112.3 \text{ kcal/mol} \cdot \text{Å}^2$ , $l_0 = 3.425 \text{ Å}$

ABA-angle		
BAC-angle	Tabulated potential, see Ref <sup>16</sup>	
ACA-angle		
ABAC-dihedral	Tabulated potential, see Ref <sup>16</sup>	
Non-bonded	$U(r) = 4\varepsilon_0\alpha(T) \left[ \left( \frac{\sigma_0\beta(T)}{r} \right)^{12} - \left( \frac{\sigma_0\beta(T)}{r} \right)^6 \right]$	$\varepsilon_{0AA} = 0.761, \varepsilon_{0BB} = 0.4599, \varepsilon_{0CC} = 0.4016, \text{ units in kcal/mol, see } \alpha(T) \text{ in Table 3.2.1-2}$ $\sigma_{0AA} = 7.55, \sigma_{0BB} = 5.81, \sigma_{0CC} = 4.21, \text{ units in } \text{\AA}, \text{ see } \beta(T) \text{ in Table 3.2.1-2}$

---

As demonstrated in the previous section, we aim to derive the ER factor  $\alpha(T)$  [i.e.,  $\varepsilon(T) = \alpha(T) \varepsilon_0$ , where  $\varepsilon$  is the cohesive interaction strength parameter in the commonly used LJ potential and  $\varepsilon_0$  is a constant estimated from the radial RDF using the IBM] by preserving  $\langle u^2 \rangle$  of the AA system to recover the  $T$ -dependent glass forming dynamics of the AA model over a wide range of  $T$  by its CG analog. In our simulations, the  $\langle u^2 \rangle$  is determined from the mean-squared displacement (MSD)  $\langle r^2(t) \rangle$  of the center of mass of monomers of the AA and CG models at around  $t \approx 3$  ps, corresponding to a caging time scale estimated from our simulations. We first examine the influence of cohesive interaction strength by systematically varying  $\alpha$  on the Debye-Waller factor  $\langle u^2 \rangle$  for the CG model systems. As shown in **Figure 3.2.1-3**, for each fixed  $\alpha$  value,  $\langle u^2 \rangle$  increases with temperature  $T$  in a nonlinear fashion for both the AA and the CG systems over a wide  $T$  range, which is typical for glass forming materials. As  $\alpha$  increases from 2.5 to 5.0, the  $\langle u^2 \rangle$  decreases at any given  $T$ , indicating a suppressed mobility when increasing the cohesive interaction strength of the CG system. For each a value, the measured  $\langle u^2 \rangle$  of the CG model intersects with the AA  $\langle u^2 \rangle$  at a different  $T$ . This demonstrates the necessity of renormalizing the cohesive interaction strength at varying  $T$  to preserve the value of  $\langle u^2 \rangle$  of the AA model under coarse-graining. Accordingly,

$\alpha(T)$  of the CG model can be phenomenologically determined by preserving  $T$ -dependent  $\langle u^2 \rangle$  of the AA model, leading to a sigmoidal variation with  $T$  (inset in **Figure 3.2.1-3**)

$$\alpha(T) = \frac{\alpha_A - \alpha_g}{1 + \exp[-k(T - T_T)]} + \alpha_g \quad (3.2.1-1)$$

where  $\alpha_g$  and  $\alpha_A$  are the  $\alpha$  values in the low- $T$  and high- $T$  limits, respectively,  $k$  is a parameter related to the temperature breadth of the transition and  $T_T$  describes the crossover point of this sigmoidal function. These parameters related to  $\alpha(T)$  are summarized in the **Table 3.2.1-2**.

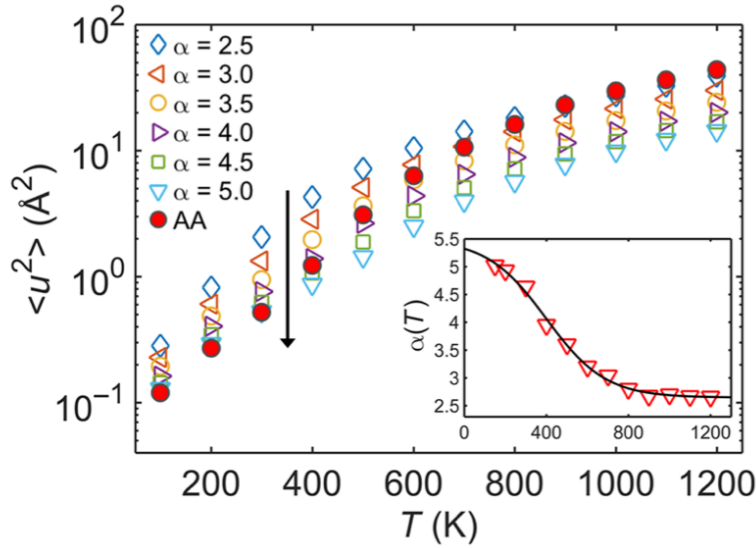


**Figure 3.2.1-3: Matching DWF to obtain  $\alpha(T)$ .** The Debye-Waller Factor  $\langle u^2 \rangle$  vs. temperature  $T$  for the AA and CG models with varying cohesive interaction strength  $\epsilon$ . The vertical arrow indicates a dataset with increase in  $\alpha$ . The result of  $\alpha(T)$  for the CG model determined by matching  $T$ -dependent AA  $\langle u^2 \rangle$  of the AA model of PC.

Similarly, we perform the renormalization procedure for the length scale parameter  $\sigma$  through the renormalization factor  $\beta(T)$ . As reported in the previous section, this  $\beta(T)$  can be readily determined by demanding the  $T$ -dependent density  $\rho$  of the CG model to be consistent with that of the AA model, which typically yields a decreasing trend of  $\beta(T)$ , with  $T$  that can be

captured by a polynomial form (**Table 3.2.1-2**). With the implementation of  $\beta(T)$ , the CG model can well capture the AA  $\rho$  over a wide  $T$  range (**Figure 3.2.1-4**). While  $\beta(T)$  is important to preserve certain static and structural properties of the polymer, such as the density and primary peak location in the RDF, the dynamics of polymer is more sensitive to  $\alpha(T)$ .

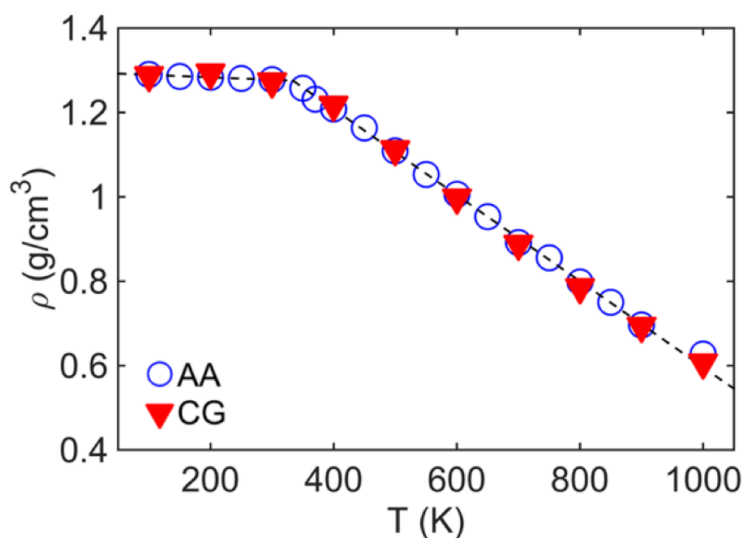


**Figure 3.2.1-4: Comparison of density between AA and CG models.** Density  $\rho$  as a function of  $T$  for the AA and CG PC models. The AA  $\rho$  is preserved by the CG model through the renormalization factor  $\beta(T)$  for the length-scale parameter  $\sigma$  in the cohesive interaction.

**Table 3.2.1-2:** Functional forms and parameters of the temperature dependent nonbonded potentials of the CG model from the energy-renormalization method.

	Functional form	Parameters
$\varepsilon(T)$	$\alpha(T) = \frac{\alpha_A - \alpha_g}{1 + \exp[-k(T - T_T)]} + \alpha_g$	$\alpha_A = 2.659 \text{ kcal/mol}, \alpha_g = 5.304 \text{ kcal/mol}$ $k = 0.0075 \text{ K}^{-1}, T_T = 419.6 \text{ K}$

$$\sigma(T) \quad \beta(T) = \beta_2 T^2 + \beta_1 T + \beta_0 \quad \beta_2 = 2.227 \times 10^{-7} \text{ \AA/K}^2, \beta_1 = -1.087 \times 10^{-4} \text{ \AA/K}, \beta_0 = 0.8245 \text{ \AA}$$


---

### 3.2.2 Simulation parameters

The coarse-grained (CG) and all-atomistic (AA) molecular dynamics simulations are carried out using the Large-scale Atomic/Molecular Massively Parallel Simulator (LAMMPS) software<sup>58</sup>. AA PC with a chain length  $N=10$  are generated using Materials Studio, and consist of 16600 atoms, corresponding to 50 chains.  $N=10$  is chosen for this work primarily due to computational efficiency – larger chain lengths will require exponentially longer simulation times to relax properly, which can cause accuracy issues on dynamics calculations. CG model of PC is generated with the same chain lengths and consists of 8000 CG beads. Periodic boundary conditions are applied in all the directions to simulate the bulk behavior of the system (i.e., without free surface effects). An integration time step of  $\Delta t= 4$  fs is applied for the CG PC and PS, while  $\Delta t= 10$  fs is applied for CG PB simulations, and these time steps are chosen based on their bonded vibrational frequency as reported in our recent study<sup>122</sup>. A time step of  $\Delta t= 1$  fs is applied for the AA-MD. The systems are prepared by equilibrating the melt in the bulk state, which begins with an energy minimization step via the conjugate gradient algorithm. Following this, the systems undergo annealing cycles above and below the glass transition temperature  $T_g$  (between about 150 K and 1000 K for PC) and pressure cycles (between 1 bar and 1000 bar for both AA and CG systems) in the NPT (i.e., constant number of beads, pressure and temperature) ensemble, and then are equilibrated for 2 ns at high temperatures. The dynamic and thermodynamic properties (i.e.,

density, diffusivity, Debye-Waller factor, mean-squared displacement and structural relaxation time) are calculated after equilibration run at each temperature.

### 3.2.3 Performance of CG model

After implementing the derived  $\alpha(T)$  and  $\beta(T)$  for the cohesive interactions into the CG model of PC, we proceed to evaluate the dynamic properties of the CG model. We first look at the MSD  $\langle r^2(t) \rangle$  of the center of mass of monomers for the AA and CG models at various  $T$  which is shown in **Figure 3.2.3-1**. By preserving the atomistic  $\langle u^2 \rangle$  (marked by the vertical dashed line) under coarse-graining through ER, the developed CG model can capture the entire  $\langle r^2(t) \rangle$  curves of the AA model to a good approximation over a wide  $T$  range spanning from the high- $T$  Arrhenius regime to the low- $T$  glassy regime.

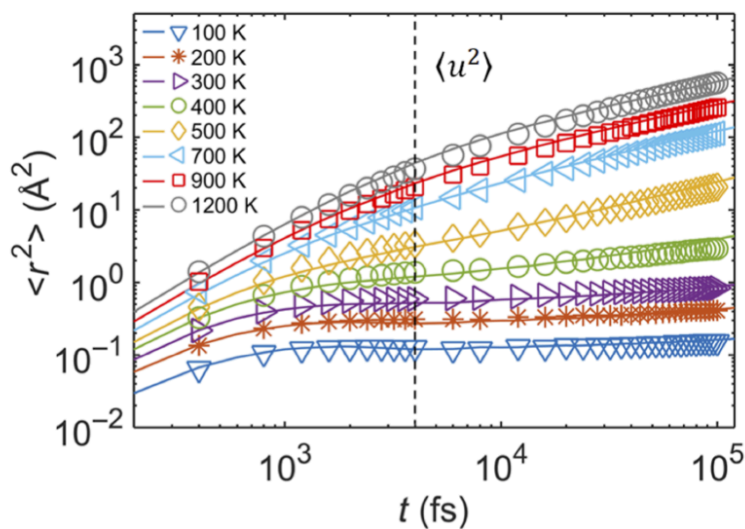


**Figure 3.2.3-1: Comparison of MSD between AA and CG models.** The MSD  $\langle r^2 \rangle$  of the center of mass of the monomer versus time for the AA (lines) and CG (symbols) models over a wide  $T$

range. The vertical dashed line marks the time scale (around the “caging” time of 4 ps) when  $\langle u^2 \rangle$  is obtained from the  $\langle r^2 \rangle$  measurement.

We next evaluate the segmental relaxation time  $\tau$  by calculating the second Legendre order parameter  $P_2(t)$  for both AA and CG models,

$$P_2(t) = \frac{3}{2} \langle \cos^2 \theta(t) \rangle - \frac{1}{2} \quad (3.2.3-1)$$

where  $\theta(t)$  is the angle of a vector under consideration at time  $t$  relative to its position at  $t = 0$ . We then fit  $P_2(t)$  with a stretched exponential function,

$$P_2(t) = \exp \left[ - \left( \frac{t}{\tau_{KWW}} \right)^{\beta_{KWW}} \right] \quad (3.2.3-2)$$

where  $\tau_{KWW}$  is the Kohlrausch-Williams-Watts (KWW) relaxation, and  $\beta_{KWW}$  is the stretch exponent, which describes the breadth of the relaxation times.  $\tau$  can be determined as the integral of the KWW curves with the expression:  $\tau = \left( \frac{\tau_{KWW}}{\beta_{KWW}} \right) \Gamma \left( \frac{1}{\beta_{KWW}} \right)$ , where  $\Gamma$  is the gamma function. **Figure 3.2.3-2** shows the results of the  $T$ -dependent  $\tau$  for the AA and CG model with ER, which yields a good consistency. As a comparison, we apply a fixed ER factor by setting  $\alpha = \alpha_A$  (by matching the high- $T$  AA activation energy) and  $\alpha = 1$  (a first estimate of the activation energy developed from IBM by matching the AA RDF) for the CG model. At temperatures outside the high- $T$  Arrhenius regime (where polymer materials are not thermally stable), it is evident that a constant rescaling of the activation energy provides an inadequate description of the  $\tau$  data, suggesting that the application of ER in a temperature-dependent fashion correctly captures the slowing down of relaxation dynamics upon approaching the glass-transition temperature ( $T_g$ ).

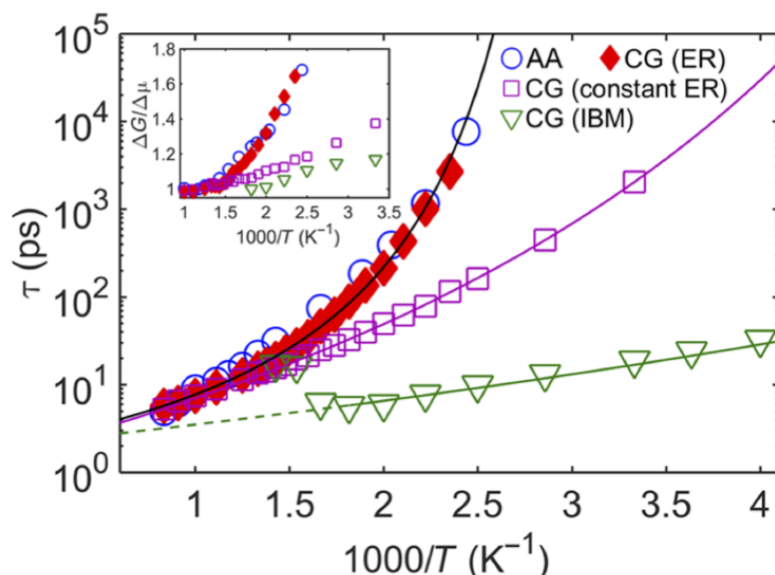


**Figure 3.2.3-2: Comparison of segmental relaxation time between AA and CG models.**  $T$ -dependent segmental relaxation time  $\tau$  for the AA and CG models. As a comparison, the  $\tau$  estimates from the CG models with constant ER (i.e.,  $\alpha = a_A$ ) and derived from the IBM exhibit a growing divergence as lowering  $T$ , while the  $\tau$  estimates from the ER describe the AA  $\tau$  to a much better approximation. The solid curves show the VFT fits of the  $\tau$  data. The dashed curve for the CG model from the IBM shows a high- $T$  regime where the onset of sample evaporation leads to an increase in  $\tau$ . Inset shows the activation energies of relaxation  $\Delta G$  normalized by its value  $\Delta\mu$  at high- $T$  Arrhenius regime for the AA and CG models.

Formally, we may determine the activation energy of relaxation  $\Delta G(T)$  through the relationship:  $\Delta G(T) = k_B T \ln[\tau/\tau_0]$ , where  $\tau_0$  is the vibrational relaxation time on the order of  $10^{-12}$  to  $10^{-13}$  s. The inset of **Figure 3.2.3-2** shows the results of  $\Delta G$  normalized by its value  $\Delta\mu$  at the high- $T$  Arrhenius regime. The CG model with ER evidently describes  $\Delta G$  of the AA model rather well, whereas  $\Delta G$  without ER remains too small at low temperatures. This analysis indicates that CG models without ER simply fail to preserve the AA dynamics in the  $T$  range of practical

application interest, an effect that we attribute to the loss of the configurational entropy  $s_c$  under coarse-graining. This “error” in CG modeling can be largely “corrected” by renormalizing the cohesive interaction strength, i.e., varying  $\alpha$ .

The  $T$  dependence of our simulation estimates of structural relaxation time  $\tau$  can be described by the well-known Vogel-Fulcher-Tammann (VFT) relation<sup>143</sup>,

$$\tau(T) = \tau_0 \exp\left(\frac{DT_0}{T-T_0}\right) \quad (3.2.3-3)$$

where  $\tau_0$ ,  $D$ , and  $T_0$  are fitting parameters that characterize the relaxation process of glass formation. Specifically, the VFT temperature  $T_0$ , dictates the “end” of glass formation, where  $\tau$  formally extrapolates to an infinite value;  $D$  is inversely related to the fragility parameter  $K$ , i.e.,  $K \sim 1/D$ <sup>144</sup>. Correspondingly, we estimate  $T_0$  to be around 301 K and the fragility  $K$  to be about 0.32 for both the AA and the CG model with ER to preserve this property. On the basis of the VFT fit, the  $T_g$  can be estimated by extrapolating the relaxation data to the empirical observation time scale  $\tau(T_g) \approx 100$  s, where we find the  $T_g$  to be around 330 K for the simulated systems.

At  $T$  above the onset temperature  $T_A$  (estimated from the  $\tau$  data), the dynamics of polymer fluids is mainly governed by the large-scale chain motion rather than the segmental mobility. We next examine the self-diffusivity  $D_s$  of polymer chains at the high-T melt states (above  $T_A \approx 700$  K) from around 700 to 1200 K.  $D_s$  is obtained from the MSD measurement of the center of mass of chains  $\langle r_{CM}^2 \rangle$  in the diffusive regime, where  $\langle r_{CM}^2 \rangle \sim t$ . At  $T$  below this high-T regime, it is challenging to accurately quantify  $D_s$  of polymers through MD, as it requires much greater time to fully get into the diffusive regime due to the dramatic slowdown of the chain mobility. **Figure 3.2.3-3** shows a good consistency of  $D_s$  between the AA and the CG using the ER method, which exhibit a slowdown of diffusion as  $T$  decreases. Their  $T$  dependence follows an apparent Arrhenius

behavior:  $D_s(T) = D_0 \exp\left(-\frac{\Delta E}{k_B T}\right)$ , where  $D_0$  is a prefactor and  $\Delta E$  is the activation energy of diffusion. From the Arrhenius fit of the data,  $\Delta E$  is estimated to be around 33.4 kJ/mol·K for both AA and CG models.

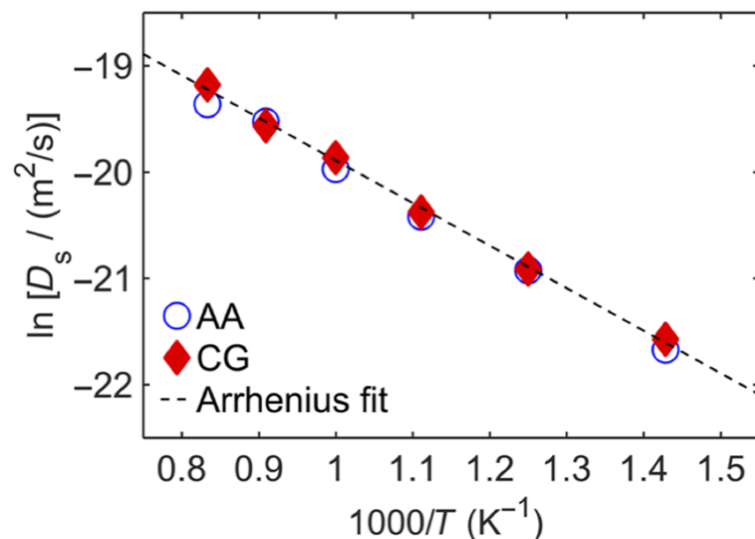


**Figure 3.2.3-3: Comparison of diffusion coefficient between AA and CG models.** Self-diffusion coefficient  $D_s$  of chains at elevated  $T$  for the AA and CG models, which is well described by an Arrhenius relation (dashed line).

As a further test of our CG procedure with regard to preserving thermodynamic properties, **Figure 3.2.3-4** also shows a good consistency of the  $T$  dependence of the isothermal compressibility  $\kappa_T$  between the AA and CG models, where we have reduced  $\kappa_T$  by its value at the onset temperature  $T_A$ . This normalization is required for scale-dependent properties whose absolute values cannot be preserved under coarse-graining.

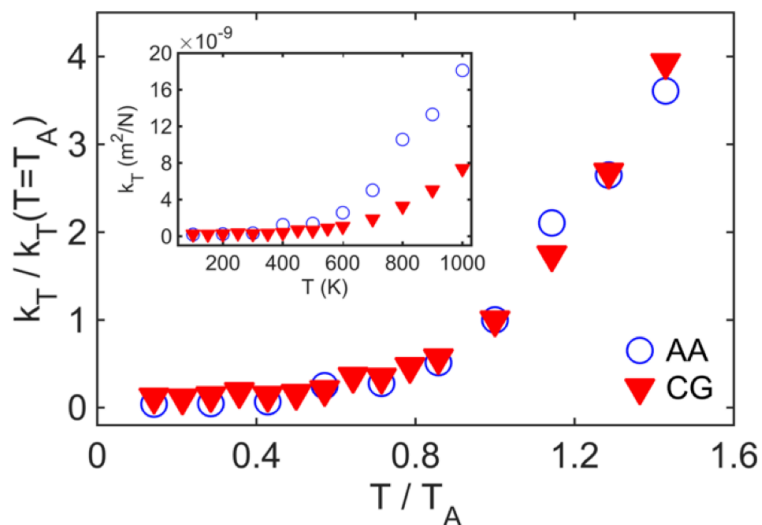


**Figure 3.2.3-4: Comparison of isothermal compressibility between AA and CG models.** Test of isothermal compressibility  $\kappa_T$  normalized by its value at  $T_A$  as a function of  $T/T_A$  for the AA and CG models, showing good consistency, while the absolute  $\kappa_T$  of the AA and CG models show divergence at higher  $T$  (inset). This result suggests the necessity of making comparison to experiments and simulation models using appropriate reduced variables.

Previous studies<sup>98, 145, 146</sup> have shown that it is possible to capture the dynamics of the AA models under coarse-graining by rescaling the time such that the  $D_s$  and the VFT behavior of relaxation can be recovered. This method works mostly at higher temperatures since the system can enter into the diffusive regime in a relatively short time. However, using a single time-rescaling factor fails to reproduce the entire  $\langle r^2(t) \rangle$  curve of the AA model at a lower temperature due to the noticeable existence of the ballistic regime and sub diffusive regime. Here, we have shown that the CG model developed using the ER approach can reproduce the atomistic dynamics and entire  $\langle r^2(t) \rangle$  curves over a wide  $T$  range, which is a significant feat in CG modeling of glass forming

polymers, whose relaxation processes are rather complex and involve different relaxation mechanisms occurring at different time scales depending on  $T$ .

### 3.2.4 Conclusion

In this study, we applied ER method to develop a temperature transferable CG model for polycarbonate. By exploiting the localization model and Adam-Gibbs theory of glass formation, we have shown that preserving the AA  $\langle u^2 \rangle$ , i.e., a fast dynamics physical property at a picosecond time scale, by renormalizing the cohesive interaction parameter  $\varepsilon$  through  $\alpha(T)$  under coarse-graining, the CG model can well capture the glass forming dynamics of the underlying AA system over a wide  $T$  range, from the high- $T$  Arrhenius regime to the intermediate non-Arrhenius regime of glass formation and low- $T$  glassy regime. Our work illustrates the effectiveness and applicability of the ER approach toward building a multiscale temperature-transferable modeling framework for the polymers having different segmental structures, and particularly implies the critical roles of glass forming properties, such as fragility, and degree of coarse-graining in influencing the CG modeling.

## 3.3 CG Modeling of Epoxy

Epoxy resins are thermosets widely employed in our society from everyday life applications<sup>147</sup> to high-tech, new generation composites<sup>148, 149</sup>. They are used as resistant anti-corrosion coatings<sup>150, 151</sup>, high-performance adhesives<sup>152-154</sup>, structural composites in the aerospace industry<sup>155-157</sup>, electrical insulators<sup>158, 159</sup>, biomedical applications<sup>160, 161</sup>, impact-resistant materials<sup>162-165</sup> and more. Their superior thermomechanical properties come from their design flexibility: the macroscopic properties of the neat epoxy resin are influenced by the choice of the

epoxy molecule (containing the epoxide group) and the curing agent, or hardener<sup>166-168</sup> via their molecular weight<sup>169-171</sup>, flexibility<sup>172, 173</sup> and chemistry<sup>174, 175</sup>. Epoxy resins are also relevant in the context of aHNPs as nanoparticles can be grafted with epoxies that are capable of crosslinking, where the stiffness of the nanocomposite can be enhanced by the nanoparticle, whereas the crosslinks can toughen the material.

All-atom molecular dynamics (AA-MD) studies have investigated epoxy resins, showing the effect of degree of crosslinking on the glass transition temperature  $T_g$  and thermomechanical properties<sup>176, 177</sup>, the effect of water absorption<sup>178</sup> or the mechanical and fracture behavior for neat epoxies<sup>179</sup> or epoxy composites<sup>180, 181</sup>. AA-MD simulations remain limited in the spatiotemporal scales they can explore<sup>182, 183</sup>. Complex MD tools such as the reactive force field ReaxFF<sup>184</sup> makes fracture studies<sup>185, 186</sup> computationally expensive, despite their accuracy. Coarse-grained (CG) models of epoxy resins are particularly useful for the molecular study of properties that depend more on the network structure and physical properties (crosslinking density, molecular weight of the components or entropic effects) rather than specific chemical interactions. Still, the development of CG models for epoxies that can capture the thermomechanical properties of the networks is a daunting task due to the high complexity and heterogeneity of their molecular structure.

In this work we extend the ER protocol to a CG model for epoxy resins. In particular, we target a resin with Bisphenol A diglycidyl ether (DGEBA) as the epoxy, and either 4,4-Diaminodicyclohexylmethane (PACM) or polyoxypropylene diamines (Jeffamines D- $x$ , where  $x$  depends on the molecular weight of the Jeffamine, or the number of repeated monomer units between the two amine groups) as the curing agents.

### 3.3.1 CG Model description

In our CG representation, shown in **Figure 3.3.1-1**, we use five beads to represent DGEBA (with only three different bead types due to the molecular symmetry), four beads to represent PACM (of two different types) and fifteen beads (of three different types) to represent D400. From here on we refer to the DGEBA beads as beads 1, 2, 3; PACM beads as beads 4,5; D400 beads as beads 5, 6, 7. Bead 5, present both in PACM and D400, corresponds to the amino group  $\text{NH}_2$  involved in the crosslinking with the epoxy DGEBA (with bead 3 in particular in the CG representation).

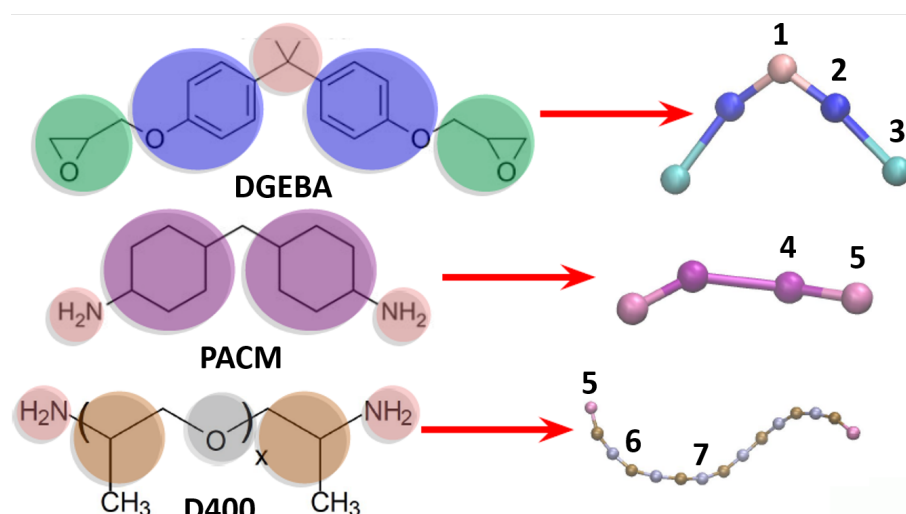


**Figure 3.3.1-1: CG mapping scheme for DGEBA, PACM and D400.** Atomistic (left) and Coarse Grained (right) representations of Bisphenol A diglycidyl (DGEBA), 4,4-Diaminodicyclohexylmethane (PACM) and polyoxypropylenediamine (Jeffamine D-400). The colored circles overlapped to the atomistic structures show which atoms are included in each CG bead. The CG beads (numbered on the right) are centered in the center of mass of the atoms they

incorporate. In the CG model, crosslinking is performed creating new bonds between beads 3 and 5.

First we calibrate the bonded parameters of the CG model using a standard Iterative Boltzmann Inversion (IBI) protocol, where the potential is calibrated from the distribution of bonds and angles of the atomistic model. We exclude dihedral interactions, which would greatly increase the complexity of the CG model in the presence of varying degree of crosslinking. For our previous polymer models<sup>187</sup> we found that dihedral interactions have little impact on the thermomechanical properties and dynamics of materials, and a slight adjustment of non-bonded interaction parameters can compensate for their effect. **Figure 3.3.1-2** shows the representative case of the beads 4 and 5 for PACM with two bonds (4-4 and 5-5) one angle (4-4-5) and one dihedral (5-4-4-5). The atomistic data are the distributions of the bond and angle between the centers of mass of the corresponding CG beads (calculated as the center of mass of the atoms included in the CG bead). We show that the CG model also has the same distributions with the potential obtained through IBI. The same is done for the DGEBA and D400, and **Table 3.3.1-1** reports all the parameters used for the bonded interactions.

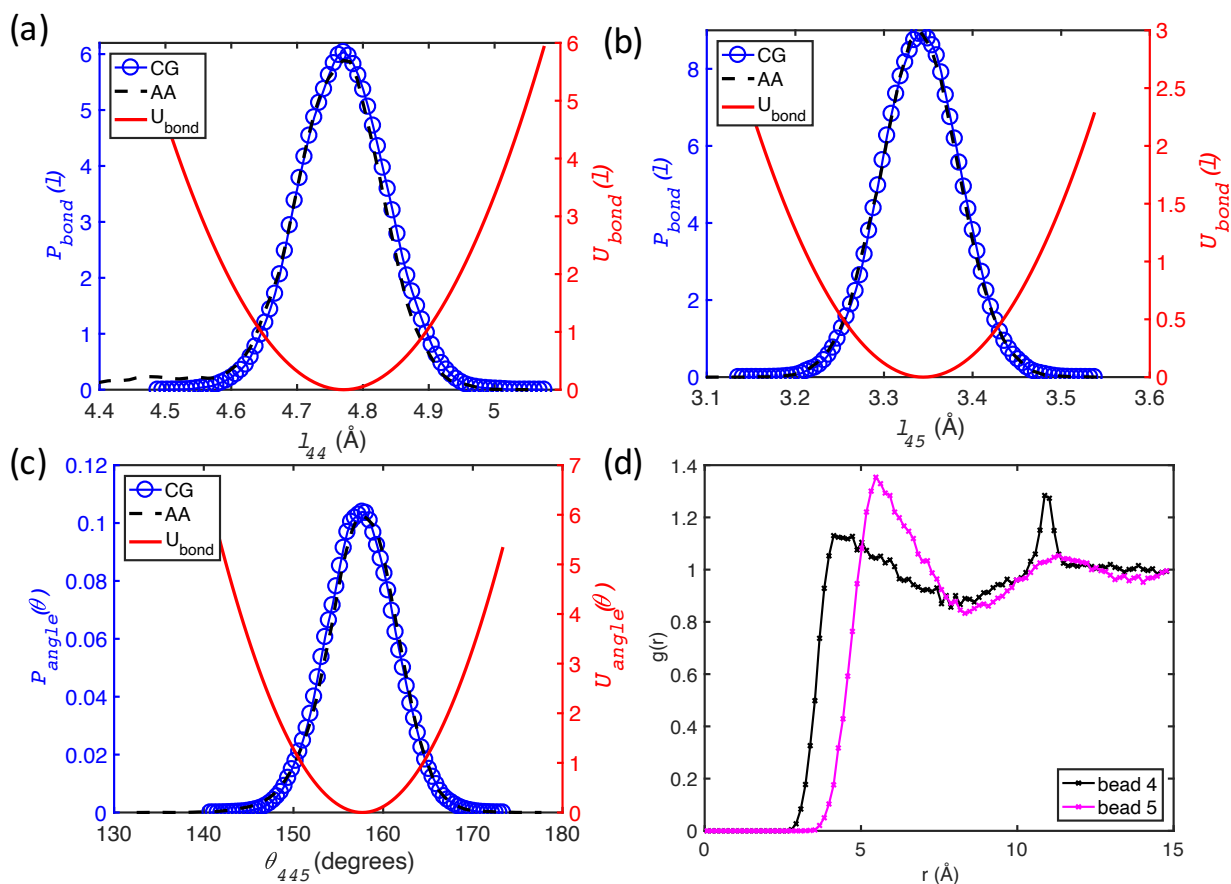


**Figure 3.3.1-2: Bond, angle and radial distribution for PACM beads and corresponding potential energies.** The probability distribution (blue) and the potential energy (red) for (a) 4-4 bond, (b) 4-5 bond, and (c) 4-4-5 angle of the CG model are obtained through Iterative Boltzmann Inversion of their distributions in the atomistic representation. (d) RDF of the centers of mass corresponding to the CG beads 4 (black) and 5 (magenta) in PACM, from which we can extract first estimates of  $\epsilon_4$ ,  $\epsilon_5$ ,  $\sigma_4$ , and  $\sigma_5$  the non-bonded cohesive energies and sizes, via Iterative Boltzmann Inversion.

**Table 3.3.1-1:** Force field forms and parameters for the CG model of DGEBA-PACM-D400.

Interaction	Potential form	Parameters
Bond	$U_{ij}(l) = k_{ij}(l - l_{ij})^2$ , i,j are atom types	$k_{12} = 201, l_{12} = 3.37, k_{23} = 22.18, l_{23} = 4.65, k_{44} = 30.25, l_{44} = 4.60, k_{45} = 11.87, l_{45} = 3.32, k_{56} = 49.72, l_{56} = 1.88, k_{67} = 114.6, l_{67} = 1.86, k_{35} = 21.48, l_{35} = 2.58$ unit of $k$ is kcal/mol·Å <sup>2</sup> , unit of $l$ is Å
Angle	$U_{ijk}(\theta) = k_{ijk}(\theta - \theta_{ijk})^2$ i,j,k are atom types	$k_{123} = 28.52, \theta_{123} = 165, k_{212} = 45.60, \theta_{212} = 108, k_{445} = 7.18, \theta_{445} = 160, k_{767} = 38.77, \theta_{767} = 138, k_{676} = 43.62, \theta_{676} = 161, k_{567} = 38.01, \theta_{567} = 138, k_{235} = 3.52, \theta_{235} = 120, k_{354} = 7.49, \theta_{354} = 124, k_{356} = 9.15, \theta_{356} = 117, k_{353} = 11.45, \theta_{353} = 120$ unit of $k$ is kcal/mol, unit of $l$ is degrees

We extract first-order estimates of the parameters for the non-bonded Lennard-Jones interactions: the cohesive energies and the effective bead sizes, from the radial distribution function between the centers of mass of the CG beads as shown in **Figure 3.3.1-2d**. We use an arithmetic rule of mixing for  $\epsilon_i$  and geometric rule of mixing for  $\sigma_i$ . While these non-bonded parameters would be suited to reproduce the structure of the AA system in CG representation, the novelty of the ER method is to recalibrate the non-bonded interactions to match important markers of the system dynamics and mechanical properties. In particular, we calibrate the  $[\epsilon_i, \sigma_i]$  parameters of the CG model to match the density, Debye-Waller factor  $\langle u^2 \rangle$  (the value of the mean square displacement measured at 3 ps, where we observe caging effects), elastic modulus and yield stress during tensile deformation of the AA systems. On the basis of theoretical results connecting the picosecond caging dynamics to the local softness of glass forming polymers<sup>188-190</sup>, previous ER papers on simpler, non-connected polymers, identified  $\langle u^2 \rangle$  as the only quantity to be matched from the AA model to be able to also predict the shear modulus of the system<sup>115, 116, 122, 123</sup>. We find that this is not the case in our system with the complex interactions of several beads of different size and interaction strength, especially in crosslinked networks, and we calibrate the

parameters to match the dynamics and mechanical properties simultaneously. Thus, we make use of machine learning to parametrize the non-bonded interactions which will be discussed in the upcoming section.

### 3.3.2 Simulation parameters

We simulate all-atomistic (AA) systems of either DGEBA-PACM or DGEBA-D400 in stoichiometric ratio for the formation of the cured epoxy resin. For the first system, we place 768 DGEBA molecules and 384 PACM molecules randomly in a cubic box with periodic boundary conditions. For the second system, we use 944 DGEBA molecules and 472 D400 molecules. These systems are large enough to accurately yield the distributions and mechanical properties.<sup>179</sup> We prepare crosslinked networks at intervals of 0.05 Degree of Crosslinking (DC), from 0 to 0.9 (DGEBA+PACM) or from 0 to 0.95 (DGEBA+D400), DC=0 being the uncrosslinked systems and DC=1 being the fully cured network. The atomistic molecules are pre-built with no hydrogen atoms in the PACM/D400 amine group and an open-ring configuration for the DGEBA epoxide group, ready for the polymerization step. The presence or absence of hydrogen does not have an observable influence on the mechanical properties of the crosslinked resins<sup>179</sup>. For each of our system we run two independent replicas to enhance the statistics. We use harmonic style for bond and angles, charmm style for dihedrals, umbrella style for improper interactions and the buck/coul/long pair style for non-bonded interactions. For the CG models, we use systems of 2000 DGEBA and 1000 PACM molecules, or 1000 DGEBA and 500 D400 molecules. We use harmonic style for bond and angles and the lj/gromacs pair style for non-bonded interactions with arithmetic rule of mixing for  $\epsilon_i$  and geometric rule of mixing for  $\sigma_i$ .

We use the Polymatic package to create crosslinks in our systems in cycles of polymerization. In each cycle, the Polymatic algorithm creates a certain number of new bonds between target particles within a distance criterion, and for each new bond it updates the topology of the system and perform an energy minimization using LAMMPS. At the end of each cycle, a molecular dynamics step is performed to further relax the system. For the atomistic systems, we create bonds between the carbon atoms of the DGEBA epoxide group and the Nitrogen atoms of the PACM or D400 amine group within a cutoff distance of 6.0 Å, creating 16 bonds per cycle. The intermediate molecular dynamics step is performed with a timestep of 1 fs for 50 ps in total, in NPT ensemble at temperature  $T=600$  K and pressure  $P=1$  atm. In the coarse grained model, we create 10 bonds per cycle between bead 3 of DGEBA and bead 5 of PACM or D400 within a cutoff distance of 15 Å. The intermediate dynamics step has a timestep of 4 ps, runs for 200 ps in total and it is done in NPT ensemble at  $T=1000$  K and  $P=0$  atm. Each amine group can be connected to two DGEBA epoxide groups. In the formation of our networks, we first prioritize the crosslinking between an epoxide group and an amine group with no other crosslinks, creating networks with a DC up to 50%. After that, we create crosslinks between amine groups and epoxide groups of DGEBA molecules that are not already in the same network, to avoid the formation of closed loops involving only a fraction of the molecules of the system. This restriction allows up to 75% crosslinked networks, at which point all molecules of the system are connected to the same network. We apply no restriction after that, and stop the procedure when the formation of a new crosslink is not achieved within 30 MD cycles. This limit was at DC=90% for the atomistic DGEBA+PACM system, at DC=95% for the atomistic DGEBA+D400 and at DC>99% for the coarse grained systems.

For all our simulations we use the LAMMPS package<sup>58</sup>. After a short run with a non-bonded soft potential at T=300 K and P=0 atm to remove overlapping atoms, we follow the protocol explained in the previous to reach an equilibrated state (signaled by zero residual stress in the system) at room temperature and pressure in NPT ensemble. For the AA systems we use a timestep of 1 fs. We first increase the temperature to T=600 K and the pressure to P=1000 atm in 50 ps in NPT ensemble, then equilibrate the system for 100 ps at high T and P, then quench down to T=300 K and P=0 atm in 100 ps and finally equilibrate at T=300 K and P=0 atm for 200 ps. The mean square displacement of the systems is calculated after the equilibration, for the following 100 ps, then a tensile deformation is performed in NPT ensemble at strain rate  $\dot{\epsilon} = 0.5 \times 10^9 s^{-1}$ . The tensile deformation is performed separately in the three different directions  $x$ ,  $y$  and  $z$  to obtain improved statistics of the mechanical properties of the systems. The CG systems use a timestep of 4 fs. They are first equilibrated at T=800 K and P=100 atm, then quenched to 500 K and 0 atm to relax the pressure, then quenched in temperature to 300 K and 0 atm, and finally equilibrated at constant T=300 K and P=0 atm. Each of these steps is performed for 2 ns. The dynamics is then measured in the equilibrated state, and a tensile test with strain rate  $\dot{\epsilon} = 0.5 \times 10^9 s^{-1}$  (same as the AA simulations) is performed in NPT ensemble.

### 3.3.3 Non-bonded parametrization using machine learning

**Figure 3.3.3-1** reports the values of density,  $\langle u^2 \rangle$ , Young's modulus and yield stress of the AA systems for DGEBA+PACM (black dots) and DGEBA+D400 (red dots).  $\langle u^2 \rangle$  is calculated from the mean square displacement at  $t^* = 3 ps$ . The Young's modulus is calculated from the stress-strain curve of the tensile test by fitting a line upto 2% strain. For both systems, the density and mechanical properties (modulus and yield stress) increases with increasing DC, while  $\langle u^2 \rangle$ ,

marker of the mobility, decreases. This is expected, and more pronounced in the DGEBA+PACM system, which is stiffer and less mobile due to the rigidity of the curing agent PACM, while the more flexible D400 polymer causes higher mobility and lower density/mechanical properties. The elastic modulus in particular, changes at different rates with DC in the two systems, since the spatial density of crosslinks that dominates the elastic response of the network is higher in the DGEBA+PACM system because of the different length between PACM and D400.

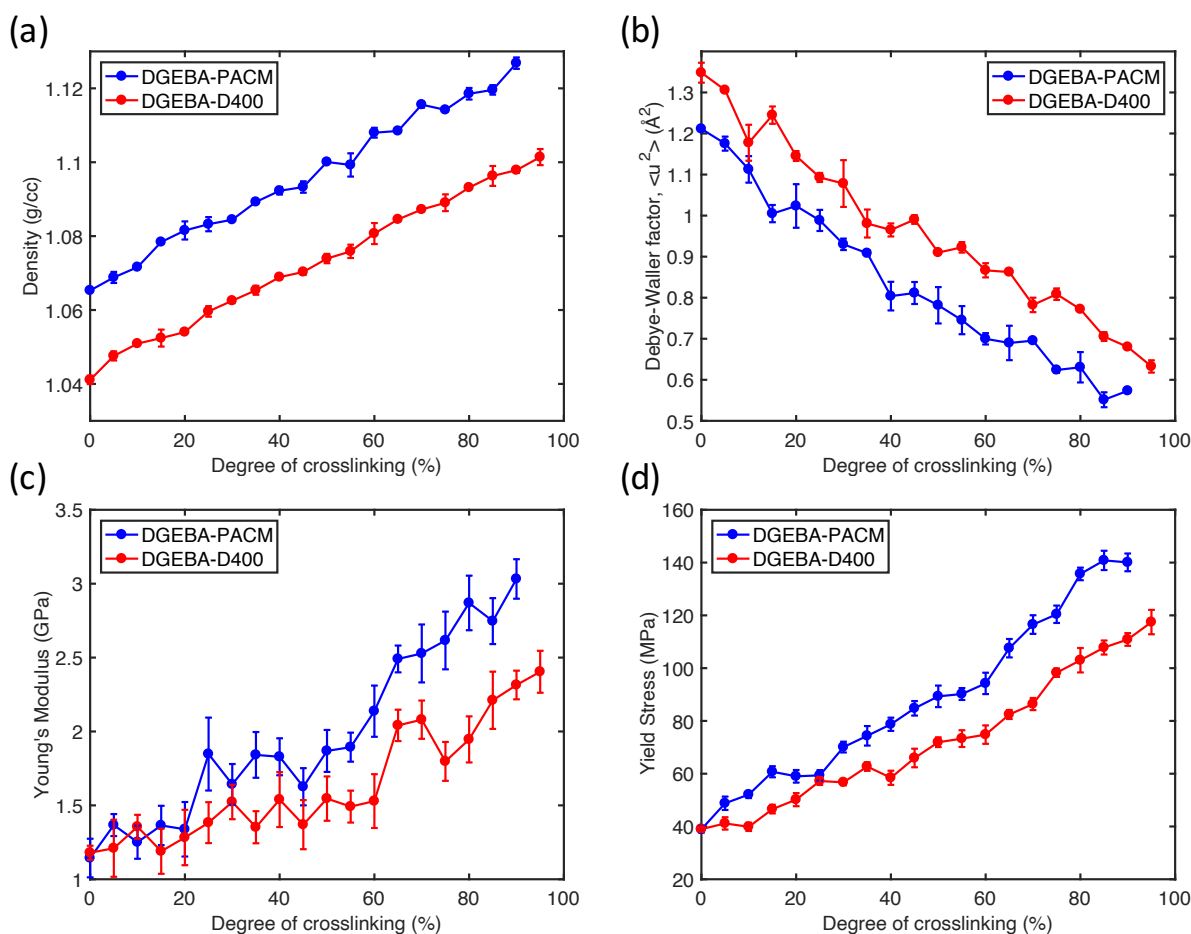


**Figure 3.3.3-1: Target macroscopic properties of the atomistic simulations: (a) density, (b) Debye-Waller factor  $\langle u^2 \rangle$ , (c) Young's modulus and (d) tensile yield stress as a function of degree of crosslinking (DC) for the DGEBA+PACM and DGEBA+D400 systems.**

To the best of our ability, we found that any fixed parametrization of the CG model is not able to match the properties of the AA system at all degrees of crosslinking. This is caused by the different rate with which the configurational entropy  $s_c$  of the AA and CG models changes with varying DC, similarly to what happens with varying  $T$  for any CG model. Thus, we introduce a DC-dependence for all non-bonded parameters  $[\varepsilon_i, \sigma_i] = [\varepsilon_i(DC), \sigma_i(DC)]$ . In previous models with highly homogeneous polymers and few CG beads, it was possible to study the dependence on temperature in a “traditional” way, with simple parameter sweeps and introducing only one additional parameter to rescale all cohesive energies (the  $\varepsilon_i$ ) and one to rescale all the effective sizes of the CG beads (the  $\sigma_i$ ). We find that this is not possible in our current epoxy model due to the high complexity of the system, including the effect of crosslinks and the large number of CG beads with very different cohesive energies and sizes. We introduce a generalization of previous protocols that relies on Machine Learning (ML) to explore the high-dimensional space of the model parameters. The idea is to select a range for each parameter and use the ML algorithm to find the set of input values that simultaneously optimizes the match between the AA and the CG model for all target responses at all degrees of crosslinking. Preserving the seminal ideas of the ER procedure, the protocol outlined here can be easily generalized to any CG model both with a top-down or bottom-up approach, and further developments will allow the creation of higher-resolution computational models in an automated way.

To select the range of the parameters, we run preliminary tests calibrating the cohesive energies either on the dynamics of the systems at DC=0% or on the elastic modulus at DC=90% (the highest DC we can achieve for the DGEBA+PACM AA network). This gives us extremes for the values of cohesive energies  $\varepsilon_i$ , and we further expand them by around 20%. We also select a

range of around +/-20% for the  $\sigma_i$  parameters from the initial estimate obtained from the IBI of the radial distribution functions. Our ranges are post-validated by our final calibration, as discussed in the following. In our Design of Experiment, each set of parameters is represented by a point in a 15-dimensional hypercube (7  $\varepsilon_i$  and 7  $\sigma_i$  parameters, plus the degree of crosslinking DC). In this space, we select more than a thousand points (700 for the DGEBA+PACM system and 500 for DGEBA+D400) and run the corresponding CG simulations, measuring for each the density,  $\langle u^2 \rangle$ , elastic modulus and yield stress like we did for the AA system.

We now use the data obtained from the CG simulations to inform the ML model, which explores the parameter space of the CG model and predicts at each degree of crosslinking the set of  $[\varepsilon_i; \sigma_i]$  which maximizes the likelihood of the AA and CG target responses to coincide. In addition to maximum likelihood, we use the insight we have on the systems to add some physics-based constraints to our parametrization. In particular, we require that each parameter has a dependence on crosslinking density  $[\varepsilon_i(\text{DC}); \sigma_i(\text{DC})]$  described analytically from DC=0% to DC=100%. We first find the optimal parametrization for the extremes (the uncrosslinked and the fully crosslinked network) and then constrain the intermediate values on some chosen functional form. In general, if one fixes the DC=0% CG parametrization for all degrees of crosslinking, the mechanical properties of the AA system increases at a faster rate than in the CG system with increasing DC, and the mobility decreases faster. From these data, we expect a general increase of the cohesive energies  $\varepsilon_i(\text{DC})$  with increasing degree of crosslinking, which will proportionally increase the mechanical properties and decrease the mobility of the CG model.

### 3.3.4 Performance of the CG model

The agreement of the two models is higher for simpler quantities like density, where the precision of the measurements is also higher as seen from **Figure 3.3.4-1**. For complex properties like elastic modulus and yield stress, the discrepancies can be larger at certain values of DC, but always within the confidence intervals that our data could provide. Despite these occasional discrepancies, we feel that our parametrization has a high level of accuracy, given the complexity of the model, and in particular for fully cured networks (DC=100%) of interest for experimental applications. In general, this protocol is easily generalizable to any polymeric system, for any set of target properties.

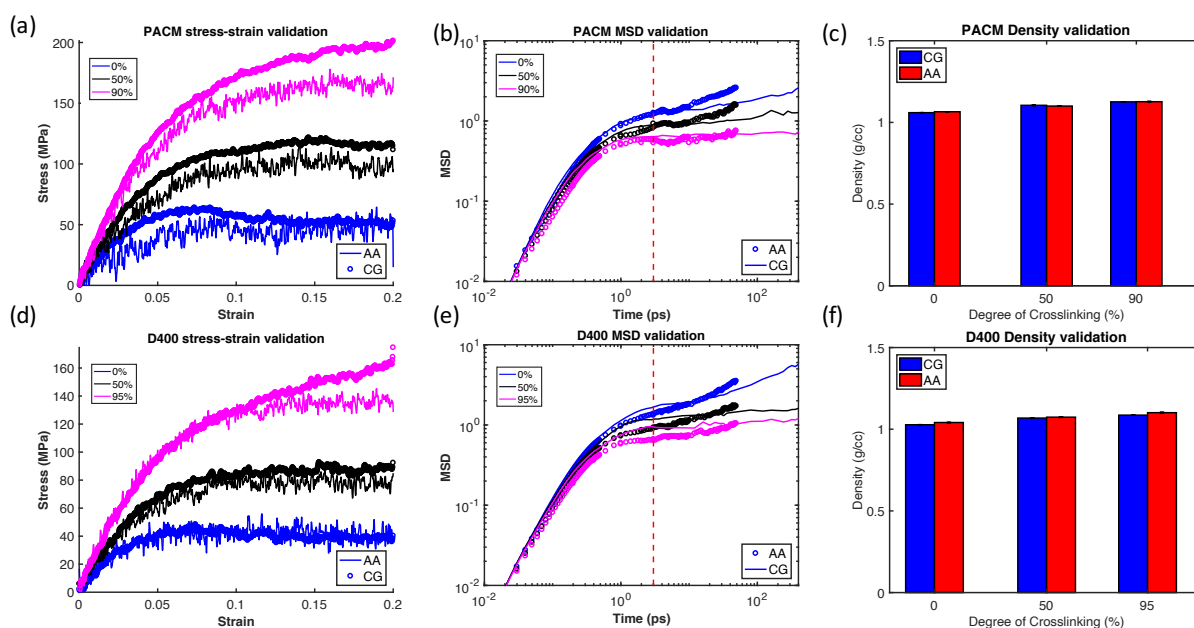


**Figure 3.3.4-1: CG validation based on predictions by the ML algorithm.** (a) to (c) shows the validation for DGEBA-PACM system for stress-strain curve, mean square displacement and density. (d) to (f) shows similar validation for DGEBA-D400 system. The dotted line in (b) and (e) mark the time at which  $\langle u^2 \rangle$  was calculated.

The CG curves validate the prediction of the ML model and show the expected values for  $\langle u^2 \rangle$ , elastic modulus and yield stress of the systems. Additionally, the comparison with the AA curves of corresponding DC show that by matching elastic modulus and yield stress, we capture the overall stress under tensile deformation for the system. By matching the Debye-Waller factor  $\langle u^2 \rangle$  of the AA system, the MSD of the DGEBA+D400 system is also matched for longer timescales beyond the picosecond caging time. This was expected, given theoretical relationships linking the picosecond caging dynamics to the segmental dynamics of glass-forming systems and validated in previous ER models for simpler homopolymers. For the DGEBA+PACM system, we find that this property does not hold so well. Despite matching the picosecond caging dynamics of the AA and CG systems, the AA has faster dynamics at longer timescales for the uncrosslinked systems. This might be caused by the variety of CG beads with different sizes and cohesive energy, which might create a broader spectrum of caging scales and relaxation times. Despite this discrepancy, the effect is greatly reduced in the fully crosslinked network of interest for experimental applications, where the system is frozen in the network conformation and there is no diffusion.

### 3.3.5 Conclusion

Our CG model is able to match the dynamics and mechanical properties of a higher-resolution AA model, which we showed in the past<sup>179</sup> to be consistent with experimental measures. In particular, we match the density, Debye-Waller factor  $\langle u^2 \rangle$ , Young's modulus and tensile yield stress at any degree of crosslinking of the network at fixed temperature  $T=300\text{K}$ . This is an extension of our ER-CG protocol<sup>187, 191</sup>, which was used to match the dynamics and mechanical properties of simpler glass-forming polymer systems by adjusting the non-bonded interactions of

the CG model in a T-dependent way. Here the external parameter considered is instead the degree of crosslinking, DC, of the epoxy network. Additionally, the chemical heterogeneity of our epoxy system requires the use of multiple different CG beads (7 in this model), leading to 14 adjustable parameters for the non-bonded interactions ( $\sigma$  and  $\epsilon$  for each LJ potential, with an arithmetic rule of mixing for cross-interactions). We calibrate all our parameters in a DC-dependent way to simultaneously match the four target properties of the AA system (density,  $\langle u^2 \rangle$ , modulus and yield stress). To find the optimal set of parameters in this high-dimensional space, we developed machine learning (ML) tools that use a training set of CG simulations from a design of experiment to extrapolate the response of a CG simulation based in the force field parameters, and find the optimal set of parameters to obtain the target properties. For each parameter we obtain a continuum response [ $\epsilon_i(\text{DC}); \sigma_i(\text{DC})$ ] which is back validated with AA simulations and shows excellent agreement.

### 3.4 Conclusion

In summary, we have established a new coarse-graining framework called the energy-renormalization approach that builds upon glass formation theories to achieve a temperature transferrable coarse-graining for three different kinds of materials: a small molecule, a polymer and an epoxy resin. For OTP and PC, the cohesive interaction parameter  $\epsilon(T)$  of the CG model from the  $\langle u^2 \rangle$  analysis exhibits a sigmoidal temperature dependence with a higher magnitude upon cooling. For epoxy, the parametrization is done with respect to the degree of crosslinking which shows a linear dependence. We find that our ER approach can quantitatively predict the dynamics of the AA system over a wide temperature range from a high- $T$  Arrhenius melt to the non-Arrhenius regime of incipient of glass formation and low- $T$  non-equilibrium glassy regime. The

ER approach should also be applicable to more complex glass forming molecules, such as branched polymers and bottle brushes.

We believe that this work will be of high relevance for multiple fields. Our findings demonstrate the effectiveness of the ER approach toward building a temperature-transferable CG modeling framework for the glass forming materials and highlight the critical role of caging dynamics in predicting the glass forming properties. The epoxy CG model itself will be useful in epoxy community, with the ability to investigate molecular features, structural heterogeneities and mechanical behavior of a wide range of epoxy resins. The ML tools developed for this model are general, and easily extended to an arbitrarily complex case of multiple input parameters to be adjusted to match any number of target macroscopic properties for the creation of CG models for nanomaterials. The conceptual extension of the ER scheme to a crosslinked polymer network is of high theoretical relevance, being linked to the role of crosslinks in the change of configurational entropy of the system and useful for the creation of CG models for a broad range of elastomers and network systems.

## Chapter 4: Materials by design for hairy nanoparticle assemblies

Having developed the energy renormalization approach for these glassy polymers, the next step was to use them to study mechanical properties of polymer nanocomposites, especially aHNPs. However, as discussed in Chapter 1:, exploring the wide parametric space that affects the mechanical properties with only CG simulations is still daunting. Hence, in this chapter we focus on utilizing the power of machine learning in combination with molecular dynamics simulations to explore this vast design space of aHNPs. This approach reveals an optimal design strategy that maximizes the mechanical properties, specifically Young's modulus and toughness, of these nanocomposites and provides six to seven orders of magnitude speed up over AA-MD simulations.

In the first section of this chapter, a brief introduction to the material system and metamodeling is provided. Next, the metamodel based design framework is discussed which includes the details of CG-MD simulation protocols, design of experiments, a brief description of the multi-response Gaussian process metamodel, construction of Pareto frontier and statistical sensitivity analysis. The next section will describe the influence of design parameters on the mechanical properties and a design strategy is proposed to optimize the mechanical properties. This work is done in collaboration with Prof. Wei Chen's group at Northwestern who helped me with developing the metamodel. Portions of the text and figures within chapter are reprinted or adapted with permission from Hansoge et al. ACS Nano 2018<sup>192</sup>.

### 4.1 Introduction

In mechanical design of a polymer nanocomposite, the objective often involves optimizing the material's properties by efficiently searching for the best combination of design variables, such as choice of polymer, nanoparticle size, polymer chain length, etc<sup>193-195</sup>. Wide parametric studies

are required to search for the optimum design parameters in this vast space. Recent systematic experimental investigations of aHNPs have provided valuable insights into their mechanical properties. However, they involve some inferences of modulus and toughness from nanoindentation<sup>29,30</sup> or buckling methods<sup>28</sup>. However, using experimental techniques to carry out such searches are very prohibitive, time-consuming and inefficient. While theoretical physics-based scaling relations such as the Daoud-Cotton model<sup>46</sup> can help with qualitative predictions of chain structure, these models often require empirical constants that require experimental studies. Computational modeling can provide the necessary answers required to optimally design a nanocomposite. Considering the nanoscale nature of these materials, molecular dynamics (MD) simulations have been employed to study structural<sup>196</sup> and conformational<sup>82</sup> properties and self-assembly<sup>41,42</sup> of polymer grafted nanoparticles. However, correlating molecular design parameters with mechanical properties using CG-MD simulation is exacting in this case due to the computational cost. Hence, to overcome this issue, we take advantage of power of machine learning/metamodeling which will be discussed in upcoming sections.

A metamodel is a surrogate model (a model of a model) that can be a mathematical algorithm that represents the input output relationships. Metamodels are usually computationally very cheap as compared to even CG-MD simulations. Metamodel-based design optimization (MBDO) is a useful framework that can be used in conjunction with computationally intensive (e.g. CG-MD) simulations<sup>197-199</sup>. The MBDO framework has been successfully applied to design of various engineering and material systems, such as fuel cells<sup>200</sup>, structural components of vehicles<sup>201</sup>, and nanocomposites<sup>202</sup>.

In this study, we aimed to combine this MBDO framework with our CG-MD simulations to rapidly explore the design space and optimize the mechanical properties for aHNPs. Specifically, we propose a multi-objective MBDO framework to uncover trade-offs offered by four key material design parameters [i.e., chain length ( $N$ ) of the polymer, grafting density ( $\sigma$ ), polymer-nanoparticle interaction strength ( $\epsilon_{pnp}$ ), and nanoparticle edge length ( $l_{np}$ )] with the ultimate goal of optimizing the transverse elastic modulus and toughness of the aHNPs. The chain length, grafting density and nanoparticle dimensions are well known to be the most influential parameters governing the mechanical properties. The interaction between polymer and nanoparticle is chosen as the fourth design parameter as it can represent the various surface functionalization on the nanoparticle surface. The various synthesis methods can lead to different surface interactions which we want to capture through this  $\epsilon_{pnp}$ . The metamodel we use in the work is called the Multi-objective Gaussian Process (MGP) model. We describe why we choose this model in section 4.2.3.

We chose cellulose nanocrystal (CNC) grafted to poly (methyl methacrylate) (PMMA) as our model aHNP system. There are a few reasons for the choice of this nanoparticle and polymer. Much of the earlier work on aHNPs focused on spherical nanoparticles such as silica<sup>29, 30, 40, 203</sup>, while higher mechanical properties can be expected from high-aspect ratio nanoparticles. Among possible filler candidates, cellulose nanocrystal (CNC) extracted from natural sources (e.g., wood, bacteria and tunicates) has come under the spotlight as transparent, eco-friendly, biocompatible, versatile building blocks for structural applications<sup>204-208</sup>. Specifically, CNCs have very high axial elastic modulus that is comparable to Kevlar<sup>209</sup>, high transparency, high aspect ratio ( $\sim 10-100$ )<sup>206</sup> and relatively low density. Reactive groups (i.e., -OH) on CNC surfaces<sup>210</sup> allow

functionalization<sup>68, 211, 212</sup> and polymer grafting<sup>213, 214</sup> to achieve tunable and multifunctional properties. Earlier studies have shown improvement in storage<sup>215</sup> and elastic modulus<sup>216</sup> of nanocomposites prepared using CNCs and poly (methyl methacrylate) (PMMA). PMMA is used in wide range of applications such as lenses for glasses, rear-lights in vehicles, LCD screens and shatter resistant windows. PMMA is one of the most commonly used polymers in nanocomposites owing to its low density and excellent mechanical and optical properties<sup>217</sup>.

## 4.2 Metamodel based design optimization framework

The metamodel-based design optimization (MBDO) framework for material design employed in this study includes a hybrid design of experiments (DOE) (optimal Latin hypercube sampling and manual selection in regions with highly nonlinear behavior), CG-MD simulations to gather the data points, Gaussian process modeling for building the metamodel, modified leave-one-out cross validation, and metamodel runs for obtaining optimal solutions under multiple objectives. Statistical sensitivity analysis (SSA) is performed on the metamodel to understand the model behavior and to determine which input factors (i.e., material design parameters) most strongly influence the mechanical response. These material design parameters along with their ranges are summarized in **Table 4.2-1**. The bounds of design variables are chosen to be within an experimentally realistic range and such that CG-MD simulations can be completed in a reasonable timeframe. Parameters studied here are comparable to the range seen in experiments reported, except for chain length, where higher molecular weights above entanglement length have been previously investigated but are challenging due to high computational cost of properly relaxing the chains.

**Table 4.2-1:** Design bounds of the material parameters studied using CG-MD simulations.

<b>Input variable</b>	<b>Lower bound</b>	<b>Upper bound</b>	<b>Units</b>
Chain length ( $N$ )	10	100	repeat units
Grafting density ( $\sigma$ )	5	50	% of surface beads grafted
Polymer-NP interaction ( $\varepsilon_{pnp}$ )	0.3	5	kcal/mol
NP edge length ( $l_{np}$ )	5	30	Å

#### 4.2.1 Design of experiments

The purpose of the design of experiments (DOE) is to carry out as few simulations as possible to capture the behavior of the nanocomposite system such that the comprehensive metamodels built from these simulations are accurate enough. Here, we apply a hybrid DOE, where 80 initial points are generated with the optimal Latin Hypercube sampling (OLHS) method<sup>218</sup>. This produces randomized yet uniformly distributed DOEs by minimizing the  $L_2$  central discrepancy between the cumulative distribution function (CDF) of an initial LHS design and the CDF of a multivariate distribution. However, due to the nonlinearity of the input-output dependencies obtained, it was observed that these data points did not adequately cover the entire range of weight % of NPs especially in the low and high weight percentages. Hence, additional 20 data points were generated in the low and high weight percentage regions, resulting in one hundred CG-MD simulations in total.

## 4.2.2 CG-MD system setup and simulation protocols

We use CG-MD simulations to obtain the modulus and toughness of the model CNC-PMMA nanocomposite in the transverse direction, which is orthogonal to the direction of particle alignment. **Figure 4.2.2-1** a-b depict the coarse-graining mapping scheme used for modeling cellulose and PMMA. Two glucose monomers are represented by one CG bead, and the entire CNC is modeled as a face-centered cubic (FCC) crystal. Although the surface of CNCs can be quite irregular, the canopy of the grafted polymeric layer should shield these surface features from affecting the mechanical properties. Harmonic bonds with high spring constants ( $k = 100$  kcal/mol/Å<sup>2</sup>) are employed in the axial direction of the nanocrystals to ensure that it has much greater stiffness axially. The properties of interest here do not require an extensive parametrization of cellulose crystals other than their transverse elastic properties, given that the polymer is much more compliant and failure should localize in the matrix or the interface. The nonbonded cohesive interaction, represented by the standard 12-6 LJ potential, is parameterized to achieve a transverse modulus of around 38 GPa, which is in agreement with experimental values reported<sup>206</sup>. PMMA is represented with a two bead per monomer CG model, one for the backbone (A) and one for sidechain (B). The interaction parameters for the CG model of PMMA are derived from all-atomistic simulations using the thermomechanically consistent coarse-graining approach, which accurately captures the mechanical behavior of PMMA<sup>219</sup>. The force field parameters are summarized for both PMMA and CNC in **Table 4.2.2-1**.

**Table 4.2.2-1:** Force field forms and parameters for the CG model of PMMA and CNC.

Interaction	Potential form	Parameters
AA-bond	$U(l) = k_b(l - l_0)^2$	$k_b = 105.0$ kcal/mol·Å <sup>2</sup> , $l_0 = 2.735$ Å

AB-bond	$U(l) = k_b(l - l_0)^2$	$k_b = 39.86 \text{ kcal/mol}\cdot\text{\AA}^2, l_0 = 3.658 \text{ \AA}$
CNC-bond	$U(l) = k_b(l - l_0)^2$	$k_b = 100 \text{ kcal/mol}\cdot\text{\AA}^2, l_0 = 5 \text{ \AA}$
AAA-angle	$U(\theta) = -k_B T \ln \left[ a_1 e^{-\frac{(\theta - \theta_1)^2}{b_1}} + a_2 e^{-\frac{(\theta - \theta_2)^2}{b_2}} \right]$	$a_1 = 2.294 \times 10^{-2}, b_1 = 9.493^0, \theta_1 = 121.0^\circ,$ $a_2 = 4.367 \times 10^{-3}, b_2 = 6.210^0, \theta_2 = 158.5^\circ$
AAB-angle	$U(\theta) = k_1(\theta - \theta_0)^2 + k_2(\theta - \theta_0)^3 + k_4(\theta - \theta_0)^4$	$k_1 = 9.881 \text{ kcal/mol}\cdot\text{rad}^2, k_2 = -15.12$ $\text{kcal/mol}\cdot\text{rad}^3, k_3 = 6.589 \text{ kcal/mol}\cdot\text{rad}^4, \theta_0 = 1.690 \text{ rads}$
AAAA-dihedral	$U(\phi) = \sum_{k=1}^5 A_k \cos^{k-1}(\phi)$	$A_1 = 4.380, A_2 = -0.8739, A_3 = -0.3571, A_4 = -0.2774, A_5 = -0.09312,$ units in kcal/mol
BAAB-dihedral	$U(\phi) = \sum_{k=1}^5 A_k \cos^{k-1}(\phi)$	$A_1 = 4.519, A_2 = -0.8859, A_3 = -1.692, A_4 = -0.5625, A_5 = -0.9562,$ units in kcal/mol
Non-bonded	$U(r) = 4\varepsilon \left[ \left(\frac{\sigma}{r}\right)^{12} - \left(\frac{\sigma}{r}\right)^6 \right]$	$\varepsilon_{AA} = 0.5, \varepsilon_{BB} = 1.5, \varepsilon_{AB} = 0.866, \varepsilon_{CNC-CNC} = 5, \varepsilon_{CNC-A/B} = 0.5,$ units in kcal/mol $\sigma_{AA} = 5.5, \sigma_{BB} = 4.42, \sigma_{AB} = 4.96, \sigma_{CNC-CNC} = 3.15, \sigma_{CNC-A/B} = 4.0,$ units in \AA

In order to mimic the high aspect ratio of CNCs (10-100) and avoid edge artifacts, we choose a representative volume element of the CNC where its length is five times the width/height, and employ periodic boundary conditions in the longitudinal direction which effectively creates infinitely long crystals. To simulate the CNC-PMMA nanocomposite, a single polymer-grafted CNC is first generated, where the location of graft sites is chosen arbitrarily, and the polymer chain is grown from the designated site using a random walk algorithm<sup>81, 220</sup>. The system is then replicated three times (resulting in 4 total aHNPs) and packed together to create a representative nanocomposite system as depicted in **Figure 4.2.2-1c**.

The CG-MD simulations are carried out using Large-scale Atomic/Molecular Massively Parallel Simulator (LAMMPS) software<sup>58</sup>. Periodic boundary conditions are applied in all the

directions to simulate the bulk behavior of the system. Before running deformation simulations, first, a soft interatomic cosine potential is used to push the polymers apart in the NVT ensemble, so that any overlap created during packing is removed. The soft potential is then turned off and replaced by the actual interatomic Lennard-Jones potential. The system is annealed at 1000 K for 2 ns to remove any residual stresses and is then equilibrated at 600 K at a high pressure of 1000 atm for 2 ns to make sure the grafted CNCs are packed well. The system is then cooled down to 300 K and equilibrated for another 2 ns under atmospheric pressure. We check that the polymers chains have relaxed by tracking the second Legendre order parameter ( $P_2$ )<sup>123</sup> and consider that a  $P_2$  value less than 0.1 indicates that the polymer is fully relaxed. **Figure 4.2.2-1d** shows the snapshot of the nanocomposite system after annealing and equilibration. An integration timestep of 4 fs is used for all the CG-MD simulations. The equilibration simulations are carried under the isothermal-isobaric ensemble (NPT). The tensile test is carried out at a strain rate of  $10^8 \text{ s}^{-1}$ , which is typically used in MD simulations<sup>123, 124, 219</sup>. It should be noted that while the strain rate used here is high compared to experiments, the design strategy and the main conclusions drawn in our study should not be affected since the strain rate dependence is relatively low in the glassy regime of the polymer. For the metamodel validation, five CG-MD simulations are run where configurations at different timesteps are taken at the end of equilibration and these structures are used for the deformation simulation with different initial velocity. From the tensile tests, Young's modulus is calculated from the slope of stress-strain curve up to 0.2% strain, and the toughness is approximated as the area under the stress-strain curve. We note that the stress-strain curve and this measure of toughness is expected to be size-dependent due to strain localization effects that depend on number of nanoparticles studied, in other words, the number of sites where localization can

occur. This effect should lead to smaller strains in experiments. Thus, toughness values reported should be taken as a qualitative measure that should correlate well with experiments in terms of the relative ranking of the systems studied, and the stress-strain curves can actually be used with further analysis to estimate fracture energies as done previously for glassy polymers<sup>179, 221</sup>.

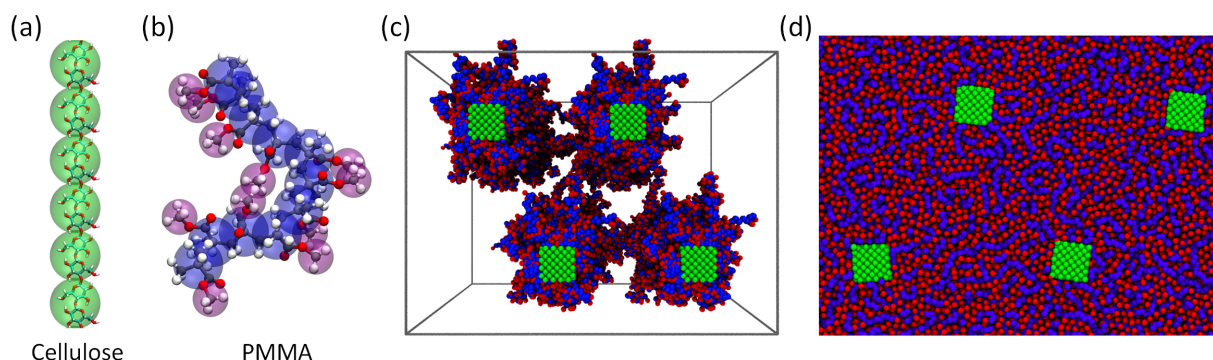


**Figure 4.2.2-1: CG mapping scheme for CNC and PMMA and representative volume element for CG simulations.** Schematic of AA structure and CG models for (a) cellulose and (b) PMMA. Two glucose monomers in the cellulose are modeled as one CG bead (green) with the force center at the center of mass. The backbone (blue) and sidechain (purple) in CG PMMA is represented by two different beads. (c) The snapshot of the initial system consisting of four PMMA grafted CNCs where the polymer is grown from the surface of the CNC using a random walk algorithm. (d) The snapshot of the system after carrying out annealing and equilibration steps.

### 4.2.3 Gaussian Process Modeling

Metamodeling provides a solution to replace the expensive CG-MD simulations to explore the entire design space. Now, there are various types of metamodels that could be employed for this purpose. In this work, we tried four different metamodels, viz., polynomial regression (PR), radial basis function (RBF), kriging (which is a Gaussian process (GP)) and multi response

Gaussian process model (MGP). Polynomial regression is one of the most commonly used regression technique to define input-output relationships. Radial basis functions are means to approximate multivariable functions by linear combinations of terms based on univariate functions (the radial basis functions). One of the greatest advantage of RBF is its versatility; it can be applied to a multi-dimensional problem. Gaussian process (GP) modeling is an ideal metamodeling approach to capture highly nonlinear and spatially or temporally correlated data<sup>198, 222, 223</sup>. An appealing aspect of GP modeling is the uncertainty due to lack of data can be estimated for the predictions, which means that confidence intervals could be obtained for the predicted material properties.

We trained each of these models with the 100 data points that we obtained from the CG-MD simulations. The models constructed in this work were validated using a modified leave-one-out cross validation (LOOCV) approach. LOOCV error is assessed through averaging the prediction error on a left-out data point using the model built with the dataset excluding the left-out data. Each of the data point in the dataset is chosen as the left-out data once. The error metric for the validation is chosen as the mean absolute percentage error (MAPE), which can be estimated by ( $\hat{y}_i$  is the model prediction for  $y_i$ ):

$$MAPE = \frac{1}{N} \sum_{i=1}^N \left| \frac{\hat{y}_i - y_i}{y_i} \right| \times 100\% \quad (4.2.3-1)$$

Since the input-output relationships are quite complicated, simplified models such as PR and RBF were unable to capture the behavior accurately. The MAPE for the four different models are summarized in **Table 4.2.3-1**. The GP model gave a reasonable estimate for the modulus, but the error in toughness measurement was quite high. Hence, we decided to use the MGP model

which provided the least error and is also in the acceptable range. The MGP model is similar to GP, but the correlation of the outputs is also considered in the model.

**Table 4.2.3-1:** Summary of MAPE for different metamodels for the two outputs, modulus and toughness.

Model	MAPE in modulus (%)	MAPE in toughness (%)
PR	12.1	30.78
RBF	19.75	65.27
GP	8.57	25.67
MGP	10.46	15.26

In this study, the multi-response GP model<sup>224</sup> (with noise corrupted responses) is fitted using an enhanced Gaussian process modeling algorithm developed by Bostanabad *et al*<sup>225</sup>. A random process  $\{Y_i\}$  is a collection of random variables (RVs) indexed by a set  $I = \{i\}$  where the indices are often interpreted as time or spatial locations. A Gaussian Process (GP) is a random process in which the marginal distribution of each of the RV,  $Y_i$ , is Gaussian and any finite subset of the process  $\{Y_j : j \in J, J \subseteq I\}$  has a multivariate Gaussian distribution. Let the indices be natural numbers and  $\mathbf{Y}$  be a column vector of the random variables  $X_i$  of size  $N$ , *i.e.*,  $\mathbf{Y} = (Y_1, \dots, Y_N)^T$ . A GP can be characterized with two mathematical objects: a mean function  $\mu_Y$  and a covariance matrix  $\Sigma$  (Eq. 4.2.3-2).

$$\mathbf{Y} \sim \mathbf{N} \left( \mu_Y, \Sigma = \begin{pmatrix} \theta_1^2 & \theta_{12} & \cdots & \theta_{1N} \\ & \theta_2^2 & \cdots & \theta_{2N} \\ & & \ddots & \vdots \\ & & & \theta_N^2 \end{pmatrix} \right) \quad (4.2.3-2)$$

The  $N \times 1$  mean vector  $\mu_Y$  gives the expected value of each  $Y_i$ . For the covariance matrix  $\Sigma$ , the diagonal element  $\theta_i^2$  is the variance of  $Y_i$ . The off-diagonal entries  $\theta_{ij}$  indicate the covariance between the two RVs  $Y_i$  and  $Y_j$ . Given an indexed 4-dimensional input and single response dataset of size  $N=100$  for this study:

$$\left\{ (\mathbf{X}, \mathbf{y}) : \mathbf{X} = [\mathbf{x}_1, \mathbf{x}_2, \dots, \mathbf{x}_{100}]^T, \mathbf{x}_i = [x_{i,1}, x_{i,2}, x_{i,3}, x_{i,4}]^T, \mathbf{y} = [y_1, y_2, \dots, y_{100}]^T \right\}, \text{ where}$$

$x_{i,1}, x_{i,2}, x_{i,3}, x_{i,4}$  are chain length ( $N$ ), grafting density ( $\sigma$ ), polymer-NP interaction strength ( $\epsilon_{pnp}$ ) and NP edge length ( $l_{np}$ ) respectively (**Table 4.2-1**) and  $y_i$  is the material property of interest, Young's modulus and toughness. Assume  $\mathbf{y}$  is a realization of a GP  $\mathbf{Y}$  and  $\mathbf{y}$  is a function of  $\mathbf{X}$ , then the mean vector  $\mu_Y$  can be predicted from a function  $m(\mathbf{X})$  and the entries of the covariance matrix  $\sigma_{ij}$  can be estimated from  $\mathbf{x}_i$  and  $\mathbf{x}_j$ . GP modeling is process of constructing the mean function and estimating the covariance matrix. The complete details of formulation of the GP model is described in the Hansoge et al, 2018<sup>192</sup>.

#### 4.2.4 Constructing the Pareto Frontier

In the context of multi-objective optimization (MOO), a Pareto solution is a point  $(y_1, \dots, y_p)$  in the multi-dimensional model output space such that any of the model responses  $y_i, 1 \leq i \leq p$  cannot be further optimized without sacrificing at least one of the remaining ones. MOO aims at finding the set of Pareto solutions of a model, which is identified as the Pareto frontier. The metamodel output space in the polymer-NP system is non-convex, which necessitates the use of non-weighted-sum based multi-objective optimization algorithms such as multi-

objective genetic algorithms (MOGA). However, since the surrogate model in this study is computationally inexpensive, it is possible to randomly sample a large number of points from design space and find the boundaries of the output space, which is by definition the Pareto frontier. In comparison to MOGA, this method provides a quick solution with a minimal loss of accuracy. We note that since the Gaussian process model is an interpolation-based method, we refrain from extrapolating the metamodel results to outside the design space (such as chain length above 100) as this may yield inaccurate predictions.

**Figure 4.2.4-1** shows the Pareto frontier marked as a red curve, which is obtained by sampling the design space with one million sets of input parameters using the metamodel. For each point on the frontier, there is no other combination of input design parameters (within the bounds studied) that can achieve higher toughness without compromising the stiffness, or vice versa. To put our results into the classical framework of nanocomposites, we plot the Ashby plot using weight % of the NP (i.e., CNC). At a high NP weight % (above 80%), we observe that the modulus increases sharply at the expense of toughness, with nanocomposites exhibiting a brittle-like failure mode (illustrated in the inset in **Figure 4.2.4-1**). As the polymer content increases, we see a transition into a more ductile-like failure. In line with the transverse rule of mixtures for composites<sup>226</sup>, we observe that the modulus generally increases with weight % of NP. As expected, the rule of mixtures cannot explain the dramatic variations in mechanical properties at a fixed weight % of NP given the important role that microstructural factors such as chain length and graft density play in these systems. We would like to point out that at a high weight percentage of NPs, the mechanical properties of the nanocomposite are mainly governed by the NP properties. The

polymer chains help in formation of nanostructured assemblies, but the chain conformations have a minimal effect on the mechanical properties.

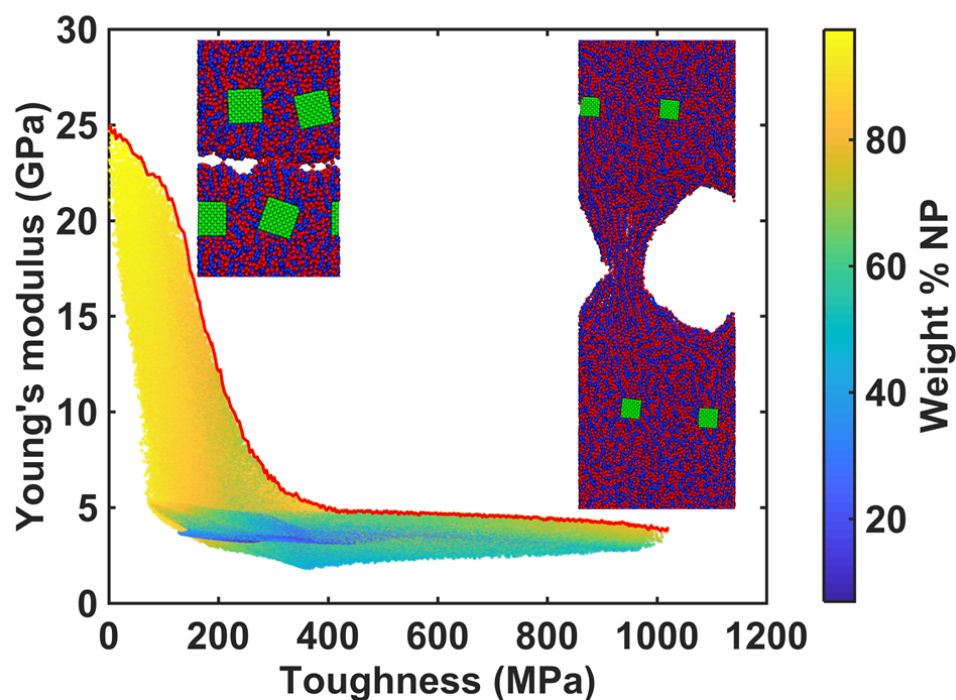


**Figure 4.2.4-1: Young's modulus vs toughness Ashby plot.** Young's modulus vs. toughness plot with points color coded with respect to the weight percentage of NP obtained from set of input parameters. The inset images show the range of failure observed, from a brittle fracture at high weight percent NP to a ductile fracture at relatively low weight percent NP.

#### 4.2.5 Metamodel Validation and Verification

Although LOOCV is widely used for validating models built from small datasets,<sup>227</sup> special care needs to be taken with the validation of GP models. Since GP models make predictions by interpolation, the prediction error for a point outside the input space (the space enclosed by the input points) can be extremely large and may not represent the prediction accuracy of the model properly. Hence, we choose to use a modified LOOCV method, with which corner points (4D

input space gives  $2^4 = 16$  points) in the Latin hypercube from the DOE are used solely for model building and not accounted in error estimation.

We present an analysis of the accuracy of the metamodel by obtaining error estimates and validating points on the Pareto frontier which marks the upper-bound of the mechanical properties. We observe a good correlation between the modulus and toughness predicted by the metamodel and CG-MD simulations (**Figure 4.2.5-1**). We find that the LOOCV error percentage obtained from the metamodel (see **Table 4.2.3-1**) is 10.46% and 15.26% for Young's modulus and toughness, respectively. These error percentages are reasonably small as they are generally within the standard deviations of property measurements from experiments or MD simulations<sup>116, 209, 219</sup>. This error analysis is necessary to validate the metamodel's ability to capture the input-output relationships based on CG-MD data and also to assure that the prediction of nanocomposite properties within the design bounds are accurate. Relative to CG-MD, the metamodel greatly expedites evaluating outputs for given a set of input parameters, without substantial loss in accuracy. Based on benchmark calculations, we estimate that generating a data point *via* the metamodel as opposed to CG-MD is about 3 to 4 orders of magnitude faster computationally, and 6 to 7 orders of magnitude faster than an all-atom MD simulation of an equivalent system. Using this metamodeling approach, systems with a higher number of design parameters can also be investigated. This would require a much larger design of experiments, *i.e.*, more simulations to train the metamodel. However, for such systems, dimension reduction techniques such as statistical sensitivity analysis (see section 4.2.6) can be used to screen out unimportant factors and reduce the total number parameters. Bostanabad *et al*<sup>225</sup>, have shown that the Gaussian process metamodel can be efficiently used for problems with dimensionality of up to 15. Since the metamodel consists

mainly of mathematical equations with parameters estimated based on the simulations, the dramatic speedup for analyzing such systems will be similar to what is observed here.

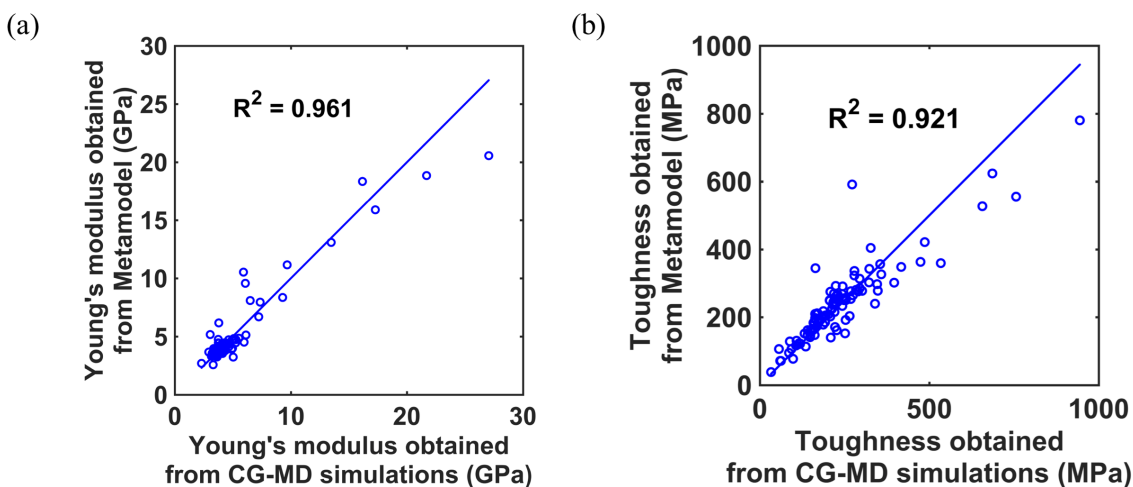


**Figure 4.2.5-1: Comparison of metamodel and CG-MD simulations.** a) Young's Modulus and b) Toughness, showing good agreement between metamodel and CG simulations.

**Figure 4.2.5-2a** shows the Pareto frontier marked as red curve and as a further validation of our metamodel, we check the accuracy of the predicted Pareto frontier at seven random points on the curve. Input parameters corresponding to these points are summarized in **Table 4.2.5-1**. These points are chosen such that they cover the wide range of the Pareto curve (purple squares in **Figure 4.2.5-2b**). We note that these new runs are not used in constructing the metamodel and can thus independently serve as validation points. **Figure 4.2.5-2c** and **d** compare the modulus and the toughness values obtained from the metamodel and CG-MD simulations on the Pareto frontier. The metamodel also gives a mean square error for each prediction, which is used to compute the confidence interval. The CG-MD results are largely consistent with the metamodel prediction. The trend of decreasing modulus and increasing toughness as we parse the curve left to right is well captured by the metamodel. Impressively, considering the error in both simulations and

metamodel, all of the points obtained seem to be in agreement and within the confidence intervals. We note that CG-MD has some variation in the results especially for predicting toughness in cases where large strains due to necking are observed. Incorporating data from multiple CG-MD simulations to build the metamodel will improve the confidence interval prediction. Despite having a highly nonlinear trend in the input-output relationship (**Figure 4.2.5-3**), the metamodel predictions are quite robust. Hence, it is computationally efficient to use the metamodel for further analysis.

**Table 4.2.5-1:** Seven random input points chosen from the Pareto curve for validation of the metamodel prediction.

Sample No	Chain Length (repeat units)	Grafting Density (% of surface beads grafted)	Polymer-NP interaction (kcal/mol)	NP edge length (Å)
1	10	5	2.21	20
2	42	5	0.40	10
3	61	5	2.56	25
4	89	11	3.38	30
5	99	11	0.94	30
6	100	8	3.90	30
7	100	6	3.72	30

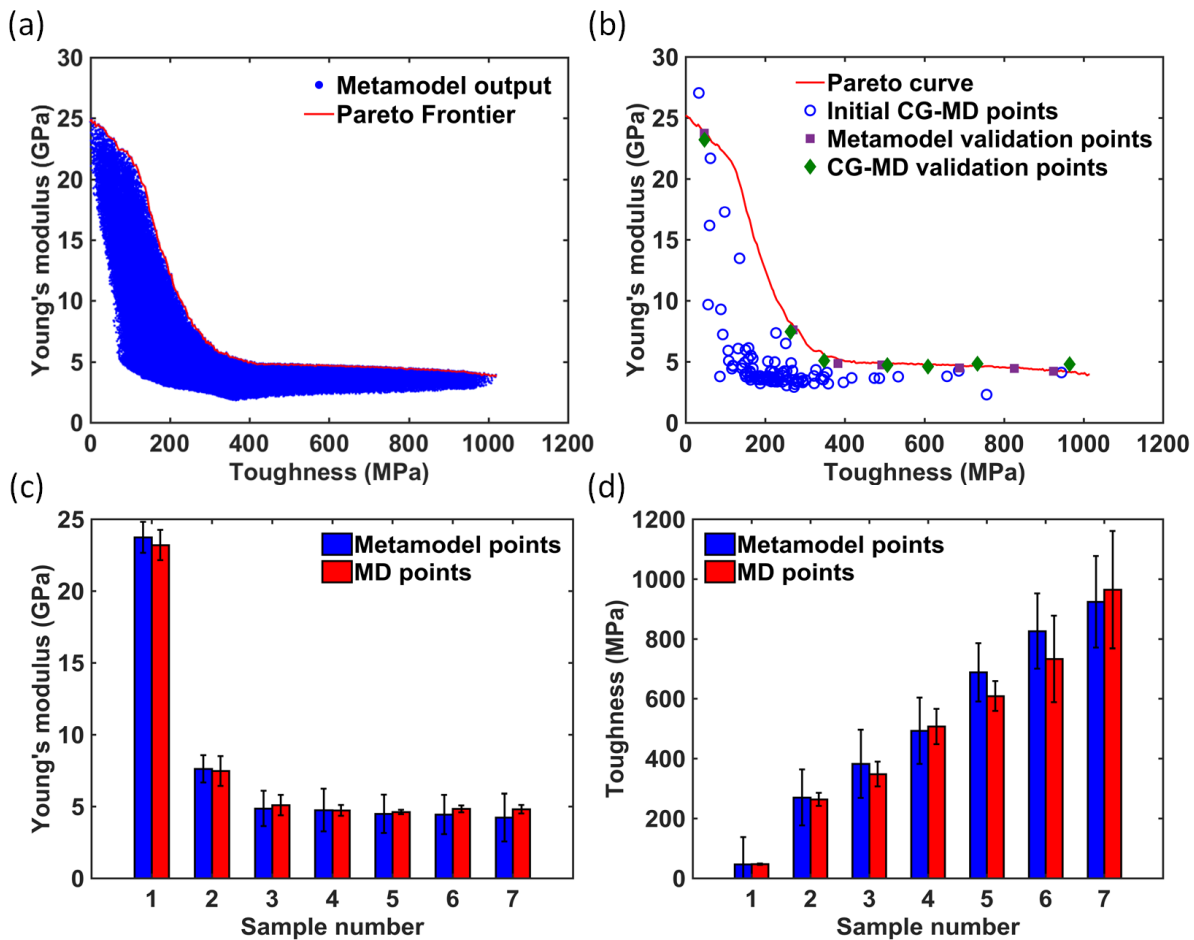


**Figure 4.2.5-2: CG-MD Validation of Pareto frontier.** (a) Pareto frontier obtained by sampling one million input parameters over the entire design space, (b) 100 initial CG-MD designs (blue dots) are used to build the metamodel. Using the metamodel, a Pareto frontier (red curve) is obtained. Seven random points from the Pareto curve are chosen (purple squares) and tested by running CG-MD simulations (green diamonds). Comparison of (c) Young's modulus and (d) toughness obtained from the metamodel and CG-MD simulations. The error bars represent a 95% confidence interval.

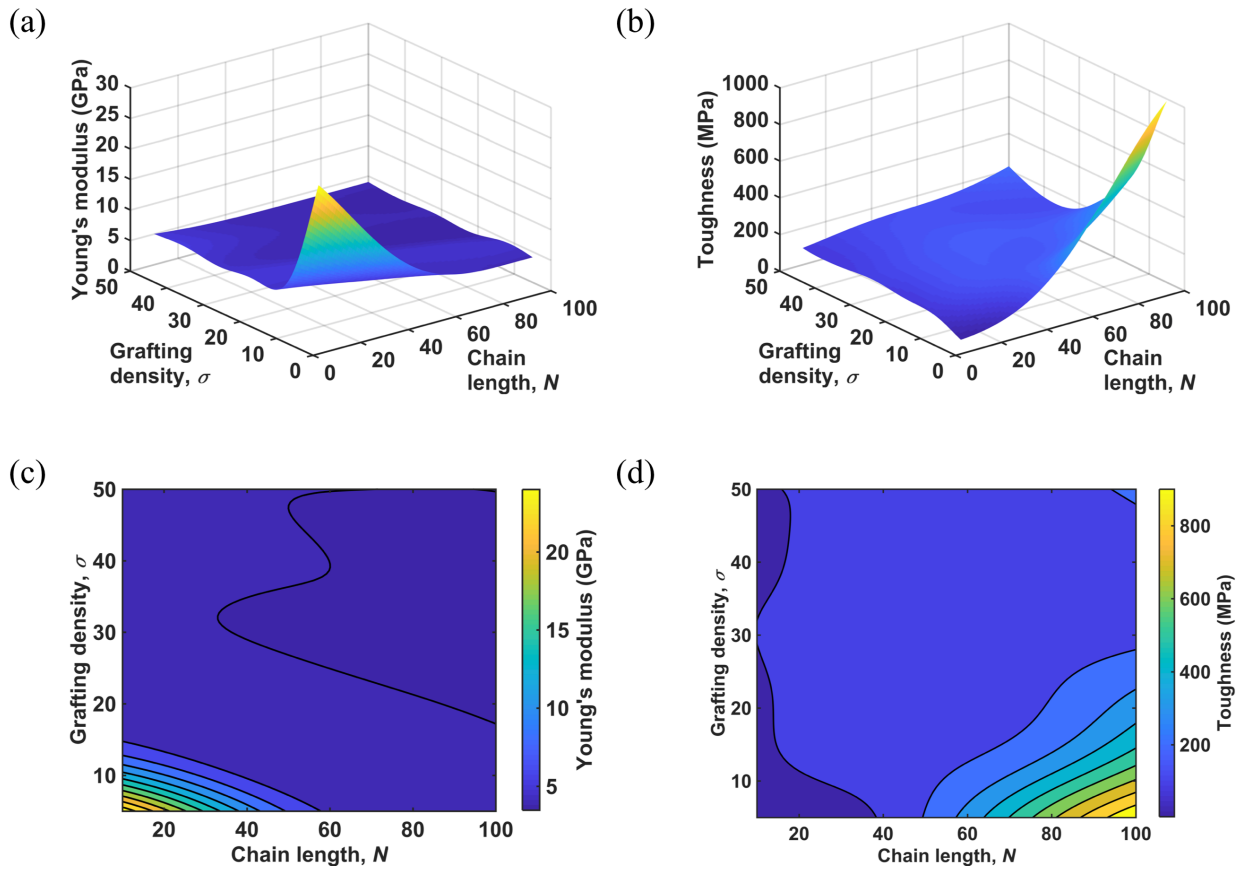


**Figure 4.2.5-3: Response surface between output and most influential inputs.** Response surface for (a) Young's modulus and (b) toughness with respect to two most influential parameters, chain length and grafting density that depicts the non-linearity in the input-output relationship. Contour maps for (c) Young's modulus and (d) toughness.

#### 4.2.6 Variance-based Statistical Sensitivity Analysis

Statistical Sensitivity Analysis (SSA) refers here to the computation of Sobol indices, *i.e.*, main sensitivity index (MSI), interaction sensitivity index (ISI), and total sensitivity index (TSI) of a model, to help understand how the variation of the model responses are decomposed with

respect to the input variables and their interactions<sup>228</sup>. Note that for the metamodel,  $Y = g(\mathbf{X})$ , the total variance of a model output can be decomposed as

$$\text{var}(Y) = \sum_{i=1}^d V_i + \sum_{i<j}^d V_{ij} + \dots + V_{12\dots d} \quad (4.2.6-1)$$

where  $V_i$  is the variance induced by varying the input factor  $x_i$ , while  $V_{i,j..k}$  is the variance from the interaction among the factors  $x_i, x_j, \dots, x_k$ . Then the MSI (denoted by  $S_i$ ) of an input  $x_i$  can be calculated with

$$S_i = \frac{V_i}{\text{var}(Y)} \quad (4.2.6-2)$$

Its TSI will be

$$S_{Ti} = \frac{E_{X_{-i}}(\text{var}_{X_i}(Y | X_{-i}))}{\text{var}(Y)} = \frac{V_i + \sum_{j=1, j \neq i}^d V_{ij} + \dots + V_{12\dots d}}{\text{var}(Y)} \quad (4.2.6-3)$$

where  $i$  is the sign for “all but excluding variable  $i$ ”. The variances are estimated via Monte Carlo integration.<sup>229</sup> SSA can be used for different scenarios, such as factor ranking (identification of important factors), dimension reduction (identification of unimportant factors), and model behavior analysis (identification of nonlinear or interaction effects)<sup>228</sup>. In this study, the SSA results are used for interpreting the model and determine which input parameters govern the mechanical response or conversely have a negligible effect on the properties calculated.

The statistical sensitivity analysis can be further utilized to corroborate these overall observations of the effects of input parameters on the mechanical properties. The sensitivity indices measure the relative importance of each input parameter on the mechanical properties of

the nanocomposite (summarized in **Table 4.2.6-1**). For both modulus and toughness, the total sensitivity index (TSI) for  $N$  is 0.702 and 0.670, respectively and for  $\sigma$ , it is 0.798 and 0.603, respectively. These values are much higher than  $\varepsilon_{pnp}$  (0.006 and 0.019) and  $l_{np}$  (0.032 and 0.106). This implies that a small change in either  $N$  or  $\sigma$  has a greater impact on the stiffness and toughness of the nanocomposite as compared to  $\varepsilon_{pnp}$  or  $l_{np}$ . The choice of  $N$  and  $\sigma$  can significantly limit the stiffness and toughness to a narrow range whereas the output space can be explored without any dependence on  $\varepsilon_{pnp}$  or  $l_{np}$  (**Figure 4.2.6-1** and **Figure 4.2.6-2**). Another important observation is that the interaction sensitivity indices (ISI) are higher than the main sensitivity indices (MSI), which suggests that varying just one input has a lesser influence on the output as compared to combined change in two or more inputs.

**Table 4.2.6-1:** Summary of the main, interaction and total sensitivity indices obtained from the statistical sensitivity analysis of the metamodel.

<b>Modulus</b>	<b>Chain length, <math>N</math></b>	<b>Grafting density, <math>\sigma</math></b>	<b>Polymer-NP interaction strength, <math>\varepsilon_{pnp}</math></b>	<b>NP edge length, <math>l_{np}</math></b>
MSI	0.179	0.262	0.006	0.021
ISI	0.523	0.537	0.000	0.011
TSI	0.702	0.798	0.006	0.032
<b>Toughness</b>	<b>Chain length, <math>N</math></b>	<b>Grafting density, <math>\sigma</math></b>	<b>Polymer-NP interaction strength, <math>\varepsilon_{pnp}</math></b>	<b>NP edge length, <math>l_{np}</math></b>
MSI	0.293	0.214	0.011	0.097
ISI	0.377	0.389	0.008	0.010
TSI	0.670	0.603	0.019	0.106

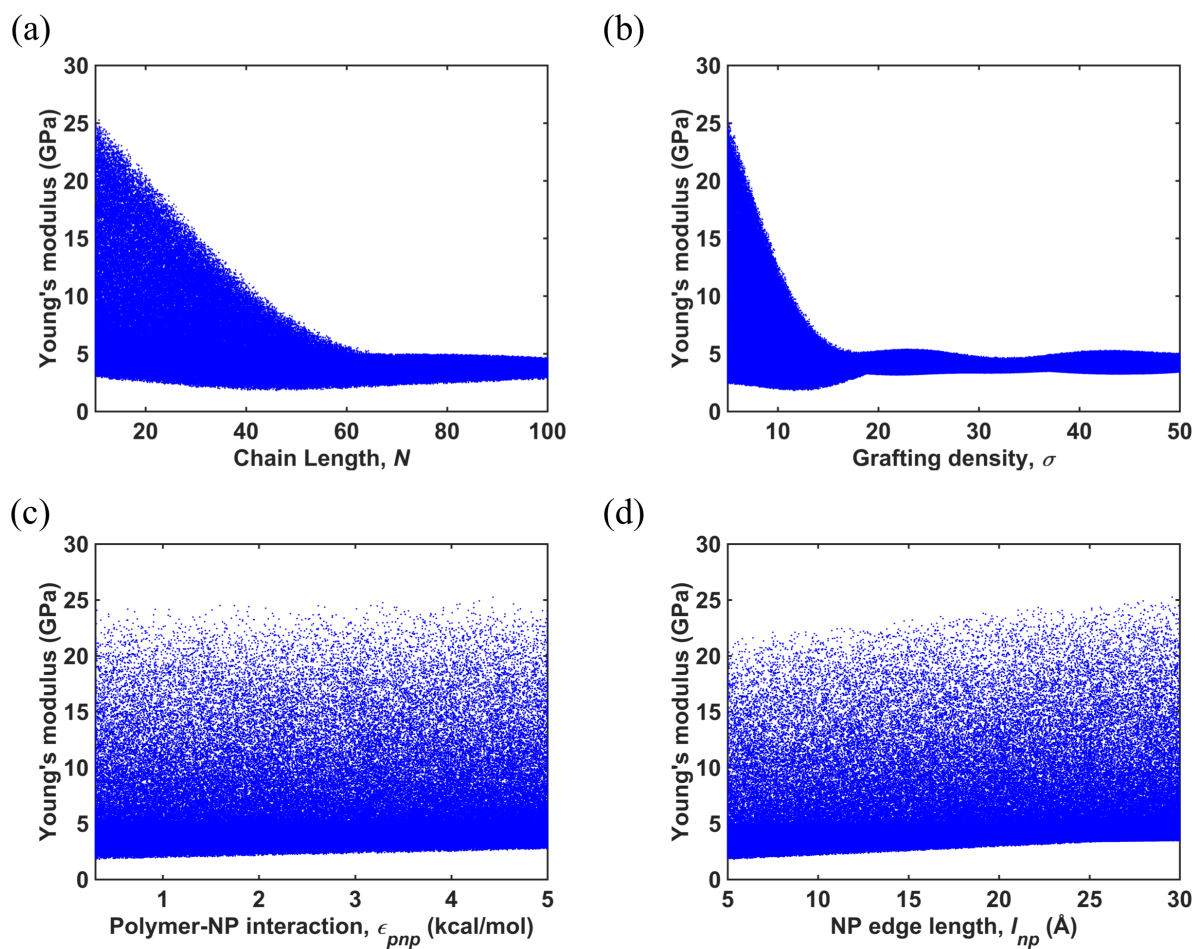


**Figure 4.2.6-1: Variation of Young's modulus of the nanocomposite with respect input parameters.** (a) chain length of polymer ( $N$ ), (b) grafting density ( $\sigma$ ), (c) interaction parameter between NP and polymer, ( $\epsilon_{pnp}$ ) and (d) NP edge length ( $l_{np}$ ).

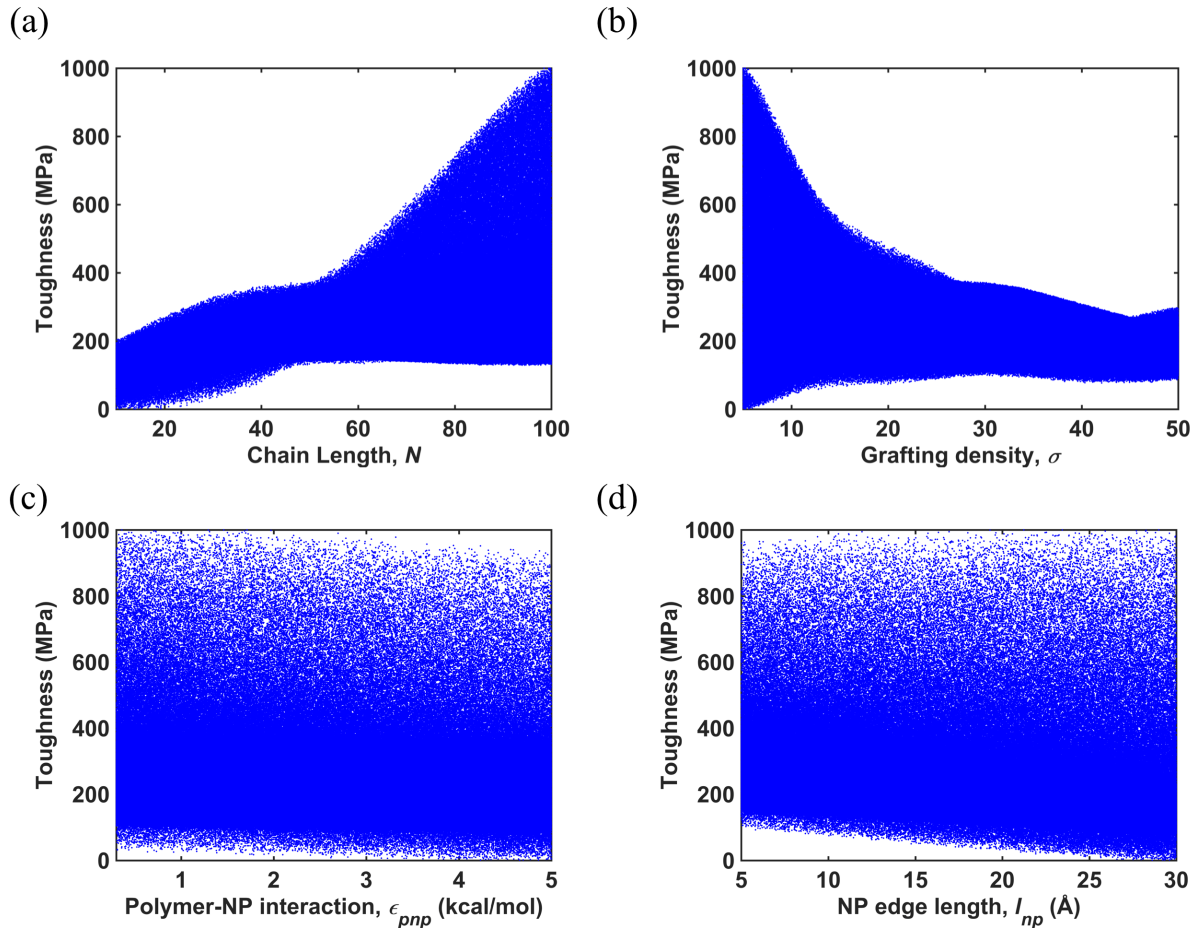


**Figure 4.2.6-2: Variation of toughness of the nanocomposite with respect to inputs parameters.** (a) chain length of polymer ( $N$ ), (b) grafting density ( $\sigma$ ), (c) interaction parameter between NP and polymer, ( $\epsilon_{pnp}$ ) and (d) NP edge length ( $l_{np}$ ).

### 4.3 Mechanical property optimization

Having validated the robustness and predictive ability of the metamodel, we proceed to evaluate the effect of each of the input parameters on properties of the nanocomposite. **Figure 4.3-1a-d** shows the Young's modulus vs. toughness relationship generated from the metamodel, where in each panel the color indicates the value of the represented input parameter – chain length  $N$ , grafting density  $\sigma$ , polymer-NP interaction strength  $\epsilon_{pnp}$  (with the unit of kcal/mol) and NP

edge length  $l_{np}$ . We first evaluate the influence of  $N$  on the mechanical properties of the nanocomposite. Since the chain lengths explored here are below the entanglement length<sup>29, 230, 231</sup>, the main toughening mechanism is the sliding and collective interactions between polymer chains arising from different nanoparticles. **Figure 4.3-1a** shows that the toughness of the nanocomposite increases with  $N$  (as marked by the change from blue to yellow). The enhancement in toughness with  $N$  can be mainly attributed to the increase in effective cohesive interactions between nanoparticles with longer grafted chains that enable better overlap across brushes. However, to obtain higher stiffness, the loading ratio of nanoparticle has to be high, which can be achieved at lower values of  $N$ . The inset in the **Figure 4.3-1a** shows the distribution of  $N$  for points that lie on the Pareto curve. As expected, the peaks are dominated at relatively low and high chain lengths, corresponding to high modulus and high toughness, respectively.

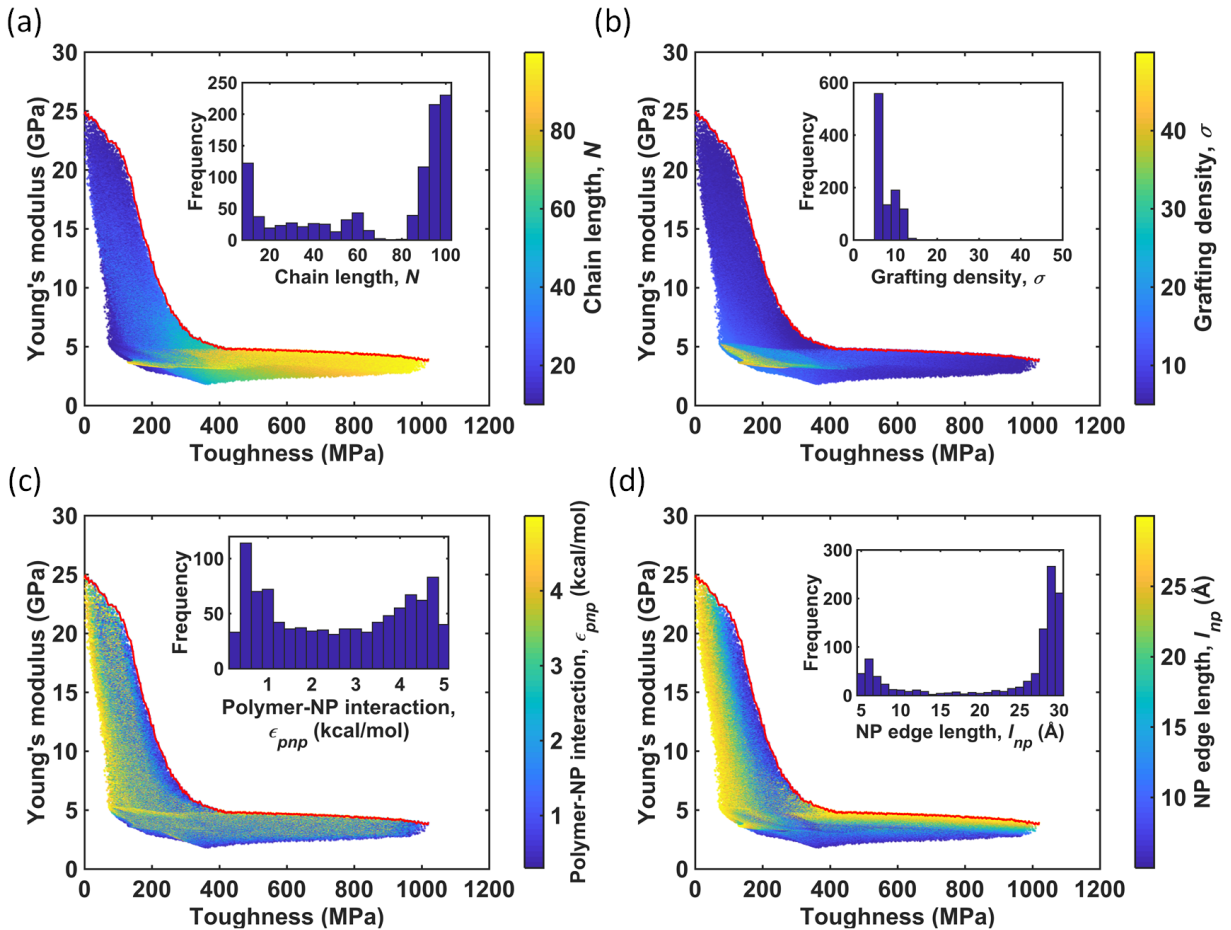


**Figure 4.3-1: Young's modulus vs toughness Ashby plot with respect to input parameters.**

Young's modulus vs. toughness for the NP-polymer nanocomposite colored by (a) chain length of polymer  $N$ , (b) grafting density  $\sigma$ , (c) polymer-NP interaction strength  $\epsilon_{pnp}$  and (d) NP edge length  $l_{np}$ . The insets show the distribution of each parameter that lie on the Pareto curve.

Next, we examine the effects of grafting density,  $\sigma$ . The grafting density of the polymers on the NP strongly affects the polymer chain conformations and thus it has a major impact on the mechanical properties of the nanocomposite. Our analysis reveals that both the modulus and toughness of the nanocomposites degrade rapidly as  $\sigma$  is increased beyond  $\sim 10\%$ . This is most evident near the elbow region of the curve in **Figure 4.3-1b**, where a shift from blue to yellow,

that is, towards higher  $\sigma$ , yields points that are far from the Pareto frontier. When  $\sigma$  is increased, a critical transition occurs, where polymer chains undergo a conformational change from a semi-dilute polymer brush regime (SDPB) to concentrated polymer brush regime (CPB)<sup>232</sup>. The monomers near the surface of the NP stretch radially outwards further due to high steric repulsion in this regime. In sections that are radially further away from the NP, the monomers become more coiled as they have more free volume available.

As shown in **Figure 4.3-1c**, the choice  $\varepsilon_{pnp}$  at lower weight % of NP (*i.e.*, correspondingly a high content of polymers) has a low influence on the mechanical properties as it is mainly dominated by the polymer-polymer interactions. However, at a higher weight % of NP,  $N$  is relatively small and  $\sigma$  is also low, as evident from **Figure 4.3-1a** and **b**, respectively. Hence, it is more beneficial to have a weaker interfacial interaction between the polymer and NP as it reduces the attraction to NP and allowing the polymer chains to become more extended and interact with chains from nearby NPs effectively. This leads to a slight enhancement in toughness of the nanocomposite pushing it towards the Pareto frontier. Therefore, we see a larger proportion of relatively lower values of  $\varepsilon_{pnp}$  in the high modulus region the Pareto curve. In summary, the relatively flat distribution (inset in **Figure 4.3-1c**) suggests that  $\varepsilon_{pnp}$  is not an important parameter practically speaking, although it is preferential to have a lower interaction energy between the grafted polymer chains and the nanoparticle for higher loading of NP.

Next, we summarize findings on the effect of NP cross-sectional dimension as determined by the edge length. At a given  $N$ ,  $\sigma$  and weight % of NP, a larger  $l_{np}$  yields a higher number of grafting sites as the NP will have more surface area. As illustrated above, the toughness is dependent on the cohesive interaction energy between polymer chains, which increases with the

number of grafts. Thus, as seen from **Figure 4.3-1d**, in the high toughness region, the optimal properties are achieved for larger NPs. Since  $N$  and  $\sigma$  are small in the high modulus region (as discussed above), NPs with larger  $l_{np}$  tend to have graft distances that are greater than radius of gyration of the polymer chain leading to mushroom like configuration. This in turn degrades the mechanical properties and hence, smaller  $l_{np}$  (blue region in **Figure 4.3-1d**) are required to reach the Pareto curve. Similar to the effect of chain length, the peaks of the distribution of NP edge lengths on the Pareto curve are dominated at smaller and larger  $l_{np}$ , corresponding to high modulus and high toughness regions, respectively.

A more illustrative way to represent our findings is shown in **Figure 4.3-2**, where we break down the range of the mechanical properties that can be achieved at different weight percentages of the NP. We further color the cases by determining whether they are expected to be above or below the critical chain length,  $N_{cr}$  that is, in SDPB vs. CPB regime. The concept of  $N_{cr}$  is explained in the Chapter 5: The weight % of NP in the system can be altered by varying  $N$ ,  $\sigma$  and  $l_{np}$  simultaneously. For a low weight % (10-25%) (**Figure 4.3-2a**), the predicted properties are well below the Pareto curve, as there is not enough NPs to provide substantial stiffness. At least 60% weight of NP (**Figure 4.3-2d, e**) is required to achieve enough reinforcement to reach the Pareto frontier. As the weight percentage is increased to be around 90% (**Figure 4.3-2f**), due to the low polymer content, the toughness of the system does not exceed 200 MPa. Hence, the ideal range to combine both stiffness and toughness appears to be around 60-90% NP by weight. The figure also reveals that the chain lengths must be above the  $N_{cr}$ , which is calculated from the scaling, to reach the Pareto frontier. Specifically, all the points on the Pareto frontier have to be above  $N_{cr}$ . As a comparison, the amount of nanofillers used in traditional polymer nanocomposites

usually lies in the range of 1-10%<sup>233</sup>, which is much lower than the ideal range identified from our modeling. However, since there are no ungrafted free chains in the simulated assemblies, the nanofiller content can be much higher than that of those commonly ungrafted polymer nanocomposites. Schmitt *et al.* have shown that up to ~ 85 weight % of grafted SiO<sub>2</sub> nanoparticles can be achieved experimentally<sup>30</sup>. Given that high aspect ratio nanocellulose particles with varying dimensions and surface functionalities can be obtained sustainably from a variety of sources<sup>204, 207</sup>, achieving the high weight percentage of CNCs as proposed here should be viable for designing future CNC based aHNPs.

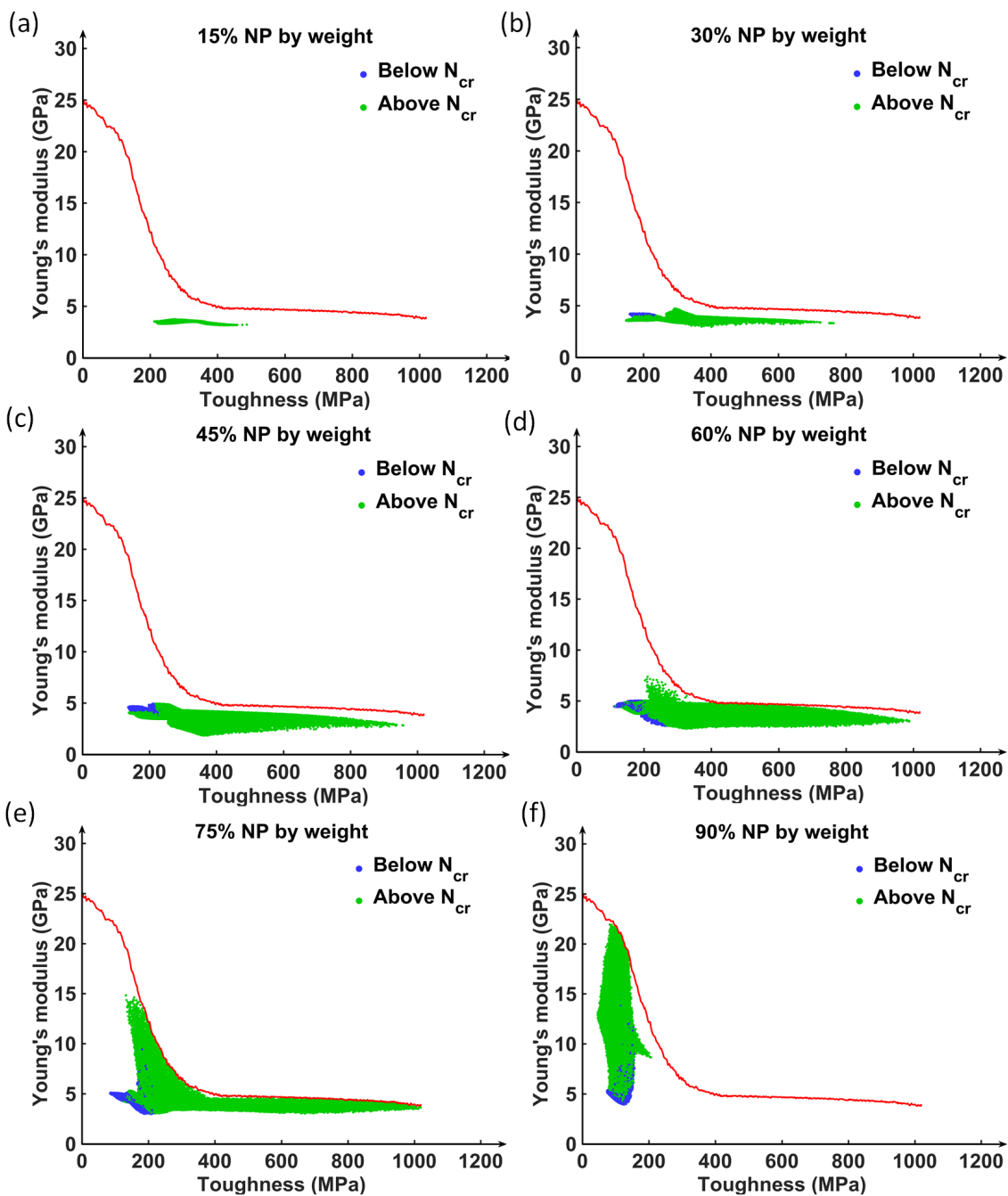


**Figure 4.3-2: Young's modulus vs. stiffness of the nanocomposite for different weight percentages of NP.** The blue shaded region in each figure shows the properties that can be achieved with a given weight %, while the red curve is the Pareto frontier for the overall material system

Experimentally, the mechanical properties of hairy nanoparticle assemblies have been studied using nanoindentation techniques where the toughness is quantified by the critical stress intensity factor<sup>29, 30, 234, 235</sup>. However, there are number of studies that have characterized the work to fracture (area under stress strain curve) of matrix dispersed CNC nanocomposites which would be useful to provide additional context with respect to our toughness values. Dong *et al.*<sup>236</sup> found the toughness of PMMA/CNF nanocomposite films to be around 1-4 MPa. Coulibaly *et al.*<sup>237</sup> reported the toughness of nanocomposite based on CNC and a metallosupramolecular polymer to be around 40-70 MPa. CNC polyurethane nanocomposite has a toughness ranging from 33-80 MPa<sup>238</sup>. A blend of polylactic acid and polyurethane reinforced with CNC gave a toughness of around 400 MPa<sup>239</sup>. Compared to these experimental values, the toughness range of 5-1000 MPa obtained from our simulations, although higher, are still reasonable considering the large strains attainable in small systems.

## 4.4 Conclusion

In this study, we have established a CG-MD based modeling framework combined with metamodels for predicting the optimal design parameters for assembled hairy nanoparticle systems using the CNC-PMMA nanocomposite as a model system. Rather than conducting a computationally expensive parameter sweep through extensive MD simulations or solving an equally complex optimization problem, we utilize a design of experiments to develop comprehensive and robust metamodels to explore the mechanical properties of the nanocomposite. Specifically, we employ the metamodels to carry out a multiobjective optimization and obtain the Pareto frontier that marks the maximum performance achievable with this particular material system and the defined design space. This bottom-up materials-by-design approach allows us to efficiently evaluate the effects of various design parameters, i.e., chain length, grafting density, polymer-NP interaction strength, and the NP edge length, on the mechanical behavior of the system. Our results indicate that the chain length and grafting density are the primary factors that influence the modulus and toughness of the model nanocomposite. The complex dependence of these parameters on the polymer configurations leads to a vast range of mechanical properties at a given NP weight percent. Our metamodel prediction suggests that at least 60% NPs by weight is required to achieve the optimal nanocomposite designs defined by the Pareto frontier. Furthermore, the chain length and grafting density have to be fine-tuned to yield systems where the polymer chains are in the SDBP regime to achieve a combination of high stiffness and toughness. In fact, we find that it is not possible to reach the Pareto frontier without ensuring that the polymers attain molecular weights in this regime.

Our metamodeling approach, in conjunction with CG-MD simulation, provides important guidelines toward designing assembled polymer-grafted nanoparticle composites to achieve optimal mechanical properties. Looking forward, this metamodeling approach will help to accelerate the materials-by-design process and inspire future studies in advancing mechanical performance of composites and other relevant structural materials. We envision that CG-MD informed metamodeling could be highly useful in the future to assess the role of polymer chemistry such as pendant group effects of methacrylate or styrene<sup>124, 219</sup> on the mechanical properties systematically and reveal key insights into the molecular design of the systems. We also believe that while being more computationally intensive, CG-MD and metamodel-based investigations of the axial properties of high-aspect-ratio CNC nanocomposites would be valuable, such as those obtained from tunicates. The higher axial modulus in CNCs and greater sliding resistance enabled by hairs may allow such systems to attain interesting strength–toughness relations that may make these materials appealing compared to conventionally engineered materials used in mechanical design.

## Chapter 5: Scaling laws to predict polymer conformation

In the previous chapter we looked at the mechanical property optimization of aHNPs. Interestingly, we observed that increasing grafting density degraded the properties. This necessitated further investigation which led to the study of polymer conformations in these aHNPs. This chapter focuses on developing theoretical scaling laws that govern the polymer conformations in aHNPs. Specifically, we derive an equation for critical chain length, the transition length where the conformation changes from a concentrated polymer brush (CPB) regime to semi dilute polymer brush (SDPB) regime. Furthermore, by simulating different chemistry, chain length and grafting density, we demonstrate the universality of these chain conformations. These laws can help to predict properties such as nanoparticle spacing in these nanocomposites. Portions of the text and figures within chapter are reprinted or adapted with permission from Hansoge et al. ACS Nano 2018<sup>192</sup> and Hansoge et al. ACS Macro Letters 2019<sup>240</sup>.

### 5.1 Introduction

The structure and conformation of polymer in a nanocomposite greatly affects the mechanical<sup>241</sup>, rheological<sup>242, 243</sup>, tribological<sup>244</sup>, optical<sup>245, 246</sup>, and electrical<sup>247</sup> properties of the materials. The conformational change in polymer structure also leads to enhancement in mechanical properties. The fracture toughness of aHNPs increases substantially beyond a certain degree of polymerization, specifically when the polymer conformations transition from a CPB to SDPB<sup>29, 30</sup>. Theoretical solutions regarding the polymer chain structure in aHNPs have also been developed to identify the transition from CPB to SDPB<sup>40, 248</sup>. Although these prior studies provide an understanding of the molecular mechanisms underpinning the chain conformations on nanoparticle surfaces, they have mainly focused on a few specific homopolymers, typically

polystyrene, and spherical nanoparticles such as gold or silica. A comparative analysis geared towards understanding the effect of different polymer chemistries on the confined conformations of anisotropic hairy nanoparticle assemblies, specifically on the CPB to SDPB transition, has not yet been carried out. It is anticipated that since polymer rigidity, side-group size, cohesive interactions and free volume all influence the properties of glass-forming polymers, understanding the role of these distinguishing features on polymer conformations in aHNPs is crucial.

## 5.2 Simulation setup

To analyze the conformational behavior of polymers in aHNPs, we take cellulose nanocrystal (CNC), an anisotropic nanoparticle grafted to four common polymers with distinct chemical groups and segmental structures, i.e., poly (methyl methacrylate) (PMMA), polystyrene (PS), polycarbonate (PC) and polybutadiene (PB). These polymers are chosen such that a wide range of properties can be examined in a single study, spanning large ranges in fragility, glass transition temperature and chemistry. Furthermore, we investigate the role of backbone rigidity and side-group size on the conformational behavior of these different polymers when grafted to a nanoparticle. The coarse-graining strategy for the CNC is identical to the one used in Chapter 4. The CG models for the polymers are derived based on the all-atomistic model using the thermomechanically consistent energy renormalization coarse-graining approach<sup>116, 123</sup>. The system setup and the equilibration protocol is similar to what was described in Chapter 4. The CG scheme and a schematic of the system is shown in **Figure 5.2-1**. Five different grafting densities are chosen for each system, 10% to 30% with an increment of 5%, where the grafting density is defined as the percentage of surface beads that are grafted to the polymer. The volume fraction of nanocrystals in these systems ranges around 1-10% as our central focus in this study is polymer

chain conformations and specifically the CPB-SDPB transition, which requires relatively high molecular weight systems and consequently low volume fraction of nanocrystals.

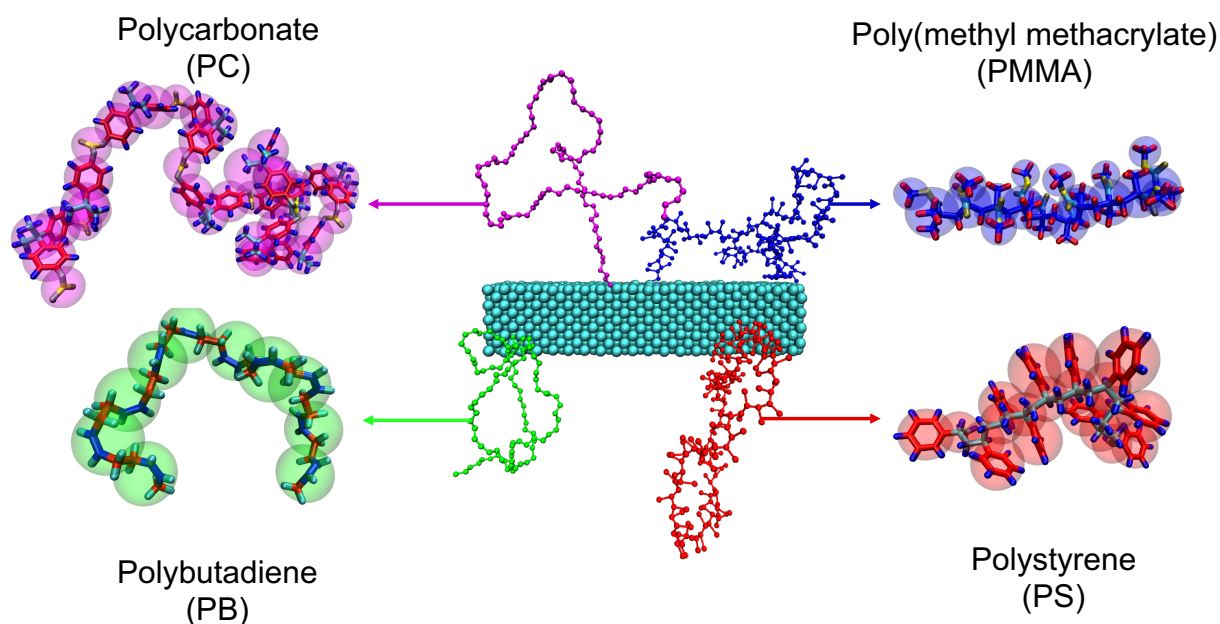


**Figure 5.2-1: CG mapping scheme for PMMA, PS, PC and PB.** Four different grafted polymers are considered in this study, i.e., poly(methyl methacrylate) (PMMA), polystyrene (PS), polycarbonate (PC) and polybutadiene (PB). The coarse-graining schemes are one bead per monomer for PB, two bead per monomer for PS and PMMA (one each for backbone and side-group) and four bead per monomer for PC (two for phenylene, one each for isopropylidene and carbonate groups).

### 5.3 Critical chain length, $N_{cr}$

In a typical polymer melt, the radius of gyration scales as  $R_g \sim N^{0.5}$ , where  $N$  is the number of monomers, which can be described by a random walk model<sup>15</sup>. However, when the polymer chain is grafted to a nanoparticle, its conformational behavior changes. In our study, the polymer

chains are grafted to an anisotropic cylindrical nanoparticle and we looked at the conformational behavior of one of the systems, CNC grafted PMMA system. We note that the length of polymer chains is much longer than the cross-sectional dimensions of nanoparticle, and that the aspect ratio of the CNC NPs are high due to the periodic boundary conditions. In this scenario, the NP can be approximated as a cylinder. The scaling analysis shown in **Figure 5.3-1a** reveals that the polymer chains adopt a slightly extended conformation in the radial direction ( $\perp$  to NP surface) as  $R_g^\perp \sim N^{0.6}$  due to the excluded volume, which is different from the melt-like conformation in the axial direction ( $\parallel$  to surface) where  $R_g^\parallel \sim N^{0.5}$ .

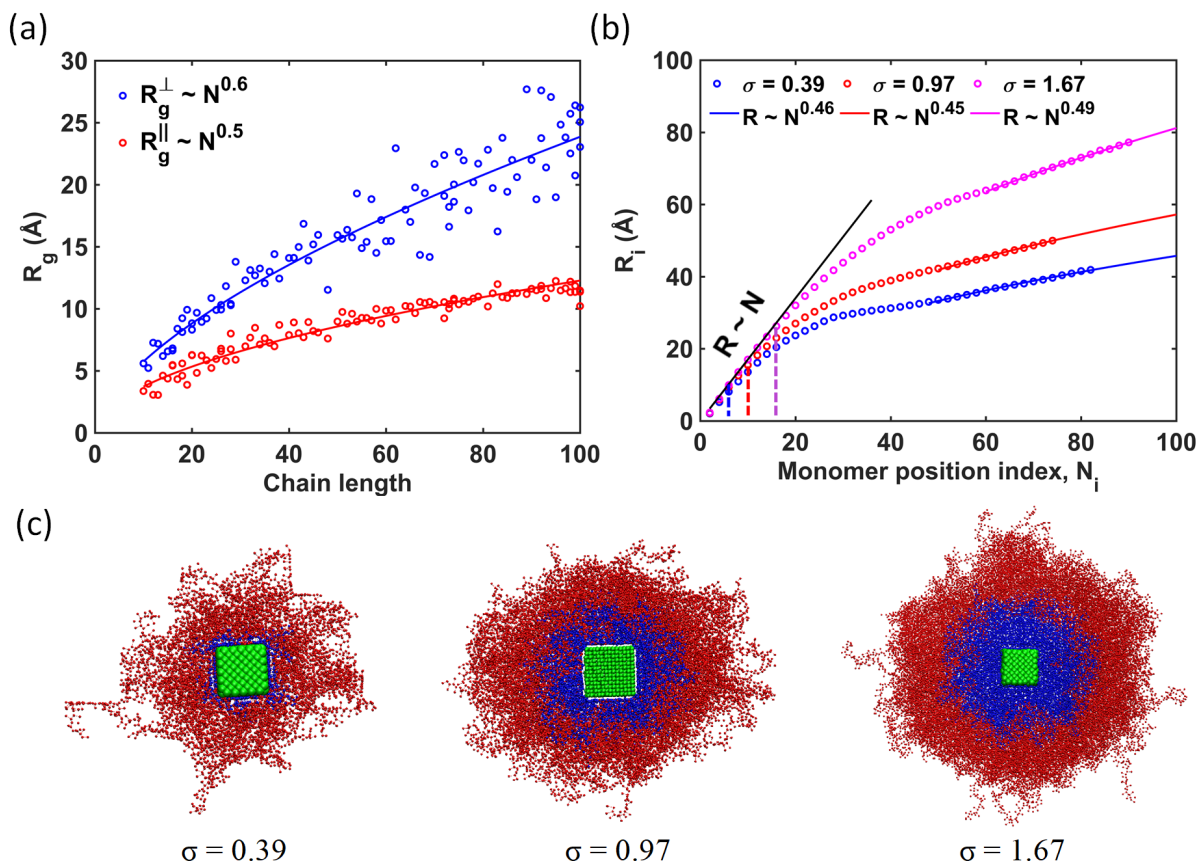


**Figure 5.3-1: Scaling relationships between monomer position and distance from nanoparticle.** (a) Scaling of radius of gyration in radial ( $R_g^\perp$ ) and axial ( $R_g^\parallel$ ) directions with chain length. (b) Scaling relationship in CPB ( $R \sim N$ ) and SDPB ( $R \sim N^{0.5}$ ) regimes.  $R_i$  is distance of  $i^{\text{th}}$  monomer from the nanoparticle surface and  $N_i$  is the monomer position index in the polymer chain. The dotted line shows the transition point from CPB to SDPB. (c) Snapshots of configurations of the hairy nanoparticle showing the onset of SDPB regime (red) from CPB regime (blue) with grafting density. All grafting densities are in the units of chains/nm<sup>2</sup>.

Examining average conformations of polymer chains in all CG-MD simulations, we look at how local properties of the chains vary near and away from the NPs. In the vicinity of the NP surface, it is observed that the polymer chains are in the CPB regime and gradually relax into the SDPB regime at larger radial distances from the surface. We find that in the CPB regime, the radial distance of polymer chains scales as  $R \sim N$  and there is a continuous transition to  $R \sim N^{0.5}$  in the SDPB regime, which is close to that of the melt state<sup>15</sup> as shown by the three representative systems in **Figure 5.3-1b**. These findings can be corroborated by theoretical scaling arguments that could be used to determine the dependence of the transition on features such as NP radius and grafting density. An extension of theoretical Daoud-Cotton (DC) model<sup>37</sup> was proposed by Ohno *et. al.*,<sup>63</sup> where they treated a star polymer as a system consisting of chains grafted onto a spherical nanoparticle. Considering a case where  $f$  polymer chains are grafted to unit surface area of a cylindrical NP with a radius  $r_0$ , the analytical scaling relation between the critical number of segments ( $N_{cr}$ ) marking the onset of SDPB regime, and nanoparticle size and the grafting density can be derived<sup>37</sup>. Based on this model, crossover radius  $r_c$  is given by

$$r_c = br_0^{1/2}\sigma_0^{*1/2} \quad (5.3-1)$$

where  $b$  is a constant which includes the proportionality term to convert the scaling relationship to an empirical relation and the excluded volume parameter defined in the DC model<sup>37</sup>.  $\sigma_0^*$  is the dimensionless grafting density given by  $\sigma_0^* = fl_m / 2\pi r_0$ , where  $l_m$  is the contour length of the monomer (about 2.75 Å estimated for our CG model). We obtain the crossover radius from each of our simulations by plotting the average radial distance of each monomer in the chain against its position index in the chain (representation in **Figure 5.3-1b**). The constant  $b$  is evaluated from the slope of  $r_c$  vs.  $r_0^{1/2}\sigma_0^{*1/2}$ . The  $b$  value of 31.64 Å<sup>1/2</sup> fits our data well (**Figure 5.3-2**).

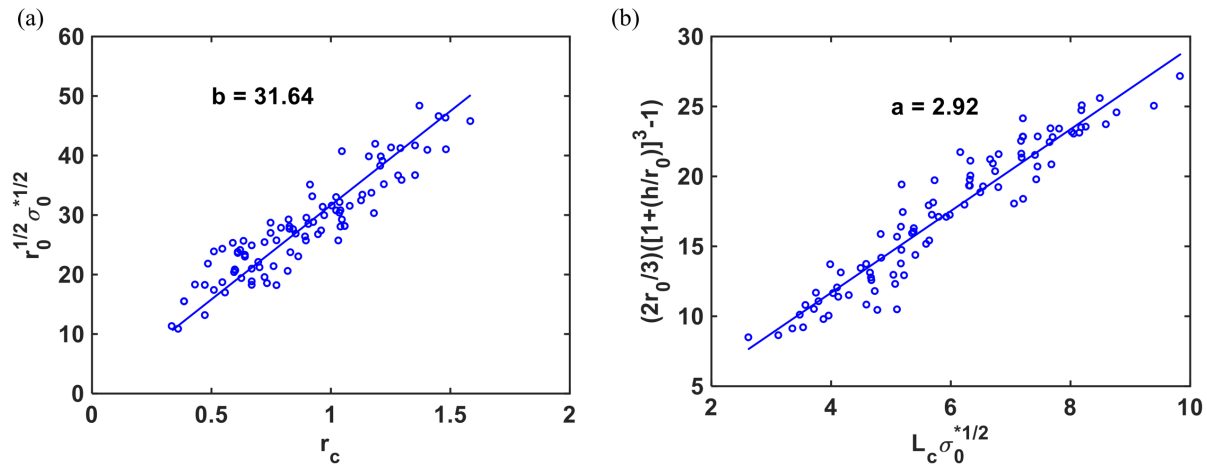


**Figure 5.3-2: Plots to obtain  $a$  and  $b$  parameters.** (a) Straight line plot of  $r_c$  vs.  $r_0^{1/2}\sigma_0^{*1/2}$  (b)

$$\text{Straight line plot of } \left(\frac{2r_0}{3}\right) \left\{ \left[ 1 + \left( \frac{h}{r_0} \right) \right]^{3/2} - 1 \right\} \text{ vs. } L_c\sigma_0^{*1/2}.$$

When the monomer segments are in the CPB regime, the brush layer height ( $h$ ) is obtained from the following equation<sup>63</sup>,

$$\left(\frac{2r_0}{3}\right) \left\{ \left[ 1 + \left( \frac{h}{r_0} \right) \right]^{3/2} - 1 \right\} = aL_c \sigma_0^{*1/2} \quad (5.3-2)$$

where  $a$  is the proportionality constant obtained by fitting the above equation to CG-MD data (**Figure 5.3-2**), and  $L_c = N_{cr} * l_m$  is the length of the graft chain in CPB regime, *i.e.*, the contour length. The  $a$  value of 2.92 is obtained from the best fits of our data. Combining Eq. 5.3-1 and 5.3-2 and given the condition that  $r_0 + h = r_c$ ,

$$r_0 + r_0 \left\{ \left[ \frac{3aN_{cr}l_m\sigma_0^{*1/2}}{2r_0} + 1 \right]^{2/3} - 1 \right\} = br_0^{1/2} \sigma_0^{*1/2} \quad (5.3-3)$$

Simplifying Eq. 5.3-3, we obtain an expression for  $N_{cr}$ ,

$$N_{cr} = \frac{2r_0}{3a\sigma_0^{*1/2}l_m} (r_0^{-3/4} \sigma_0^{*3/4} b^{3/2} - 1) \quad (5.3-4)$$

This analytical expression for  $N_{cr}$ , with empirical parameters ( $a$ ,  $b$ ) estimated from CG-MD can be used to determine, for a given nanoparticle radius and grafting density, the minimum molecular weight of the grafted polymer that ensures that chain segments crossover to the SDPB regime. **Figure 5.3-1c** illustrates molecular configurations that show the increase in  $N_{cr}$  as  $\sigma$  increases. Since the chain segments in the SDPB regime are relaxed and can intermingle with chain segments arising from other nanoparticles, the mechanical properties of the assembly, especially the toughness, can be enhanced by having a greater number of polymer segments in the SDPB regime. Having a lower  $\sigma$  leads to an early onset of the SDPB regime, which is preferred for the chains to self-interact and thus achieve the optimal properties. Equating  $N_{cr}$  to zero will ensure all the polymer segments are in the SDPB regime. This yields a critical value of the grafting density,

*i.e.*,  $\sigma_0^* = \frac{r_0}{b^2}$ , below which all the polymer segments can effectively contribute to the enhancement of toughness. While it is plausible that having very low  $\sigma$  and  $N$  may lead to mushroom configuration of polymer chains, these systems correspond to high weight % of NP. For such systems, the polymer chains help in formation of these nanostructured assemblies rather than influencing the mechanical properties. Thus, we believe having extremely low grafting density may not necessarily be undesirable to achieve high stiffness comparing to pure CNC systems.

A similar behavior has also been experimentally observed by Bockstaller *et al.*<sup>14</sup>, where toughness increased at lower  $\sigma$ . This observation was attributed to the chain conformational change from CPB to SDPB, for which the critical transition was determined from a simplified application of DC model where the grafting density dependence on the brush height was not considered. Since, it is challenging to observe molecular level details from experiments, the critical radius and chain length obtained from experimental studies are approximate. However, from our simulations, we can precisely obtain the transition point as illustrated in in **Figure 5.3-1b** by evaluating each monomer's radial position along the length of the polymer chain to determine where the linear scaling of CPB ends. Thus, the empirical constants obtained from the simulations are expected to be more precise relative to the experiments. Our analysis extends the experimental observations on spherical NPs to the cylindrical case and provides the first molecular level simulation evidence that connects polymer configurations to mechanical properties in aHNPs.

We further quantify the conformational behavior associated with the toughness of the nanocomposite by calculating the inter-NP cohesive energy. This is measured by computing the pairwise interaction energy  $\gamma_{pp}$  between the polymer chains arising from different NPs, normalized by the number of polymer beads arising from a single NP. The value of  $\gamma_{pp}$  gives an

estimate of the normalized cohesive interactions between the polymer chains connecting two NPs, which is directly related to the work that must be carried out to fully separate the NPs, and thus the toughness of the system. At very high grafting density, it is evident that the lack of free volume makes it difficult for polymers grafted from different nanoparticles to interact with each other. This reduces the  $\gamma_{pp}$  and thus the toughness of the system (**Figure 5.3-3**). This concept can be visualized directly from the molecular structure, as depicted in **Figure 5.3-4**.

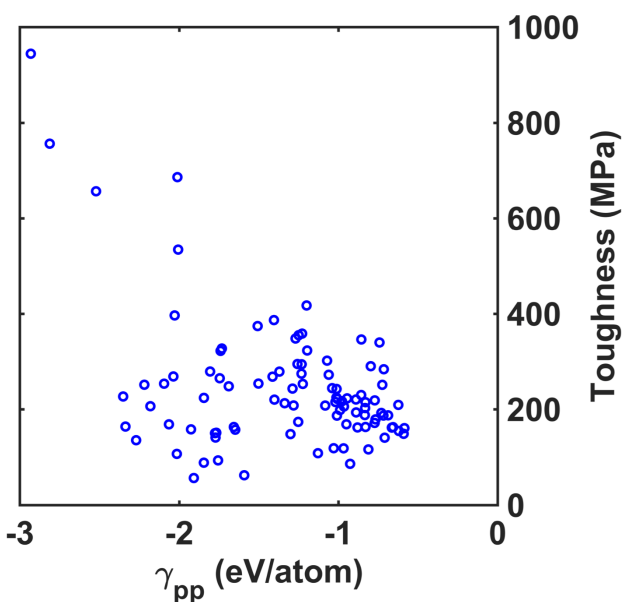


**Figure 5.3-3: Relation between  $\gamma_{pp}$  and toughness.** Relation between toughness and inter-NP cohesive energy, which is computed from the pairwise interaction energy per atom  $\gamma_{pp}$ .

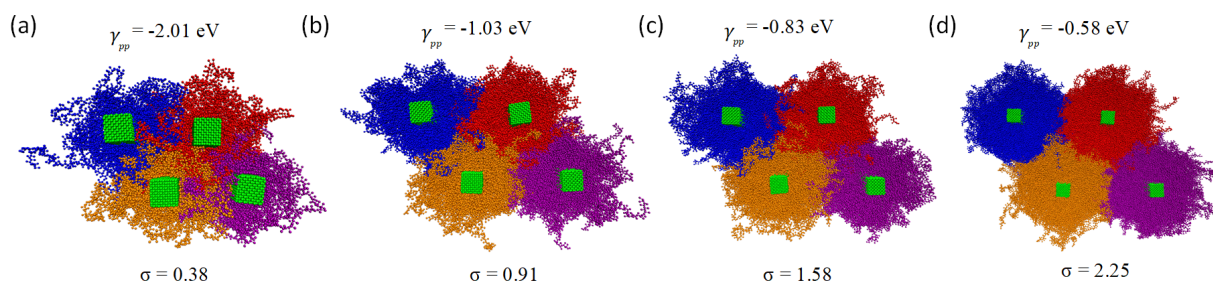


**Figure 5.3-4: Schematic of intermingling of polymer chains at various grafting densities.** The schematic shows the pairwise interaction energy between polymer chains as the grafting density is increased from 0.38 to 2.25 (a-d). Each color represents the polymer chains tether to a different nanoparticle. All grafting densities are in the units of chains/nm<sup>2</sup>.

In order to ensure that choosing a representative volume element (RVE) of four particles does not bias our results, we validated our findings by simulating an RVE consisting of 4 and 64 particles. **Figure 5.3-5** shows that there is virtually no difference in the average chain conformations in the two systems. The inset in **Figure 5.3-5** shows the schematic of the setup for each system.

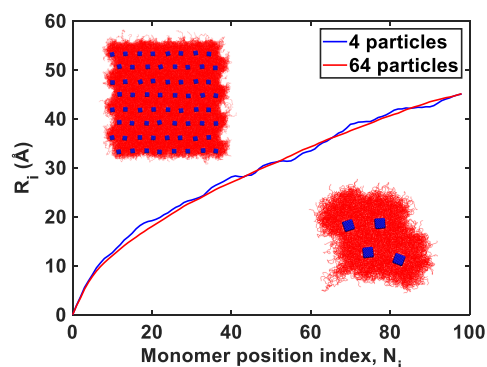


**Figure 5.3-5: Size effect on chain conformations.** Plot of  $R_g$  vs  $N_i$  showing virtually no difference in chain conformations in the two systems consisting of 4 and 64 particles. The insets show the equilibrated data structures of the two systems.

## 5.4 $N_{cr}$ for other polymers

$N_{cr}$  is an important design parameter for aHNPs as we have showed that the degree of polymerization needs to be greater than the  $N_{cr}$  to obtain optimal mechanical properties<sup>240</sup>. In the previous section we derived the equation for  $N_{cr}$  using CNC grafted PMMA system. We extend this analysis to three other polymers as well (PS, PC and PB). The system setup and equilibration protocols are same as mentioned above. A comparison of  $N_{cr}$  values for the highest grafting case

(30%) is shown in **Figure 5.4-1**, which reveals that PS has the largest value of  $N_{cr}$  among all the polymers studied. It also indicates that semi flexible polymers with more prominent side groups, such as PS and PMMA, have a higher  $N_{cr}$  in linear polymers. On the other hand, flexible rubbery polymers such as PB have a low  $N_{cr}$ .

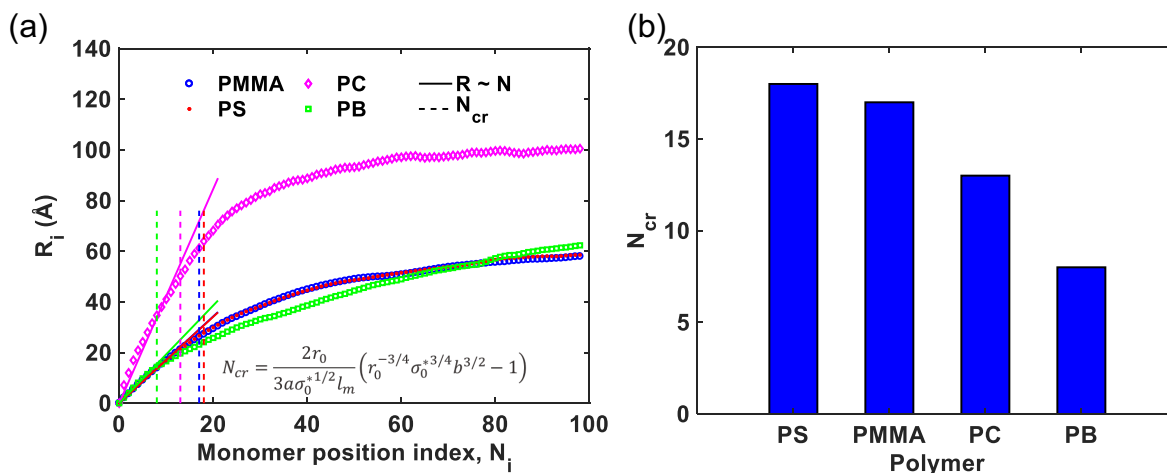


**Figure 5.4-1: Scaling of monomer position index with respect to distance from nanoparticle for various polymers.** a) Plot of distance of monomer from the nanoparticle surface versus monomer position index.  $R_i$  is distance of  $i^{\text{th}}$  monomer ( $N_i$ ) from the nanoparticle surface. The linear solid line shows the scaling relationship in CPB ( $R \sim N$ ) regime and the dotted line shows the transition point from CPB to SDPB  $R \sim N^{0.5}$ , identified as critical chain length,  $N_{cr}$ . The inset shows the equation of  $N_{cr}$ . b) Bar plot showing the comparison of  $N_{cr}$  for the different polymers at 30% grafting density.

Eq. 5.3-4 has two polymer specific constants, i.e.,  $a$  and  $b$ , which can be obtained by making a linear fit to Eq. 5.3-2 & 5.3-3 which are shown in **Figure 5.4-2a** and b. aHNPs with five different grafting densities are simulated to extract the brush height,  $h$ , and crossover radius,  $r_c$ . The  $a$  and  $b$  values for PS and PMMA are very close with PS having slightly higher values. PC

has the smallest  $a$  value whereas PB has the smallest  $b$  value. The constant  $a$  affects the height of the polymer brush which is expected to be larger for polymer with a stiffer backbone or larger monomer length,  $l_m$ , for a given grafting density. Since Eq. 5.3-4 already includes  $l_m$ , it indicates that the backbone stiffness is the key factor governing this constant. Persistence length is used as the metric to quantify the backbone stiffness, which is obtained from the decay of cosine of angle between a vector that is tangent to the polymer at position 0 and a tangent vector at a distance  $l$  away from position zero. By fitting the equation,  $\langle \cos\theta \rangle = e^{-\frac{l}{l_p}}$ ,<sup>249</sup> we can obtain the persistence length of the polymer chain,  $l_p$ . It is expected that the value of  $a$  will correlate with the  $l_p$  of the polymer. Based on the DC theory,<sup>46</sup>  $b$  incorporates the excluded volume parameter, which can be obtained from the peak of radial distribution function (RDF) of monomer units,  $\sigma_{com}$ . Thus, it is expected that the  $b$  value will scale with the  $\sigma_{com}$ , or equivalently the bulkiness of the monomer. In order to obtain  $l_p$  and  $\sigma_{com}$ , we generated bulk polymer systems with no nanoparticles. **Figure 5.4-2c** shows the decay of  $\cos\theta$  along the length for these pure polymer melts from which we evaluated  $l_p$ . We then analyzed the RDF of monomer units which is shown in **Figure 5.4-2d** to obtain  $\sigma_{com}$ . **Table 5.4-1** summarizes the material parameters  $a$  and  $b$ ,  $l_m$ ,  $l_p$  and  $\sigma_{com}$  for different polymer grafted aHNPs. The measurement uncertainty shows the 95% confidence interval of the values obtained by fitting. The  $l_m$  values have very low uncertainty (less than 0.01%) and hence their error is not reported.

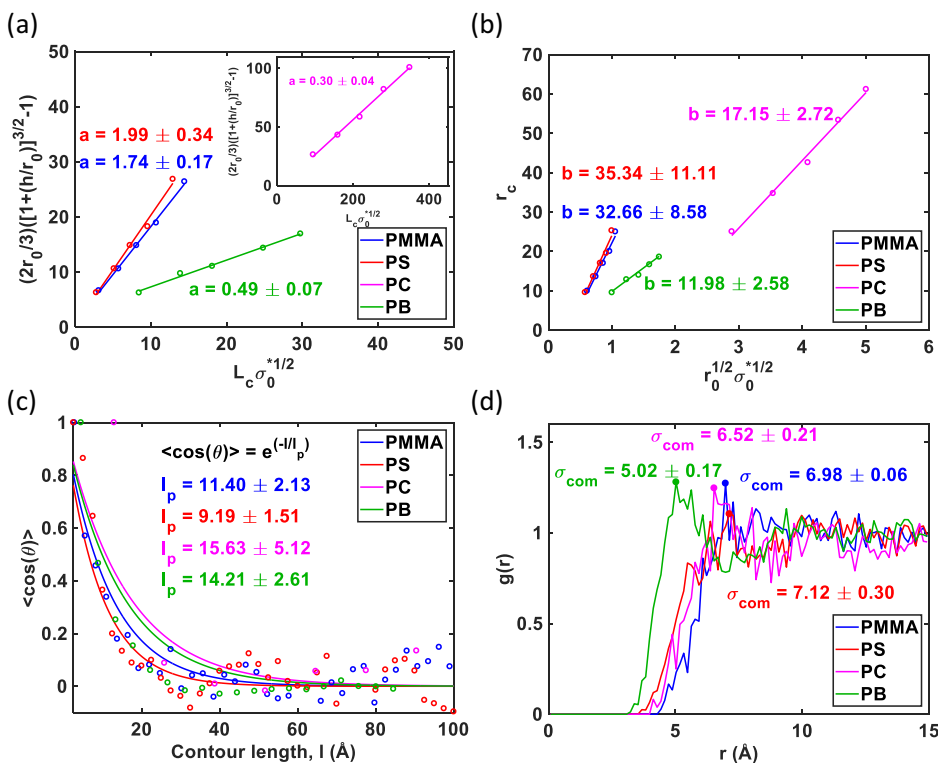


**Figure 5.4-2: Obtaining parameters  $a$  and  $b$  for various polymers.** (a) The slope of  $\frac{2r_0}{3} \left( \left[ 1 + \left( \frac{h}{r_0} \right)^2 \right]^{3/2} - 1 \right)$  vs  $L_c \sigma_0^{*1/2}$  gives the value of  $a$  for the polymer. (b) The slope of  $r_c$  vs  $r_0^{1/2} \sigma_0^{*1/2}$  gives the value of  $b$  for the polymer. (c) Decay of angle between consecutive bonds along the backbone of the polymer chain. (d) RDF plots of monomer units for different polymers.

**Table 5.4-1: Material parameters and polymer characteristics for different aHNPs.**

Polymer	$l_m$	$a$	$b$	$l_p$ (Å)	$\sigma_{com}$ (Å)
PS	2.57	$1.99 \pm 0.34$	$35.34 \pm 11.11$	$9.19 \pm 1.51$	$7.12 \pm 0.30$
PMMA	2.71	$1.74 \pm 0.17$	$32.66 \pm 8.58$	$11.40 \pm 2.13$	$6.98 \pm 0.06$
PC	12.92	$0.30 \pm 0.04$	$17.15 \pm 2.72$	$15.63 \pm 5.12$	$6.52 \pm 0.21$
PB	4.48	$0.49 \pm 0.07$	$11.98 \pm 2.58$	$14.21 \pm 2.61$	$5.02 \pm 0.17$

Having related the physical design parameters to  $a$  and  $b$ , the next step is to get in-depth insight into the effect of these material parameters on  $N_{cr}$ . We carried out a systematic study of the effect of  $l_p$  and  $\sigma_{com}$  on  $N_{cr}$ . It is convenient to use our CG models for this work because we can vary  $l_p$  or  $\sigma_{com}$  by changing only a single force field parameter. To understand the influence of  $l_p$ , the backbone rigidity of a modified PB model is varied by changing the strength of angle coefficient, which results in model polymers with  $l_p$  ranging from 10 Å to 70 Å. PB is chosen as the model polymer for the systematic analysis of effect of persistence length,  $l_p$ , as the CG scheme of 1 bead per monomer allows us to vary only one angle between the beads to obtain the desired range of  $l_p$ . One caveat in this analysis is that the original PB model has an equilibrium angle of  $120^\circ$ , where stiffening the angle term would give rise to strongly coiled polymeric chains. Therefore, in order to effectively change  $l_p$ , we modified the equilibrium angle of the PB model to be  $180^\circ$ . The rest of the parameters are the same as the original PB model<sup>122</sup>. **Figure 5.4-4a** shows the polymer conformations for the extreme cases of  $l_p$ . As seen from **Figure 5.4-4b**,  $N_{cr}$  changes dramatically by varying  $l_p$ , with stiffer polymers having a higher  $N_{cr}$  for the same grafting density. A greater number of monomer segments is required for a polymer with a stiffer backbone to transition to SDPB regime, despite the lack of steric hindrance away from the nanoparticle surface. This causes the transition point between CPB to SDPB to shift further away from the nanoparticle surface, thus increasing  $N_{cr}$ .

Next, we look at the effect of  $\sigma_{com}$  on  $N_{cr}$ . In order to change  $\sigma_{com}$ , we varied the side-group van der Waals radius in the PMMA CG model by varying the LJ  $\sigma$  value for the side-group interactions only,  $\sigma_{sg}$ , from 2 Å to 6 Å. The CG scheme of two bead per monomer for PMMA allows us to conveniently vary  $\sigma_{com}$ . The parameter  $b$  represents the excluded volume of the

monomer. If we consider  $\sigma_{com}$  as the radius of the monomer, then we would expect  $b$  to scale with  $\sigma_{com}^3$ . **Figure 5.4-3a** show this scaling. The density of the polymer will decrease as the side group size increases. This is due to the increases in excluded volume generated as a result of larger side group. There is linear relationship between the polymer density and the side group size as shown in **Figure 5.4-3b**.

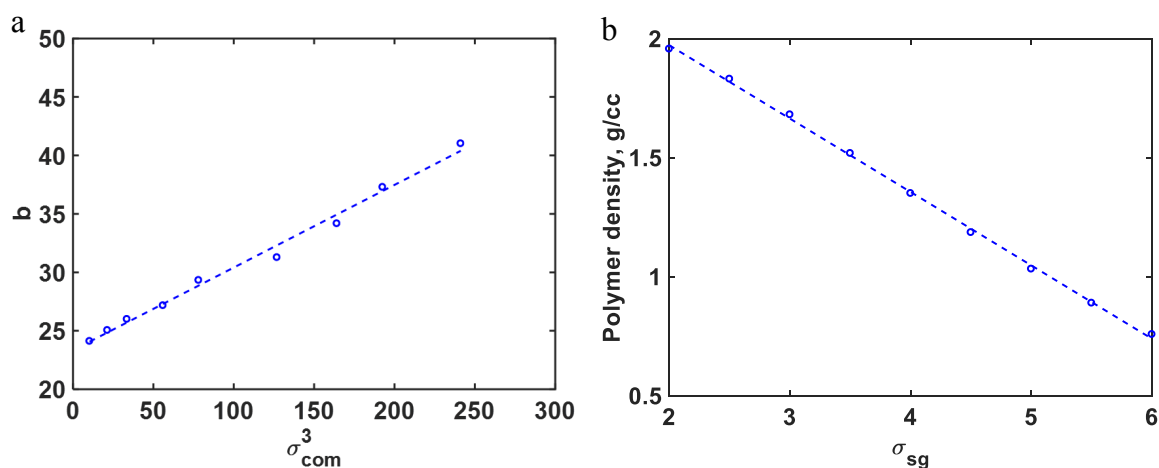


**Figure 5.4-3: Relation between length scale parameters.** (a) Plot of  $b$  vs  $\sigma_{com}^3$ . (b) Plot of density vs  $\sigma_{sg}$

**Figure 5.4-4c** shows the extreme cases of different  $\sigma_{sg}$  that we studied. It is observed that  $N_{cr}$  does not vary substantially over the range of  $\sigma_{sg}$  analyzed (**Figure 5.4-4d**). However, the initial slope of  $R_i$  vs.  $N_i$ , ( $dR_i/dN_i$ ) is strongly affected by  $\sigma_{sg}$  for segments in the CPB regime. The slope quantifies the extension state of the chain, which increases with the  $\sigma_{sg}$ . The observation that as  $\sigma_{sg}$  increases, chain segments in the CPB regime become more extended can be argued on the basis of steric hindrance due to bulky side groups, which cause confinement and consequently extension of the chains. The increase in local chain extension due to bulky side-groups have been observed in previous studies of grafted systems<sup>40</sup>. However, the number of monomers in the CPB regime

remains the same. This is a crucial observation as it illustrates that having bulky side groups does not alter  $N_{cr}$  appreciably.

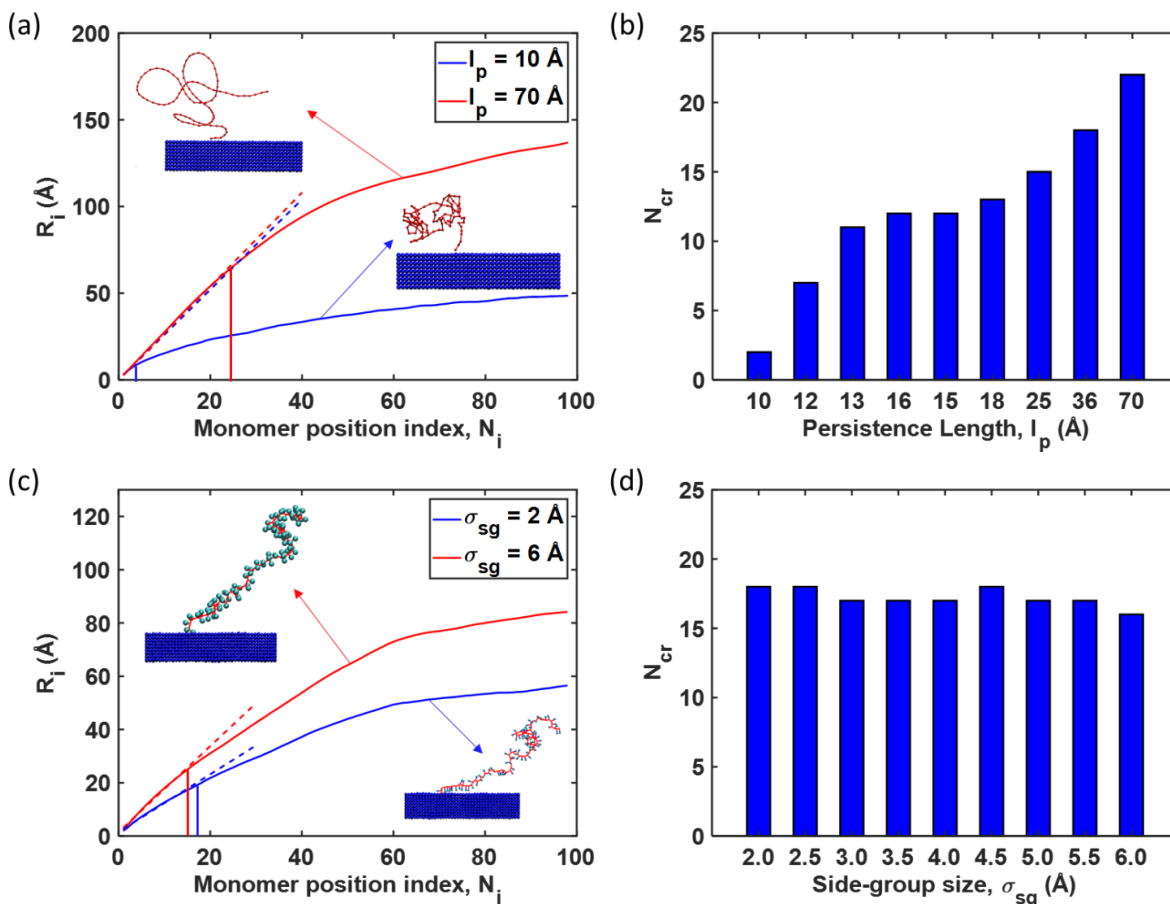


**Figure 5.4-4: Scaling of monomer position index with respect to distance from nanoparticle as a function of persistence length and side-group size.**  $R_i$  is distance of the  $i^{\text{th}}$  monomer from the nanoparticle surface and  $N_i$  is the monomer position index in the polymer chain. The dotted line shows the linear relationship in the CPB regime and the solid line shows the transition point from the CPB to the SDPB regime. a)  $R_i$  vs  $N_i$  plot for the lowest and highest backbone rigidities with the inset showing a snapshot of the polymer chain conformations. b) Bar plot showing the variation in  $N_{cr}$  with varying  $l_p$  for 30% grafting density. c)  $R_i$  vs  $N_i$  plot for the smallest and

largest side group sizes with the inset showing a snapshot of the polymer chain conformations. d) Bar plot showing the variation in  $N_{cr}$  with changing  $\sigma_{sg}$  for 30% grafting density.

The distance of each monomer from the nanoparticle surface ( $R_i$ ) can be used to measure the local extension state of the chain, and depends on material parameters  $a$ ,  $b$ ,  $r_0$ ,  $l_m$  and  $\sigma^*$ . We evaluated the dependencies of these parameters and normalized the  $R_i$  vs  $N_i$  plots for 110 distinct aHNP models (five grafting densities for each of the four actual polymers, nine different  $\sigma_{sg}$  and  $l_p$ ). The consistent collapse of the data onto a single curve suggests a universal relation governing the polymer chain conformations in these hairy nanoparticle assemblies (shown in **Figure 5.4-5**). When  $N_i < N_{cr}$ , the polymer chains are extended in the CPB regime and the distance scales linearly with the number of monomers ( $R \sim N_i$ ). When  $N_i > N_{cr}$ , the scaling becomes  $R \sim N_i^{0.5}$  which is same as the melt state. In our simulations, we haven't varied the radius of the nanoparticle, however, in order to make the value dimensionless, we multiply the numerator with  $r_0^{1/2}$ . The proportionality constant for both the curves is empirically found to be 0.1. Hence, the position of a monomer can be obtained by the following equations:

$$R_i = \frac{0.1ab\sigma^*l_m}{r_0^{1/2}} \frac{N_i}{N_{cr}} \quad \text{for } N_i < N_{cr} \quad (5.4-1)$$

$$R_i = \frac{0.1ab\sigma^*l_m}{r_0^{1/2}} \left(\frac{N_i}{N_{cr}}\right)^{0.5} \quad \text{for } N_i > N_{cr} \quad (5.4-2)$$

From this universal equation, we can obtain the position of any monomer along the backbone of the polymer chain in aHNPs.

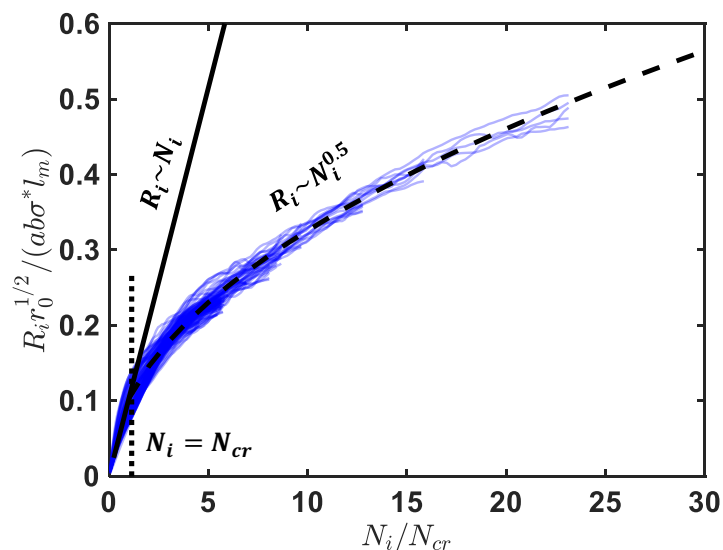


**Figure 5.4-5: Universal scaling law governing chain conformations.** The monomer index  $N_i$  is normalized with  $N_{cr}$  and the radial distance ( $R_i$ ) is normalized with material design parameters  $a$ ,  $b$ ,  $r_0$ ,  $l_m$  and  $\sigma^*$ , shown for 110 different aHNP systems.

## 5.5 Conclusion

In summary, we have taken advantage of chemistry specific CG models to analyze the role of polymer chemistries on the chain conformations in anisotropic hairy nanoparticle assemblies. Specifically, we utilized CG-MD simulations to reveal the correlation between the material parameters  $a$  and  $b$  derived based on DC model to physical design parameters, persistence length and monomer excluded volume respectively. The analysis of the effect of side group size and backbone rigidity on the chain conformations indicates that polymers with stiffer backbones tend to have a higher  $N_{cr}$ , whereas the bulkiness of side group does not significantly affect  $N_{cr}$ . Building upon these findings, it can be said that aHNPs based on semi flexible glassy polymers (PS and PMMA) will require a much higher molecular weight to overcome the  $N_{cr}$  barrier compared to

flexible rubbery polymers (PB) in order to have optimal mechanical properties. Moreover, we obtained a universal equation predicting the monomer position along the chain of the polymer backbone in these aHNPs. This crucial information is useful for determining the equilibrium spacing between the nanoparticles in aHNPs, which can be used to evaluate the volume fractions and carry out further predictions of mechanical properties based on theoretical relations such as rule of mixtures. It can also help us identify systems that have high cohesive interactions and yet low  $N_{cr}$ , for instance due to low conjugation density or low confinement effects, thereby improving total nanoparticle interaction energies and overall mechanical behavior. High-throughput calculation of these influential parameters for a broader library of polymer/nanoparticle combinations will be instrumental for accelerating the design of these systems. This study sets the stage for it by establishing key molecular details governing the conformational behavior of polymers in grafted systems, demonstrating path forward for more rapidly designing aHNPs.

## Chapter 6: Mesoscale modeling based on potential of mean force

In Chapter 2:, we briefly discussed about parameterized and derived CG methods. The ER approach discussed in Chapter 3: falls under the parametrized CG method. This chapter focuses on developing a derived CG method; a mesoscale modeling technique using potential of mean force approach. This approach aims at developing an interatomic potential between nanoparticles in aHNPs which will eliminate the need to explicitly simulate polymer chains, thus increasing the spatiotemporal scale and will help to link interfacial effects of grafting on structure and mobility directly to macroscale constitutive relations for nanocomposites. Portions of the text and figures within chapter are reprinted or adapted with permission from Hansoge et al. ACS Macromolecules 2021<sup>250</sup>.

### 6.1 Introduction

Multiscale modeling techniques such as coarse-grained molecular dynamics (CG-MD) simulations have been used to evaluate the self-assembly, mechanical properties and chain conformations in aHNPs<sup>20, 39, 42, 192, 240, 251, 252</sup>. The length and time scales accessible through these CG-MD simulations are several tens of nanometers and nanoseconds. While these models are adequate to evaluate the dynamics and structural conformation of the polymer chains, the movement and structure of the nanoparticles themselves and macroscopic properties, such as fracture energy or ballistic penetration energy of thin films, remain out of reach. This necessitates the development of a much coarser model that can access micron-size scales without loss of chemical specificity. One way to achieve this is to develop an effective pair-wise mesoscopic interatomic potential between nanoparticles, eliminating the explicit simulation of the grafted polymer chains.

There are several studies in literature that have developed effective potentials using integral equation theories<sup>253-259</sup>, umbrella sampling approach<sup>203, 260, 261</sup>, and self-consistent field theory (SCFT)<sup>262-264</sup>. Polymer Reference Interaction Site Model (PRISM) theory has been used to calculate the potential of mean force (PMF) between polymer grafted nanoparticles in a polymeric matrix<sup>253-255, 265</sup>. These studies reveal that at lower grafting densities, the PMF becomes more attractive due to decrease in wettability of grafted chains. A similar approach has also been adopted by several other researchers to evaluate the PMF between nanoparticles in a polymeric matrix<sup>256-259</sup>. Monte-Carlo simulations has been used to formulate a logarithmic repulsive force and an exponentially decaying attractive force between star polymers<sup>266, 267</sup>. Other methods such as the umbrella sampling approach<sup>203, 260, 261</sup>, which is a free energy calculation method that reliably computes the PMF, has been used to come up with derivations of effective interactions between nanoparticles. These studies have provided timely and significant insights into the nature of these effective interactions, but have commonly utilized generic interatomic potentials, such as Lennard-Jones or FENE, to describe the polymer chains. Since the confined behavior of polymers in grafted systems strongly depends on molecular chemical features such as side-group size or polarity, there is a critical need to develop a numerical framework for linking the effective interactions between nanoparticles to these molecular design parameters.

In this work, we address this shortcoming by developing a relation that describes the interaction between polymer grafted nanoparticles with respect to the chemistry of the polymer chains, the chain length and the grafting density. We simplify the model by investigating polymers grafted between two infinite slabs, which is representative of systems where nanoparticles have a lamellar ordering, or of spherical nanoparticles large enough that the local curvature is negligible.

While most computational studies on polymer grafted nanoparticles involve a spherical nanoparticle<sup>253, 254, 256, 260, 268</sup>, the advent of high aspect ratio nanoparticles such as cellulose nanocrystals<sup>206, 208</sup>, 2D nanomaterials or platelets<sup>269, 270</sup>, and other lamellar systems renders the understanding of effective interactions between two planar brush surfaces critical. We note that the general framework developed here can be applied to particles of any arbitrary curvature with an appropriate setup of the simulated representative volume. Here, we carry out tensile and compressive simulations of nanoparticles grafted with four common polymers with distinct chemical groups and segmental structures, i.e., poly (methyl methacrylate) (PMMA), polystyrene (PS), polycarbonate (PC) and polybutadiene (PB). This choice allows for a wide range of properties to be examined in a single study, spanning large ranges of fragility, glass transition temperature and chemistry. **Figure 6.2-1a** shows a schematic of a high aspect ratio polymer grafted nanoparticle assembly along with the coarse graining strategy used for each polymer. We take a subsection of the assembly to evaluate the transverse properties at the interface between the nanoparticles. The approach taken here is similar to the use of a surface force apparatus that can measure the adhesion force between polymer and substrate<sup>63, 64</sup>. We extract the potential of mean force (PMF), which is the work required to move the plates, and describe it analytically. The empirical constants of our analytical expression are related to the design parameters; chain length, grafting density and chemistry. Moreover, we also evaluate the dependence of the PMF on strain rate and extrapolate the zero-rate limit to our data. These results provide a new interparticle potential for the study of nanoparticle assemblies at the mesoscale for the design parameters investigated without loss of chemistry specificity, and the numerical framework developed can easily be extended to a broader class of systems.

## 6.2 Simulation methods

Our group previously developed CG models of the above mentioned polymers using an energy renormalization approach that accurately captures the mechanical properties while preserving the dynamics of the full atomistic system. We use harmonic potential for the bonds, tabulated potentials for angles and dihedrals and the non-bonded interactions are described by LJ potential, the parameters are in our previous papers<sup>115, 116, 123</sup>. The CG-mapping of these polymers is shown in **Figure 6.2-1a**. We use atactic structures for polymers with side-groups (PS and PMMA) and idealize nanoparticle cores as two planar surfaces from which polymers emerge and interdigitate, a model that could be broadly applicable to large, stiff 1D-2D nanoparticles or strongly cohesive assemblies of these particles in a lamellar configuration. The nanoparticle is modeled as a rigid plate with dimensions of 5 nm × 10 nm with each bead placed at a distance of 5 Å. The mass of the bead can be chosen based on the density of nanoparticle to be modeled; in this case, we chose 324 g/mol, which is consistent with the mass of a coarse-grained bead of a cellulose nanocrystal<sup>192</sup>. In order to evaluate the influence of chain length and grafting density, we first created a design of experiments where we systematically vary the polymer chain length from 20 to 100 monomer units while keeping the grafting density constant at 0.5 chains/nm<sup>2</sup>. We then vary the grafting density from 0.08 to 1.14 chains/nm<sup>2</sup> while keeping the chain length constant at 50 monomer units. The grafting density here is defined as the number of polymer chains grafted per unit area of the nanoparticle surface. We note that the chain lengths used in this study are below the physical entanglement length for the polymers as the relaxation of an entangled polymer network is computationally expensive.

All the CG-MD simulations are carried out using Large-scale Atomic/Molecular Massively Parallel Simulator (LAMMPS) software<sup>58</sup>. We use periodic boundary conditions along the edges of the slabs ( $x - y$  plane) to mimic infinite plates, whereas the box is non-periodic in the normal ( $z$ ) direction where the force is applied (**Figure 6.2-1b**). To generate the structure, a flat plate is created and random beads are chosen to be grafted based on each grafting density. The polymer chain is then grown from the grafted point using a random walk algorithm.<sup>81</sup> The grafted plate is subsequently replicated and inverted to create two parallel grafted plates as shown in **Figure 6.2-1a**. We use the equilibration protocol reported in our previous works<sup>192, 240</sup>. In order to remove any overlap between polymer beads, a soft interatomic cosine potential is initially applied to push the polymer beads apart. Afterward, the actual potential is switched on and a brief equilibration is carried out under NVT ensemble for 2 ns. Next, the system is subjected to a high pressure and temperature to anneal and remove any residual stresses, and then cooled down to the room temperature and equilibrated for 2 ns. The second Legendre order parameter ( $P_2$ )<sup>116</sup> value is checked to be below 0.1 to ensure the chains are well relaxed. The equilibrated system is then subjected to tensile force using steered molecular dynamics (SMD) simulations where the bottom plate is fixed and the top plate is pulled with a constant velocity of 5 m/s, which is equivalent to a strain rate of around  $10^9 \text{ s}^{-1}$ . The strain rate used here is much higher than typical experiments, but for a subset of our systems we show how we can easily extrapolate our results to the limit of zero pulling velocity, fitting our PMF results with a Cowper-Symonds model<sup>271</sup>. A schematic of the tensile test is shown in **Figure 6.2-1b**. The sum of forces in the pulling direction is calculated, multiplied with the displacement and divided by the volume (which is the area of the plate multiplied by the equilibrium distance between the plates) to provide the potential of mean force

per volume ( $\psi$ ). Each setup is run for five different trials to obtain statistically significant data.

**Figure 6.2-1c** shows a representative PMF curve for different polymer grafted systems.

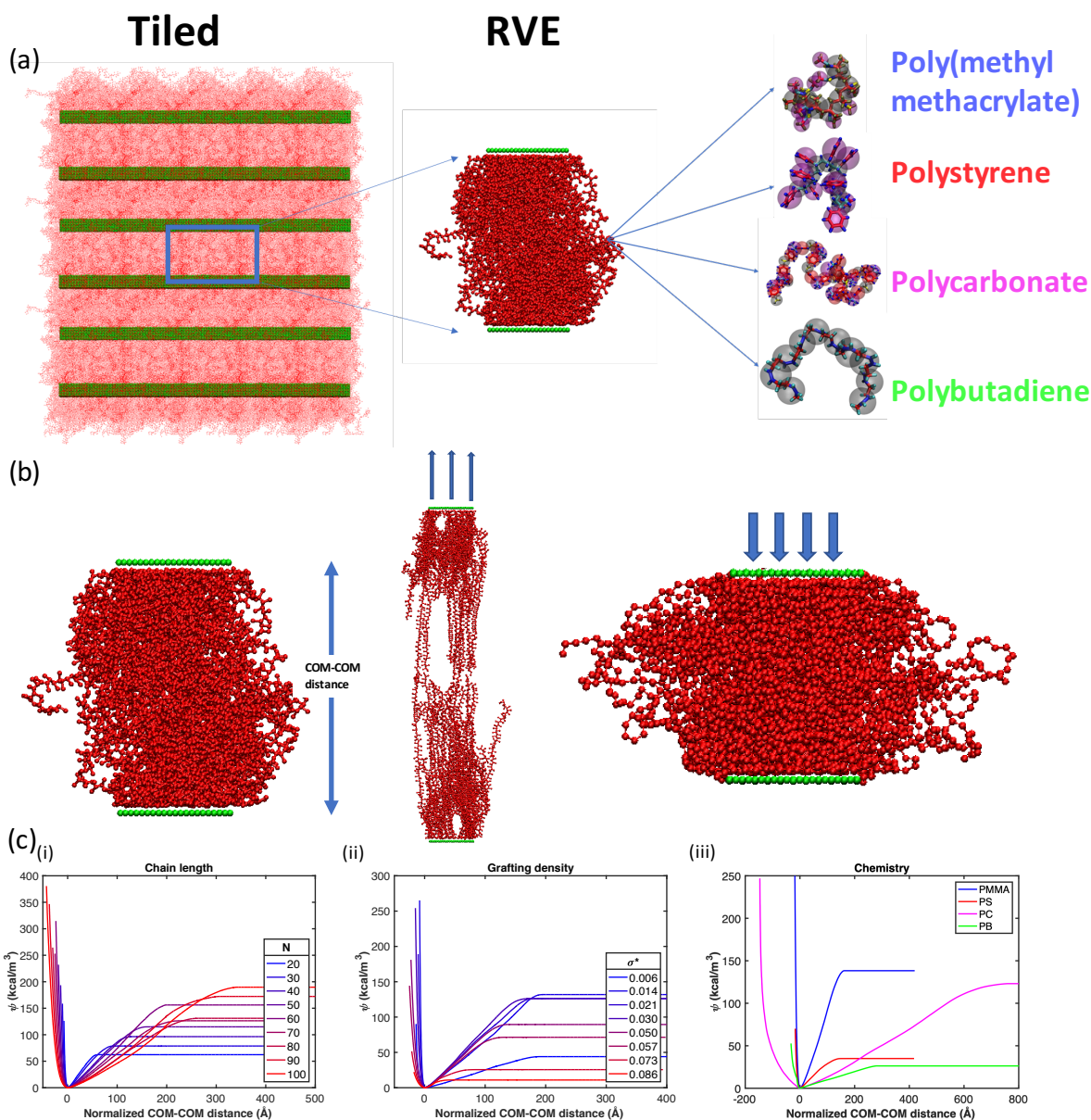


**Figure 6.2-1: Schematic of system setup and representative PMF curves.** (a) Schematic of the layered polymer grafted to a high aspect ratio nanoparticle assembly. A representative volume element (RVE) is used to analyze the transverse properties of these assemblies. The various

polymers and their atomistic and coarse-grained representations are shown on the right. The RVE shown is of PMMA grafted nanoparticle system with chain length of 100 and grafting density of 0.5 chains/nm<sup>2</sup>. (b) CG-MD simulations are carried out by fixing the bottom plate and pulling/pushing on the top plate with a constant velocity. The schematic is of the same system as in panel a. (c) Representative plots of potential of mean force ( $\psi$ ) with respect to center of mass (COM) distance between the nanoparticles normalized by their equilibrium distance. Here normalized means that the distance between the plates has been subtracted by the equilibrium distance. The three plots show the variation with (i) chain length of PMMA grafted nanoparticle at constant grafting density of 0.5 chains/nm<sup>2</sup>, (ii) grafting density of PMMA grafted nanoparticle at constant chain length of 50 and (iii) polymer chemistry at chain length of 50 and grafting density of 0.5 chains/nm<sup>2</sup>.

### 6.3 Cohesive energy and entanglement analysis

We first look at the individual effect of chain length,  $N$ , and grafting density,  $\sigma$ , on the peak of the potential of mean force,  $\psi_{max}$ . The grafting density,  $\sigma$ , is defined as  $\sigma = \frac{f}{w * l}$  where  $f$  is the number of grafts, and  $w$  and  $l$  are width and length of the plate respectively. The total work required to completely separate the plates starting from their equilibrium position is defined as  $\psi_{max}$ , which is the plateau of the PMF curve or depth of the energy well. The trends of  $\psi_{max}$  with respect to the design parameters,  $N$  and  $\sigma$ , are shown in **Figure 6.3-1**. From **Figure 6.3-1a**, we can see that there is a linear increase in  $\psi_{max}$  with increase in chain length.  $\psi_{max}$  gives an indication of the toughness (area under stress-strain curve) of the system and it is well known that longer chains enhance toughness in pure polymers<sup>27,28</sup> and polymer grafted nanoparticle systems<sup>29, 30</sup>. Our

simulation results support this theory for all different polymer grafted systems. Therefore, it is possible that trends may change and there may be saturation at sufficiently high chain lengths; brittle fracture due to chain scission may also occur for strongly interacting chains. Regardless, the range we study is perhaps of greater interest for aHNPs since the physical behavior begins to converge to that of neat polymers as  $N$  becomes large.

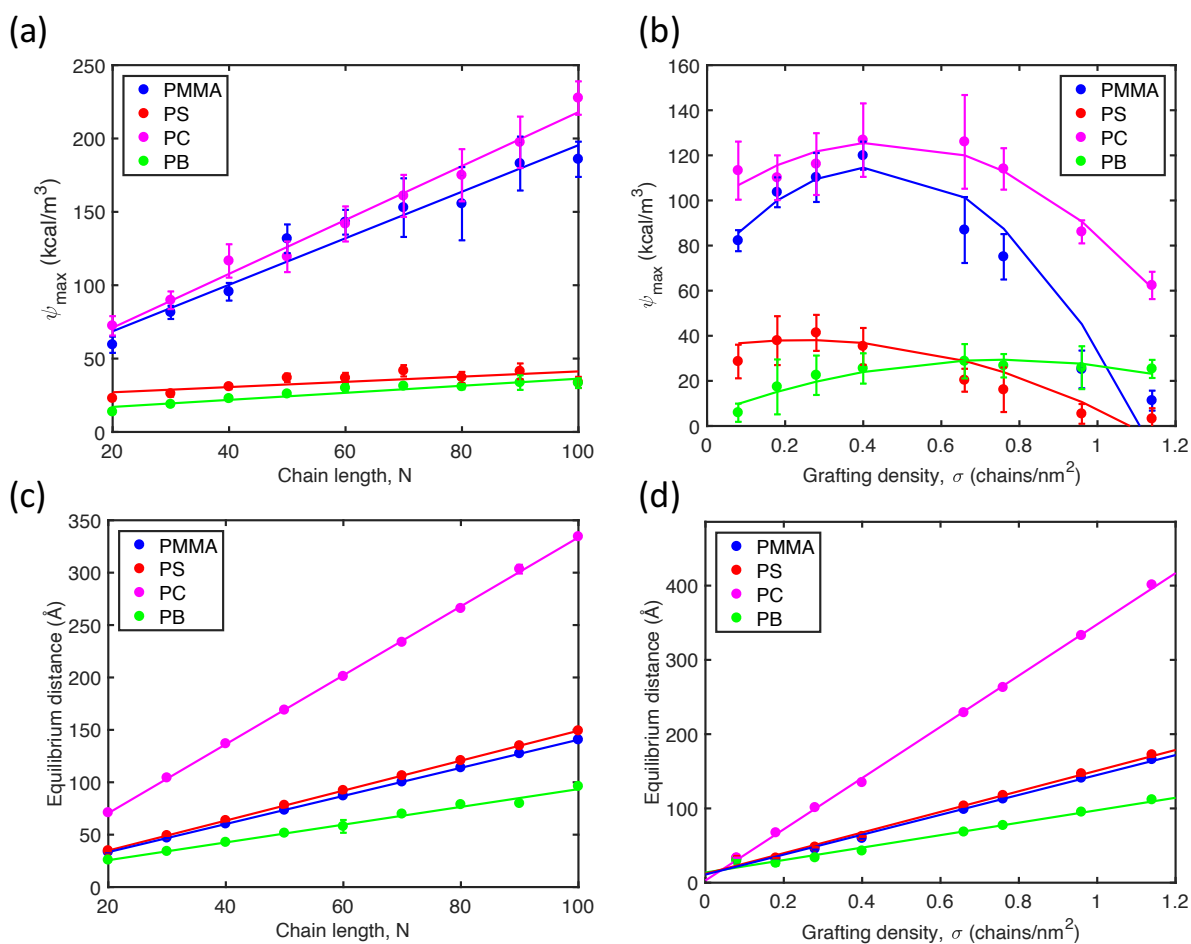


**Figure 6.3-1: Relation of peak PMF and equilibrium distance with respect to chain length and grafting density.** (a) The peak of potential of mean force ( $\psi_{max}$ ) increases linearly with chain length,  $N$ . (b)  $\psi_{max}$  first increases with grafting density,  $\sigma$ , up to about 0.2-0.4 chains/nm<sup>2</sup>, beyond which the value starts to decrease. The lines in the figure are the best fits obtained from the data,

a linear fit for variation with  $N$  and a quadratic fit for variation  $\sigma$ . The equilibrium distance between the plates increases linearly with (c) chain length,  $N$  and (d) grafting density,  $\sigma$ . The error bars indicate the variance in values from five different trials.

When the grafting density increases,  $\psi_{max}$  first increases and then starts to decrease (**Figure 6.3-1b**). At lower grafting density, the cohesive interactions between the polymer chains arising from the two nanoparticles are minimal, leading to a low  $\psi_{max}$ . These interactions increase as  $\sigma$  is increased due to increase in number of polymer chains. However, they start decreasing again beyond a certain threshold (around 0.2-0.4 chains/nm<sup>2</sup>) due to a reduction in interdigitation of polymer chains caused by steric hindrance. As the grafting density increases, the close spacing leads to entropically unfavorable conformations of the grafted polymer chains. Experiments have shown that even at high pressures, the concentrated polymer brushes (highly grafted nanoparticles) hardly interpenetrate each other<sup>47, 248</sup>. Similar observations were made in our previous study,<sup>192</sup> where we saw a decrease in cohesive interactions with increasing grafting density, which we attributed to fewer monomer segments being in the semi dilute polymer brush (SDPB) regime. The grafted polymer chains need to be in SDPB regime to effectively interact with other polymer chains<sup>192</sup>. **Figure 6.2-1c** shows the PMF curves for the different polymer chemistries. It can be seen that PB, which is rubbery as compared to other polymers at room temperature, has the lowest value of  $\psi_{max}$ , whereas tough glassy polymers, PMMA and PC have high values of  $\psi_{max}$ . The initial curvature of the attractive part of the PMF curve is related to the modulus of the system. PMMA, which has the highest modulus among the four polymers, has the highest curvature, whereas PB has the lowest curvature and thus the modulus. **Figure 6.3-1c** and **d** shows that the equilibrium distance is linearly dependent on the chain length and grafting density respectively. In

general, as the polymer content increases (with either grafting density or chain length) in the system, the equilibrium distance increases. One can also extract the PMF on per unit area ( $\gamma$ ) basis by multiplying the PMF per volume ( $\psi_{max}$ ) with the equilibrium distance ( $x_0$ ) (**Figure 6.3-2**).

$$\gamma = \psi_{max} \times x_0 \quad (6.3-1)$$

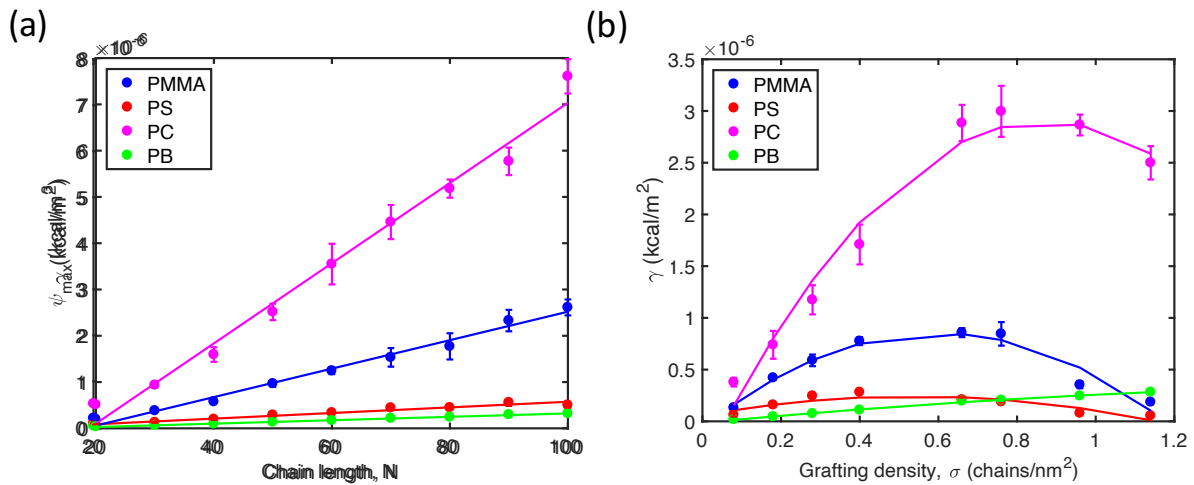


**Figure 6.3-2: Peak PMF in per unit area.** Variation of peak PMF ( $\psi_{max}$ ) per unit area with respect to (a) chain length,  $N$ , and (b) grafting density,  $\sigma$ .

The cohesive interaction energy between the polymer chains ( $\gamma_{pp}$ ) is a key factor that governs the tensile properties ( $\psi_{max}$ ) of the composite. Here, we quantify  $\gamma_{pp}$  by calculating the pairwise energy between polymer beads arising from the top and bottom nanoparticle normalized by the total number of polymer beads ( $N_p$ ) as described in Eq. 6.3-2.

$$\gamma_{pp} = \frac{1}{N_t} \sum_{i,j=1, i \neq j}^{N_p} 4\varepsilon \left( \left( \frac{\delta}{r_{ij}} \right)^{12} - \left( \frac{\delta}{r_{ij}} \right)^6 \right) \quad r_{ij} < r_c \quad (6.3-2)$$

where  $\delta$  is the size of the bead,  $\varepsilon$  is the cohesive energy between the beads, and  $r_{ij}$  is the distance between the beads. Varying  $\sigma$  showed a proportional increase in  $\psi_{max}$  with  $\gamma_{pp}$  (**Figure**

6.3-3a). However, when  $N$  was varied at a fixed  $\sigma$ , we observed no apparent relation between  $\psi_{max}$  and  $\gamma_{pp}$ , as shown in **Figure 6.3-3** (b).

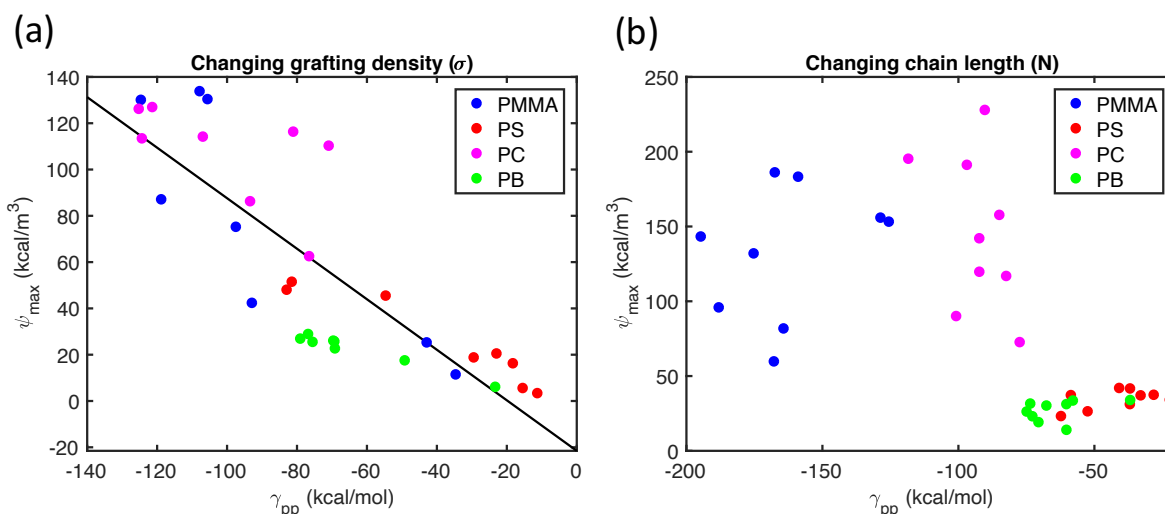


**Figure 6.3-3: Relation between  $\gamma_{pp}$  and  $\psi_{max}$ .** Relationship between the cohesive interaction energy ( $\gamma_{pp}$ ) between chains grafted to different nanoparticles and  $\psi_{max}$  for designs with (a) varying grafting densities at fixed chain length of 50 and (b) varying chain lengths at a fixed grafting density of 0.5 chains/nm<sup>2</sup>. The line in panel (a) is a guide for the eye, showing a linear relation between  $\gamma_{pp}$  and  $\psi_{max}$ , whereas panel (b) shows that there is no evident correlation between  $\gamma_{pp}$  and  $\psi_{max}$ .

This warranted further investigation into these systems and we evaluated the geometric entanglement in the system using the Z1 code developed by Martin Kroger<sup>273, 274</sup>. The Z1 code returns the primitive path (PP) and the related number and positions of entanglements (kinks) for all chains in the simulation box. From that, we obtain the average value of entanglements per chain,  $\langle Z \rangle$ . This value gives a sense of how intertwined the chains are in the system.  $\langle Z \rangle$  is not necessarily the same as physical entanglement in polymer chains, where the movement of chains

changes from sliding to entanglement. **Figure 6.3-4** shows the relation between  $\langle Z \rangle$  and  $\psi_{max}$ . We observe that as the entanglement per chain increases with chain length,  $\psi_{max}$  also increases. This indicates that even though the interaction energies between polymer chains are similar,  $\psi_{max}$  depends on the entanglement in the system. It also ties with the increase in entropic elasticity as the molecular weight of the polymer increases<sup>275</sup>. We also observe the same behavior at low (0.18 chains/nm<sup>2</sup>) and high (0.96 chains/nm<sup>2</sup>) grafting densities (**Figure 6.3-5**). Thus, as the chain length increases, the enthalpic contribution ( $\gamma_{pp}$ ) remains the same, but due to increase in entropic contributions, the  $\psi_{max}$  increases. However, when the grafting density changes,  $\langle Z \rangle$  remains similar in value as seen from **Figure 6.3-4**. This indicates that changing grafting density affects the enthalpic contribution ( $\gamma_{pp}$ ) whereas the entropic contribution remains the same.

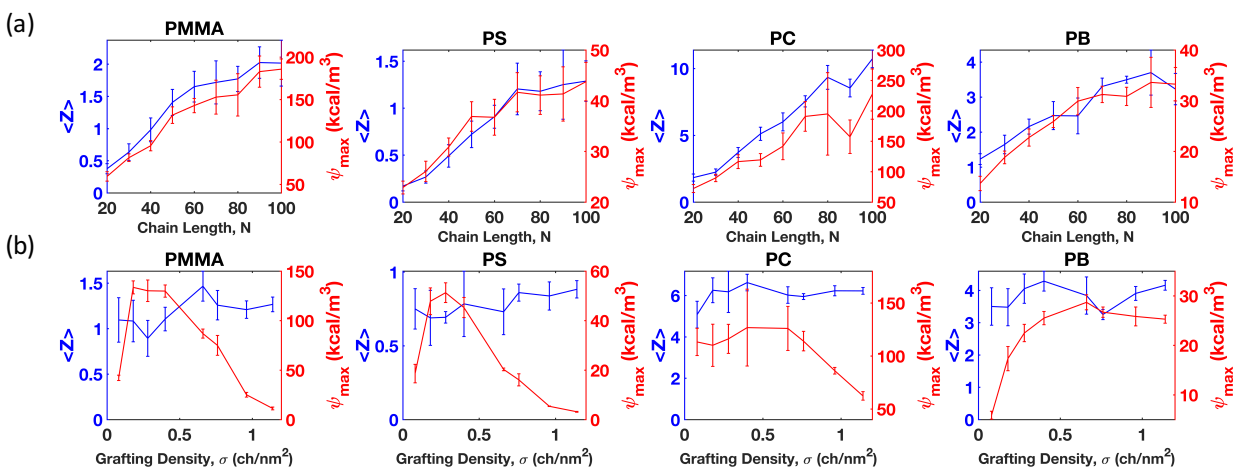


**Figure 6.3-4: Relation between  $\langle Z \rangle$  and  $\psi_{max}$ .** Relation between entanglement per chain ( $\langle Z \rangle$ ) and  $\psi_{max}$  for (a) varying chain lengths and (b) varying grafting densities.  $\langle Z \rangle$  correlates with  $\psi_{max}$  with increasing chain length; however, there is no evident correlation between  $\langle Z \rangle$  and  $\psi_{max}$  when varying grafting density

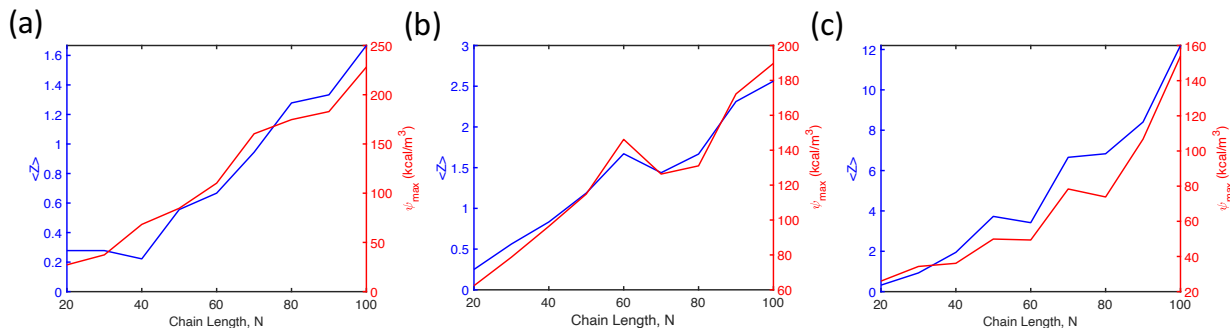


**Figure 6.3-5: Relation between  $\langle Z \rangle$  and  $\psi_{max}$  for varioud grafting densities.** Relation between entanglement per chain ( $\langle Z \rangle$ ) and peak PMF ( $\psi_{max}$ ) at grafting density of (a) 0.18 chains/nm<sup>2</sup>, (b) 0.5 chains/nm<sup>2</sup>, and (c) 0.96 chains/nm<sup>2</sup>.

The polymer grafted surfaces here should be analogous to semi crystalline polymers where polymer chains emerge from adjacent crystal surfaces. There have been several studies that looked at stress-strain curves and stress-transfer mechanisms between crystals with both atomistic and coarse-grained force fields for semi-crystalline polymers such as polyethylene<sup>276</sup>. They have evaluated the strain rate effect and carried out analysis on entanglements using Z1 code, where they show that the bridging entanglements leads to dramatic increase in stress values at a given strain<sup>277, 278</sup>. This observation is similar to what we see in our systems, which strengthens our argument on the importance of entanglements.

In summary, it is evident that increasing the chain length of the polymer increases the entanglements per chain, which in turn increases  $\psi_{max}$ . On the other hand, changing the grafting density affects the cohesive interactions between the polymer chains which in turn affects  $\psi_{max}$ . As  $\psi_{max}$  is directly correlated to the toughness, it is desirable to have longer chains (closer to chain length of 100 in this case which is the maximum of the range we studied) and grafting densities in between 0.2-0.4 chains/nm<sup>2</sup> to maximize the toughness of the nanocomposite. The

peak PMF gives an indication of toughness of the system and we observe that the peak PMF increases with chain length. This has been experimentally and computationally observed before<sup>192, 279, 280</sup>. Even with respect to the grafting density, the decrease in toughness at higher grafting densities has also been observed<sup>192</sup>. Regarding the entanglements, increase in entanglements with higher chain length is also expected from these systems<sup>281</sup>. In summary, we can safely say that the computed trends and conclusions are in line with expected behavior at macroscale, but so far experiments have not focused on direct measurements of the PMFs in these cohesive systems without matrices, making a direct quantitative comparison difficult.

#### 6.4 Functional form of the potential

After understanding the role of chain length and grafting density on  $\psi$ , we proceed to find an analytical equation that can fit all PMF curves and seek to determine a relationship between the physical parameters,  $N$  and  $\sigma^*$ , and the empirical parameters of the equation. Here  $\sigma^* = \frac{f l_m^2}{w * l}$  is the reduced grafting density used as the non-dimensional quantity to describe the equation. Standard interactions such as Lennard-Jones and Mie potentials fail to capture the behavior of the PMF curves as seen from **Figure 6.4-1**. The Lennard Jones potential does not fit our data at all. While the Morse potential has a parameter to control the width of the energy well, it cannot capture the repulsive and the attractive portion simultaneously. Finally, the 4-2 form of the Mie potential, which provides the best fit, still fails to capture the curvature of the attractive portion. The functional forms are shown below. The parameters for the LJ, Morse and Mie are obtained by carrying out regression to fit the data. All the potentials were fit to match the equilibrium distance and peak PMF value.

$$LJ: V(r) = 4\varepsilon \left( \frac{\sigma^{12}}{r} - \frac{\sigma^6}{r} \right), \varepsilon = 180 \frac{kcal}{m^3}, \sigma = 125.1 \text{ \AA}$$

$$Morse: V(r) = D(1 - e^{-\alpha(r-r_0)})^2, D = 168.4 \frac{kcal}{m^3}, \alpha = 0.02, r_0 = 140 \text{ \AA}$$

$$Mie: V(r) = \left( \frac{n}{n-m} \right) \left( \frac{n}{m} \right)^{\frac{m}{n-m}} * \varepsilon \left( \frac{\sigma^n}{r} - \frac{\sigma^m}{r} \right), n = 4, m = 2, \varepsilon = 102.5 \frac{kcal}{m^3}, \sigma = 150.4 \text{ \AA}$$

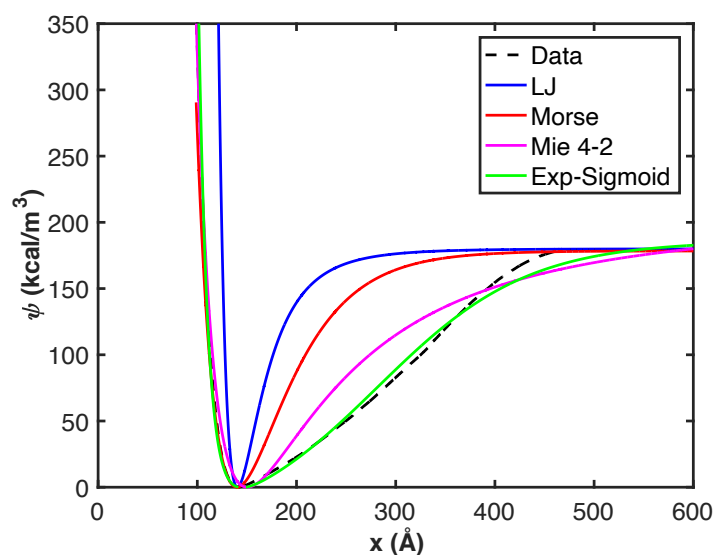


**Figure 6.4-1: Comparison of fitting of the data with different potential forms.** The figure clearly shows that LJ, Morse and Mie potential cannot fit our data accurately.

While a rigorous machine learning approach may provide a perfect fit to the data, an empirical relation that can capture the behavior can accurately provide more information. Our goal in this work is to build an empirical model with reasonable accuracy with constants that can be linked to design parameters, providing insight into the mechanical properties of the system. Hence, we decided to understand the behavior of the attractive and repulsive portion of the PMF separately to develop an empirical function. The repulsive portion of the curve we chose an exponential form shown in Eq 6.4-1. The exponential repulsion term is widely used in molecular simulations, which goes back to the idea of Pauli exclusion principle<sup>282</sup>. When we picked this model, we drew an analogy that can be made between electron clouds and polymer grafts.

$$\psi_r(x) = a_r \times e^{-b_r x} + c_r \quad (6.4-1)$$

where  $a_r$ ,  $b_r$  and  $c_r$  are the empirical constants and  $x$  is the center of mass distance between the plates. The parameters  $a_r$  and  $b_r$  depend on  $N$  and  $\sigma^*$ , and the parameter  $c_r$ , which is a very small number compared to first term, shifts the potential to zero at equilibrium distance. The attractive functional form was chosen on the basis of having to use a general sigmoidal form that goes from the zero energy state to the detached state smoothly and in a tunable fashion as given by Eq. 6.4-2.

$$\psi_a(x) = \frac{a_a}{b_a + e^{-c_a x}} - \frac{a_a}{b_a + e^{-c_a x_0}} \quad (6.4-2)$$

The constants  $a_a$  and  $b_a$  control the plateau of the PMF curve ( $\psi_{max}$ ), whereas  $c_a$  controls the curvature of the curve. The constant  $\frac{a_a}{b_a + e^{-c_a x_0}}$  is added to shift the curves to zero at equilibrium distance ( $x = x_0$ ). We obtain these empirical constants by fitting our data with the above equation. For each polymer chemistry, chain length and grafting density, we run five separate trials to get better statistics. Adding the attractive and repulsive forms gives us the final expression for the effective potential:

$$\psi(x) = a_r \times e^{-b_r x} + \frac{a_a}{b_a + e^{-c_a x}} - \frac{a_a}{b_a + e^{-c_a x_0}} \quad (6.4-3)$$

We note that  $\frac{a_a}{b_a + e^{-c_a x_0}} - c_r \sim \frac{a_a}{b_a + e^{-c_a x_0}}$  as  $c_r$  is negligible. This five-parameter equation describes the interaction between nanoparticles in all different designs of aHNPs. **Figure 6.4-2** shows a representative fit of the function to the data obtained from the simulations along with the residual, which is calculated as the difference between the actual and the fitted value.

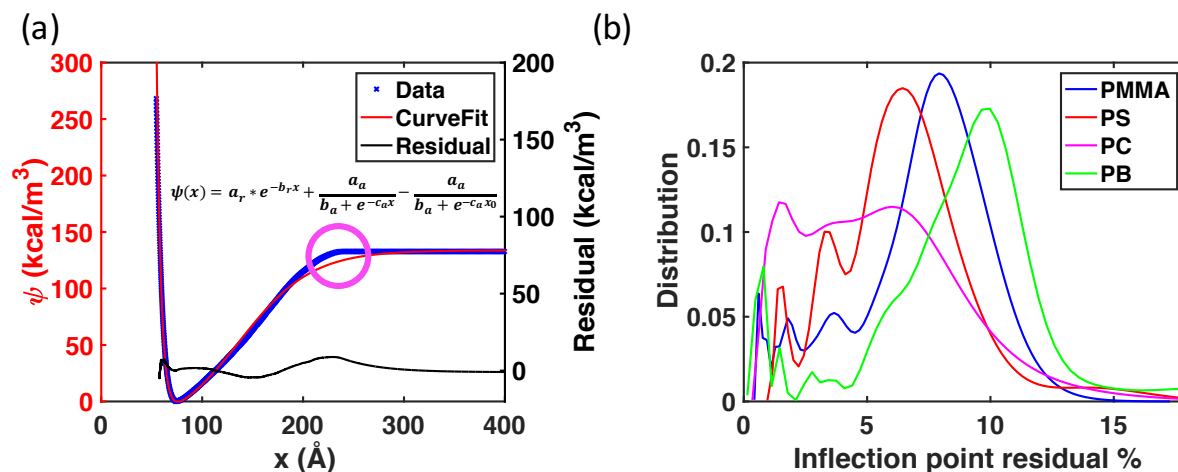


**Figure 6.4-2: Functional form of the potential with residual values.** (a) Fitting the functional form to the PMF data obtained from the CG-MD simulations. The figure shows a representative curve for chain length  $N=50$  and grafting density  $\sigma = 0.5$  chains/nm<sup>2</sup> of the PMMA grafted nanoparticle system. The circle indicates the point where the analytical function shows the highest discrepancy. (b) The distribution of the residual percentage between the data and the fit at the highest discrepancy point for all the curves (5 trials for 9 different chain lengths and 8 different grafting densities for a total of 85 simulations for each chemistry), indicating that on average the error is around 6-10%. The distributions are obtained from a binning of the data points using the *kdensity* function in MATLAB with 100 bins.

The point where the derivative of the potential (given by Eq. 6.4-4) becomes zero is the equilibrium distance between the nanoparticles,  $x_0$ .

$$\psi' = -b_r \times a_r * e^{-b_r x} + \frac{a_a \times c_a \times e^{-c_a x}}{(b_a + e^{-c_a x})^2} \quad (6.4-4)$$

The solution for  $\psi' = 0$  cannot be determined analytically as a general expression for all possible values of the empirical constants. However, since the potential consists of two continuous smooth curves, the derivative can be found numerically for each curve once the empirical constants

are determined from fitting  $\psi$ . The equilibrium distance obtained from the derivative is compared to the equilibrium distance from the simulations and it is observed that the two values are within 2% of each other. This, along with the goodness of fit measures, ensures that the fitting parameters accurately capture the equilibrium position and the shape of the curves.

The functional form of the equation fits the data for all the cases with a total mean square error (MSE) <1%. In **Figure 6.4-2a**, we also show the residual of the fitted values for an example case. The residual is calculated as the difference between the actual value from the simulation and the fitted value. The highest residual is observed at the tail end of the attractive part of the interaction (circled in **Figure 6.4-2a**) for 100% of the 340 cases studied herein. This is due to the sharp transition to zero interaction observed in the simulation when all the chains from the two plates are separated, a feature not captured by the continuous potential employed. Nevertheless, the residual at the highest discrepancy point is below 15% for most of our simulations (as shown in **Figure 6.4-2b** for all 5 trials, 9 different chain lengths, 8 different grafting densities and 4 chemistries), and much lower for any other point of the PMF curve.

## 6.5 Relations between constants and design parameters

Next we evaluate the dependencies of the empirical constants  $a_r$  and  $b_r$  on the design parameters. The repulsive parameters  $a_r$  and  $b_r$  show a negative correlation with  $N$  as seen from the first two panels of **Figure 6.5-1a**. At high enough grafting density, the grafted polymers form a dense corona around the nanoparticle, in the so-called CPB regime (as originally identified for star polymers in the Daoud-Cotton model<sup>46</sup> and discussed recently for polymer grafted nanoparticles in several papers<sup>19, 232, 283</sup> including our previous work<sup>192, 240</sup>). The extent of the CPB regime is identified by the grafting density and nanoparticle radius, and long enough chains will

extend beyond this regime, into the SDPB regime with higher NP-NP interpenetration. As such, the hard-core repulsion observed between NPs for short chains is softened in the case of longer chains (extended in the semi-dilute regime of the NP), leading to the negative correlation between  $a_r$  and  $b_r$  and  $N$ . With respect to  $\sigma^*$ , the value of  $a_r$  increases exponentially due to the increase in steric hindrance induced by closely grafted chains. The polymer chains tethered to different nanoparticles do not have adequate free space to interdigitate, thus increasing the repulsion. The equilibrium distance,  $x_0$ , increases linearly with  $\sigma^*$ , which means the repulsion part of the curve spreads over a greater distance, thus reducing the parameter  $b_r$ . The first two panels of **Figure 6.5-1b** summarize this observation. Considering these dependencies, we can form an equation relating  $a_r$  and  $b_r$  with  $N$  and  $\sigma^*$ :

$$a_r = k_{1ar} \times e^{(-k_{2ar} \times N)} + k_{3ar} \times e^{(k_{4ar} \times \sigma^*)} \quad (6.5-1)$$

$$b_r = \frac{k_{1br}}{N} + \frac{k_{2br}}{\sigma^*} + k_{3br} \quad (6.5-2)$$

The constants of the above equations are summarized in **Table 6.5-1**.

**Table 6.5-1:** Constants of relation between repulsive parameters and  $N$  and  $\sigma^*$ .

Polymer	$k_{1ar}$	$k_{2ar}$	$k_{3ar}$	$k_{4ar}$	$k_{1br}$	$k_{2br}$	$k_{3br}$
PMMA	2.40E8	1.99E-2	2.34E7	1.56E1	1.06E1	5.64E-3	7.97E-2
PS	3.66E7	5.72E-3	6.52E6	2.29E1	8.62E0	4.86E-3	8.08E-2
PC	6.64E2	1.53E-2	4.22E2	2.15E0	9.65E-1	1.963E-2	1.29E-2
PB	1.38E7	1.30E-1	1.72E3	5.36E0	1.39E1	8.76E-3	1.12E-1

The attractive parameters have a different dependence on the design parameters. In the sigmoidal curve, the plateau of the curve ( $\psi_{max}$ ) is mainly dependent on the ratio  $\frac{a_a}{b_a}$  and the curvature of the sigmoid is mainly dependent on  $c_a$ . A higher value of  $c_a$  implies a more gradual

increase in PMF with distance; in other words, the response is softer. We observe that  $\frac{a_a}{b_a}$  vs.  $N$  is linear, as longer chains require a larger amount of work to be separated. However,  $\frac{a_a}{b_a}$  vs.  $\sigma^*$  is quadratic in nature (as a first order approximation), which can be explained with the help of the cohesive interaction energy  $\gamma_{pp}$ . The main correlation between the fit parameters and the cohesive energy is between the ratio  $\frac{a_a}{b_a}$  and  $\gamma_{pp}$ . As both these quantities relate to the toughness or  $\psi_{\max}$  of the systems, there is a direct linear correlation between these two values. For sparsely tethered designs ( $\sigma < 0.4$  chains/nm<sup>2</sup>),  $\gamma_{pp}$  increases with the number of chains; however, in the high grafting density regime ( $\sigma > 0.4$  chains/nm<sup>2</sup>), the polymer chains are grafted close to each other such that they start repelling the other chains due to steric hindrance. Due to this, the interdigitation of the chains decreases, which reduces  $\gamma_{pp}$ . The parameter  $c_a$  is inversely proportional to  $N$ , implying that longer chains provide higher stiffness, thus reducing  $c_a$ . The trend of  $c_a$  vs.  $\sigma^*$  is similar to that of  $\frac{a_a}{b_a}$  vs.  $\sigma^*$ . The last two panels of **Figure 6.5-1a** and **b** show the dependencies of the attractive parameters on  $N$  and  $\sigma^*$  respectively. Based on these trends, we can get the following equations:

$$\frac{a_a}{b_a} = k_{1aa} \times N + k_{2aa} \sigma^{*2} + k_{3aa} \sigma^* + k_{4aa} \quad (6.5-3)$$

$$c_a = \frac{k_{1ca}}{N} + k_{2ca} \sigma^{*2} + k_{3ca} \sigma^* + k_{4ca} \quad (6.5-4)$$

The constants of the above equations are summarized in **Table 6.5-2**. The constant  $b_a$  is equal to 0.025, 0.012, 0.036 and 0.31 for PMMA, PS, PC and PB respectively.

**Table 6.5-2:** Constants of relation between attractive parameters and  $N$  and  $\sigma^*$ 

Polymer	$k_{1aa}$	$k_{2aa}$	$k_{3aa}$	$k_{4aa}$	$k_{1ca}$	$k_{2ca}$	$k_{3ca}$	$k_{4ca}$
PMMA	1.91E0	-5.71E4	3.93E3	1.36E2	1.51E0	9.09E0	-2.76E-1	2.17E-2
PS	2.81E-1	-1.69E4	5.84E2	7.08E1	1.74E0	7.56E0	-6.84E-1	1.48E-2
PC	1.92E0	-3.94E1	5.61E1	1.28E2	4.47E-1	5.09E-5	-3.76E-3	3.73E-3
PB	4.95E-1	-1.32E3	3.86E2	2.13E1	8.85E-1	2.01E-1	-9.11E-3	1.29E-2

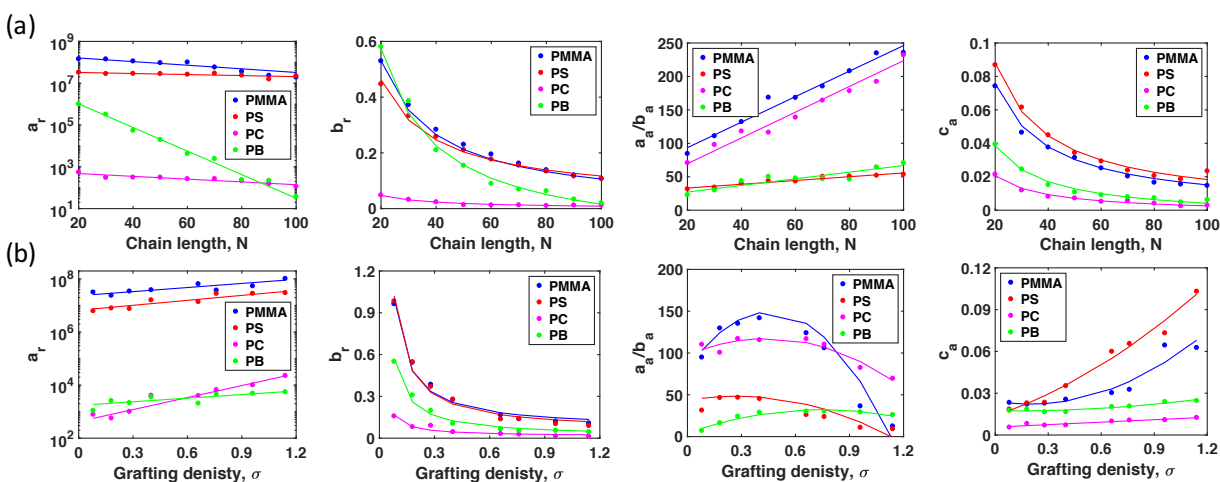


**Figure 6.5-1: Dependencies of the empirical parameters on (a) chain length and (b) grafting density.** The points are the actual values obtained from the fitting the PMF curve to Eq. 6.4-3 and the lines are the fits based on Eq. 6.5-1 to 6.5-4.

In summary, we first fit the PMF curve for each set of the design parameter to obtain the empirical constants. We then relate these empirical constants to the design parameters,  $N$  and  $\sigma^*$ . After developing the relations between the design parameters ( $N$  and  $\sigma^*$ ) and the empirical constants, we now check the estimation of the PMF curve based on the above equations. **Figure 6.5-2** shows the data, the fit, and the estimation based on Eq. 6.5-1 to 6.5-4 along with the residual obtained from the difference between the data and the estimation. As seen from the figure, the

estimation from the equation is very close to the actual PMF curve. We also show the comparison between the actual and estimated values of the equilibrium distance,  $x_0$ , and the peak PMF,  $\psi_{max}$  (Figure 6.5-2b and c). The equilibrium distance and the peak PMF are the two key factors that a potential should capture and our functional form can accurately estimate these values within reasonable range. Representative fits for different chemistries, couple different chain lengths and grafting densities are shown in Figure 6.5-3 and Figure 6.5-4.

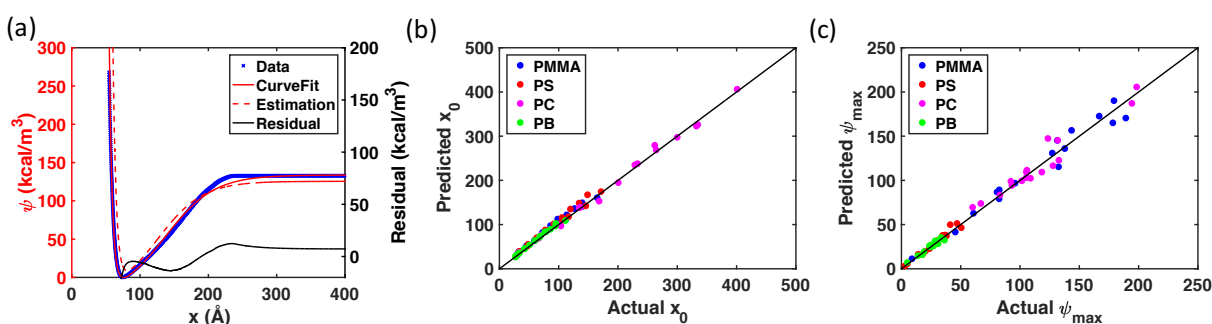


**Figure 6.5-2: Estimated potential from empirical constants along with predicted  $x_0$  and  $\psi_{max}$ .** (a) The figure shows the data, the fit from Eq. 6.4-3, the estimation based on Eq. 6.5-1 to 6.5-4, and the residual for a representative PMMA grafted nanoparticle system with chain length 50 grafting density=0.5 chains/nm<sup>2</sup>. Comparison between the actual and estimated values of (b) equilibrium distance  $x_0$  and (c) peak PMF  $\psi_{max}$ . These figures clearly indicate that the proposed functional form captures these two key metrics describing the interparticle interaction.

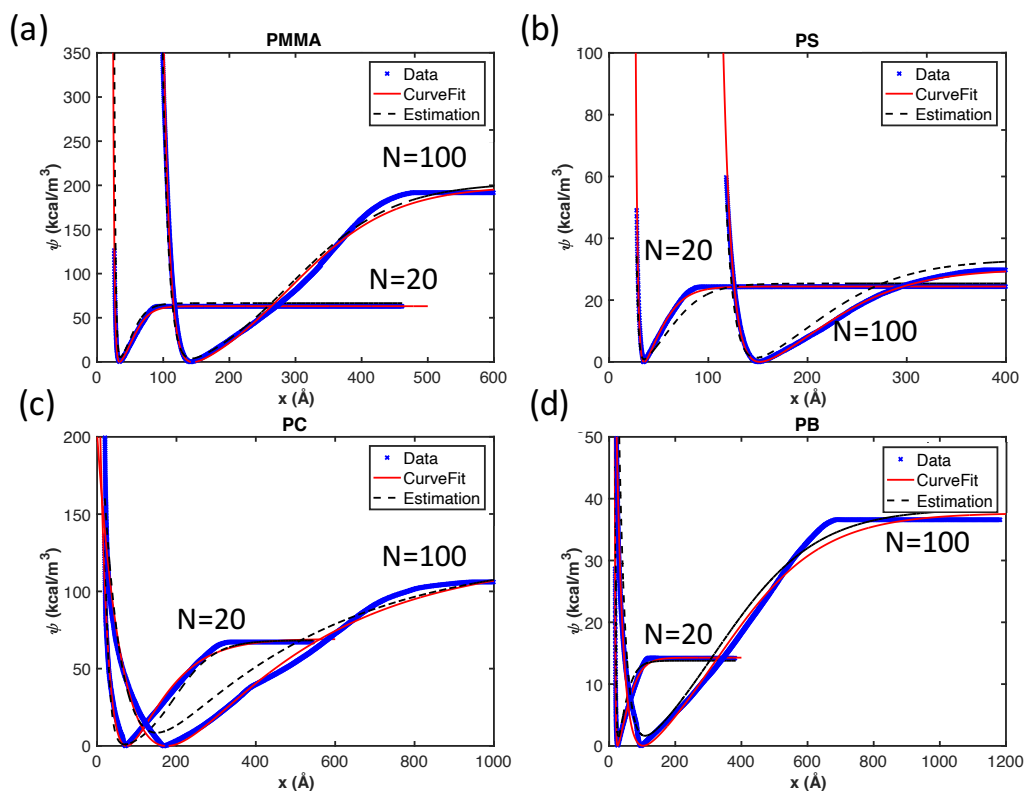


**Figure 6.5-3: Representative PMF curves for each polymer chemistry at different chain lengths.** Representative curve fits along with the estimation from the equation for the constants  $k$ 's (Eq. 6.5-1 to 6.5-4), are shown for (a) PMMA, (b) PS (c) PC and (d) PB grafted nanoparticle system. For each panel, the left curve represents the system with chain length=20 and the right one represents chain length=100. The grafting density in all cases are constant at 0.5 chains/nm<sup>2</sup>.

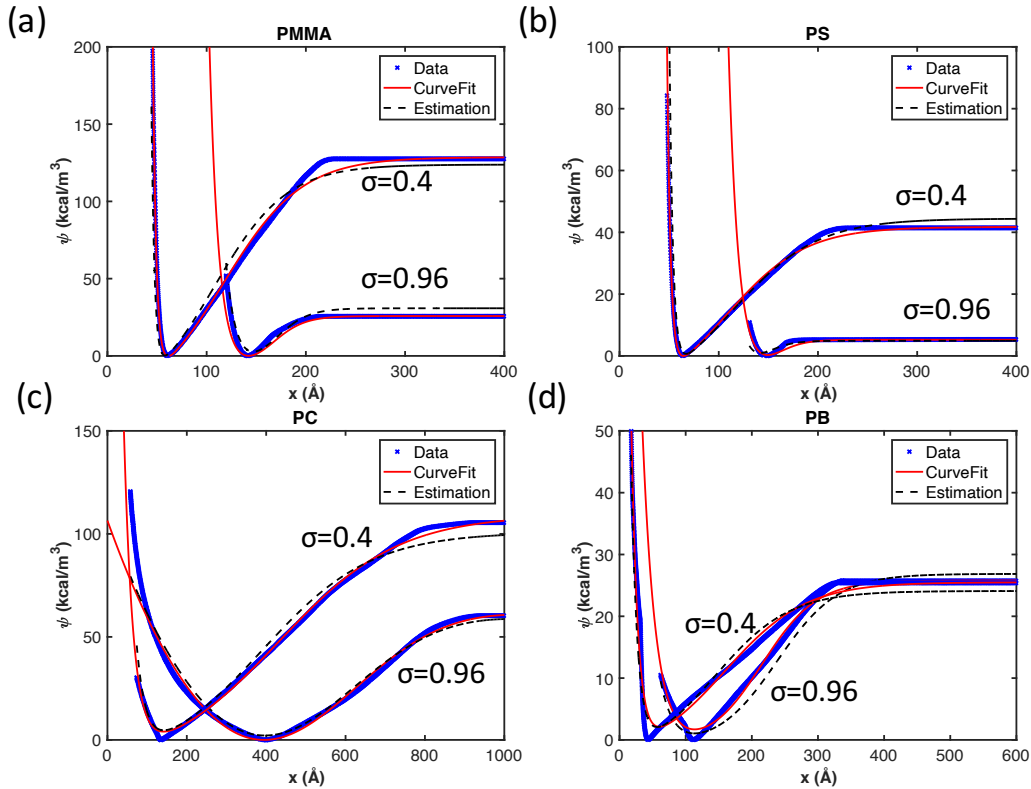


**Figure 6.5-4: Representative PMF curves for each polymer chemistry at different grafting densities.** Representative curve fits along with the estimation from the equation for the constants  $k$ 's (Eq. 6.5-1 to 6.5-4) are shown for (a) PMMA, (b) PS (c) PC and (d) PB grafted nanoparticle system. For each panel, the left curve represents the system with grafting density=0.4 chains/nm<sup>2</sup> and the right one represents grafting density=0.96 chains/nm<sup>2</sup>. The chain length in all cases is constant at 50.

As discussed above,  $\psi_{max}$  can be related to the toughness as it is the total work required to pull the plates apart. On the other hand, using the concept Cauchy-Born approximation<sup>284</sup>, we can convert the PMF curve to a strain energy density function  $\psi(\varepsilon)$ , where  $\varepsilon = \Delta x/x_0$  is the strain.

The double derivative of  $\psi(\varepsilon)$  is shown in Eq 6.5-5,

$$\psi(\varepsilon)'' = a_r b_r^2 e^{-b_r \varepsilon} + a_a \left[ \left( \frac{2c_a e^{-2c_a \varepsilon}}{(b_a + e^{-c_a \varepsilon})^3} \right) - \left( \frac{c_a^2 e^{-c_a \varepsilon}}{(b_a + e^{-c_a \varepsilon})^2} \right) \right] \quad (6.5-5)$$

Evaluating  $\psi(\varepsilon)''$  at  $\varepsilon = 0$  will provide the modulus of the polymer (E):

$$E = a_r b_r^2 + a_a \left[ \left( \frac{2c_a}{b_a^3} \right) - \left( \frac{c_a^2}{b_a^2} \right) \right] \quad (6.5-6)$$

Assuming uniaxial deformations of a network of these particles, we can generate an Ashby<sup>285</sup> plot of modulus vs toughness for different polymers as shown in **Figure 6.5-5**. As expected, PMMA and PS have a high modulus, PC has a high toughness, and PB (being a rubbery material as compared to the other polymers) has low toughness and modulus. The few outliers lying on the bottom right (low modulus and toughness for PMMA and PS) correspond to the lowest grafting density, where the number of chains are too low to contribute towards modulus and toughness. The range of modulus and toughness are comparable to experimental and computational values<sup>192, 280, 286, 287</sup>. We note that the modulus of PC is slightly on the lower end, which we attribute to the confined conformations of the polymer chains. The slightly higher toughness values (compared to experiments) are reasonable considering the large strains attainable in small systems and we observed similar toughness values in our previous work<sup>192</sup>. We also note that the actual value of modulus and toughness of the nanocomposite will depend on microstructure and other factors. However, the constants determined herein effectively capture the trend of material properties with the molecular-scale design variables. Alternatively, running mechanical tests on mesoscopic particle networks will have the additional benefit of illustrating non-affine fracture and failure mechanisms.

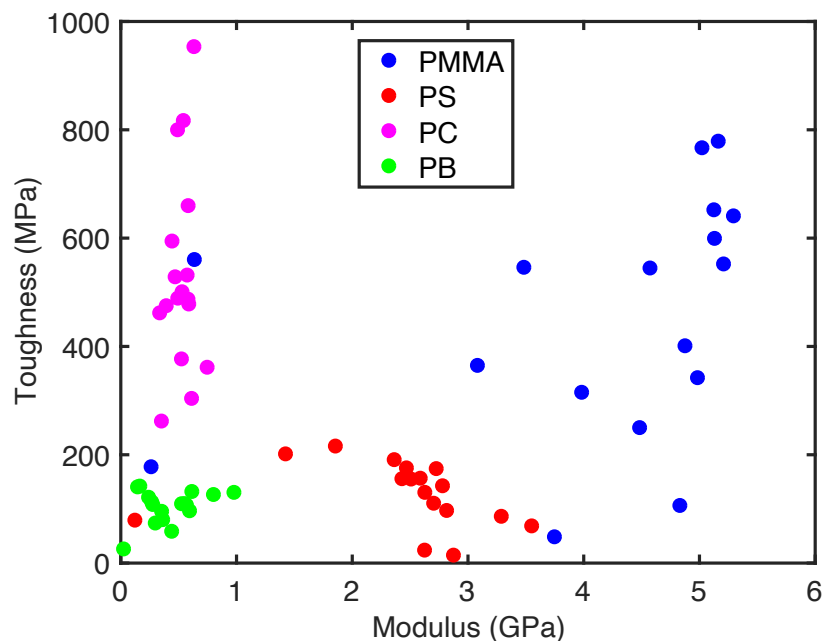


**Figure 6.5-5: Ashby plot of Young's modulus vs toughness for different polymers.**

The trends observed in this work are in line with the macroscale behavior. The peak PMF gives an indication of toughness of the system, and we observe that the peak PMF increases with chain length. This has been experimentally and computationally observed before<sup>192, 279, 280</sup>. Even with respect to the grafting density, a decrease in toughness at higher grafting densities has also been observed.<sup>192</sup> Regarding the entanglements, an increase in entanglements with higher chain length is also expected from these systems<sup>281</sup>. The modulus and toughness measurements are in line with experimental values<sup>280, 286, 287</sup>. Based on this, we can safely say that the computed trends and conclusions are in line with expected behavior at macroscale, but so far experiments have not focused on direct measurements of the PMFs in these cohesive systems without matrices, making a direct quantitative comparison difficult.

## 6.6 Rate dependence

The simulations presented so far are performed at finite pulling velocity,  $v$ . One might argue that proper implementation of this model in mesoscale simulations requires consideration of the rate dependence of PMF ( $\psi$ ) (where the strain rate  $\dot{\epsilon}$  is related to the pulling velocity via  $v = \dot{\epsilon}x_0$ ). To address this, we show the effects of pulling velocity on our results as well as the extraction of the zero-rate limit to be used at equilibrium. Due to the large computational cost of low pulling velocity simulations, we restrict this discussion to a subset of our systems. The approach proposed, however, can readily be applied to any of the systems studied.

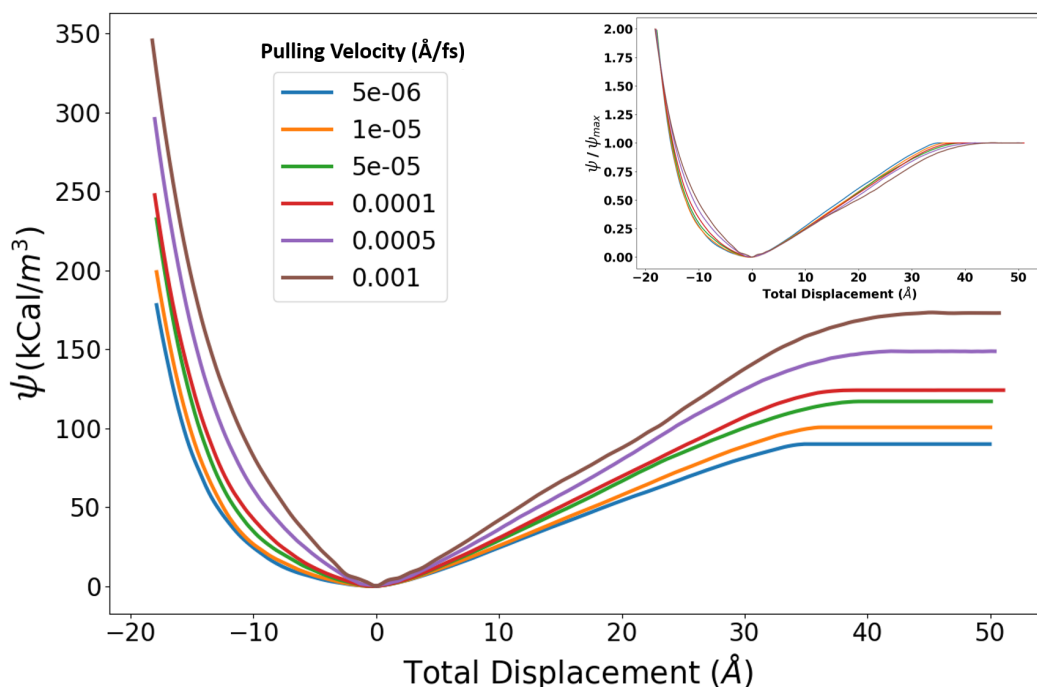


**Figure 6.6-1: Rate dependence of PMF.** PMF as a function of pulling velocity for the system with  $N=50$  and  $\sigma^*=0.05$ . As expected, the amount of work required to separate or compress the plates is higher at increasing pulling velocities. The inset shows that normalization by the PMF plateau in  $\psi_{max}$  produces a reasonable collapse of the curves (especially for lower pulling

velocities, where the concavity around the equilibrium is constant within a few percent, see **Figure 6.6-2**), indicating that capturing the rate-dependent behavior of  $\psi_{max}$  is sufficient to describe the entire PMF curve.

In **Figure 6.6-1** we show the PMF function for PMMA with  $\sigma^*=0.05$  and  $N=50$  as a function of pulling velocity. Aside from small deviations at very high pulling velocities, the curvature of the PMF is unaffected by the pulling velocity and all the curves collapse once normalized by the peak PMF value,  $\psi_{max}$  (**Figure 6.6-1inset**). The dependence of peak PMF on strain rate can be described by the zero-rate limit provided that the local shapes of the PMF curves are generally the same. A quadratic equation  $\psi_{max}(\dot{\epsilon}v) = 0. v5k\dot{\epsilon}^2$  was fit to the concavity around the equilibrium values of the PMF (displacement  $\pm 12$  Å) to evaluate the similarity of their curvatures, represented by the parameter  $k$  in the aforementioned equation. Each PMF curve was normalized by its peak value for ease of comparison. While the fit of the equation does not align perfectly with the data (see **Figure 6.6-2a**), it is sufficient to be used in comparison of the equilibrium PMF curvatures for different simulation parameters. As seen in **Figure 6.6-2b**, it is evident from this analysis that the value of  $k$  tends to slightly increase with faster strain rates, mildly increasing the concavity of the PMF curvature around equilibrium PMF. However, for the pulling velocity lower than what is used to carry out all the analysis (0.00005 Å/fs), the value of  $k$  does not change by more than 4% and the shape of the PMF curves around equilibrium is minimally variant. Thus we use a higher pulling velocity of 0.00005 Å/fs to speed up our simulation while maintaining realistic physics of deformation.

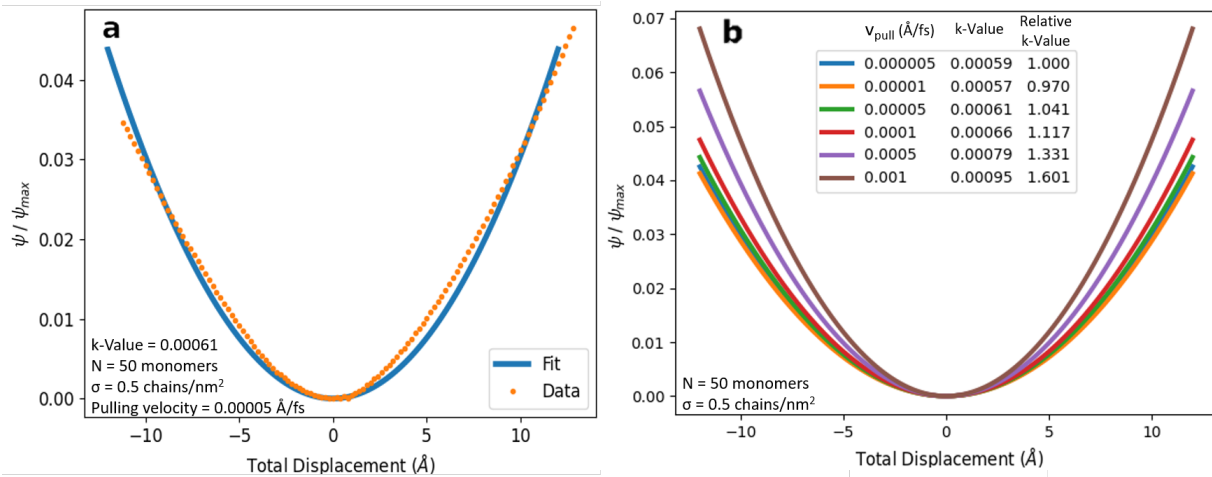


**Figure 6.6-2: Harmonic approximation of PMF around equilibrium position.** Fit of quadratic equation  $\psi_{max}(v\dot{\epsilon}) = 0. v5k\dot{\epsilon}^2$  around minimum  $x_0$  for chain length  $N = 50$  monomers, grafting density  $\sigma = 0.5$  chains/nm<sup>2</sup>, and strain rate  $v = 0.00005$  Å/fs (panel a), as well as comparisons of fits for varying strain rates of chain length  $N = 50$  monomers, grafting density  $\sigma = 0.5$  chains/nm<sup>2</sup> (panel b).

The change in  $\psi_{max}$  is then enough to capture the rate dependence of the effective interaction. In **Figure 6.6-3** we plot  $\psi_{max}$  for PMMA systems at  $\sigma^*=0.05$  and varying  $N$  (panel a), as well as for systems at  $N=50$  and varying  $\sigma^*$  (panel b) as a function of  $v$ , the pulling velocity. From dimensional analysis,  $\psi_{max}$  is related to the stress of the system multiplied by a volume. In our case, the length scale of the system  $x_0$  is unaffected by the pulling velocity, so we can explain the rate dependence of the  $\psi_{max}$  in analogy with flow stress models for viscoelastic materials. We apply here the Cowper-Symonds model<sup>271</sup>, developed to characterize flow stress, but also applicable to other deformation-related pulling velocity effects (like yield stress, elastic modulus, or cumulative strain energy) for a large variety of materials<sup>288-293</sup>. We then arrive at the equation for  $\psi_{max}$ :

$$\psi_{max}(v) = \psi_0 \{1 + (v/v_c)^n\} \quad (6.6-1)$$

where the critical pulling velocity  $v_c$  signals the onset of non-Newtonian behavior, before which (for  $(v/v_c) \ll 1$ ) the dependence on the pulling velocity is negligible. The power-law exponent  $n$  describes the deviation from the Newtonian behavior in the high pulling velocity regime, where  $(v/v_c) \gg 1$ , and  $\psi_0$  is the zero-rate limit of the peak PMF.  $v_c$  and  $n$  are typically material dependent constants. The curves in **Figure 6.6-3** are fits of Eq. 6.6-1 to our data. To validate the use of  $\psi_0$  to describe the rate dependence of peak PMF, we fit the quadratic equation  $\psi_{max}(v) = 0.5kv^2$  around the minimum  $x_0$  (within  $3\text{\AA}$ ) and evaluated the difference in the parameter  $k$  among the values of  $v$ .  $k$  showed little variation between the pulling velocities, indicating that it is reasonable to use the zero-rate limit of the peak PMF to describe its rate dependence.

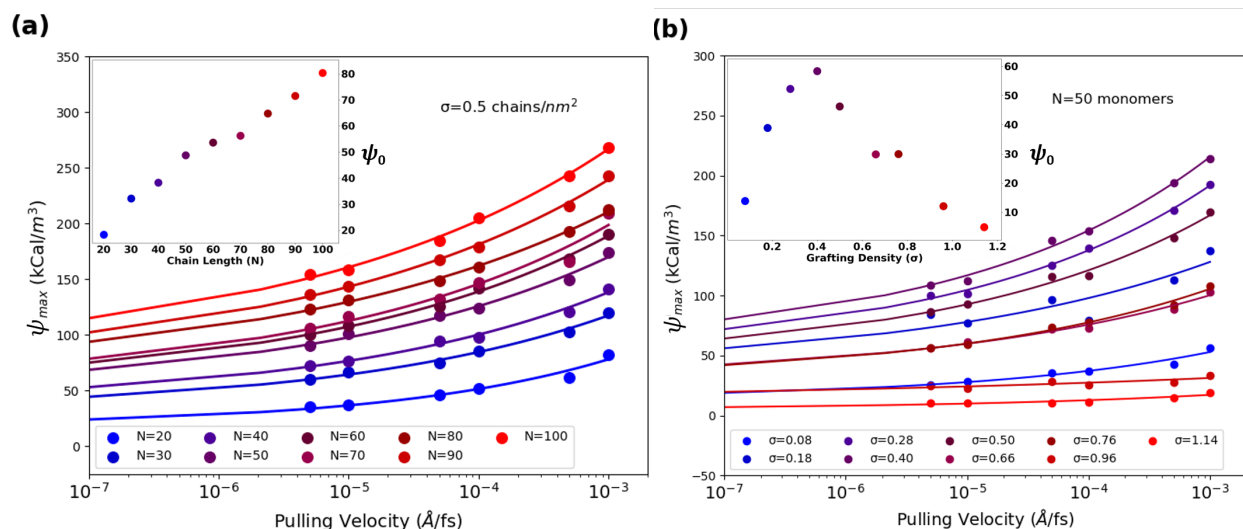


**Figure 6.6-3: Rate dependence of  $\psi_{max}$ .** Rate dependence of the PMF plateau  $\psi_{max}$  for systems with varying  $N$  (panel a) or  $\sigma^*$  (panel b). The Cowper-Symonds model<sup>271</sup> correctly fits our data (see Eq. 6.6-1) and we can extract the zero-rate limit  $\psi_0$ . The insets show the corresponding values

of  $\psi_0$ , with a linear dependence on  $N$  and a bell-shaped dependence on  $\sigma^*$ , similarly to what observed at finite strain-rate in **Figure 6.5-1b**.

We find that  $v_c$  does not have a strong dependence on  $N$  and  $\sigma^*$  in our systems, and we can fix it to  $v_c = 1e-5$ , removing one free parameter. This value we find empirically corresponds to strain rates  $\dot{\epsilon} = v/x_0$  on the order of  $10^8 \text{ s}^{-1}$ , in line with the inverse of the segmental relaxation times we expect for our PMMA model at  $T=300\text{K}$ <sup>294</sup>.  $n$  appears to be independent of  $\sigma^*$ , so it can be fixed to an average value of  $n=0.2$  (in **Figure 6.6-3b**) which is consistently within the range of  $n$  between 0.1 and 0.3 reported in simulation and experimental studies of many different materials<sup>288-293</sup>. We observe a slight decrease of  $n$  with increasing chain length  $N$ , from around 0.25 for  $N=20$  to 0.18 for  $N=100$ . Our chains are always below the entanglement regime, where the rate dependence is dominated by the segmental dynamics relaxation<sup>295</sup>, which is not strongly affected by molecular weight. As such, we would not expect this effect in free polymer chains of varying length, and attribute it here to the fact that dynamics of shorter chains are more strongly affected by their grafted extremities. Regardless, the explanation of the dependence of  $n$  on  $N$  is beyond the scope of this work, and we allow  $n$  to vary (**Figure 6.6-3a**). Following this procedure, we can extract the values of  $\psi_0$  for each system (see **Figure 6.6-3** insets), which can then be used in our analytical formulation for the equilibrium potentials. We also note that  $\psi_0$  has a linear dependence on  $N$  and a bell-shaped dependence on  $\sigma^*$ , similar to what is observed at finite pulling velocity (**Figure 6.5-1**). The method outlined here to extrapolate the zero-rate limit of the PMF curve will allow us to use our model in the future for larger, mesoscale simulations both in equilibrium and under deformation.

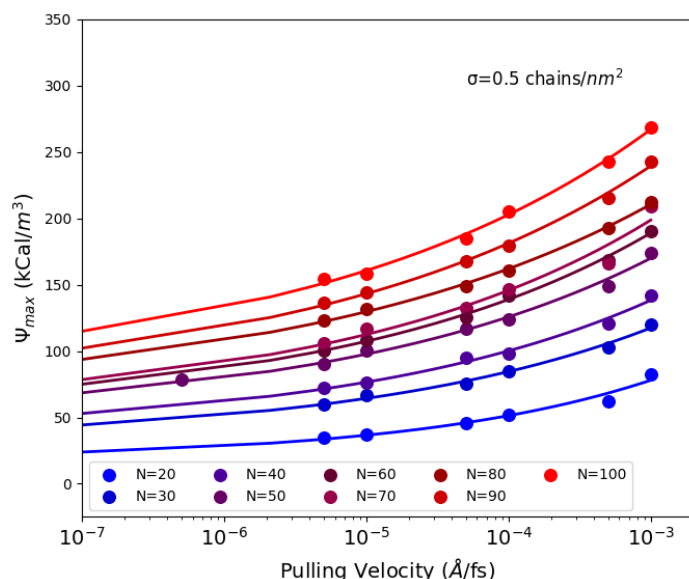


**Figure 6.6-4: Validation of extrapolation to zero rate.** An additional data point at pulling velocity  $5e-7$  Å/fs (which needed 200h to simulate) is placed on top of **Figure 6.6-3a**, which shows the predictive ability of the fit when extrapolating at lower velocities.

While the fit we obtained in **Figure 6.6-3** is able to capture the rate-dependence of all our measured PMFs, extrapolating to the equilibrium, zero-rate case might suffer from errors introduced by extending the fit across several orders of magnitude. While it is impossible to validate our extrapolation for our system at equilibrium since we are below the  $T_g$  of the system, we show in **Figure 6.6-4** that an additional simulation performed for the system with  $\sigma=0.5$ ,  $N=50$  at pulling velocity of  $5e-7$  (one order of magnitude lower than the rest of the simulations) has a measured peak PMF consistent with what predicted by our fit. An extrapolation several orders of magnitude beyond our measured data points should be taken with caution.

## 6.7 Conclusion

In conclusion, we used our chemistry specific CG polymeric models to carry out tensile/compressive CG-MD simulations of polymer grafted nanoparticles. We show that increasing the chain length increases the entanglement per chain, which in turn increases  $\psi_{max}$ . The grafting density affects the interaction energy between the polymer chains grafted to different nanoparticles. We evaluate the potential of mean force by pulling/pushing the plates from their equilibrium position and find that the repulsive part of the potential can be described by an exponential equation and the attractive part can be described by a sigmoid function. Finally, the PMF curves of all polymer chemistries, chain lengths and grafting densities follow a universal expression that can be used to describe the interaction between polymer grafted nanoparticles. The residual analysis revealed that our model can capture most of the PMF curve accurately, barring the tail end of the attractive portion (still less than 15%), which is due to the sudden transition arising from chains separating out completely. In addition, we show how to extrapolate the quasi-static limit of our results from the rate dependence of the PMF curves. The results presented in this paper are obtained in the limit of two interacting particles with size much larger than the scales of the polymer chains, having in mind large high-aspect ratio particles like CNC grafted nanoparticles.<sup>206</sup> Future investigations should examine the validity of the functional form under different loading conditions such as shear, while also ascertaining its applicability to other nanoparticle shapes such as spheres where many-body effects may become significant.. This effective potential can be used to simulate large scale aHNP films without having to explicitly model the grafted polymer chains, while still preserving structural design variables and polymer chemistry. Despite limiting our study to homopolymers here, the same protocol can be applied to

more complex architectures with branched polymers, block copolymers and polydisperse systems, all of which are of interest in novel functional composites. The spatiotemporal extent of the simulations can be increased multifold with the help of this potential. Eliminating the need to explicitly simulate the polymer beads reduces the number of particles in the simulation by more than five orders of magnitude as compared to all atomistic models. With a conservative scaling of  $O(n \log(n))$  for MD simulations, a speedup of 6-7 orders of magnitude can be obtained from these mesoscale models. This study sets the stage to accelerate the design of aHNP thin films by enabling the prediction of macroscale size dependent properties.

## Chapter 7: Conclusion

Throughout this dissertation, I have presented computational techniques that accelerate the material by design process. We started out with the development of the energy renormalization approach to develop coarse-grain models, which is explained in Chapter 3:. These CG models provide a speedup of 2-3 orders of magnitude as compared to all-atomistic (AA) simulations. This method can capture the dynamics accurately over a wide range of temperature and it requires only a picosecond time scale measure, Debye-Waller factor, for calibration. We show the versatility of this approach by developing CG models for different kinds of materials: a small molecule, a polymer and an epoxy resin.

Next, in Chapter 4:, we developed a computational materials-by-design framework combining MD simulations with machine learning to optimize the design of aHNPs. Leveraging the computationally inexpensive metamodel, we explore the entire design space by sampling with a million “pseudo-CG” simulations to reveal the Pareto frontier. Our prediction suggests that at least 60% nanoparticle by weight is required and that the polymer chain length has to be above the critical chain length to achieve the optimal nanocomposite designs. This metamodel based design approach provides a speedup of 6-7 orders of magnitude as compared to AA simulations.

Chapter 5: focuses on analysis of the polymer chain conformations in these aHNPs, deriving an equation for critical chain length that governs the conformational transition from concentrated polymer brush regime to semi dilute polymer brush regime. We verify these scaling laws for polymers with different chemistries, persistence lengths and side-group sizes. We developed a universal scaling law that governs the positions of the monomers along the chain.

Finally, in Chapter 6:, we developed a mesoscopic model framework to model effective interaction between nanoparticles based on potential of mean force (PMF). We obtain an analytical functional form for the interaction which proves to be universal for different polymers. This meso-scale approach eliminates the need to model the polymer chain explicitly, thus improving the computational efficiency and extending the spatiotemporal scales of MD simulations to experimental level.

## 7.1 Future outlook

This thesis sets a foundation to further extend the computational approaches developed to much more complicated material systems. The energy renormalization approach towards developing coarse-grained (CG) models can be further extended to complicated polymeric systems such as branched polymers, copolymers, bottle brushes etc. Our group has already extended this ER approach to a biomimetic copolymer<sup>296</sup>. Current CG approaches for bottle brushes involves use of generic bead-spring models<sup>297, 298</sup>. Chemistry specific ER based CG models for bottle brushes will definitely help in exploring the intricate molecular mechanisms in complex bottle-brush structures. Moreover, we have demonstrated an effective use of machine learning (ML) algorithms to facilitate the CG parameterization for crosslinked epoxy resins. Recently published papers show that the current trend is to use ML algorithms to develop CG models for highly complicated polymeric systems<sup>299-301</sup>.

While we chose aHNPs as a model material to demonstrate metamodel based design optimization, the computational frameworks developed in this dissertation can be applied to any material. The combination of machine learning with molecular dynamics has led to quick optimization of the mechanical properties. This concept can be further extended to study other

properties such as glass transition ( $T_g$ ), ballistic properties and fracture energies. The inputs for the metamodel can be extended to include parameters such as temperature, polydispersity etc. Efficient metamodels can be trained to capture the complex input output relationships which will enhance the characterization of material properties. The scaling laws governing chain conformations can be extended to complex polymer architectures.

Currently, the PMF based approach towards developing a meso-scale model is applicable for plate like nanoparticle such graphene platelets. However, this concept can be further extended to incorporate the effect of nanoparticle curvature. Specifically, the PMFs arising from spherical nanoparticles is of particular interest as there are range of studies that have focused on aHNPs based on spherical nanoparticles<sup>29, 30, 36, 40</sup>. Developing meso-scale models with spherical nanoparticles will allow us to simulate experimental size thin films of these hairy nanoparticle assemblies which can then be used to study macroscale properties such as fracture and ballistic properties.

The computational tools developed in this dissertation complements the traditional experiments, reducing the iterative characterization loops required to optimize the properties and thus accelerating the materials design process.

## REFERENCES

1. Materials Genome Initiative for Global Competitiveness. **2011**.
2. Fang Ren, L. W., Travis Williams, Kevin J. Laws, Christopher Wolverton, Jason Hattrick-Simpers, Apurva Mehta, Accelerated discovery of metallic glasses through iteration of machine learning and high-throughput experiments. *Science Advances* **2018**, *4*, 1-11.
3. Tjong, S. C., Structural and mechanical properties of polymer nanocomposites. *Materials Science and Engineering: R: Reports* **2006**, *53* (3-4), 73-197.
4. Anna C. Balazs, T. E., Thomas P. Russell, Nanoparticle Polymer Composites: Where Two Small Worlds Meet. *Science* **2006**, *314* (17).
5. Potts, J. R.; Dreyer, D. R.; Bielawski, C. W.; Ruoff, R. S., Graphene-based polymer nanocomposites. *Polymer* **2011**, *52* (1), 5-25.
6. Hussain, F.; Hojjati, M.; Okamoto, M.; Gorga, R. E., Review article: Polymer-matrix Nanocomposites, Processing, Manufacturing, and Application: An Overview. *Journal of Composite Materials* **2006**, *40* (17), 1511-1575.
7. Winey, K. I.; Vaia, R. A., Polymer Nanocomposites. *MRS Bulletin* **2011**, *32* (4), 314-322.
8. Coleman, J. N.; Khan, U.; Blau, W. J.; Gun'ko, Y. K., Small but strong: A review of the mechanical properties of carbon nanotube-polymer composites. *Carbon* **2006**, *44* (9), 1624-1652.
9. Caseri, W. R., Nanocomposites of polymers and inorganic particles: preparation, structure and properties. *Materials Science and Technology* **2013**, *22* (7), 807-817.
10. Mohammad Moniruzzaman, K. W., Polymer Nanocomposites Containing Carbon Nanotubes. *Macromolecules* **2006**, *36*, 5194-5205.
11. Wright, W. W., Polymers in Aerospace Applications. *Materials & Design* **1991**, *12* (4), 222-227.
12. Moliton, A.; Hiorns, R. C., Review of electronic and optical properties of semiconducting  $\pi$ -conjugated polymers: applications in optoelectronics. *Polymer International* **2004**, *53* (10), 1397-1412.
13. Hou, W.; Xiao, Y.; Han, G.; Lin, J. Y., The Applications of Polymers in Solar Cells: A Review. *Polymers (Basel)* **2019**, *11* (1).
14. Jones, D., *Pharmaceutical Applications of Polymers for Drug Delivery*. Rapra Technology: 2004; Vol. 15.
15. Martina, M.; Hutmacher, D. W., Biodegradable polymers applied in tissue engineering research: a review. *Polymer International* **2007**, *56* (2), 145-157.
16. Jouault, N.; Lee, D.; Zhao, D.; Kumar, S. K., Block-copolymer-mediated nanoparticle dispersion and assembly in polymer nanocomposites. *Adv Mater* **2014**, *26* (24), 4031-6.
17. Jancar, J.; Douglas, J. F.; Starr, F. W.; Kumar, S. K.; Cassagnau, P.; Lesser, A. J.; Sternstein, S. S.; Buehler, M. J., Current issues in research on structure-property relationships in polymer nanocomposites. *Polymer* **2010**, *51* (15), 3321-3343.
18. Guerrini, L.; Alvarez-Puebla, R. A.; Pazos-Perez, N., Surface Modifications of Nanoparticles for Stability in Biological Fluids. *Materials (Basel)* **2018**, *11* (7).

19. Kumar, S. K.; Jouault, N.; Benicewicz, B.; Neely, T., Nanocomposites with Polymer Grafted Nanoparticles. *Macromolecules* **2013**, *46* (9), 3199-3214.
20. Akcora, P.; Liu, H.; Kumar, S. K.; Moll, J.; Li, Y.; Benicewicz, B. C.; Schadler, L. S.; Acehan, D.; Panagiotopoulos, A. Z.; Pryamitsyn, V.; Ganesan, V.; Ilavsky, J.; Thiyagarajan, P.; Colby, R. H.; Douglas, J. F., Anisotropic self-assembly of spherical polymer-grafted nanoparticles. *Nat Mater* **2009**, *8* (4), 354-9.
21. Krishnamoorti, R., Strategies for Dispersing Nanoparticles in Polymers. *MRS Bulletin* **2011**, *32* (4), 341-347.
22. Chevigny, C.; Dalmas, F.; Di Cola, E.; Gimes, D.; Bertin, D.; Boué, F. o.; Jestin, J., Polymer-Grafted-Nanoparticles Nanocomposites: Dispersion, Grafted Chain Conformation, and Rheological Behavior. *Macromolecules* **2011**, *44* (1), 122-133.
23. Grabowski, C. A.; Koerner, H.; Meth, J. S.; Dang, A.; Hui, C. M.; Matyjaszewski, K.; Bockstaller, M. R.; Durstock, M. F.; Vaia, R. A., Performance of dielectric nanocomposites: matrix-free, hairy nanoparticle assemblies and amorphous polymer-nanoparticle blends. *ACS Appl Mater Interfaces* **2014**, *6* (23), 21500-9.
24. Koerner, H.; Drummy, L. F.; Benicewicz, B.; Li, Y.; Vaia, R. A., Nonisotropic Self-Organization of Single-Component Hairy Nanoparticle Assemblies. *ACS Macro Letters* **2013**, *2* (8), 670-676.
25. Maillard, D.; Kumar, S. K.; Fragneaud, B.; Kysar, J. W.; Rungta, A.; Benicewicz, B. C.; Deng, H.; Brinson, L. C.; Douglas, J. F., Mechanical properties of thin glassy polymer films filled with spherical polymer-grafted nanoparticles. *Nano Lett* **2012**, *12* (8), 3909-14.
26. Ye, X.; Zhu, C.; Ercius, P.; Raja, S. N.; He, B.; Jones, M. R.; Hauwiller, M. R.; Liu, Y.; Xu, T.; Alivisatos, A. P., Structural diversity in binary superlattices self-assembled from polymer-grafted nanocrystals. *Nat Commun* **2015**, *6*, 10052.
27. Fernandes, N. J.; Koerner, H.; Giannelis, E. P.; Vaia, R. A., Hairy nanoparticle assemblies as one-component functional polymer nanocomposites: opportunities and challenges. *MRS Communications* **2013**, *3* (1), 13-29.
28. Gu, X. W.; Ye, X.; Koshy, D. M.; Vachhani, S.; Hosemann, P.; Alivisatos, A. P., Tolerance to structural disorder and tunable mechanical behavior in self-assembled superlattices of polymer-grafted nanocrystals. *Proc Natl Acad Sci U S A* **2017**, *114* (11), 2836-2841.
29. Choi, J.; Hui, C. M.; Pietrasik, J.; Dong, H.; Matyjaszewski, K.; Bockstaller, M. R., Toughening fragile matter: mechanical properties of particle solids assembled from polymer-grafted hybrid particles synthesized by ATRP. *Soft Matter* **2012**, *8* (15).
30. Schmitt, M.; Choi, J.; Hui, C. M.; Chen, B.; Korkmaz, E.; Yan, J.; Margel, S.; Ozdoganlar, O. B.; Matyjaszewski, K.; Bockstaller, M. R., Processing fragile matter: effect of polymer graft modification on the mechanical properties and processibility of (nano-) particulate solids. *Soft Matter* **2016**, *12* (15), 3527-37.
31. Nobuyuki Sakai, G. K. P., Yasuo Ebina, Kazunori Takada, and Takayoshi Sasaki, Layer-by-Layer Assembled TiO<sub>2</sub> Nanoparticle/ PEDOT-PSS Composite Films for Switching of Electric Conductivity in Response to Ultraviolet and Visible Light. *Chem Matter* **2006**, *18*, 3596-3598.

32. Mauter, M. S.; Wang, Y.; Okemgbo, K. C.; Osuji, C. O.; Giannelis, E. P.; Elimelech, M., Antifouling ultrafiltration membranes via post-fabrication grafting of biocidal nanomaterials. *ACS Appl Mater Interfaces* **2011**, *3* (8), 2861-8.
33. Zhang, J.; Li, Q.; Di, X.; Liu, Z.; Xu, G., Layer-by-layer assembly of multicolored semiconductor quantum dots towards efficient blue, green, red and full color optical films. *Nanotechnology* **2008**, *19* (43), 435606.
34. Labastide, J. A.; Baghgar, M.; Dujovne, I.; Yang, Y.; Dinsmore, A. D.; G. Sumpter, B.; Venkataraman, D.; Barnes, M. D., Polymer Nanoparticle Superlattices for Organic Photovoltaic Applications. *The Journal of Physical Chemistry Letters* **2011**, *2* (24), 3085-3091.
35. Youngjune Park, J. D., Kun-Yi Andrew Lin and Ah-Hyung Alissa Park, Investigation of CO<sub>2</sub> capture mechanisms of liquid-like nanoparticle organic hybrid materials via structural characterization. *Phys Chem Chem Phys* **2011**, *40*, 18115-18122
36. Midya, J.; Cang, Y.; Egorov, S. A.; Matyjaszewski, K.; Bockstaller, M. R.; Nikoubashman, A.; Fytas, G., Disentangling the Role of Chain Conformation on the Mechanics of Polymer Tethered Particle Materials. *Nano Lett* **2019**, *19* (4), 2715-2722.
37. Agrawal, A.; Yu, H.-Y.; Sagar, A.; Choudhury, S.; Archer, L. A., Molecular Origins of Temperature-Induced Jamming in Self-Suspended Hairy Nanoparticles. *Macromolecules* **2016**, *49* (22), 8738-8747.
38. Kim, S. A.; Mangal, R.; Archer, L. A., Relaxation Dynamics of Nanoparticle-Tethered Polymer Chains. *Macromolecules* **2015**, *48* (17), 6280-6293.
39. Lafitte, T.; Kumar, S. K.; Panagiotopoulos, A. Z., Self-assembly of polymer-grafted nanoparticles in thin films. *Soft Matter* **2014**, *10* (5), 786-94.
40. Asai, M.; Zhao, D.; Kumar, S. K., Role of Grafting Mechanism on the Polymer Coverage and Self-Assembly of Hairy Nanoparticles. *ACS Nano* **2017**, *11* (7), 7028-7035.
41. Glotzer, S. C.; Paul, W., Molecular and Mesoscale Simulation Methods for Polymer Materials. *Annual Review of Materials Research* **2002**, *32* (1), 401-436.
42. Nguyen, T. D.; Zhang, Z.; Glotzer, S. C., Molecular simulation study of self-assembly of tethered V-shaped nanoparticles. *J Chem Phys* **2008**, *129* (24), 244903.
43. Staszewski, T., Structural Changes in Hairy Nanoparticles—Insights from Molecular Simulations. *The Journal of Physical Chemistry C* **2020**, *124* (49), 27118-27129.
44. Borowko, M.; Sokolowski, S.; Staszewski, T.; Pizio, O., Adsorption of hairy particles with mobile ligands: Molecular dynamics and density functional study. *J Chem Phys* **2018**, *148* (4), 044705.
45. Chen, G.; Li, H.; Das, S., Scaling Relationships for Spherical Polymer Brushes Revisited. *J Phys Chem B* **2016**, *120* (23), 5272-7.
46. Daoud, M.; Cotton, J. P., Star shaped polymers : a model for the conformation and its concentration dependence. *Journal de Physique* **1982**, *43* (3), 531-538.
47. Kohji Ohno, T. M., Satoshi Takeno, Yoshinobu Tsujii, and Takeshi Fukuda, Suspensions of Silica Particles Grafted with Concentrated Polymer Brush A New Family of Colloidal Crystals. *Macromolecules* **2006**, *39*, 1245-1249.
48. Alder, B. J.; Wainwright, T. E., Studies in Molecular Dynamics. I. General Method. *The Journal of Chemical Physics* **1959**, *31* (2), 459-466.

49. Rahman, A., Correlations in the Motion of Atoms in Liquid Argon. *Physical Review* **1964**, *136* (2A), A405-A411.
50. Rapaport, D. C., Molecular dynamics simulation of polymer chains with excluded volume. *J. Phys A* **1978**, *11* (8), 213-217.
51. Gotlib, Y. Y.; Balabaev, N. K.; Darinskii, A. A.; Neelov, I. M., Investigation of Local Motions in Polymers by the Method of Molecular Dynamics. *Macromolecules* **1980**, *13* (3), 602-608.
52. Rapaport, D. C., Molecular dynamics study of a polymer chain in solution. *The Journal of Chemical Physics* **1979**, *71* (8), 3299-3303.
53. Bernard R. Brooks, R. E. B., Barry D. Olafson, David J. States, S. Swaminathan, Martin Karplus, CHARMM: A Program for Macromolecular Energy, Minimization and Dynamics Calculations. *Journal of Computational Chemistry* **1983**, *4* (2), 187-217.
54. Verlet, L., Computer "Experiments" on Classical Fluids. I. Thermodynamical Properties of Lennard-Jones Molecules. *Physical Review* **1967**, *159* (1), 98-103.
55. William L. Jorgensen, D. S. M., Julian Tirado-Rives, Development and Testing of the OPLS All-Atom Force Field on Conformational Energetics and Properties of Organic Liquids. *Journal of American Chemical Society* **1996**, *118*, 11225-11236.
56. David A. Pearlman, D. A. C., James W. Caldwell, Wilson S. Ross, Thomas E. Cheatham III, Steve De Bolt, David Ferguson, George Seibel, Peter Kollman, AMBER, a package of computer programs for applying molecular mechanics, normal mode analysis, molecular dynamics and free energy calculations to simulate the structural and energetic properties of molecules. *Computer Physics Communications* **1995**, *91* (1-3), 1-41.
57. Oostenbrink, C.; Villa, A.; Mark, A. E.; van Gunsteren, W. F., A biomolecular force field based on the free enthalpy of hydration and solvation: the GROMOS force-field parameter sets 53A5 and 53A6. *J Comput Chem* **2004**, *25* (13), 1656-76.
58. Plimpton, S., Fast Parallel Algorithms for Short-Range Molecular Dynamics. *Journal of Computational Physics* **1995**, *117*, 1-19.
59. Phillips, J. C.; Braun, R.; Wang, W.; Gumbart, J.; Tajkhorshid, E.; Villa, E.; Chipot, C.; Skeel, R. D.; Kale, L.; Schulten, K., Scalable molecular dynamics with NAMD. *J Comput Chem* **2005**, *26* (16), 1781-802.
60. H.J.C. Berendsen, D. v. d. S., R. van Drunen, GROMACS: A message-passing parallel molecular dynamics implementation. *Computer Physics Communications* **1995**, *91*, 43-56.
61. Jung, J.; Nishima, W.; Daniels, M.; Bascom, G.; Kobayashi, C.; Adedoyin, A.; Wall, M.; Lappala, A.; Phillips, D.; Fischer, W.; Tung, C. S.; Schlick, T.; Sugita, Y.; Sanbonmatsu, K. Y., Scaling molecular dynamics beyond 100,000 processor cores for large-scale biophysical simulations. *J Comput Chem* **2019**, *40* (21), 1919-1930.
62. S. Izrailev, S. S., B. Isralewitz, D. Kosztin, H. Lu, F. Molnar, W. Wriggers, and K. Schulten, Steered Molecular Dynamics. *Computational Molecular Dynamics: Challenges, Methods, Ideas* **1998**, *4*, 39-65.
63. Faghijnejad, A.; Feldman, K. E.; Yu, J.; Tirrell, M. V.; Israelachvili, J. N.; Hawker, C. J.; Kramer, E. J.; Zeng, H., Adhesion and Surface Interactions of a Self-Healing Polymer with Multiple Hydrogen-Bonding Groups. *Advanced Functional Materials* **2014**, *24* (16), 2322-2333.

64. Zeng, H.; Huang, J.; Tian, Y.; Li, L.; Tirrell, M. V.; Israelachvili, J. N., Adhesion and Detachment Mechanisms between Polymer and Solid Substrate Surfaces: Using Polystyrene–Mica as a Model System. *Macromolecules* **2016**, *49* (14), 5223-5231.
65. B. Cappella, G. D., Force-distance curves by atomic force microscopy. *Surface Science Reports* **1999**, *34*, 1-104.
66. Park, S.; Khalili-Araghi, F.; Tajkhorshid, E.; Schulten, K., Free energy calculation from steered molecular dynamics simulations using Jarzynski's equality. *The Journal of Chemical Physics* **2003**, *119* (6), 3559-3566.
67. Jarzynski, C., Nonequilibrium Equality of Free Energy Difference. *Physical Review Letters* **1997**, *78* (14), 2690-2693.
68. Qin, X.; Xia, W.; Sinko, R.; Keten, S., Tuning Glass Transition in Polymer Nanocomposites with Functionalized Cellulose Nanocrystals through Nanoconfinement. *Nano Lett* **2015**, *15* (10), 6738-44.
69. Sinko, R.; Keten, S., Effect of moisture on the traction-separation behavior of cellulose nanocrystal interfaces. *Applied Physics Letters* **2014**, *105* (24).
70. de Pablo, J. J., Coarse-grained simulations of macromolecules: from DNA to nanocomposites. *Annu Rev Phys Chem* **2011**, *62*, 555-74.
71. Noid, W. G., Perspective: Coarse-grained models for biomolecular systems. *J Chem Phys* **2013**, *139* (9), 090901.
72. Flory, P. J., *Principles of polymer chemistry*. 1953.
73. de Gennes, P. G.; Witten, T. A., Scaling Concepts in Polymer Physics. *Physics Today* **1980**, *33* (6), 51-54.
74. Michael Rubenstein, R. H. C., *Polymer Physics*. Oxford Univesity Press **2003**.
75. M. Doi, S. F. E., *Theory of Polymer Dynamics*. Oxford Univeristy Press: 1996.
76. Michael Levitt, A. W., Computer simulation of protein folding. *Nature* **1975**, *253*, 694-698.
77. A. R. Atilgan, S. R. D., R. L. Jernigan, M. C. Demirel, O. Keskin, and I. Bahar, Anisotropy of Fluctuation Dynamics of Proteins with an Elastic Network Model. **2001**, *80*, 505-515.
78. Seo, M.; Rauscher, S.; Pomes, R.; Tieleman, D. P., Improving Internal Peptide Dynamics in the Coarse-Grained MARTINI Model: Toward Large-Scale Simulations of Amyloid- and Elastin-like Peptides. *J Chem Theory Comput* **2012**, *8* (5), 1774-1785.
79. R.B. Bird, P. J. D. a. N. L. J., Polymer solution rheology based on a finitely extenisble bead-spring chain model. *Journal of Non-Newtonian Fluid Mechanics* **1980**, *7*, 213-235.
80. Grest, G. S., Grafted Polymer Brushes A Constant Surface Pressure Molecular Dynamics Simulation. *Macromolecules* **1994**, *27*, 418-426.
81. Grest, G. S.; Kremer, K., Molecular dynamics simulation for polymers in the presence of a heat bath. *Phys Rev A Gen Phys* **1986**, *33* (5), 3628-3631.
82. Grest, M. M. a. G. S., Polymers End-Grafted onto a Cylindrical Surface. *Macromolecules* **1991**, *24*, 704-706.
83. Grest, M. M. a. G. S., Structure of a Grafted Polymer Brush A Molecular Dynamics Simulation. *Macromolecules* **1989**, *22*, 4054-4059.
84. Murat, G. S. G. a. M., Structure of Grafted Polymeric Brushes in Solvents of Varying Quality A Molecular Dynamics Study. *Macromolecules* **1993**, *26*, 3108-3117.

85. E.B. Zhulina, T. A. V., Scaling Theory of Planar Brushes Formed by Branched Polymers. *Macromolecules* **1995**, *28*, 1008-1015.
86. V. A. Harmandaris, V. G. M., D. N. Theodorou, M. Kro1ger, J. Ramirez, H. C. Ottinger, and D. Vlassopoulos, Crossover from the Rouse to the Entangled Polymer Melt Regime: Signals from Long, Detailed Atomistic Molecular Dynamics Simulations, Supported by Rheological Experiments. *Macromolecules* **2003**, *36*, 1376-1387.
87. Li, Y.; Abberton, B.; Kröger, M.; Liu, W., Challenges in Multiscale Modeling of Polymer Dynamics. *Polymers* **2013**, *5* (2), 751-832.
88. Dirk Reith, M. P., Florian Muller-Plathe, Deriving Effective Mesoscale Potentials from Atomistic Simulations. *J Comput Chem* **2003**, *24*, 1624-1636.
89. Noid, W. G.; Chu, J. W.; Ayton, G. S.; Krishna, V.; Izvekov, S.; Voth, G. A.; Das, A.; Andersen, H. C., The multiscale coarse-graining method. I. A rigorous bridge between atomistic and coarse-grained models. *J Chem Phys* **2008**, *128* (24), 244114.
90. Sergei Izvekov, G. A. V., A Multiscale Coarse-Graining Method for Biomolecular Systems. *JOURNAL OF PHYSICAL CHEMISTRY B LETTERS* **2004**, *109*, 2469-2473.
91. Shell, M. S., Coarse-graining with the relative entropy. *ADVANCES IN CHEMICAL PHYSICS* **2016**, *161*, 395-441.
92. Lyubartsev, A. P.; Laaksonen, A., Calculation of effective interaction potentials from radial distribution functions: A reverse Monte Carlo approach. *Phys Rev E Stat Phys Plasmas Fluids Relat Interdiscip Topics* **1995**, *52* (4), 3730-3737.
93. Fritz, D.; Koschke, K.; Harmandaris, V. A.; van der Vegt, N. F.; Kremer, K., Multiscale modeling of soft matter: scaling of dynamics. *Phys Chem Chem Phys* **2011**, *13* (22), 10412-20.
94. Karimi-Varzaneh, H. A.; van der Vegt, N. F.; Muller-Plathe, F.; Carbone, P., How good are coarse-grained polymer models? A comparison for atactic polystyrene. *Chemphyschem* **2012**, *13* (15), 3428-39.
95. Shell, M. S., COARSE-GRAINING WITH THE RELATIVE ENTROPY. In *Advances in Chemical Physics*, John Wiley & Sons, Inc.: 2016; pp 395-441.
96. Grmela, M.; Öttinger, H. C., Dynamics and thermodynamics of complex fluids. I. Development of a general formalism. *Physical Review E* **1997**, *56* (6), 6620-6632.
97. Öttinger, H. C.; Grmela, M., Dynamics and thermodynamics of complex fluids. II. Illustrations of a general formalism. *Physical Review E* **1997**, *56* (6), 6633-6655.
98. Depa, P. K.; Maranas, J. K., Speed up of dynamic observables in coarse-grained molecular-dynamics simulations of unentangled polymers. *J Chem Phys* **2005**, *123* (9), 94901.
99. Lyubimov, I. Y.; McCarty, J.; Clark, A.; Guenza, M. G., Analytical rescaling of polymer dynamics from mesoscale simulations. *J Chem Phys* **2010**, *132* (22), 224903.
100. Davtyan, A.; Dama, J. F.; Voth, G. A.; Andersen, H. C., Dynamic force matching: A method for constructing dynamical coarse-grained models with realistic time dependence. *J Chem Phys* **2015**, *142* (15), 154104.
101. Carbone, P.; Varzaneh, H. A.; Chen, X.; Muller-Plathe, F., Transferability of coarse-grained force fields: the polymer case. *J Chem Phys* **2008**, *128* (6), 064904.

102. Rosch, T. W.; Brennan, J. K.; Izvekov, S.; Andzelm, J. W., Exploring the ability of a multiscale coarse-grained potential to describe the stress-strain response of glassy polystyrene. *Phys Rev E Stat Nonlin Soft Matter Phys* **2013**, *87* (4), 042606.
103. Dunn, N. J.; Foley, T. T.; Noid, W. G., Van der Waals Perspective on Coarse-Graining: Progress toward Solving Representability and Transferability Problems. *Acc Chem Res* **2016**, *49* (12), 2832-2840.
104. Farah, K.; Fogarty, A. C.; Bohm, M. C.; Muller-Plathe, F., Temperature dependence of coarse-grained potentials for liquid hexane. *Phys Chem Chem Phys* **2011**, *13* (7), 2894-902.
105. Rosenberger, D.; van der Vegt, N. F. A., Addressing the temperature transferability of structure based coarse graining models. *Phys Chem Chem Phys* **2018**, *20* (9), 6617-6628.
106. Adam, G.; Gibbs, J. H., On the temperature dependence of cooperative relaxation properties in glass-forming liquids. *The journal of chemical physics* **1965**, *43* (1), 139-146.
107. Dudowicz, J.; Freed, K. F.; Douglas, J. F., Generalized Entropy Theory of Polymer Glass Formation. In *Advances in Chemical Physics*, John Wiley & Sons, Inc.: 2008; pp 125-222.
108. Yelon, A.; Movaghar, B., Microscopic explanation of the compensation (Meyer-Neldel) rule. *Physical Review Letters* **1990**, *65* (5), 618-620.
109. Betancourt, B. A. P.; Hanakata, P. Z.; Starr, F. W.; Douglas, J. F., Quantitative relations between cooperative motion, emergent elasticity, and free volume in model glass-forming polymer materials. *Proceedings of the National Academy of Sciences* **2015**, *112* (10), 2966-2971.
110. Lumry, R.; Rajender, S., Enthalpy-entropy compensation phenomena in water solutions of proteins and small molecules: A ubiquitous property of water. *Biopolymers* **1970**, *9* (10), 1125-1227.
111. Xu, W.-S.; Freed, K. F., Influence of Cohesive Energy and Chain Stiffness on Polymer Glass Formation. *Macromolecules* **2014**, *47* (19), 6990-6997.
112. Xu, W.-S.; Douglas, J. F.; Freed, K. F., Influence of Cohesive Energy on the Thermodynamic Properties of a Model Glass-Forming Polymer Melt. *Macromolecules* **2016**, *49* (21), 8341-8354.
113. Grant Smith, W. P., United Atom Force Field for Molecular Dynamics Simulations of 1,4 Polybutadiene Based on Quantum Chemistry Calculations on Model Molecules. *Journal of Physical CHEMISTRY A* **1998**, *102*, 1200-1208.
114. Dysthe, D. K.; Fuchs, A. H.; Rousseau, B., Fluid transport properties by equilibrium molecular dynamics. III. Evaluation of united atom interaction potential models for pure alkanes. *The Journal of Chemical Physics* **2000**, *112* (17), 7581-7590.
115. Xia, W.; Song, J.; Hansoge, N. K.; Phelan, F. R., Jr.; Keten, S.; Douglas, J. F., Energy Renormalization for Coarse-Graining the Dynamics of a Model Glass-Forming Liquid. *J Phys Chem B* **2018**, *122* (6), 2040-2045.
116. Wenjie Xia, N. K. H., Wen-Sheng Xu, Frederick R. Phelan Jr.,; Sinan Keten, J. F. D., Energy renormalization for coarse-graining polymers having different segmental structures. *Science Advances* **2019**, *5* (4).
117. McCall, D. W.; Douglass, D. C.; Falcone, D. R., Molecular Motion in ortho-Terphenyl. *The Journal of Chemical Physics* **1969**, *50* (9), 3839-3843.
118. R.J. Greet, D. T., Glass Transition in o-Terphenyl. *J Chem Phys* **1967**, *46* (4), 1243-1251.

119. Hansen, C.; Stickel, F.; Berger, T.; Richert, R.; Fischer, E. W., Dynamics of glass-forming liquids. III. Comparing the dielectric  $\alpha$ - and  $\beta$ -relaxation of 1-propanol and o-terphenyl. *The Journal of Chemical Physics* **1997**, *107* (4), 1086-1093.
120. Niblett, S. P.; de Souza, V. K.; Stevenson, J. D.; Wales, D. J., Dynamics of a molecular glass former: Energy landscapes for diffusion in ortho-terphenyl. *J Chem Phys* **2016**, *145* (2), 024505.
121. Ghosh, J.; Faller, R., State point dependence of systematically coarse-grained potentials. *Mol Simulat* **2007**, *33* (9-10), 759-767.
122. Song, J.; Hsu, D. D.; Shull, K. R.; Phelan, F. R., Jr.; Douglas, J. F.; Xia, W.; Keten, S., Energy Renormalization Method for the Coarse-Graining of Polymer Viscoelasticity. *Macromolecules* **2018**, *51*.
123. Xia, W.; Song, J.; Jeong, C.; Hsu, D. D.; Phelan, F. R., Jr.; Douglas, J. F.; Keten, S., Energy-Renormalization for Achieving Temperature Transferable Coarse-Graining of Polymer Dynamics. *Macromolecules* **2017**, *50*.
124. Hsu, D. D.; Xia, W.; Arturo, S. G.; Keten, S., Thermomechanically Consistent and Temperature Transferable Coarse-Graining of Atactic Polystyrene. *Macromolecules* **2015**, *48* (9), 3057-3068.
125. Xu, W.-S.; Douglas, J. F.; Freed, K. F., Influence of Cohesive Energy on Relaxation in a Model Glass-Forming Polymer Melt. *Macromolecules* **2016**, *49* (21), 8355-8370.
126. Pazmiño Betancourt, B. A.; Douglas, J. F.; Starr, F. W., String model for the dynamics of glass-forming liquids. *The Journal of Chemical Physics* **2014**, *140* (20), 204509.
127. Hanakata, P. Z.; Douglas, J. F.; Starr, F. W., Interfacial mobility scale determines the scale of collective motion and relaxation rate in polymer films. *Nat Commun* **2014**, *5*, 4163.
128. Cornell, W. D.; Cieplak, P.; Bayly, C. I.; Gould, I. R.; Merz, K. M.; Ferguson, D. M.; Spellmeyer, D. C.; Fox, T.; Caldwell, J. W.; Kollman, P. A., A Second Generation Force Field for the Simulation of Proteins, Nucleic Acids, and Organic Molecules. *Journal of the American Chemical Society* **1995**, *117* (19), 5179-5197.
129. Payne, M. C.; Teter, M. P.; Allan, D. C.; Arias, T. A.; Joannopoulos, J. D., Iterative Minimization Techniques for Abinitio Total-Energy Calculations - Molecular-Dynamics and Conjugate Gradients. *Rev Mod Phys* **1992**, *64* (4), 1045-1097.
130. Bartsch, E.; Bertagnolli, H.; Chieux, P.; David, A.; Sillescu, H., Temperature-Dependence of the Static Structure Factor of Ortho-Terphenyl in the Supercooled Liquid Regime Close to the Glass-Transition. *Chem Phys* **1993**, *169* (3), 373-378.
131. Vogel, H., The temperature dependence law of the viscosity of fluids. *Phys Z* **1921**, *22*, 645-646.
132. Fulcher, G. S., Analysis of recent measurements of the viscosity of glasses. *J Am Ceram Soc* **1925**, *8* (6), 339-355.
133. Tammann, G.; Hesse, W., Die Abhängigkeit der Viskosität von der Temperatur bei unterkühlten Flüssigkeiten. *Zeitschrift für anorganische und allgemeine Chemie* **1926**, *156* (1), 245-257.
134. Hohenberg, P. C.; Halperin, B. I., Theory of Dynamic Critical Phenomena. *Rev Mod Phys* **1977**, *49* (3), 435-479.

135. Tolle, A., Neutron scattering studies of the model glass former ortho-terphenyl. *Reports on Progress in Physics* **2001**, *64* (11), 1473-1532.
136. Greet, R. J.; Turnbull, D., Glass Transition in o-Terphenyl. *The Journal of Chemical Physics* **1967**, *46* (4), 1243-1251.
137. Bartsch, E.; Fujara, F.; Kiebel, M.; Sillescu, H.; Petry, W., Inelastic Neutron Scattering Experiments on Van der Waals Glasses — A Test of Recent Microscopic Theories of the Glass Transition. *Berichte der Bunsengesellschaft für physikalische Chemie* **1989**, *93* (11), 1252-1259.
138. Jack, F. D.; Beatriz, A. P. B.; Xuhang, T.; Hao, Z., Localization model description of diffusion and structural relaxation in glass-forming Cu–Zr alloys. *Journal of Statistical Mechanics: Theory and Experiment* **2016**, *2016* (5), 054048.
139. Douglas, J. F.; Leporini, D., Obstruction model of the fractional Stokes-Einstein relation in glass-forming liquids. *Journal of Non-Crystalline Solids* **1998**, *235*, 137-141.
140. Legrand, D. G., *Handbook of Polycarbonate Science and Technology*. Marcel Dekker Inc.: 2000.
141. Hess, B.; León, S.; van der Vegt, N.; Kremer, K., Long time atomistic polymer trajectories from coarse grained simulations: bisphenol-A polycarbonate. *Soft Matter* **2006**, *2* (5), 409-414.
142. S. Leon, N. v. d. V., L. Delle Site, and K. Kremer, Bisphenol A Polycarbonate Entanglement Analysis from Coarse-Grained MD Simulations. *Macromolecules* **2005**, *38*, 8078-8092.
143. Garca-Coln, L. S.; del Castillo, L. F.; Goldstein, P., Theoretical basis for the Vogel-Fulcher-Tammann equation. *Phys Rev B Condens Matter* **1989**, *40* (10), 7040-7044.
144. Stukalin, E. B.; Douglas, J. F.; Freed, K. F., Application of the entropy theory of glass formation to poly(alpha-olefins). *J Chem Phys* **2009**, *131* (11), 114905.
145. W. Tschop, K. K., J. Batoulis, T. Burger and O. Hahn, Simulation of polymer melts. II. Coarse-graining procedure for polycarbonates. *Acta Polymer* **1998**, *49*.
146. W. Tschop, K. K., J. Batoulis, T. Burger and O. Hahn, Simulation of polymer melts. I. Coarse-graining procedure for polycarbonates. *Acta Polymer* **1998**, *49*, 61-74.
147. B. T. Marouf, R. B., *Handbook of Epoxy Blends*. Springer, Cham: 2017.
148. Capricho, J. C.; Fox, B.; Hameed, N., Multifunctionality in Epoxy Resins. *Polymer Reviews* **2019**, *60* (1), 1-41.
149. Jin, F.-L.; Li, X.; Park, S.-J., Synthesis and application of epoxy resins: A review. *Journal of Industrial and Engineering Chemistry* **2015**, *29*, 1-11.
150. Jlassi, K.; Radwan, A. B.; Sadasivuni, K. K.; Mrlik, M.; Abdullah, A. M.; Chehimi, M. M.; Krupa, I., Anti-corrosive and oil sensitive coatings based on epoxy/polyaniline/magnetite-clay composites through diazonium interfacial chemistry. *Sci Rep* **2018**, *8* (1), 13369.
151. Yarahmadi, E.; Didehban, K.; Sari, M. G.; Saeb, M. R.; Shabaniyan, M.; Aryaniasab, F.; Zarrintaj, P.; Paran, S. M. R.; Mozafari, M.; Rallini, M.; Puglia, D., Development and curing potential of epoxy/starch-functionalized graphene oxide nanocomposite coatings. *Progress in Organic Coatings* **2018**, *119*, 194-202.
152. Hu, J. B., High-performance ceramic/epoxy composite adhesives enabled by rational ceramic bandgaps. *Sci Rep* **2020**, *10* (1), 484.

153. Jouyandeh, M.; Moini Jazani, O.; Navarchian, A. H.; Saeb, M. R., High-performance epoxy-based adhesives reinforced with alumina and silica for carbon fiber composite/steel bonded joints. *Journal of Reinforced Plastics and Composites* **2016**, *35* (23), 1685-1695.
154. Yildiz, Z.; Gungor, A.; Onen, A.; Usta, I., Synthesis and characterization of dual-curable epoxyacrylates for polyester cord/rubber applications. *Journal of Industrial Textiles* **2015**, *46* (2), 596-610.
155. Jakubinek, M. B.; Ashrafi, B.; Zhang, Y.; Martinez-Rubi, Y.; Kingston, C. T.; Johnston, A.; Simard, B., Single-walled carbon nanotube–epoxy composites for structural and conductive aerospace adhesives. *Composites Part B: Engineering* **2015**, *69*, 87-93.
156. Mangalgi, P. D., Composite materials for aerospace applications. *Bull. Mater. Sci.* **1999**, *22* (3), 657-664.
157. Guadagno, L.; Raimondo, M.; Vittoria, V.; Vertuccio, L.; Naddeo, C.; Russo, S.; De Vivo, B.; Lamberti, P.; Spinelli, G.; Tucci, V., Development of epoxy mixtures for application in aeronautics and aerospace. *RSC Adv.* **2014**, *4* (30), 15474-15488.
158. Wang, T. Y.; Zhang, B. Y.; Li, D. Y.; Hou, Y. C.; Zhang, G. X., Metal nanoparticle-doped epoxy resin to suppress surface charge accumulation on insulators under DC voltage. *Nanotechnology* **2020**, *31* (32), 324001.
159. Li, C.; Hu, J.; Lin, C.; He, J., The control mechanism of surface traps on surface charge behavior in alumina-filled epoxy composites. *Journal of Physics D: Applied Physics* **2016**, *49* (44).
160. Bobby, S.; Samad, M. A., Epoxy composites in biomedical engineering. In *Materials for Biomedical Engineering*, 2019; pp 145-174.
161. Stastny, P.; Chlup, Z.; Kalasova, D.; Zikmund, T.; Kaiser, J.; Trunec, M., Epoxy-based gelcasting of machinable hydroxyapatite foams for medical applications. *Journal of the American Ceramic Society* **2018**, *101* (8), 3317-3327.
162. Long, T. R.; Knorr, D. B.; Masser, K. A.; Elder, R. M.; Sirk, T. W.; Hindenlang, M. D.; Yu, J. H.; Richardson, A. D.; Boyd, S. E.; Spurgeon, W. A.; Lenhart, J. L. In *Ballistic response of polydicyclopentadiene vs. epoxy resins and effects of crosslinking*, 2017; Springer New York LLC: pp 285-290.
163. Rohen, L. A.; Margem, F. M.; Monteiro, S. N.; Vieira, C. M. F.; Madeira de Araujo, B.; Lima, E. S., Ballistic Efficiency of an Individual Epoxy Composite Reinforced with Sisal Fibers in Multilayered Armor. *Materials Research* **2015**, *18* (suppl 2), 55-62.
164. Vashisth, A.; Bakis, C. E.; Ruggeri, C. R.; Henry, T. C.; Roberts, G. D., Ballistic impact response of carbon/epoxy tubes with variable nanosilica content. *Journal of Composite Materials* **2017**, *52* (12), 1589-1604.
165. Rahman, M.; Hosur, M.; Zainuddin, S.; Vaidya, U.; Tauhid, A.; Kumar, A.; Trovillion, J.; Jeelani, S., Effects of amino-functionalized MWCNTs on ballistic impact performance of E-glass/epoxy composites using a spherical projectile. *International Journal of Impact Engineering* **2013**, *57*, 108-118.
166. W. Erich, M. J. B., Effect of Molecular Structure on Mechanical Properties of Epoxy Resins *Journal of Applied Polymer Science* **1960**, *3* (9), 296-301.
167. Gao, L.; Zhang, Q.; Li, H.; Yu, S.; Zhong, W.; Sui, G.; Yang, X., Effect of epoxy monomer structure on the curing process and thermo-mechanical characteristics of tri-functional

epoxy/amine systems: a methodology combining atomistic molecular simulation with experimental analyses. *Polymer Chemistry* **2017**, *8* (13), 2016-2027.

168. Lv, G.; Jensen, E.; Shen, C.; Yang, K.; Evans, C. M.; Cahill, D. G., Effect of Amine Hardener Molecular Structure on the Thermal Conductivity of Epoxy Resins. *ACS Applied Polymer Materials* **2020**, *3* (1), 259-267.

169. Liang, G.; Ren, P.; Zhang, Z.; Lu, T., Effect of the epoxy molecular weight on the properties of a cyanate ester/epoxy resin system. *Journal of Applied Polymer Science* **2006**, *101* (3), 1744-1750.

170. Caroselli, C. D.; Pramanik, M.; Achord, B. C.; Rawlins, J. W., Molecular weight effects on the mechanical properties of novel epoxy thermoplastics. *High Performance Polymers* **2012**, *24* (3), 161-172.

171. Ito, A.; Semba, T.; Taki, K.; Ohshima, M., Effect of the molecular weight between crosslinks of thermally cured epoxy resins on the CO<sub>2</sub>-bubble nucleation in a batch physical foaming process. *Journal of Applied Polymer Science* **2014**, *131* (12), n/a-n/a.

172. Nakka, J. S.; Jansen, K. M. B.; Ernst, L. J., Effect of chain flexibility in the network structure on the viscoelasticity of epoxy thermosets. *Journal of Polymer Research* **2011**, *18* (6), 1879-1888.

173. Chen, Z.; Liu, Z.; Shen, G.; Wen, R.; Lv, J.; Huo, J.; Yu, Y., Effect of Chain Flexibility of Epoxy Encapsulants on the Performance and Reliability of Light-Emitting Diodes. *Industrial & Engineering Chemistry Research* **2016**, *55* (28), 7635-7645.

174. Abrahami, S. T.; Hauffman, T.; de Kok, J. M. M.; Mol, J. M. C.; Terryn, H., Effect of Anodic Aluminum Oxide Chemistry on Adhesive Bonding of Epoxy. *The Journal of Physical Chemistry C* **2016**, *120* (35), 19670-19677.

175. Yu, S.; Li, X.; Zou, M.; Guo, X.; Ma, H.; Wang, S., Effect of the Aromatic Amine Curing Agent Structure on Properties of Epoxy Resin-Based Syntactic Foams. *ACS Omega* **2020**, *5* (36), 23268-23275.

176. Pavel V. Komarov, C. Y.-T., Chen Shih-Ming, Pavel G. Khalatur,; Reineker, P., Highly Cross-Linked Epoxy Resins: An Atomistic Molecular Dynamics Simulation Combined with a Mapping/Reverse Mapping Procedure. *Macromolecules* **2007**, (40), 8104-8113.

177. Bandyopadhyay, A.; Valavala, P. K.; Clancy, T. C.; Wise, K. E.; Odegard, G. M., Molecular modeling of crosslinked epoxy polymers: The effect of crosslink density on thermomechanical properties. *Polymer* **2011**, *52* (11), 2445-2452.

178. Wu, C.; Xu, W., Atomistic simulation study of absorbed water influence on structure and properties of crosslinked epoxy resin. *Polymer* **2007**, *48* (18), 5440-5448.

179. Meng, Z.; Bessa, M. A.; Xia, W.; Kam Liu, W.; Keten, S., Predicting the Macroscopic Fracture Energy of Epoxy Resins from Atomistic Molecular Simulations. *Macromolecules* **2016**, *49* (24), 9474-9483.

180. King, J. A.; Klimek, D. R.; Miskioglu, I.; Odegard, G. M., Mechanical properties of graphene nanoplatelet/epoxy composites. *Journal of Applied Polymer Science* **2013**, *128* (6), 4217-4223.

181. Li, C.; Browning, A. R.; Christensen, S.; Strachan, A., Atomistic simulations on multilayer graphene reinforced epoxy composites. *Composites Part A: Applied Science and Manufacturing* **2012**, *43* (8), 1293-1300.

182. Khare, K. S.; Phelan, F. R., Quantitative Comparison of Atomistic Simulations with Experiment for a Cross-Linked Epoxy: A Specific Volume-Cooling Rate Analysis. *Macromolecules* **2018**, *51* (2), 564-575.
183. Khare, K. S.; Phelan, F. R. *Integration of Atomistic Simulation with Experiment using Time-Temperature Superposition for a Cross-linked Epoxy Network*; 2019.
184. Senftle, T. P.; Hong, S.; Islam, M. M.; Kylasa, S. B.; Zheng, Y.; Shin, Y. K.; Junkermeier, C.; Engel-Herbert, R.; Janik, M. J.; Aktulga, H. M.; Verstraelen, T.; Grama, A.; van Duin, A. C. T., The ReaxFF reactive force-field: development, applications and future directions. *npj Computational Materials* **2016**, *2* (1).
185. Odegard, G. M.; Jensen, B. D.; Gowtham, S.; Wu, J.; He, J.; Zhang, Z., Predicting mechanical response of crosslinked epoxy using ReaxFF. *Chemical Physics Letters* **2014**, *591*, 175-178.
186. Koo, B.; Subramanian, N.; Chattopadhyay, A., Molecular dynamics study of brittle fracture in epoxy-based thermoset polymer. *Composites Part B: Engineering* **2016**, *95*, 433-439.
187. Xia, W.; Hansoge, N. K.; Xu, W.-S.; Phelan, F. R.; Keten, S.; Douglas, J. F. *Energy renormalization for coarse-graining polymers having different segmental structures*; 2019.
188. Dudowicz, J.; Douglas, J. F.; Freed, K. F., Advances in the generalized entropy theory of glass-formation in polymer melts. *J Chem Phys* **2014**, *141* (23), 234903.
189. Dudowicz, J.; Freed, K. F.; Douglas, J. F., Entropy theory of polymer glass formation revisited. I. General formulation. *J Chem Phys* **2006**, *124* (6), 64901.
190. Dudowicz, J. F., K.F.; Douglas, J.F., Generalized Entropy Theory of Polymer Glass Formation. *Advances in Chemical Physics* **2008**, 125-222.
191. **!!! INVALID CITATION !!!** {}.
192. Hansoge, N. K.; Huang, T.; Sinko, R.; Xia, W.; Chen, W.; Keten, S., Materials by Design for Stiff and Tough Hairy Nanoparticle Assemblies. *ACS Nano* **2018**, *12* (8), 7946-7958.
193. *Optimization of Polymer Nanocomposite Properties*. John Wiley & Sons: 2009.
194. Xu, H.; Li, Y.; Brinson, C.; Chen, W., A Descriptor-Based Design Methodology for Developing Heterogeneous Microstructural Materials System. *Journal of Mechanical Design* **2014**, *136* (5).
195. Zhao, H.; Li, X.; Zhang, Y.; Schadler, L. S.; Chen, W.; Brinson, L. C., Perspective: NanoMine: A material genome approach for polymer nanocomposites analysis and design. *APL Materials* **2016**, *4* (5).
196. Goyal, S.; Escobedo, F. A., Structure and transport properties of polymer grafted nanoparticles. *J Chem Phys* **2011**, *135* (18), 184902.
197. Barton, R. R.; Meckesheimer, M., Chapter 18 Metamodel-Based Simulation Optimization. In *Simulation*, 2006; pp 535-574.
198. Wang, G. G.; Shan, S., Review of Metamodeling Techniques in Support of Engineering Design Optimization. *Journal of Mechanical Design* **2007**, *129* (4), 370-380.
199. Shan, S.; Wang, G. G., Survey of modeling and optimization strategies to solve high-dimensional design problems with computationally-expensive black-box functions. *Structural and Multidisciplinary Optimization* **2009**, *41* (2), 219-241.

200. Miao, J.-M.; Cheng, S.-J.; Wu, S.-J., Metamodel based design optimization approach in promoting the performance of proton exchange membrane fuel cells. *International Journal of Hydrogen Energy* **2011**, *36* (23), 15283-15294.
201. Fang, H.; Rais-Rohani, M.; Liu, Z.; Horstemeyer, M. F., A comparative study of metamodeling methods for multiobjective crashworthiness optimization. *Computers & Structures* **2005**, *83* (25-26), 2121-2136.
202. Ghasemi, H.; Rafiee, R.; Zhuang, X.; Muthu, J.; Rabczuk, T., Uncertainties propagation in metamodel-based probabilistic optimization of CNT/polymer composite structure using stochastic multi-scale modeling. *Computational Materials Science* **2014**, *85*, 295-305.
203. Pryamtsyn, V.; Ganesan, V.; Panagiotopoulos, A. Z.; Liu, H.; Kumar, S. K., Modeling the anisotropic self-assembly of spherical polymer-grafted nanoparticles. *J Chem Phys* **2009**, *131* (22), 221102.
204. Lee, K.-Y.; Aitomäki, Y.; Berglund, L. A.; Oksman, K.; Bismarck, A., On the use of nanocellulose as reinforcement in polymer matrix composites. *Composites Science and Technology* **2014**, *105*, 15-27.
205. Eichhorn, S. J.; Dufresne, A.; Aranguren, M.; Marcovich, N. E.; Capadona, J. R.; Rowan, S. J.; Weder, C.; Thielemans, W.; Roman, M.; Renneckar, S.; Gindl, W.; Veigel, S.; Keckes, J.; Yano, H.; Abe, K.; Nogi, M.; Nakagaito, A. N.; Mangalam, A.; Simonsen, J.; Benight, A. S.; Bismarck, A.; Berglund, L. A.; Peijs, T., Review: current international research into cellulose nanofibres and nanocomposites. *Journal of Materials Science* **2010**, *45* (1), 1-33.
206. Moon, R. J.; Martini, A.; Nairn, J.; Simonsen, J.; Youngblood, J., Cellulose nanomaterials review: structure, properties and nanocomposites. *Chem Soc Rev* **2011**, *40* (7), 3941-94.
207. Cudjoe, E.; Hunsen, M.; Xue, Z.; Way, A. E.; Barrios, E.; Olson, R. A.; Hore, M. J.; Rowan, S. J., Miscanthus Giganteus: A commercially viable sustainable source of cellulose nanocrystals. *Carbohydr Polym* **2017**, *155*, 230-241.
208. George, J.; Sabapathi, S. N., Cellulose nanocrystals: synthesis, functional properties, and applications. *Nanotechnol Sci Appl* **2015**, *8*, 45-54.
209. Dufresne, A., Cellulose nanomaterial reinforced polymer nanocomposites. *Current Opinion in Colloid & Interface Science* **2017**, *29*, 1-8.
210. Yoshiharu Nishiyama, G. P. J., Alfred D. French, V. Trevor Forsyth, and Paul Langan, Neutron Crystallography, Molecular Dynamics, and Quantum Mechanics Studies of the Nature of Hydrogen Bonding in Cellulose IB. *Biomacromolecules* **2008**, *9*, 3133-3140.
211. Youssef Habibi, L. A. L., and Orlando J. Rojas, Cellulose Nanocrystals: Chemistry, Self-Assembly, and Applications. *Chem Rev* **2010**, *110*, 3479-3500.
212. Zhang, Y.; Karimkhani, V.; Makowski, B. T.; Samaranayake, G.; Rowan, S. J., Nanoemulsions and Nanolatexes Stabilized by Hydrophobically Functionalized Cellulose Nanocrystals. *Macromolecules* **2017**, *50* (16), 6032-6042.
213. Morandi, G.; Heath, L.; Thielemans, W., Cellulose nanocrystals grafted with polystyrene chains through surface-initiated atom transfer radical polymerization (SI-ATRP). *Langmuir* **2009**, *25* (14), 8280-6.
214. Kan, K. H.; Li, J.; Wijesekera, K.; Cranston, E. D., Polymer-grafted cellulose nanocrystals as pH-responsive reversible flocculants. *Biomacromolecules* **2013**, *14* (9), 3130-9.

215. Spinella, S.; Samuel, C.; Raquez, J.-M.; McCallum, S. A.; Gross, R.; Dubois, P., Green and Efficient Synthesis of Dispersible Cellulose Nanocrystals in Biobased Polyesters for Engineering Applications. *ACS Sustainable Chemistry & Engineering* **2016**, *4* (5), 2517-2527.
216. Kedzior, S. A.; Graham, L.; Moorlag, C.; Dooley, B. M.; Cranston, E. D., Poly(methyl methacrylate)-grafted cellulose nanocrystals: One-step synthesis, nanocomposite preparation, and characterization. *The Canadian Journal of Chemical Engineering* **2016**, *94* (5), 811-822.
217. Ali, U.; Karim, K. J. B. A.; Buang, N. A., A Review of the Properties and Applications of Poly (Methyl Methacrylate) (PMMA). *Polymer Reviews* **2015**, *55* (4), 678-705.
218. Jin, R.; Chen, W.; Sudjianto, A., An efficient algorithm for constructing optimal design of computer experiments. *Journal of Statistical Planning and Inference* **2005**, *134* (1), 268-287.
219. Hsu, D. D.; Xia, W.; Arturo, S. G.; Keten, S., Systematic Method for Thermomechanically Consistent Coarse-Graining: A Universal Model for Methacrylate-Based Polymers. *J Chem Theory Comput* **2014**, *10* (6), 2514-27.
220. Parreno, O.; Ramos, P. M.; Karayiannis, N. C.; Laso, M., Self-Avoiding Random Walks as a Model to Study Athermal Linear Polymers under Extreme Plate Confinement. *Polymers (Basel)* **2020**, *12* (4).
221. Rottler, J.; Barsky, S.; Robbins, M. O., Cracks and crazes: on calculating the macroscopic fracture energy of glassy polymers from molecular simulations. *Phys Rev Lett* **2002**, *89* (14), 148304.
222. Martin, J. D.; Simpson, T. W., Use of Kriging Models to Approximate Deterministic Computer Models. *AIAA Journal* **2005**, *43* (4), 853-863.
223. Simpson, T. W.; Mauery, T. M.; Korte, J. J.; Mistree, F., Kriging Models for Global Approximation in Simulation-Based Multidisciplinary Design Optimization. *AIAA Journal* **2001**, *39* (12), 2233-2241.
224. Conti, S.; Gosling, J. P.; Oakley, J. E.; O'Hagan, A., Gaussian process emulation of dynamic computer codes. *Biometrika* **2009**, *96* (3), 663-676.
225. Bostanabad, R.; Kearney, T.; Tao, S.; Apley, D. W.; Chen, W., Leveraging the nugget parameter for efficient Gaussian process modeling. *International Journal for Numerical Methods in Engineering* **2018**, *114* (5), 501-516.
226. J.C. Halpin, J. L. K., The Halpin-Tsai Equations: A Review. *Polymer Engineering and Science* **1976**, *16* (5), 344-353.
227. *Encyclopedia of Database Systems*. Springer US: 2009.
228. A. Saltelli, M. R., T. Andres, F. Campolongo, J. Carboni, D. Gatelli, M. Saisana, S. Tarantola, Global Sensitivity Analysis: The Primer. *John Wiley & Sons: New York* **2008**.
229. Sobol, I. M., Global Sensitivity Indices for Nonlinear Mathematicla models and their Monte Carlo estimates. *Mathematics and Computers in Simulation* **2001**, *55*, 271-280.
230. K. Fuchs, C. F., J. Weese, Viscoelastic Properties of Narrow-Distribution Poly(methyl methacrylates). *Macromolecules* **1996**, *29*, 5893-5901.
231. Toshiro Masuda, K. K., Shigeharu Onogi, Viscoelastic Properties of Poly(methyl methacrylates) Prepared by Anionic Polymerization. *Polymer Journal* **1970**, *1*, 418-424.

232. Dukes, D.; Li, Y.; Lewis, S.; Benicewicz, B.; Schadler, L.; Kumar, S. K., Conformational Transitions of Spherical Polymer Brushes: Synthesis, Characterization, and Theory. *Macromolecules* **2010**, *43* (3), 1564-1570.
233. Ramanathan, T.; Abdala, A. A.; Stankovich, S.; Dikin, D. A.; Herrera-Alonso, M.; Piner, R. D.; Adamson, D. H.; Schniepp, H. C.; Chen, X.; Ruoff, R. S.; Nguyen, S. T.; Aksay, I. A.; Prud'Homme, R. K.; Brinson, L. C., Functionalized graphene sheets for polymer nanocomposites. *Nat Nanotechnol* **2008**, *3* (6), 327-31.
234. Choi, J.; Hui, C. M.; Schmitt, M.; Pietrasik, J.; Margel, S.; Matyjaszewski, K.; Bockstaller, M. R., Effect of polymer-graft modification on the order formation in particle assembly structures. *Langmuir* **2013**, *29* (21), 6452-9.
235. Jihoon Choi, H. D., Krzysztof Matyjaszewski, Michael Bockstaller, Flexible Particle Array Structures by Controlling Polymer Graft Architecture. *Journal of American Chemical Society* **2010**, *132*, 12537-12539.
236. Dong, H.; Sliozberg, Y. R.; Snyder, J. F.; Steele, J.; Chantawansri, T. L.; Orlicki, J. A.; Walck, S. D.; Reiner, R. S.; Rudie, A. W., Highly Transparent and Toughened Poly(methyl methacrylate) Nanocomposite Films Containing Networks of Cellulose Nanofibrils. *ACS Appl Mater Interfaces* **2015**, *7* (45), 25464-72.
237. Coulibaly, S.; Roulin, A.; Balog, S.; Biyani, M. V.; Foster, E. J.; Rowan, S. J.; Fiore, G. L.; Weder, C., Reinforcement of Optically Healable Supramolecular Polymers with Cellulose Nanocrystals. *Macromolecules* **2013**, *47* (1), 152-160.
238. Saralegi, A.; Gonzalez, M. L.; Valea, A.; Eceiza, A.; Corcuera, M. A., The role of cellulose nanocrystals in the improvement of the shape-memory properties of castor oil-based segmented thermoplastic polyurethanes. *Composites Science and Technology* **2014**, *92*, 27-33.
239. Sethi, J.; Illikainen, M.; Sain, M.; Oksman, K., Polylactic acid/polyurethane blend reinforced with cellulose nanocrystals with semi-interpenetrating polymer network (S-IPN) structure. *European Polymer Journal* **2017**, *86*, 188-199.
240. Hansoge, N. K.; Keten, S., Effect of Polymer Chemistry on Chain Conformations in Hairy Nanoparticle Assemblies. *ACS Macro Letters* **2019**, *8* (10), 1209-1215.
241. Crosby, A. J.; Lee, J. Y., Polymer Nanocomposites: The "Nano" Effect on Mechanical Properties. *Polymer Reviews* **2007**, *47* (2), 217-229.
242. Michael E. Mackay, A. T., Phillip M. Duxbury, Craig J. Hawker, Brooke Van Horn, Zhibin Guan, Guanghui Chen, R. S. Krishnan, General Strategies for Nanoparticle Dispersion. *Science Reports* **2006**, *311*, 1740-1743.
243. Mackay, M. E.; Dao, T. T.; Tuteja, A.; Ho, D. L.; van Horn, B.; Kim, H. C.; Hawker, C. J., Nanoscale effects leading to non-Einstein-like decrease in viscosity. *Nat Mater* **2003**, *2* (11), 762-6.
244. Min Zhi Rong, M. Q. Z., Hong Liu, Hanmin Zeng, Bernd Wetzels, Klaus Friedrich, Microstructure and tribological behavior of polymeric nanocomposites. *Industrial Lubrication and Tribology* **2001**, *53*, 72-77.
245. Guoqian Jiang, M. J. A. H., Sangah Gam, and Russell J. Composto, Gold nanorods dispersed in homopolymer films: optical properties controlled by self-assembly and percolation of nanorods. *ACS Nano* **2012**, *6* (2), 1578-1588.

246. Hore, M. J. A.; Frischknecht, A. L.; Composto, R. J., Nanorod Assemblies in Polymer Films and Their Dispersion-Dependent Optical Properties. *ACS Macro Letters* **2011**, *1* (1), 115-121.
247. Koerner, H.; Price, G.; Pearce, N. A.; Alexander, M.; Vaia, R. A., Remotely actuated polymer nanocomposites--stress-recovery of carbon-nanotube-filled thermoplastic elastomers. *Nat Mater* **2004**, *3* (2), 115-20.
248. Kohji Ohno, T. M., Satoshi Takeno, Yoshinobu Tsujii, and Takeshi Fukuda, Suspensions of Silica Particles Grafted with Concentrated Polymer Brush- Effects of Graft Chain Length on Brush Layer Thickness and Colloidal Crystallization. *Macromolecules* **2007**, *40*, 9143-9150.
249. Cifra, P., Differences and limits in estimates of persistence length for semi-flexible macromolecules. *Polymer* **2004**, *45* (17), 5995-6002.
250. Nitin K. Hansoge, A. G., Heather White, Andrea Giuntoli, Sinan Keten, Universal relation for effective interaction between polymer grafted nanoparticles. *Macromolecules* **2021**.
251. Hattemer, G. D.; Arya, G., Viscoelastic Properties of Polymer-Grafted Nanoparticle Composites from Molecular Dynamics Simulations. *Macromolecules* **2015**, *48* (4), 1240-1255.
252. Tang, T.-Y.; Arya, G., Anisotropic Three-Particle Interactions between Spherical Polymer-Grafted Nanoparticles in a Polymer Matrix. *Macromolecules* **2017**, *50* (3), 1167-1183.
253. Jayaraman, A.; Schweizer, K. S., Effective Interactions and Self-Assembly of Hybrid Polymer Grafted Nanoparticles in a Homopolymer Matrix. *Macromolecules* **2009**, *42* (21), 8423-8434.
254. Martin, T. B.; Jayaraman, A., Using Theory and Simulations To Calculate Effective Interactions in Polymer Nanocomposites with Polymer-Grafted Nanoparticles. *Macromolecules* **2016**, *49* (24), 9684-9692.
255. Nair, N.; Wentzel, N.; Jayaraman, A., Effect of bidispersity in grafted chain length on grafted chain conformations and potential of mean force between polymer grafted nanoparticles in a homopolymer matrix. *J Chem Phys* **2011**, *134* (19), 194906.
256. Doxastakis, M.; Chen, Y. L.; de Pablo, J. J., Potential of mean force between two nanometer-scale particles in a polymer solution. *J Chem Phys* **2005**, *123* (3), 34901.
257. Doxastakis, M.; Chen, Y. L.; Guzman, O.; de Pablo, J. J., Polymer-particle mixtures: depletion and packing effects. *J Chem Phys* **2004**, *120* (19), 9335-42.
258. Zhao, L.; Li, Y. G.; Zhong, C.; Mi, J., Structure and effective interactions in polymer nanocomposite melts: an integral equation theory study. *J Chem Phys* **2006**, *124* (14), 144913.
259. Clark, A. J.; McCarty, J.; Guenza, M. G., Effective potentials for representing polymers in melts as chains of interacting soft particles. *J Chem Phys* **2013**, *139* (12), 124906.
260. Meng, D.; Kumar, S. K.; D. Lane, J. M.; Grest, G. S., Effective interactions between grafted nanoparticles in a polymer matrix. *Soft Matter* **2012**, *8* (18).
261. You, W.; Tang, Z.; Chang, C. A., Potential Mean Force from Umbrella Sampling Simulations: What Can We Learn and What Is Missed? *J Chem Theory Comput* **2019**, *15* (4), 2433-2443.
262. Trombly, D. M.; Ganesan, V., Curvature effects upon interactions of polymer-grafted nanoparticles in chemically identical polymer matrices. *J Chem Phys* **2010**, *133* (15), 154904.
263. Egorov, S. A., Interactions between polymer brushes in solvents of variable quality: a density functional theory study. *J Chem Phys* **2008**, *129* (6), 064901.

264. Lo Verso, F.; Yelash, L.; Egorov, S. A.; Binder, K., Interactions between polymer brush-coated spherical nanoparticles: the good solvent case. *J Chem Phys* **2011**, *135* (21), 214902.
265. Ganesan, V.; Jayaraman, A., Theory and simulation studies of effective interactions, phase behavior and morphology in polymer nanocomposites. *Soft Matter* **2014**, *10* (1), 13-38.
266. A. Jusufi, M. W., and H. Lowen, Effective Interaction between Star Polymers. *Macromolecules* **1999**, *32*, 4470-4473.
267. C. N. Likos, H. L. w., M. Watzlawek, B. Abbas, O. Jucknischke, J. Allgaier, and D. Richter, Star Polymers Viewed as Ultrasoft Colloidal Particles. *Physical Review Letters* **1998**, *80* (20), 4450-4453.
268. Smith, G. D.; Bedrov, D., Dispersing nanoparticles in a polymer matrix: are long, dense polymer tethers really necessary? *Langmuir* **2009**, *25* (19), 11239-43.
269. Pakdel, A.; Zhi, C.; Bando, Y.; Golberg, D., Low-dimensional boron nitride nanomaterials. *Materials Today* **2012**, *15* (6), 256-265.
270. Vivek Dhand, K. Y. R., Hyun Ju Kim, and Dong Ho Jung, A Comprehensive Review of Graphene Nanocomposites: Research Status and Trends. *Journal of Nanomaterials* **2013**, *2013*.
271. Cowper, G. R. S., P. S. , Strain-Hardening and Strain-Rate Effects in the Impact Loading of Cantilever Beams. **1957**.
272. Martin, J. R.; Johnson, J. F.; Cooper, A. R., Mechanical Properties of Polymers: The Influence of Molecular Weight and Molecular Weight Distribution. *Journal of Macromolecular Science, Part C* **2006**, *8* (1), 57-199.
273. Foteinopoulou, K.; Karayiannis, N. C.; Mavrantzas, V. G.; Kröger, M., Primitive Path Identification and Entanglement Statistics in Polymer Melts: Results from Direct Topological Analysis on Atomistic Polyethylene Models. *Macromolecules* **2006**, *39* (12), 4207-4216.
274. Kröger, M., Shortest multiple disconnected path for the analysis of entanglements in two- and three-dimensional polymeric systems. *Computer Physics Communications* **2005**, *168* (3), 209-232.
275. Hadziioannou, C. O. a. G., Entropic elasticity of single polymer chains of Poly(methacrylic acid) measured by Atomic Force Microscopy. *Macromolecules* **1999**, *32*, 780-87.
276. Olsson, P. A. T.; in 't Veld, P. J.; Andreasson, E.; Bergvall, E.; Persson Jutemar, E.; Petersson, V.; Rutledge, G. C.; Kroon, M., All-atomic and coarse-grained molecular dynamics investigation of deformation in semi-crystalline lamellar polyethylene. *Polymer* **2018**, *153*, 305-316.
277. Kim, J. M.; Locker, R.; Rutledge, G. C., Plastic Deformation of Semicrystalline Polyethylene under Extension, Compression, and Shear Using Molecular Dynamics Simulation. *Macromolecules* **2014**, *47* (7), 2515-2528.
278. Che, J.; Locker, C. R.; Lee, S.; Rutledge, G. C.; Hsiao, B. S.; Tsou, A. H., Plastic Deformation of Semicrystalline Polyethylene by X-ray Scattering: Comparison with Atomistic Simulations. *Macromolecules* **2013**, *46* (13), 5279-5289.
279. Kantesh Balani, V. V., Arvind Agarwal, Roger Narayan, PHYSICAL, THERMAL, AND MECHANICAL PROPERTIES OF POLYMERS. *Biosurfaces: A Materials Science and Engineering Perspective* **2015**, 329-344.

280. Merz, E. J.; Nielsen, L. E.; Buchdahl, R., Influence of Molecular Weight on the Properties of Polystyrene. *Industrial & Engineering Chemistry* **1951**, *43* (6), 1396-1401.
281. Sukumaran, S. K.; Grest, G. S.; Kremer, K.; Everaers, R., Identifying the primitive path mesh in entangled polymer liquids. *Journal of Polymer Science Part B: Polymer Physics* **2005**, *43* (8), 917-933.
282. Smith, F. T., Atomic Distortion and the Combining Rule for Repulsive Potentials. *Physical Review A* **1972**, *5* (4), 1708-1713.
283. Bentz, K. C.; Savin, D. A., Chain Dispersity Effects on Brush Properties of Surface-Grafted Polycaprolactone-Modified Silica Nanoparticles: Unique Scaling Behavior in the Concentrated Polymer Brush Regime. *Macromolecules* **2017**, *50* (14), 5565-5573.
284. Marino Arroyo, T. B., An atomistic-based finite deformation membrane for single layer crystalline films. *Journal of the Mechanics and Physics of Solids* **2002**, 1941-1977.
285. Ashby, M. F.; Cebon, D., Materials selection in mechanical design. *Le Journal de Physique IV* **1993**, *03* (C7), C7-1-C7-9.
286. Richard Robertson, R. B., Some Elastic moduli of Bisphenol A Polycarbonate. *Journal of Polymer Science Part A* **1964**, *2*, 4889-4901.
287. J. Brandrup, E. H. I., E. A. Grulke, *Polymer Handbook*. Wiley: New York, 1999.
288. Kubo, A.; Albina, J.-M.; Umeno, Y., Construction of master yield stress curves for polycarbonate: A coarse-grained molecular dynamics study. *Polymer* **2019**, *177*, 84-90.
289. Nishida, M.; Yamaguchi, M.; Todo, M.; Takayama, T.; Häggblad, H. Å.; Jonsén, P., Evaluation of dynamic compressive properties of PLA polymer blends using split Hopkinson pressure bar. In *DYMAT 2009 - 9th International Conferences on the Mechanical and Physical Behaviour of Materials under Dynamic Loading*, 2009; pp 909-915.
290. Hernandez, C.; Maranon, A.; Ashcroft, I. A.; Casas-Rodriguez, J. P., A computational determination of the Cowper-Symonds parameters from a single Taylor test. *Applied Mathematical Modelling* **2013**, *37* (7), 4698-4708.
291. Xu, M. M.; Huang, G. Y.; Feng, S. S.; McShane, G. J.; Stronge, W. J., Static and Dynamic Properties of Semi-Crystalline Polyethylene. *Polymers (Basel)* **2016**, *8* (4).
292. Snedeker, J. G.; Niederer, P.; Schmidlin, F. R.; Farshad, M.; Demetropoulos, C. K.; Lee, J. B.; Yang, K. H., Strain-rate dependent material properties of the porcine and human kidney capsule. *J Biomech* **2005**, *38* (5), 1011-21.
293. Shadlou, S.; Ahmadi-Moghadam, B.; Taheri, F., The effect of strain-rate on the tensile and compressive behavior of graphene reinforced epoxy/nanocomposites. *Materials & Design* **2014**, *59*, 439-447.
294. Hsu, D. D.; Xia, W.; Song, J.; Keten, S., Glass-Transition and Side-Chain Dynamics in Thin Films: Explaining Dissimilar Free Surface Effects for Polystyrene vs Poly(methyl methacrylate). *ACS Macro Letters* **2016**, *5* (4), 481-486.
295. Giuntoli, A.; Puosi, F.; Leporini, D.; Starr, F. W.; Douglas, J. F., Predictive relation for the alpha-relaxation time of a coarse-grained polymer melt under steady shear. *Science Advances* **2020**, *6*, 1-9.
296. Dunbar, M.; Keten, S., Energy Renormalization for Coarse-Graining a Biomimetic Copolymer, Poly(catechol-styrene). *Macromolecules* **2020**, *53* (21), 9397-9405.

297. Corsi, P.; Roma, E.; Gasperi, T.; Bruni, F.; Capone, B., Exploiting scaling laws for designing polymeric bottle brushes: a theoretical coarse-graining for homopolymeric branched polymers. *Phys Chem Chem Phys* **2019**, *21* (27), 14873-14878.
298. Hsu, H.-P.; Paul, W.; Rathgeber, S.; Binder, K., Characteristic Length Scales and Radial Monomer Density Profiles of Molecular Bottle-Brushes: Simulation and Experiment. *Macromolecules* **2010**, *43* (3), 1592-1601.
299. Wang, Y.; Xie, T.; France-Lanord, A.; Berkley, A.; Johnson, J. A.; Shao-Horn, Y.; Grossman, J. C., Toward Designing Highly Conductive Polymer Electrolytes by Machine Learning Assisted Coarse-Grained Molecular Dynamics. *Chemistry of Materials* **2020**, *32* (10), 4144-4151.
300. Husic, B. E.; Charron, N. E.; Lemm, D.; Wang, J.; Perez, A.; Majewski, M.; Kramer, A.; Chen, Y.; Olsson, S.; de Fabritiis, G.; Noe, F.; Clementi, C., Coarse graining molecular dynamics with graph neural networks. *J Chem Phys* **2020**, *153* (19), 194101.
301. Li, W.; Burkhart, C.; Polinska, P.; Harmandaris, V.; Doxastakis, M., Backmapping coarse-grained macromolecules: An efficient and versatile machine learning approach. *J Chem Phys* **2020**, *153* (4), 041101.